



HAL
open science

Nanosensor technology for road pavements monitoring

Maria Barriera

► **To cite this version:**

Maria Barriera. Nanosensor technology for road pavements monitoring. Infrastructures de transport. Institut Polytechnique de Paris, 2020. English. NNT : 2020IPPAX092 . tel-03168047

HAL Id: tel-03168047

<https://theses.hal.science/tel-03168047v1>

Submitted on 12 Mar 2021

HAL is a multi-disciplinary open access archive for the deposit and dissemination of scientific research documents, whether they are published or not. The documents may come from teaching and research institutions in France or abroad, or from public or private research centers.

L'archive ouverte pluridisciplinaire **HAL**, est destinée au dépôt et à la diffusion de documents scientifiques de niveau recherche, publiés ou non, émanant des établissements d'enseignement et de recherche français ou étrangers, des laboratoires publics ou privés.

Nanosensor technology for road pavement monitoring

Thèse de doctorat de l'Institut Polytechnique de Paris
préparée à l'Ecole Polytechnique

École doctorale n°626 Ecole Doctorale de l'Institut Polytechnique de
Paris (ED IP Paris)
Spécialité de doctorat: Sciences et technologies industrielles

Thèse présentée et soutenue à Palaiseau, le 18/12/2020, par

Maria Barriera

Composition du Jury :

Cédric SAUZEAT IDTPE, Université de Lyon	Président
John HARVEY Professeur, University of California	Rapporteur
Nizar LAJNEF Professeur associé, Michigan State University	Rapporteur
Juliette BLANC ITPE, Université Gustave Eiffel	Examineur
Cédric SAUZEAT IDTPE, Université de Lyon	Examineur
Bérengère LEBENTAL ICPC, Université Gustave Eiffel/Ecole Polytechnique	Directeur de thèse
Simon POUGET Directeur Recherche & Innovation, Eiffage Route	Co-Directeur de thèse
Pierre HORNYCH IDTPE, Université Gustave Eiffel	Invité
Julien VAN ROMPU ITPE, Eiffage Route	Invité



INSTITUT
POLYTECHNIQUE
DE PARIS



EIFFAGE



Université
Gustave Eiffel

Thèse de Doctorat de
L'ÉCOLE POLYTECHNIQUE
Spécialité: Sciences et technologies industrielles

Nanosensor technology for road pavement monitoring

par **Maria BARRIERA**

Soutenue le 18 Décembre 2020
devant le jury composé de

Rapporteur	M. John Harvey	University of California
Rapporteur	M. Nizar Lajnef	Michigan State University
Examinatrice	Mme Juliette Blanc	Université Gustave Eiffel
Examineur/Président	M. Cédric Sauzeat	Université de Lyon / ENTPE
Invité	M. Pierre Hornych	Université Gustave Eiffel
Invité	M. Julien Van Rompu	EIFFAGE Route
Directrice de thèse	Mme Bérengère LEBENTAL	Université Gustave Eiffel LPCICM (Ecole Polytechnique/CNRS)
Encadrant	M. Simon POUGET	EIFFAGE Route

FUNDING

This research was carried out within the network-wide training programme SMARTI ETN (Sustainable Multi-functional Automated Resilient Transport Infrastructures European Training Network). SMARTI has received funding from the European Union's Horizon 2020 Programme under the Marie Curie-Sklodowska Actions for research, technological development, and demonstration, grant n. 721493.

Al mio coraggio e alla mia forza di volontà.

ACKNOWLEDGEMENTS

I would first like to express my gratitude to all the members of the dissertation committee: Professors John HARVEY and Nizar LAJNEF, Dr Juliette BLANC, Dr Cédric SAUZEAT, and Dr Pierre HORNYCH. Thank you for taking the time to read my dissertation and providing such detailed comments and feedbacks. I greatly appreciated that and I believe that you helped me to improve this work and have a better approach to research in the future. The completion of this dissertation would not have been possible without the support of my supervisors, Dr Bérengère LEBENTAL and Dr Simon POUGET who supervised my work since the beginning and Dr Julien VAN ROMPU who I have had the pleasure to work with in the last year. My immense gratitude for believing in me, for sharing your deep knowledge with me, and for your commitment to this work. All the discussions that we had in the last three years were very helpful and constructive. Working with you was an honour and I feel very lucky. To all the people that want to start a PhD, I wish to be supervised by people like you.

I am also grateful to my colleagues of the SMARTI project, Nilo, Domenico, Giulia, Rufus, Iain, Mario, Gaspare, Philippe, Konstantinos, Pawan, Ronald, Antonino, Paulina, and Natasha. I would also like to extend my gratitude to the project coordinator Dr Davide LO PRESTI, the project managers Dr Ana JIMÉNEZ DEL BARCO CARRIÓN and Dr Ahmed ABED, and all the supervisors. Being part of this project has been one of the best experiences of my life. Within SMARTI, I had the opportunity to grow as a professional and to spend really good time with amazing people.

I am extremely grateful to my colleagues of the R&D department of Eiffage Route, Samira, Julien W., Flavien, Diego, and Frédéric (now Director of the Research Centre of Eiffage Route). I also wish to thank all the staff of the Research Centre of Eiffage Route. Three years ago, when I walked in the door of the laboratory for the first time, I was new to the country and I could not speak a word of French. Thank you for welcoming me with joy and warmth, for your patience, for the work that we have done together and for your support.

Many thanks to François OLARD for supporting and believing in me and for all the discussions that we had in the last three years.

I also wish to thank all the staff of the LPICM, the Université Gustave Eiffel and Altaroad, for the work that we have done together. It was a pleasure to work with you.

I wish to thank all my friends, Roberta, Federica, Giada, Cristina, Caterina, Maria Giovanna, Marco, Michel, Natalia, Mirela and Ana. Your help and support has been fundamental for the accomplishment of this work.

And last but not least, I am extremely grateful to my family. To my mom, dad, brother, sister, grandparents and all my relatives, you are the pillars of my life.

RESUME

Le réseau routier est l'un des atouts majeurs d'un pays. L'évaluation des conditions routières et de leur évolution dans le temps est essentielle pour l'établissement des plans d'entretien rentables. Ces derniers doivent être adaptés aux données sur l'état des chaussées collectées en continu tout au long de la durée de vie d'une route, dont l'analyse peut déclencher des actions de maintenance au bon moment. À cet égard, l'instrumentation de la chaussée permet un suivi continu et à distance sans interruption de la circulation. Cependant, cela reste un défi scientifique et technologique majeur en termes de résilience des dispositifs à l'environnement routier difficile ainsi que de stratégies d'interprétation des données des capteurs. L'objectif global de cette thèse est de prouver la faisabilité du monitoring des routes par technologies de détection embarquées en démontrant l'exploitabilité des données des capteurs pour évaluer le vieillissement de la route et en fournissant une technologie à haute performance et faible intrusion.

Dans un premier temps, nous avons étudié la pertinence de l'instrumentation pour le diagnostic précoce de l'endommagement: nous avons travaillé sur un essai de fatigue accélère à échelle 1 réalisé sur quatre structures ayant des couches bitumineuses différentes. L'ensemble de données a été fourni par l'essai réalisé à l'Université Gustave Eiffel dans le cadre du projet BioReparation. Les performances des sections ont fait l'objet d'un suivi comprenant des méthodes traditionnelles (telles que les déflexions du faisceau de Benkelman, les déviations FWD et l'inspection visuelle) et l'instrumentation (tels que des jauges de déformation et des sondes de température). Il a été constaté que les mesures des capteurs permettaient de détecter l'apparition d'un endommagement par fatigue bien avant les méthodes de surveillance traditionnelles et de fournir des informations fiables sur les conditions mécaniques réelles de la chaussée pendant la durée de l'essai.

Ainsi, nous avons approfondi l'utilisation des capteurs embarqués pour le calcul inverse des conditions mécaniques des chaussées par l'instrumentation d'une route existante (site industriel d'Eiffage Route) avec des jauges de déformation et la solution InTRACK d'Altaroad. L'InTRACK a donné des résultats très prometteurs en termes de conception et d'adaptabilité du système à l'environnement routier. Les jauges de déformation ont été exploitées lors d'une campagne de mesures avec un camion de charge connue. Il a été constaté qu'à des températures élevées, la sensibilité des mesures des capteurs à la position transversale du camion par rapport à l'emplacement des capteurs est très élevée. Des calculs ont ensuite été réalisés dans Viscoroute© pour évaluer le comportement de différentes

couches. Les résultats montrent qu'à des températures élevées, un modèle viscoélastique de la chaussée avec des interfaces viscoélastiques contribue à une meilleure prédiction du comportement de la chaussée sous une charge mobile.

Dans l'ensemble, les études effectuées dans les deux premières parties ont montré que l'instrumentation peut être déployée pour suivre l'état de la chaussée tout au long de sa durée de vie et alerter pour la maintenance. Cependant, un grand nombre de capteurs est nécessaire pour développer des stratégies de traitement des données qui tiennent compte de l'influence de différentes conditions de chargement (température, vitesse, trajectoire du véhicule). Le déploiement d'un grand réseau de capteurs semble être limité par les coûts des dispositifs disponibles sur le marché ainsi que par leur géométrie et leur éventuel caractère intrusif dans la chaussée. À cet égard, les résultats prometteurs obtenus avec l'InTRACK ont motivé l'étude menée dans la dernière partie de la thèse. En particulier, nous avons exploité les propriétés exceptionnelles des nanomatériaux de carbone pour améliorer la solution InTRACK d'Altroad avec des capteurs de déformation plus sensibles. Nous avons fabriqué un capteur de déformation à base de nanocarbone sans hystérésis, de haute stabilité et noyable, et nous avons validé sa pertinence pour le monitoring des routes avec un essai accéléré à échelle 1. Le matériau nanocarbone actif était un nanocomposite carbone-argile: des feuilles de graphène supportées sur sépiolite ont été mélangées à des nanotubes de carbone, formant un matériau piézorésistif. Il a été dispersé dans l'eau et coulé goutte à goutte sur un substrat en verre E sur une surface de 1600 mm² et un substrat en polyimide sur une surface de 30 mm². Les dispositifs sur polyimide ont en outre été encapsulés entre deux feuilles thermoplastiques compatibles avec le bitume puis intégrés dans la chaussée. La structure résultante a été testée à l'aide d'un essai accéléré de l'Université Gustave Eiffel. Les résultats ont clairement prouvé la pertinence des nanocapteurs à une utilisation dans des conditions réelles de suivi des routes: les capteurs sont restés opérationnels pendant toute la durée du test, leurs signaux ont suivi les conditions de charge, avec une sensibilité à la déformation augmentée d'un facteur 600 par rapport aux capteurs commerciaux.

ABSTRACT

The road network is one of the major assets in our countries. The assessment of pavement conditions and their evolution with time is essential for the establishment of cost-effective maintenance plans. The latter need to be tuned to pavement conditions data continuously collected along the lifetime of a road, whose analysis can trigger maintenance actions at the right time. In this respect, pavement instrumentation allows remote and continuous monitoring with no traffic disruption. However, it remains a major scientific and technological challenge in terms of devices resilience to the harsh road environment as well as of strategies for sensor data interpretation. The overall goal of this thesis is to prove the feasibility of embedded pavement monitoring by demonstrating the exploitability of embedded sensor data to assess road ageing, and by providing a high performance, low intrusiveness technology.

First, the relevance of instrumentation for early damage detection was investigated: we worked on the full-scale fatigue test carried out on four pavement structures having different bituminous layers. The dataset was provided by the accelerated pavement test performed at the University Gustave Eiffel within the BioRepavation project. The performances of all sections were monitored regularly by using traditional monitoring methods (such as Benkelman beam deflections, FWD deflections, and visual inspection) and instrumentation (such as asphalt strain gauges and temperature probes). It emerged that sensor measurements were able to detect the occurrence of fatigue well before traditional monitoring methods and provide reliable information about the actual pavement mechanical conditions over the duration of the test.

Thus, we further explored the use of embedded sensors for inverse calculation of pavement mechanical conditions via the instrumentation of an existing road (Eiffage Route industrial site) with asphalt strain gauges (ASGs) and the Altaroad's InTRACK solution. The InTRACK gave very promising results in terms of design, and adaptability of the system to the road environment. The asphalt strain gauges were exploited during a measurements campaign with a truck of known load. It emerged that, at high temperatures, the sensitivity of sensor measurements to the truck transverse position with respect to the sensor location is very high. To this respect the InTRACK, integrating a large number of sensors, could be deployed to develop data interpretation strategies to account for trajectory variation. Finally, a model was built in Viscoroute© to fit measured strain profiles and inverse calculate the pavement mechanical conditions. It emerged that at high temperatures a viscoelastic model

that takes into account the viscoelastic behaviour of the interfaces can better predict the pavement response under moving loads. The elastic model with fully bonded interfaces (used in French pavement design method) does not fit experimental results.

Overall, the first two parts showed that instrumentation can be deployed to track pavement conditions over its service life and alert for maintenance. However, a large number of sensors is required for the development of data treatment strategies that account for the influence of varying loading conditions (temperature, speed, vehicle trajectory). The deployment of a large sensor network seems to be restricted by the costs of devices available on the market as well as their geometry and their possible intrusiveness in the road pavement. In this respect, the promising results obtained with the InTRACK motivated the study conducted in the last part of the thesis. In particular we exploited the properties of carbon nanomaterials to upgrade the Altaroad's InTRACK solution with higher sensitivity strain sensors and we lay the foundations to make the device wireless. We fabricated a hysteresis-free, high-stability, embeddable nanocarbon-based strain sensor and we validated its relevance for pavement monitoring with accelerated pavement testing. The active nanocarbon material was a carbon-clay nanocomposite: graphene sheets supported on sepiolite were mixed with multi-walled carbon nanotubes, forming a piezoresistive material. It was dispersed in water and drop-casted onto E-glass substrate over 1600 mm² area and polyimide substrate over 30 mm² surface area. The devices on polyimide were further encapsulated between two bitumen-compatible thermoplastic sheets and then integrated into pavement. The resulting structure was tested using an accelerated pavement testing facility at the University Gustave Eiffel. The results clearly proved the suitability of the nanosensors for use in real-life pavement monitoring conditions: the sensors remained operational over the duration of the test, their signals followed the loadings conditions, with sensitivity to strain enhanced by a factor of 600 compared to commercial sensors.

TABLE OF CONTENTS

1	Context: Road pavement monitoring and nanotechnologies.....	1
1.1	Introduction.....	1
1.2	Road pavement	3
1.2.1	Pavement structure composition.....	3
1.2.2	Pavement structures in France.....	4
1.2.3	Mechanical behaviour of pavement structure.....	6
1.3	Bituminous materials	8
1.3.1	Aggregates	8
1.3.2	Bituminous binders.....	9
1.3.3	Overview of bituminous mixtures in the road industry.....	10
1.4	Thermo-mechanical behaviour of bituminous materials	11
1.4.1	Linear viscoelasticity (LVE) of bituminous materials	12
1.4.1.1	Creep and relaxation for a LVE material	12
1.4.1.2	Definition of complex modulus and Poisson ratio.....	14
1.4.1.3	Time Temperature Superposition Principle (TTSP)	16
1.4.2	Modelling LVE behaviour of bituminous materials.....	17
1.5	Modelling and pavement design	20
1.5.1	Modelling of pavement mechanical behaviour	20
1.5.1.1	Alizé-LCPC.....	22
1.5.1.2	Viscoroute©	23
1.5.2	Notions of pavement design	25
1.5.2.1	The ASSHTO pavement design guide	26
1.5.2.2	The French pavement design guide.....	27
1.6	In situ pavement monitoring with traditional technologies	28
1.6.1	Sensing solutions	29
1.6.1.1	Strain measurements	29
1.6.1.2	Deflection measurements	33

1.6.1.3	Temperature measurements	35
1.6.1.4	Moisture measurements	36
1.6.1.5	Pressure measurements	37
1.6.2	Instrumented sections	37
1.6.2.1	The Virginia Smart Road (Al-Qadi et al., 2004)	37
1.6.2.2	Test section in the State of Maine (Swett et al., 2008)	38
1.6.2.3	State of Virginia: instrumentation of Route 114 in Christiansburg (L. Wang et al., 2012)	40
1.6.2.4	The instrumentation of the A41N highway in France (Gaborit et al., 2014) 42	
1.6.2.5	SMARTVIA®, the smart road (Pouteau et al., 2016)	43
1.6.2.6	Instrumented test section in China (Ai et al., 2017)	44
1.6.2.7	Monitoring of the motorway A10 in France (Juliette Blanc et al., 2017) 45	
1.6.2.8	Continuous monitoring by using geophones and ASGs (French motorway) (Duong, Blanc, Hornych, Bouveret, et al., 2018)	46
1.7	Potential of carbon nanomaterials (CNMs) for road pavement monitoring	47
1.7.1	Carbon nanomaterials (CNMs): definition, structure and main properties ...	48
1.7.2	Applications in civil engineering	50
1.7.2.1	CNM-based composite materials	51
1.7.2.2	CNM-based strain sensors	55
1.8	Conclusions	59
2	Detection of pavement ageing based on instrumentation – Accelerated Pavement Testing	62
2.1	Introduction	62
2.2	Description of the full scale experiment and monitoring methods	63
2.2.1	The fatigue carousel facility	63
2.2.2	Tested pavement sections	64
2.2.3	Outline of the fatigue evaluation	65
2.2.4	Monitoring methods	65
2.2.4.1	Visual crack inspections	66

2.2.4.2	Benkelman beam deflections	66
2.2.4.3	Falling Weight Deflectometer (FWD) deflections.....	67
2.2.4.4	Pavement instrumentation	67
2.3	Comparison between traditional monitoring methods and instrumentation.....	69
2.3.1	Traditional monitoring methods	69
2.3.1.1	Visual crack inspections.....	69
2.3.1.2	Benkelman beam deflections	70
2.3.1.3	Falling Weight Deflectometer (FWD) deflections.....	72
2.3.2	Monitoring based on instrumentation.....	74
2.3.2.1	Survival rate to installation	74
2.3.2.2	Definition of signal shape parameters	75
2.3.2.3	Evolution of the maximum longitudinal strain	76
2.3.2.4	Signal shape evolution	77
2.3.3	Discussion.....	81
2.4	Comparison between field measured strain and inverse calculated strain.....	83
2.4.1	Assessment of pavement conditions via inverse calculation of FWD measurements: methodology	83
2.4.1.1	Inverse calculation from representative basin.....	86
2.4.1.2	Inverse calculation from basin in non-damaged zone.....	89
2.4.1.3	Inverse calculation from basin in damaged zone	92
2.4.2	Comparison between numerical and experimental strains at the bottom of the bituminous layers.....	94
2.5	Development of a procedure for temperature correction of measured strains.....	95
2.6	Conclusions.....	102
3	Inverse calculation of pavement response based on instrumentation – Corbas trial section.....	105
3.1	Introduction.....	105
3.2	Description of the trial section.....	106
3.2.1	Experimental site	106
3.2.2	Sensors installation.....	106

3.2.3	Data acquisition system.....	108
3.2.4	Measurement campaign.....	109
3.2.4.1	Geometry of the truck used for the measurement campaign	109
3.2.4.2	Definition of truck trajectories.....	110
3.2.4.3	Truck speed.....	111
3.2.5	Modelling in Viscoroute©.....	111
3.3	Feedback from the InTRACK solution	111
3.3.1	Resilience to construction phase	112
3.3.2	Quality of interface and impact on the road pavement	113
3.3.3	Discussion	113
3.4	Laboratory characterizations of the pavement structure.....	114
3.4.1	Coring campaign	114
3.4.2	Characterization of the bitumen of the tack coat emulsion.....	115
3.4.2.1	Complex modulus test: procedure description.....	115
3.4.2.2	Complex modulus test: analysis of results.....	116
3.4.3	Asphalt mixes.....	117
3.4.3.1	Cyclic Indirect Tensile Test (CITT): procedure and results	117
3.4.3.2	Modal Test (MT): procedure and results	119
3.4.3.3	Direct Tension-Compression Test (DTCT): procedure and results	121
3.4.3.4	Comparison of results and comments	122
3.5	Measurement campaign: results	123
3.6	Modelling in Viscoroute©: results	131
3.7	Conclusions	135
4	Development and deployment of an embeddable nano-carbon based strain technology	138
4.1	Introduction	138
4.2	Device fabrication process.....	140
4.2.1	Materials: Carbon-clay nanocomposite.....	140
4.2.2	Water based ink formulation	140
4.2.3	Device design, ink deposition and encapsulation.....	141

4.2.3.1	For layer morphology analysis.....	141
4.2.3.2	For electrical, thermal and electromechanical characterizations in the lab 141	
4.2.3.3	For deployment in the pavement.....	142
4.2.4	Deployment in the pavement.....	145
4.3	Device characterizations.....	148
4.3.1	Lab characterization.....	148
4.3.2	Field characterization.....	149
4.3.2.1	Accelerated pavement test.....	149
4.3.2.2	Acquisition system.....	150
4.3.2.3	Data post-processing.....	151
4.4	Performances of C/Sep-MWCNT-bases strain sensors.....	152
4.4.1	Morphology and electrical properties of the C/Sep-MWCNT material.....	152
4.4.2	Device variability on E-glass.....	154
4.4.3	Strain sensors on E-glass.....	155
4.4.4	Strain sensors on PI PCBs.....	157
4.5	Performances of C/Sep-MWCNT-bases strain sensors under accelerated pavement testing159	
4.5.1	Resilience to the construction phase.....	159
4.5.2	Resilience to the accelerated pavement testing.....	160
4.5.3	Sensitivity to wheel passage.....	161
4.5.4	Quality of interface and impact on the road.....	163
4.6	Conclusions.....	164
5	Conclusions and Perspectives.....	166
5.1	Conclusions.....	166
5.2	Perspectives.....	171
6	Appendixes.....	174
6.1	Appendix 1.....	174
6.2	Appendix 2.....	175
6.3	Appendix 3.....	178

6.4	Appendix 4	178
6.5	Appendix 5	181
6.5.1	Bitumen of the tack coat emulsion	181
6.5.2	Asphalt mixes	182
6.6	Appendix 6	185
6.7	Appendix 7	189
6.7.1	Four-point bending test	189
6.7.2	Gauge factor calculation and regression coefficients.....	190
6.7.3	Definition of the densification ratio	190
6.7.4	Resistance of devices on E-glass as a function of the number of drops for batch B34	191
6.7.5	Thermal sensitivity of device NA30 on E-glass.....	192
6.7.6	Loading of the sensors with strain cycles.....	192
6.7.7	Geometry and resistance values for the devices used for pavement embedding 194	
6.7.8	Sensitivity to wheel passage and on-site GF	195
6.7.9	Regression statistics and coefficients	196
7	Bibliography of the author	197
7.1	List of publications	197
7.1.1	Published papers.....	197
7.1.2	Papers under review	198
7.1.3	Papers under submission	198
7.2	Presentations in conferences and workshops.....	198
7.3	Awards.....	198
8	Bibliography	199

LIST OF FIGURES

Figure 1.1 Use of preventive maintenance to extend the expected time between pavement failure and so extend its service life. (Adapted from (European Union Road Federation, 2014))	2
Figure 1.2 Structure of a road pavement.	4
Figure 1.3 Pavement structure categories in France: (a) Flexible pavements; (b) Bituminous pavements; (c)Semi-rigid pavements; (d) Rigid pavements; (e) Pavement with mixed structure; (f) Pavements with inverse structure.	6
Figure 1.4 Stresses due to traffic.	7
Figure 1.5 (Right) Fatigue cracking; (Left) Rutting (Source: https://pavementinteractive.org/).	7
Figure 1.6 Transverse (thermal) cracking (Source: https://pavementinteractive.org/).	8
Figure 1.7 Typical mechanical behaviour domains of bituminous mixtures with respect to strain amplitude (ϵ) and number of applied loading cycles (N) for a given temperature (T) (François Olard et al., 2003) (François Olard & Di Benedetto, 2003) (Hervé Di Benedetto, Sauzéat, et al., 2004).	11
Figure 1.8 Typical response of a viscoelastic material. (Left) Applied strain. (Right) Response in terms of stress.	12
Figure 1.9 Creep test for a LVE material: (Left) applied stress; (Right) resulting strain. ...	13
Figure 1.10 Relaxation test for a LVE material: (Left) applied strain; (Right) resulting stress.	14
Figure 1.11 Representation of the Huet-Sayegh model.	18
Figure 1.12 Representation of the 2S2P1D model (François Olard et al., 2003) (François Olard & Di Benedetto, 2003) (Hervé Di Benedetto, Sauzéat, et al., 2004).	19
Figure 1.13 Representation of the 2S2P1D model parameters on the Cole-Cole plot.	20
Figure 1.14 Burmister's multi layered system.	21
Figure 1.15 Example of structure composition in Alizé-LCPC (https://www.alize-lcpc.com/documents/ALIZE-LCPC-MU-v1.5-EN.pdf).	22
Figure 1.16 Standard loading condition in Alizé-LCPC (https://www.alize-lcpc.com/documents/ALIZE-LCPC-MU-v1.5-EN.pdf).	23
Figure 1.17 Modelling of the pavement under moving load in Viscoroute© (readapted from (A Chabot et al., 2010)).	24
Figure 1.18 Example of the pavement structure composition in Viscoroute©.	24

Figure 1.19 Example of loading setup in Viscoroute©.....	25
Figure 1.20 Loading geometries available in Viscoroute©: (Left) rectangular, (Right) elliptical.....	25
Figure 1.21 Schematics of an H-gauge (adapted from http://www.jewellinstruments.com/).	30
Figure 1.22 Schematics of H-gauges orientation with respect to traffic direction: longitudinal and transverse directions.	30
Figure 1.23 Schematics of a vertical asphalt strain gauge (adapted from https://www.ctlgroupp.com/).	31
Figure 1.24 FBG functioning principle.	33
Figure 1.25 Schematics of LVDT single-layer deflectometer installed in a road pavement (reproduced from (Tabatabaee & Sebaaly, 1990))......	34
Figure 1.26 Geophone functioning principle.	35
Figure 1.27 K-type thermocouple probes.....	36
Figure 1.28 Sensor installation. (a) Pressure cells; (b) H-shaped asphalt strain gauges; (c) Thermocouples; (d) TDR probes; (e) Vibrating wire strain gauges (reproduced from (Al-Qadi et al., 2004))......	38
Figure 1.29 Layout of the instrumented section in the state of Maine (reproduced from (Swett et al., 2008)).	39
Figure 1.30 Test section in the state of Maine. Time of loading as a function of speed at different depths in the pavement structure (reproduced from (Swett et al., 2008)).	39
Figure 1.31 . Layout of the sensors in Route 114 (reproduced from (L. Wang et al., 2012)).	41
Figure 1.32 Pavement monitoring system designed for Route 114 in Christiansburg (reproduced from (L. Wang et al., 2012)).	42
Figure 1.33 Instrumentation of the A41N highway in France. (a) Longitudinal strain in the subbase course for different truck trajectories (V=12 km/h, T=20 °C) and (b) longitudinal strain in the subbase for different speed (same trajectory, T=23 °C) (reproduced from (Gaborit et al., 2014))......	43
Figure 1.34 Architecture of the data acquisition system of SMARTVIA® (reproduced from (Pouteau et al., 2016)).	44
Figure 1.35 Instrumented section in China. (a) Layout of the instrumentation and (b) focus on the sensors (reproduced from (Ai et al., 2017)).	45

Figure 1.36 Road structure and sensors layout of the motorway A10 in France. (a) Sections PR15+700, PR15+900, PR16+850, and PR17+100 and (b) section PR16+026 (reproduced from (Juliette Blanc et al., 2017)).	46
Figure 1.37 French motorway. (left) Pavement structure and (right) sensors layout (reproduced from (Duong, Blanc, Hornych, Bouveret, et al., 2018)).	47
Figure 1.38 Lateral position of geophones G1, G3, and G4 installed on a French motorway (reproduced from (Duong, Blanc, Hornych, Bouveret, et al., 2018)).	47
Figure 1.39 Outline of the piezoresistive behaviour of percolating layer of conducting material. (a) Resting configuration; (b) Application of tensile stress; (c) Application of compressive stress.	51
Figure 1.40 (a) Outline of the laboratory equipment used for compressive loading and impulse loading; (b) CNT/cement composite embedded in concrete pavement; (c) Response of the CNT/cement composite under the passage of a minivan (reproduced from (Han et al., 2009)).	54
Figure 1.41 Resistivity response of 5.3 % CNFs/asphalt composite under compressive stress at (a) 25 Hz and (b) 10 Hz (reproduced from (Rizvi et al., 2016)).	54
Figure 1.42 (Left) Change in resistance versus strain of the SWCNTs-PE sensor under monotonic loading (sensor mounted on the side of an aluminium coupon); (Right) Change in resistance of the SWCNTs-PE sensor and reference gauge under cyclic loading (sensors mounted on a cementitious plate) (reproduced from (Loh et al., 2005)).	56
Figure 1.43 Composite beam-column connection in the laboratory (reproduced from (Burton et al., 2016)).	56
Figure 1.44 Strain-resistance response of CNT polymer composite film under quasi-static loading: initial loading (a) and failure of the structure (b) (reproduced from (Burton et al., 2016)).	57
Figure 1.45 Data collected from a graphite-based flexible sensor attached to a metal girder of a highway bridge (reproduced from (Zymelka et al., 2017)).	57
Figure 1.46 Laboratory test of graphene-based sensor. (a) Monotonic test: relative resistance change versus applied strain. (b) Cyclic test: relative resistance change with repeated tensile strain of 0.16 % (reproduced from (Nie et al., 2019)).	58
Figure 1.47 Survival rate of commercial strain gauges (left) and CNT-based ones (right) (reproduced from (Michelis, 2016)).	58
Figure 1.48 Outline of the specimen (reproduced from (Ghaddab et al., 2014)).	59

Figure 2.1 The University Gustave Eiffel fatigue carousel: four arms are controlled by a central electro-hydraulic motor unit. The perimeter is 120 m long.	64
Figure 2.2 Sections on the APT. (Left) Pavement structure; (Right) layout of the test site.	65
Figure 2.3 Benkelman beam (a) Photo; (b) Schematics.	66
Figure 2.4 Outline of the FWD loading and measurement conditions. The load is applied with a load plate and the pavement response is measured by 9 geophones.	67
Figure 2.5 Plan of the location of instrumented areas in the fatigue carousel.	68
Figure 2.6 Outline of Mix1 and Mix3: ASGs locations.	68
Figure 2.7 Outline of Mix2: ASGs locations. Sensors L1, L2, L3, and T1 are part of this study.	69
Figure 2.8 Outline of EME2: ASGs locations. Sensors L1, L2, L3, T1, CTL1, CTL2, Dyn1 and Dyn2 are part of this study.	69
Figure 2.9 Pictures of the damaged sections at the end of the test (1.4 million loads). (Left) Mix3 section; (Right) EME2 section.	70
Figure 2.10 Deflection measured with the Benkelman beam on the four sections. Measurements are spaced about every 4 m. The mean temperature in the bituminous layers is recorded.	71
Figure 2.11 Basin representative of the behaviour of the overall section calculated at 0, 500000, 1 million, 1.1 million, 1.2 million, 1.3 million and 1.4 million loads. (a) Mix 1, (b) Mix 2, (c) Mix 3, (d) EME2.	73
Figure 2.12 Deflection measured by geophone D1 of the FWD on the four sections. At 0 and 500000 loads measurements are spaced about every 5 meters; from 1 million to 1.4 million loads measurements are spaced about every 1 meter. The mean temperature in the bituminous layers is recorded.	74
Figure 2.13 Signal treatment process on the APT. (Left) 4 arms passages. (Right) Average of the 4 arms passages and time-to-distance transformation of the x-axis.	75
Figure 2.14 Definition of the signal shape parameters.	76
Figure 2.15 Evolution of the maximum longitudinal strain (ϵ_{\max}) at the bottom of the asphalt layer over the duration of the fatigue test. (Left) Response for each section obtained by averaging the response of the sensors. (Right) Response of each sensor.	77
Figure 2.16 Evolution of the asymmetry factor F for all the sensors over the duration of the fatigue test.	78

Figure 2.17 Evolution of the shape parameters A_1 , A_2 and d_{tot} with the increase of the number of loads. Sensors: (a) Mix1-L3, (b) Mix2-L2, (c) Mix3-L1, (d) EME2-Dyn2.....	79
Figure 2.18 Representation of sensors location on the plots" FWD deflection - distance on the track": (a) section Mix1, (b) section Mix2, (c) section Mix3 and (d) section EME2....	82
Figure 2.19 Representation of sensors location on the crack pattern produced for sections Mix3 (top) and EME2 (bottom). The crack pattern reports the cracks observed at 1 million and 1.1 million loads. Sensors are located in the areas where the first cracks arose.....	83
Figure 2.20 Outline of the adopted inverse calculation methodology.....	86
Figure 2.21 Results obtained in Alizé by performing an inverse calculation from the measured basins representative of the whole structures: (top-left) Mix1, (top-right) Mix2, (bottom-left) Mix3 and (bottom-right) EME2. The measured basins are well predicted by the model.	88
Figure 2.22 Mix 3 section, FWD deflection measured by geophone D1 at 1 million loads as a function of the distance on the track. The bracket indicates the range of FWD measurements taken into account for the calculation of deflection basin representative of the non-damaged zone.	90
Figure 2.23 EME2 section, FWD deflection measured by geophone D1 at 1 million loads as a function of the distance on the track. The bracket indicates the range of FWD measurements taken into account for the calculation of deflection basin representative of the non-damaged zone.	90
Figure 2.24 Results obtained in Alizé by performing an inverse calculation from the measured basins representative of the non-damaged zone: (left) Mix3, (right) EME2. The measured basins are well predicted by the model.	91
Figure 2.25 Mix 3 section, FWD deflection measured by geophone D1 at 1 million loads as a function of the distance on the track. The bracket indicates the range of FWD measurements taken into account for the calculation of deflection basin representative of the non-damaged zone.	92
Figure 2.26 EME2 section, FWD deflection measured by geophone D1 at 1 million loads as a function of the distance on the track. The bracket indicates the range of FWD measurements taken into account for the calculation of deflection basin representative of the non-damaged zone.	93
Figure 2.27 Results obtained in Alizé by performing an inverse calculation from the measured basins representative of the damaged zone: (left) Mix3, (right) EME2. The measured basins are well predicted by the model.	94

Figure 2.28 Fig. 5 Longitudinal maximum strain evolution in the first 136 800 loads.	97
Figure 2.29 Strain ($\mu\epsilon$)-Temperature ($^{\circ}\text{C}$) numerical relations and polynomial fits.....	98
Figure 2.30 Equivalent maximum longitudinal strain at the reference temperature of 10°C for sensors (a) Mix1-L1, (b) Mix2-L3, (c) Mix1-L3 and (d) EME2-Dyn2. Correction applied in the first 136800 loads.	99
Figure 2.31 Comparison between the slopes of the trendlines fitting the measured and the equivalent strain values. Correction applied in the first 136800 loads.	100
Figure 2.32 Longitudinal maximum strain evolution from 178000 to 500000 loads.	101
Figure 2.33 Equivalent maximum longitudinal strain at the reference temperature of 10°C for sensors (a) Mix1-L1, (b) Mix1-L3, (c) Mix2-L2 and (d) Mix2-L3. Loading range: 178000 - 500000 loads	101
Figure 2.34 Comparison between the slopes of the trendlines fitting the measured and the equivalent strain values. Loading range: 178000 - 500000 loads.....	102
Figure 3.1 Altaroad's InTrack solution during installation on experimental construction site (October 2017).	107
Figure 3.2 ASGs provided by CTL Group employed for the instrumentation of the section. The sensors are characterised by an H-shape measuring 10 cm x 13 cm with a thickness of 2 cm.	108
Figure 3.3 Sensors configuration in the experimental site. The sensors are located on the top of the existing pavement. Two types of sensors are employed: ASGs from CTL Group and Altaroad InTRACK system. All wired are collected in the inspection sump.	108
Figure 3.4 Experimental site: location of the external box and the inspection sump.	109
Figure 3.5 Temperature measurements at the surfaces of the road pavement recorded the 17 th and 18 th July 2018.	110
Figure 3.6 Geometry of the loading truck used for the measurement campaign.	110
Figure 3.7 Truck trajectory: (Left) sand strip placed on the top of the asphalt layer for the identification of the $\Delta D_{y,\text{ref}}$ and ΔD_y parameters, (Right) visualisation of the two trajectories in the field.....	111
Figure 3.8 Response of one of the sensors of the Altaroad's InTrack during the construction process (acquisition frequency of 0.1 Hz). The different phases of the installation can be clearly recognised: hot mix asphalt paving, compaction, cooling down.	112
Figure 3.9 Sample cored on the trial section 2 months after the installation: very good bonding at the interfaces InTrack/asphalt.	113

Figure 3.10 Sample cored in the experimental site: the road structure is composed of 5 bituminous layers.....	115
Figure 3.11 Samples used to perform the complex modulus test on the bitumen of the tack coat emulsion: (Left) 25 mm test sample; (Right) 8 mm test sample.....	116
Figure 3.12 2S2P1D model fitting for bitumen 70/100 tested with DSR (from -20 °C to 70 °C and from 0.01 Hz to 10 Hz): (Left) master curve ($T_{ref} = 15\text{ °C}$), (Right) Cole-Cole diagram.	117
Figure 3.13 Cyclic indirect tensile test on BBSG 2 0/10-35/50. Loading application and failure mechanism.....	118
Figure 3.14 2S2P1D model fitting for BBSG 2 0/10-35/50 tested under CIT test (from -25 °C to 30 °C and from 0.031 Hz to 10 Hz): (Left) master curve ($T_{ref} = 15\text{ °C}$), (Right) Cole-Cole diagram.	119
Figure 3.15 Equipment and test set-up for the modal test: the impact hammer and the accelerometer are connected to a signal conditioner, which is connected to a data acquisition device, which is connected to a laptop.	120
Figure 3.16 2S2P1D model fitting for BBSG 2 0/10-35/50 tested under modal test (at 17 °C, 35 °C and 50 °C): (Left) master curve ($T_{ref} = 15\text{ °C}$), (Right) Cole-Cole diagram.	120
Figure 3.17 Slab are compacted using a French wheel compactor. Samples are cored in two directions, the vertical direction (II) and the compacting direction (I).	121
Figure 3.18 (Left) instrumented sample before the test; (Right) visualization of the three extensometers used to measure the axial deformation.	122
Figure 3.19 2S2P1D model fitting for BBSG 2 0/10-35/50 tested under direct tension-compression test (from -20 °C to 50 °C and from 0.01 Hz to 20 Hz): (Left) master curves ($T_{ref} = 15\text{ °C}$), (Right) Cole-Cole diagrams.	122
Figure 3.20 Superposition of the 2S2P1D models fitted for the cyclic indirect tensile test, the modal test, and the direct tension-compression test performed on the BBSG 2 0/10-35/50 (Layer 1 in the experimental site).....	123
Figure 3.21 Example of a signal collected during the campaign of measurements. Knowing the geometry of the passing truck, the actual speed can be determined with the time interval of the two peaks caused by two axles. The abscissa $x = 0\text{ m}$ identifies the passage of the front axle.	124
Figure 3.22 Methodology used to analyse sensor data. (Top left) Definition of the maximum longitudinal strain ϵ_{max} for each peak corresponding to the truck axles. (Top right) Grouping of all measurements of the same sensor recorded at the same main truck speed and trajectory.	

(Bottom) Visualization of ϵ_{\max} by passage and by axle and calculation of the coefficients of variation.....	125
Figure 3.23 Average of strain measurements recorded for sensor B66 (longitudinal) on 17 th July. The black curve is the average of passages from P1 to P5, while the red curve is the average of passages P6 and P7.....	131
Figure 3.24 Average of strain measurements recorded for sensor B66 (longitudinal) on 17 th July and 18 th July. The black curve is the average of passages P6 and P7, while the red curve is the average of passages from P12 to P17.	131
Figure 3.25 Example of a loading configuration entered in Viscoroute©. The wheels load moves horizontally along the x-axis at the actual truck speed. The wheel-to-pavement contact area is considered as elliptical.	133
Figure 4.1 (Left) Geometry of a prepared substrate. (Right) Image of a finalized device.	142
Figure 4.2 Top left - composition of the substrate. Top right - image of the substrate. Bottom - Geometry of the substrate.	143
Figure 4.3 Four devices after fabrication.	144
Figure 4.4 Sensors after encapsulation: Kapton tape on top and silicon on bottom.	144
Figure 4.5 Resistance measurements of two sensors encapsulated with Kapton tape (Sensor 6) and silicon (Sensor 8).....	145
Figure 4.6 (a) Layout of sensing layer assembly process; (b) Nanosensors and strain gauges glued to thermoplastic sheet.	146
Figure 4.7 The left bar is the assembled system before inclusion in the pavement. The four bars to the right are Altaroad's regular InTrack solutions.	146
Figure 4.8 Pavement structure (Left); test track (Right).	147
Figure 4.9 Different phases of the construction process: tack-coat emulsion application (top left), paving (top right), 1st compaction (bottom left), and 2nd compaction (bottom right).	148
Figure 4.10 Multiphysics bench enabling four-point bending with or without temperature control. (Left) Bending setup, motors and load cells with current source and acquisition cards. (Right) Bending setup mounted within the environmental chamber enabling temperature and relative humidity control.	149
Figure 4.11 FABAC machine from University Gustave Eiffel: (Left) functioning principle, (Right) zoom of wheels and chain while turning.	150
Figure 4.12 Signal treatment process of two data acquisitions from a nanosensor. Loading case V: 7.5 t at 3 m/s; temperature recorded at -4 cm below pavement equal to 14.3 °C.	152

Figure 4.13 SEM images of C/Sep-MWCNT particles (0.5 % wt MWCNTs) at different scales. Well separated MWNTs and sepiolite fibers are encased in a disordered, porous carbon matrix.....	153
Figure 4.14 SEM (a-c) and AFM (d) images of a 30-drop C/Sep-MWNT layer at different scales. a) The layer surface is characterized by marked valleys and ridges, while at lower scales (b-c), the material appear continuous and very disordered. d) AFM estimated roughness.....	154
Figure 4.15 Relationship between thickness of the C/Sep-MWCNTs layer, resistance and drop number.....	154
Figure 4.16 Response of E-glass device NA32 of batch B34 to a ramp-wise loading up to 0.06 % strain; (a) extension ramp; (b) unloading ramp; (c) time response.	156
Figure 4.17 Device c5 resistance variation under strain cycles up to 0.06% strain at 2 mHz: (top left) time response, (top right) resistance-strain curve, (bottom) resistance-strain curve, zoom on the 1st and 13th cycle.	158
Figure 4.18 Response of nanosensor N 2-3 during the construction process (acquisition frequency of 0.1 Hz). The different phases of the installation can be clearly recognised: hot mix asphalt placement, 1 st compaction and 2 nd compaction (heavier than the 1 st).....	160
Figure 4.19 Low frequency (1 Hz) acquisition over the duration of the test (1 week). (Left) dR/R evolution for nanosensors. (Right) strain (%) evolution for commercial strain gauges.	161
Figure 4.20 Sensors N 2-3 and C 2-3: 100 Hz acquisition on 09/04/2019 at 10:22. Load = 5.5 t, speed = 0.5 km/h, and temperature = 9.5 °C. (Left) time-response. (Right) resistance-strain response. Sensor N 2-3 features saturation.....	162
Figure 4.21 Maximum peak values evolution over the duration of the test. Left: sensors N 2-3 and C 2-3. Right: sensors N 1-1 and C 1-1.....	163
Figure 4.22.....	164
Figure 6.1 Sensor Mix1-L1: evolution of the shape parameters A1, A2 and dtot with the increase of the number of loads.....	174
Figure 6.2 Sensor Mix2-L3: evolution of the shape parameters A1, A2 and dtot with the increase of the number of loads.....	174
Figure 6.3 Sensor EME2-L1: evolution of the shape parameters A1, A2 and dtot with the increase of the number of loads.....	175
Figure 6.4 Sensor EME2-L2: evolution of the shape parameters A1, A2 and dtot with the increase of the number of loads.....	175

Figure 6.5 Equivalent maximum longitudinal strain at the reference temperature of 10 °C for Mix1-L3. Correction applied in the first 136800 loads.....	176
Figure 6.6 Equivalent maximum longitudinal strain at the reference temperature of 10 °C for Mix2-L2. Correction applied in the first 136800 loads.....	176
Figure 6.7 Equivalent maximum longitudinal strain at the reference temperature of 10 °C for EME2-L1. Correction applied in the first 136800 loads.....	177
Figure 6.8 Equivalent maximum longitudinal strain at the reference temperature of 10 °C for EME2-L1. Correction applied in the first 136800 loads.....	177
Figure 6.9 (Top) Trajectory T0: $\Delta D_y - \Delta D_{y,ref} = 0$ cm. (Bottom) Trajectory T1: $\Delta D_y - \Delta D_{y,ref} = 30$ cm.....	178
Figure 6.10 Coring plan followed on the experimental site to extract 4 samples: C7, C8, C9 and C10. A coring drill with a diameter of 230 mm was applied down to a depth of about 200 mm.....	179
Figure 6.11 DSR device EC-Twist 502 manufactured by Anton-Paar at the Eiffage Route Research Centre.....	181
Figure 6.12 Overview of the MTS hydraulic press used for the CIT and DTCT on the asphalt mix. The press is equipped with a hydraulic power control, a load unit control and an environmental chamber (MTS 651).	183
Figure 6.13 2S2P1D model fitting for Layer 5 beam-shaped sample tested under modal test (at 17 °C, 35 °C and 50 °C): (Left) master curve ($T_{ref} = 15$ °C), (Right) Cole-Cole diagram.	184
Figure 6.14 Schematics of the four-point bending test.	190
Figure 6.15 Densification ratio as a function of the number of drop.	191
Figure 6.16 Thermal sensitivity of E-glass device NA30.	192
Figure 6.17 NA30 resistance variation under strain cycles at 0.15 mm/s - 0.003%/s –0.05 Hz. Left – time response. Right – resistance-strain curve.....	193
Figure 6.18 Device c7 resistance variation under strain cycles up to 0.06% strain at 2 mHz: (top left) time response, (top right) resistance-strain curve, (bottom) resistance-strain curve, zoom on the 1st and 13th cycle.	194
Figure 6.19 4 devices on PI PCBs, later used for embedding in pavement, imaged through confocal microscopy. Note that the colour scale is qualitative only, as confocal microscopy does not provide accurate evaluation of thickness for such type of materials.	195

Figure 6.20 Sensors N 2-3 and C 2-3: 100 Hz acquisition on 10/04/2019 at 10:50. Load = 6.5 t, speed = 1.5 km/h, and temperature = 9.5 °C. (Left) time-response. (Right) resistance-strain response. 196

Figure 6.21 Sensors N 2-3 and C 2-3: 100 Hz acquisition on 10/04/2019 at 12:12. Load = 6.5 t, speed = 2.5 km/h, and temperature = 10.1 °C. (Left) time-response. (Right) resistance-strain response. 196

LIST OF TABLES

Table 1.1 Granular classes of aggregates according to the European Standard (NF EN 13043:2003-08) (AFNOR, 2003).	9
Table 1.2 Boltzmann superposition principle.....	12
Table 1.3 Specifications of some H-gauges available on the market.....	31
Table 1.4 Examples of carbon allotropes structures: fullerene, single-walled carbon nanotubes, multi-walled carbon nanotubes, graphene, graphite, and diamond.....	49
Table 2.1 Fatigue test loading conditions. 65 kN 1 million loads at 72 km/h followed by additional 75 kN 400000 loads at 43 km/h.....	65
Table 2.2 Mean Benkelman beam deflections recorded at 0, 500000, 1 million, 1.1 million, 1.2 million, 1.3 million and 1.4 million loads on the four sections. The mean temperature in the asphalt layer is also reported.....	71
Table 2.3 Survival rate of ASGs to installation for each section.	74
Table 2.4 Mean value of the asymmetry factor F calculated over 1.4 million loads along with the standard deviation. The coefficient of variation is calculated as the ration between the standard deviation and the mean.	78
Table 2.5 Correlation between A_1 , A_2 and d_{tot} . R^2 is obtained by plotting the mean value between A_1 and A_2 as a function of d_{tot} for all sensors.....	80
Table 2.6 Correlation between A_1 , A_2 and ϵ_{max} , $\epsilon_{min,1}$ and $\epsilon_{min,2}$. R^2 is obtained by plotting the mean value between A_1 and A_2 as a function of ϵ_{max} , $\epsilon_{min,1}$ and $\epsilon_{min,2}$ for all sensors.	80
Table 2.7 Comparison between Benkelman beam measured deflections (average between 800000 and 1 million loads) and deflections calculated in Alizé.....	88
Table 2.8 Comparison between mechanical properties of the structure at the beginning and at the end of the test. Sections Mix1 and Mix2. The moduli of bituminous layers are considered at 10 °C and 10 Hz.	88
Table 2.9 Comparison between mechanical properties of the structure at the beginning and at the end of the test. Sections Mix3 and EME2. The moduli of bituminous layers are considered at 10 °C and 10 Hz.	89
Table 2.10 Comparison between Benkelman beam deflections measured in the non-damaged zone (average between 800000 and 1 million loads) and deflections calculated in Alizé..	91
Table 2.11 Comparison between mechanical properties of the structure in the non-damaged zone at the beginning and at the end of the test. Sections Mix3 and EME2. Sections Mix3 and EME2. The moduli of bituminous layers are considered at 10 °C and 10 Hz.....	91

Table 2.12 Comparison between Benkelman beam deflections measured in the damaged zone (average between 800000 and 1 million loads) and deflections calculated in Alizé..	94
Table 2.13 Comparison between mechanical properties of the structure in the damaged zone at the beginning and at the end of the test. Sections Mix3 and EME2. Sections Mix3 and EME2. The moduli of bituminous layers are considered at 10 °C and 10 Hz.	94
Table 2.14 Maximum strain at the bottom of the asphalt layer calculated in Alizé considering the structures inversed calculated from FWD deflection basins at 1 million loads and strains measured with ASGs.	95
Table 2.15 Surface layers viscoelastic parameters entered in Viscoroute©	97
Table 2.16 Unbound granular base and subgrade parameters entered in Viscoroute©	97
Table 2.17 Coefficients of the polynomial functions used to fit the numerical results.....	98
Table 3.1 Loading conditions during the measurement campaign.....	111
Table 3.2 Structure of the pavement derived from the cores extracted in the field.	115
Table 3.3 Summary of all tests performed on the mix BBSG 2 0/10-35/50.....	117
Table 3.4 Summary of all tests performed on the road structure of the experimental site.	123
Table 3.5 Deformations measured on the experimental site during the campaign of measurements with a truck: surface temperature from 50 °C to 54 °C, $\Delta D_y - \Delta D_{y,ref} = 0$ cm (trajectory T0), speed = 10 km/h. The signals are grouped per sensors. Positive values correspond to extension.....	126
Table 3.6 Deformations measured on the experimental site during the campaign of measurements with a truck: surface temperature = 50 °C, $\Delta D_y - \Delta D_{y,ref} = 30$ cm (trajectory T1), speed = 10 km/h. The signals are grouped per sensors. Positive values correspond to extension.....	128
Table 3.7 Characteristic of the structure implemented in Viscoroute©.....	132
Table 3.8 Example of the pavement layers parameters used for the viscoelastic calculation in Viscoroute©.	133
Table 3.9 Comparison between experimental and model data based on pavement response in terms of horizontal (longitudinal and transverse) strain. Red curves are measured strains. Purple curves are results obtained from elastic model with fully bonded interfaces. Orange curves are results obtained from viscoelastic model with fully bonded interfaces. Blue curves are results obtained from viscoelastic model with viscoelastic interfaces.	134
Table 4.1 Loading cases description: 5 loading configurations.	150
Table 6.1 Nomenclature, height and picture of the cores extracted in the field.....	179

Table 6.2 Temperatures and frequencies used for DSR complex modulus test on the bitumen of the tack coat emulsion.	181
Table 6.3 2S2P1D model parameters for the bitumen of the tack coat emulsion.	182
Table 6.4 Composition of the BBSG 2 0/10-35/50.	182
Table 6.5 2S2P1D model parameters and air void content for the tested specimens (Layer 1).	183
Table 6.6 Measurements retained after performing the CITT on a disk-shaped sample of Layer 3: temperatures of 15, 25 and 35 °C and frequency of 10 Hz.	184
Table 6.7 2S2P1D model parameters for Layer 5.	184
Table 6.8 Details of all the truck passages: theoretical loading configuration, actual loading configuration and measured surface temperature.	185
Table 6.9 Deformations measured on the experimental site during the campaign of measurements with a truck: surface temperature = 55 °C, $\Delta D_y - \Delta D_{y,ref} = 0$ cm (trajectory T0), speed = 20 km/h. The signals are grouped per sensors. Positive values correspond to extension.	186
Table 6.10 Deformations measured on the experimental site during the campaign of measurements with a truck: surface temperature from 36 °C to 37 °C, $\Delta D_y - \Delta D_{y,ref} = 0$ cm (trajectory T0), speed = 20 km/h. The signals are grouped per sensors. Positive values correspond to extension.	187
Table 6.11 Values of resistance (k Ω) for different numbers of drops for six devices prepared with the same ink.	191
Table 6.12 Geometry (mm) and values of resistance (M Ω) for 4 devices batch prepared with the same ink.	195
Table 6.13 Regression statistics and coefficients obtained from the multiple linear regression carried out for sensors N2-3 and C2-3.	196

1 CONTEXT: ROAD PAVEMENT MONITORING AND NANOTECHNOLOGIES

1.1

1.2 Introduction

It is widely acknowledged that any country needs strong road networks for social and economic development, and, consequently, efficiency and proper functioning. According to the last statistics provided by the European Union Road Federation (ERF) the European road network consists of about 5 million km, out of them about 1 million just in France, and its estimated value is over 8000 billion €. Furthermore, according to the ERF, roads carry more freight (50.1 %) and more passengers (70.9 %) than all other modes combined, and they provides jobs for about 10.6 million people (European Union Road Federation, 2020).

It is easy to deduce that a non-adequate road network can strongly affect the distribution of goods, people movement, and the accessibility of places, causing damage to economic growth and to people quality of life. In this respect one of the strategic objectives of EU transport policy is the improvement of the transport infrastructure system in order to make it more efficient, safe, and secure (European Commission, 2019).

Roads, like any physical asset, deteriorate with time due to normal aging, usage, environmental causes, and accidental events. When it comes to road management and maintenance, the traditional approach used by road owners and road management entities

consist in focusing their budget on pavements that are in the worst conditions. However studies show that roads might need maintenance even if they visually appear in good conditions (European Union Road Federation, 2014) (Figure 1.1). This concept is at the basis of the “preventive maintenance” approach, which takes the form of a series of treatments applied on the pavement in order to fix small deteriorations, extend the expected time between failure and so extend its service life. The ERF reports on how road conditions get worse exponentially during their own service life, and how the latter can be prolonged efficiently if regular maintenance is conducted (Figure 1.1).

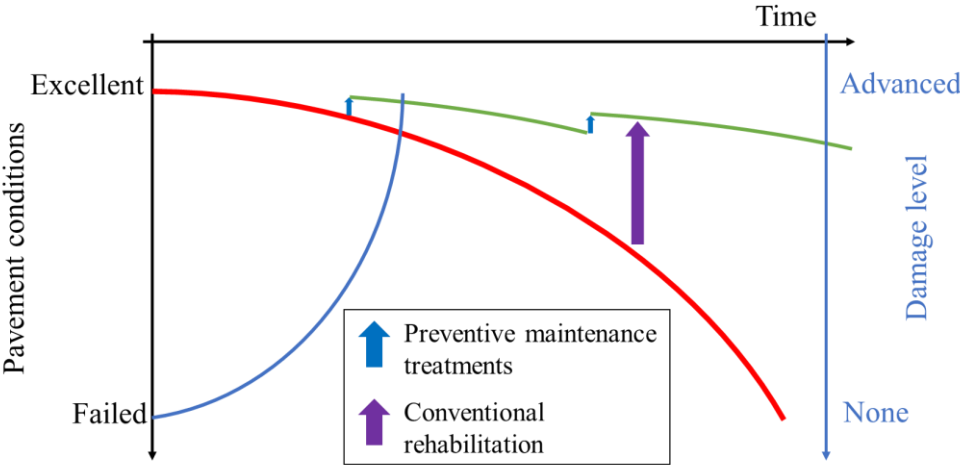


Figure 1.1 Use of preventive maintenance to extend the expected time between pavement failure and so extend its service life. (Adapted from (European Union Road Federation, 2014))

The implementation of such a strategy requires the diagnosis of pavement mechanical state. In this respect structural health-monitoring (SHM) is a widely applied concept for damage detection, localization and quantification (Balageas et al., 2006). This information is fundamental for the establishment of adequate pavement management systems (PMS) aimed at operating, maintaining, upgrading, and expanding the pavement through cost-effective practices (AASHTO, 1990).

Nowadays, the two approaches generally adopted for pavement evaluation are the detection of pavement surface conditions and the assessment of its structural state. Surface conditions are usually investigated manually, by visual inspections, or automatically, through specially equipped vehicles, such as a pavement profile scanner (Medina et al., 2014) (Tsai & Chatterjee, 2018) (Dejin Zhang et al., 2018) (Xiao Li & Goldberg, 2018). Pavement-bearing capacity can be calculated through the Falling Weigh Deflectometer (FWD) (Henia & Braber, 2008), the curviameter (Paquet, 1977), the Benkelman beam (Carneiro, 1966), and

the deflectograph (De Boissoudy et al., n.d.). These ex-situ monitoring solutions enable a homogenous observation of the overall road network surface conditions, but they are time-consuming (especially in the post-processing phase) and tend to detect damage when they have already appeared. They require traffic flow disruption, are costly, and provide only punctual at best, periodic (1 to 5 years) information. By contrast, in situ pavement monitoring designates solutions that allow continuous monitoring of the road health condition. These solutions rely on pavement instrumentation, namely integrating sensors within the road (Weinmann et al., 2004). The goal is to allow an accurate measurement of pavement response (in terms of stress, strain, deflection, temperature, etc.) at different layers of the road structure. Compared to the above-mentioned methodologies for pavement investigation, the interest in this type of approaches relies on the fact that the use of embedded sensors allows remote and continuous supervision of multiple layers without any traffic disruption. They pave the way towards the so-called “smart road” (Sun et al., 2018). This thesis will focus on road pavement monitoring via embedded sensing technologies.

Through a bibliographic approach, this section aims at exploring the current practices for in situ pavement monitoring and the promising approach based on nanotechnology. However, in a first place we set out what a pavement structure is in terms of composition and materials, as well as the tools for pavement modelling and design.

1.3 Road pavement

1.3.1 Pavement structure composition

The road pavement is a structure made of multiple superimposed layers of compacted and processed materials having different thickness. It has the function of reducing and distributing the stress so as not to damage the subgrade (native material underneath a constructed road), as well as providing adequate friction and smooth riding quality.

Typically the structure of a road pavement (Figure 1.2) consist of (SETRA & LCPC, 1994) (IDRRIM, 2017):

- The surface layer. The top layer of the pavement structure, thus the one that is directly in contact with the vehicle loads. It provides characteristics such as friction, smoothness, noise control, rutting resistance, drainage, and waterproofing. This layer is sometimes composed of two layers, the wearing course (top) and the binder course (bottom).

- The foundation layer is composed of the base course and subbase course. These layers provide the mechanical resistance to loads induced by vehicles to the structure. They contribute to drainage and to the distribution of stress over a larger area of the compacted subgrade in order not to exceed its strength. The subbase course also minimizes the intrusion of fines from the subgrade into the pavement structure and is usually made of lower quality materials than the base course.
- The compacted subgrade. The layer of natural soil adequately compacted to receive the stress from the layers above. It has the role of mechanical and thermal protection of the non-compacted soil (natural subgrade). In addition, during the construction process it allows the circulation of site machinery and the realization of the foundation layer.

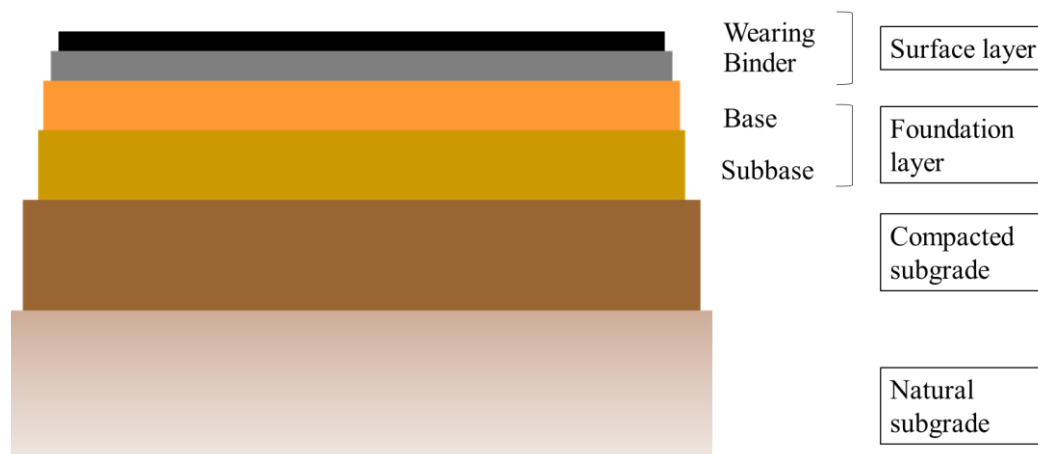


Figure 1.2 Structure of a road pavement.

Based on their structural behaviour, pavements are typically classified into rigid and flexible. The difference between them is based on the materials used and the manner in which loads are distributed to the subgrade: by flexural strength of the pavement in the first case, by grain-to-grain contacts of the aggregates in the latter. Hence, flexible pavements, having less flexural strength, act like a flexible sheet, while rigid pavements act like a rigid plate. In rigid pavements the base course and the surface layer usually form a unique layer.

1.3.2 Pavement structures in France

According to their layer composition and the constituent materials of each layer, road pavements in France can be classified in six categories (Figure 1.3) (SETRA & LCPC, 1994) (IDRRIM, 2017).

Flexible pavements are characterised by bituminous surface layer with a ≤ 12 cm-thickness resting on a foundation layer made of unbound granular material (UGM). Due to the composition of the foundation layer, the lateral distribution of vertical load is limited and strongly depends on its thickness. This type of structure is used in low traffic roads and need regular maintenance of the surface course in order to guarantee waterproofing.

Bituminous pavements consist of bituminous surface and base course where the subbase can be a bituminous layer or made of UGM. The presence of bituminous materials in the foundation layer guarantees the mitigation of load coming from the top layers. A tack coat bituminous emulsion is applied during the construction process in order to guarantee bonding between different layers, namely continuity in the transmission of load. Therefore, the maximum strain in extension occurs at the bottom of the last bituminous layer (base or subbase). This kind of structure is the most used in the French highway network.

Semi-rigid pavements are composed of a bituminous surface layer resting on a foundation course made of materials treated with hydraulic binders, which gives rigidity to the structure. The most critical areas in this type of structure are the interface between the surface and the foundation layer subjected to shear stress that can lead to debonding, and the bottom of the foundation layer subjected to tensile stress. This structure can be deployed for road networks subjected to high traffic. However, the surface course requires regular maintenance operation in order to remain waterproof.

Rigid pavements include a cement concrete slab as surface/base layer with at least a thickness of 12 cm. The subbase course, if present, can be in concrete or made of materials treated with hydraulic binder. Due to its high rigidity the concrete slab takes the stress caused by traffic, thus the subgrade is less stressed. This type of structures can be used for high traffic roads. Concerning the maintenance work, they mostly need joint filling.

Pavements with mixed structure are characterized by bituminous surface and base layers resting on a subbase layer with materials treated with hydraulic binders. The bituminous layers guarantee thermic protection and waterproofing. The bonding between the layers ensures less tensile stress on the bituminous layer, while the bottom of the subbase course takes bending stress.

Pavement with inverse structure are composed by bituminous surface and base layers and a subbase layer made of materials treated with hydraulic binders. A layer of UGM is interposed between the base and subbase courses, which avoids the rise of cracks due to thermally induced movements and shrinkage phenomena occurring in the subbase. This

latter provides rigidity to the structure. The bottom of the base course is subjected to tensile stress due to traffic loads, the amount of which depends on the thickness of the layer below.

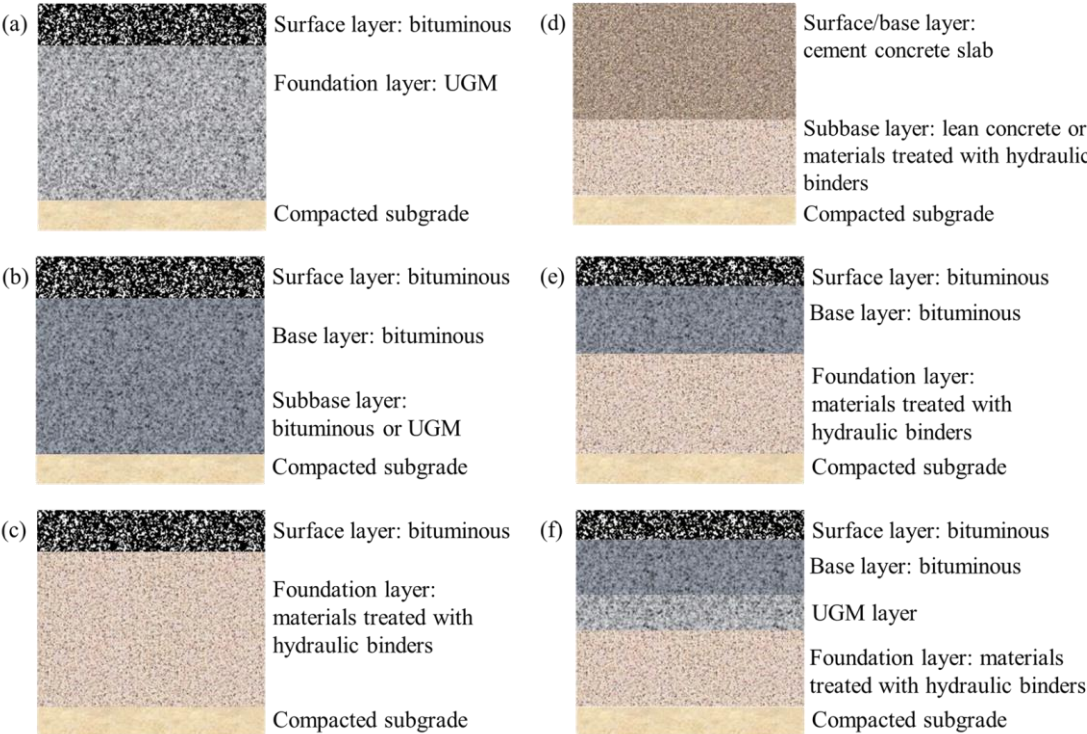


Figure 1.3 Pavement structure categories in France: (a) Flexible pavements; (b) Bituminous pavements; (c) Semi-rigid pavements; (d) Rigid pavements; (e) Pavement with mixed structure; (f) Pavements with inverse structure.

1.3.3 Mechanical behaviour of pavement structure

Due to the interaction with users and environment as well as through normal aging, road pavements is subjected to mechanical, thermal, physical and chemical events. The latter often act in a coupled manner and also result in mechanical stress to the pavement structure whose specifics depend on layers properties (materials and thickness) as well as on the degree of bonding at the interfaces. The main causes of stress and strain state in a pavement are traffic and temperature variations (Herve Di Benedetto & Corté, 2004).

Vehicle passages act as repeated loading cycles (up to several millions) to which the road pavement is subjected during its lifetime. This generates repeated stress in the structure both in the horizontal and vertical direction (Figure 1.4). Despite the stress associated to each loading cycle can be considered as small (deformation in the order of 10^{-4}), the cycles repetition may generate strain accumulation and irreversible damage. If the interfaces are glued, the structure acts as a monolithic beam. The repeated horizontal tensile stress at the bottom of each layer may induce micro degradations and lead to crack propagation into the

structure (fatigue) (Figure 1.5). Repeated vertical compressions may lead to the occurrence of permanent deformations (rutting) (Figure 1.5) (Moghaddam et al., 2011).

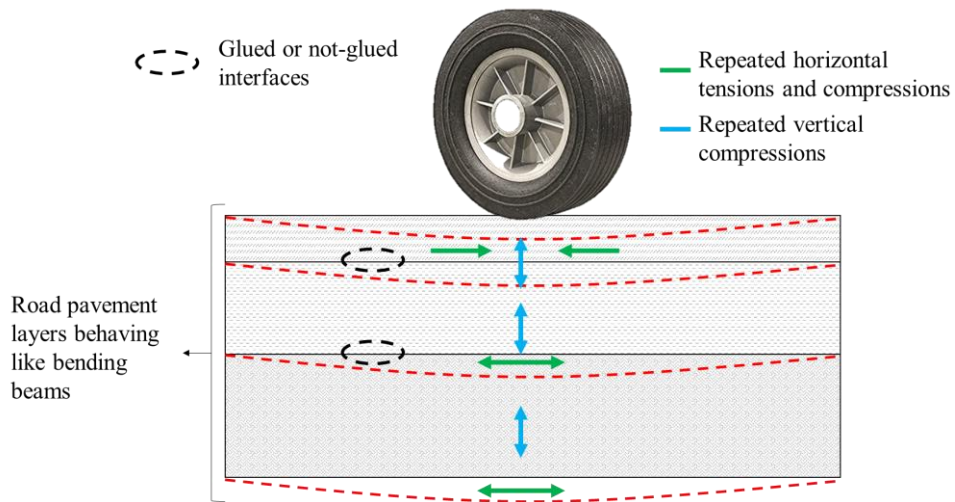


Figure 1.4 Stresses due to traffic.



Figure 1.5 (Right) Fatigue cracking; (Left) Rutting (Source: <https://pavementinteractive.org/>).

Similarly to traffic, weather variations generate mechanical stresses in pavement structures which depend on the nature of the materials composing each layer. Bituminous materials are thermosensitive, thus temperature variation generates a change of their modulus (stiffness). In addition, temperature oscillations (daily and seasonal) cause expansion-contraction phenomena. Cracks may be generated due to low temperature and may spread because of thermal cycles (top-down phenomenon) (Figure 1.6). Moreover, layers made of materials treated with hydraulic binders are subjected to shrinkage. The constraint due to friction at the interfaces may generate cracks in the bituminous layers, which may progress and cross the layer vertically or horizontally because of thermal cycles (bottom-up phenomenon).



Figure 1.6 Transverse (thermal) cracking (Source: <https://pavementinteractive.org/>).

1.4 Bituminous materials

A base knowledge of bituminous materials and their viscoelastic behaviour is an essential requisite before addressing pavement modelling and design methods.

A bituminous mixture can be defined as a composite material consisting of bitumen binder and mineral aggregates (coarse aggregates, fine aggregates, filler) (Herve Di Benedetto & Corté, 2004). The aggregates constitute the "skeleton" of the material and provide mechanical properties; cohesion is guaranteed by the binder or rather by the mix between the bitumen and the filler (mastic). Air is also present in the voids between the aggregates that are not filled with bitumen or mastic. The mechanical properties of each mix depend on the types and proportions of the "ingredients". In addition, depending on the field conditions and expectations in terms of mechanical behaviours, additives can be added to the mixture in order to improve its properties. The main features of a mix are workability, water sensitivity, strength, durability, rutting resistance, fatigue resistance, and costs.

1.4.1 Aggregates

Mineral aggregates are the main constituent of bituminous mixtures, hence the principal load-bearing components. They represent about the 95 % of the total mass, i.e. the 80-85 % of the total volume (Barksdale & National Stone Association, 1996). Their properties are governed by the European Standard (NF EN 13043:2003-08) (AFNOR, 2003).

Concerning their geometry, aggregates can have either a round or a crushed aspect depending on their origin. Typically, they present a round aspect when they come from

natural sources, like alluvial deposit, while a crushed aspect is characteristic of aggregates extracted from quarries by mechanical procedures. Aggregates can be then further processed in order to obtain a certain grain size, through screening, crushing, sieving, dusting, and washing. The grain size is important for aggregate classification, hence for any classification of bituminous mixture.

In fact, depending on the grain size, aggregates can be classified into homogeneous granular classes. Each class is defined by a minimal (d) and a maximal (D) grain size (Table 1.1). In order to avoid excessive dispersion in a class, the ratio D/d is set to 1.4, as reported in the European Standard (NF EN 13043:2003-08) (AFNOR, 2003).

By adding and mixing several grain classes it is possible to obtain the granular skeleton of a bituminous mixture (H. Schreuders & Marek, 1989) (Hervé Di Benedetto & Corté, 2004), which is characterized by a gradation. This latter has to be designed in order to maximize contacts between grains and minimize the air void content. However, sufficient air voids should be left in order to allow adequate bitumen penetration and avoid durability problems of the mix (F. Olard & Pouget, 2015b) (Fang et al., 2019).

Table 1.1 Granular classes of aggregates according to the European Standard (NF EN 13043:2003-08) (AFNOR, 2003).

	d (mm)	D (mm)
Coarse aggregates	≥ 2	≤ 45
Fine aggregates	> 0.063	≤ 2
Filler	-	≤ 0.063

1.4.2 Bituminous binders

Bituminous binders are adhesive materials containing bitumen. The term "bitumen" refers to a non-volatile, adhesive, and waterproof material, derived from crude oil (industrially produced bitumen) or present in natural asphalt (naturally occurring bitumen, from natural asphalt lakes and rock asphalt). The first form is the most used in paving industry (Neves et al., 2015) (Widyatmoko, 2016).

Despite its presence in low concentration (about 5 % in mass; 10-15 % in volume) in a bituminous mixture (compared to aggregate concentration), bitumen has important properties that strongly influence the rigidity of the mix and its response to traffic and thermal loads. Among these properties, adhesion to the aggregates, cohesion, viscoelasticity,

and waterproofing are the most important. Bitumen composition and consequently its properties, undergo changes between the application in the field and the end of its service life. This process is called "ageing" and depends on the initial composition of bitumen, the original type of crude oil used and how it was refined, the thermal cycles suffered after leaving the refinery, temperature and exposure to the environment during paving operations as well as during its service life (Neves et al., 2015).

Along with conventional bitumen, the paving industry also uses Polymer Modified Bitumen (PMBs) in order to improve mixture performances. Usually the content of polymer added is about the 3-7 wt% with respect to the bitumen. The two polymers most widely used for bitumen modification in road industry are an elastomer and a plastomer, respectively SBS (Styrene-Butadiene-Styrene) and EVA (Ethylene Vinyl Acetate). In Europe bitumen are classified according to their consistency through the needle penetration test (AFNOR, 2007b) measuring the depth of a standard needle in a bitumen sample at 25 °C. The penetration depth is measured in 1/10mm and allows placing the bitumen in one of the standard penetration grade classes. These classes are defined by lower and upper penetration depth thresholds. For example, the class 50/70 comprises all bitumen whose needle penetration test result at 25°C is comprised between 50/10 mm and 70/10 mm.

1.4.3 Overview of bituminous mixtures in the road industry

The European Standard (NF EN 13108-1) (AFNOR, 2007a) specifies the features, in terms of composition and mechanical performances, of bituminous mixtures for surface and foundation layer. For this latter, the standard indicates two families of acceptable materials in the French context:

- The GB ("*grave bitume*" in French), divided into three classes (2, 3, 4) and characterised by crushed aggregates, usually having a continuous gradation, and a bitumen 35/50 or 50/70. The bitumen content is low (around 4 wt%).
- The EME ("*enrobés à module élevé*" in French) divided into two classes (1, 2) and characterised by a high content of a hard bitumen (about 5.5 %) and continuous gradation in order to ensure a good fatigue resistance.

The mixtures used in France for the surface layer, as indicated in the standard, belong to the family of the BB ("*bétons bitumineux*" in French), having a high bitumen content (between 5 and 7 %). The BBSG ("*béton bitumineux semi-grenu*" in French) and BBME ("*béton bitumineux à module élevé*" in French) are deployed for thick surface layers (from 5 to 9

cm). The BBM ("*bétons bitumineux minces*" in French) are used for thicknesses between 3 and 5 cm; while the BBTM ("*bétons bitumineux très minces*" in French) and the BBUM ("*bétons bitumineux ultra minces*" in French) are used for thicknesses below 3 cm. Hence, the BBM, BBTM, and BBUM are used for wearing courses only.

1.5 Thermo-mechanical behaviour of bituminous materials

Bituminous mixtures behaviour depends on temperature (T), strain amplitude (ϵ), and number of applied loading cycles (N). For a given temperature it is possible to identify four mechanical behaviour domains as a function of strain amplitude and number of applied loading cycles (Figure 1.7).

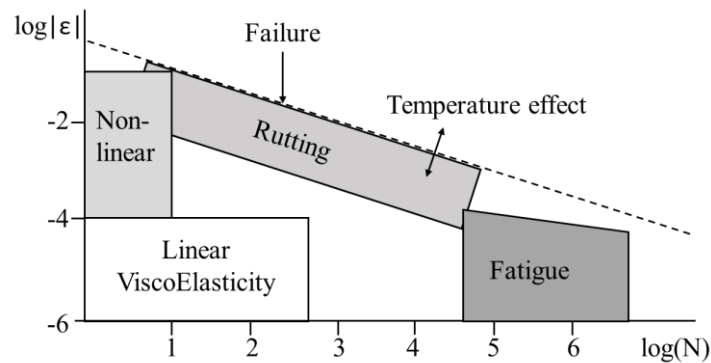


Figure 1.7 Typical mechanical behaviour domains of bituminous mixtures with respect to strain amplitude (ϵ) and number of applied loading cycles (N) for a given temperature (T) (François Olard et al., 2003) (François Olard & Di Benedetto, 2003) (Hervé Di Benedetto, Sauzéat, et al., 2004).

For strain amplitudes between 0.01% and about 3% and relatively small number of loading cycles (of the order of tens) the behaviour is non-linear. In the "small strain domain" ($\epsilon < 10^{-4}$) and up to few hundreds of loading cycles, bituminous mixtures exhibits a linear viscoelastic (LVE) behaviour. If the mixture undergoes small strains for a relatively high number of cycles (several tens of thousands) fatigue damage occurs. Finally, the application of repeated stress cycles non centred on zero (typical of traffic loads) can lead to the accumulation of permanent deformation (rutting). The proposed scheme (Figure 1.7) has to be considered as an indicative description of mixture mechanical behaviour domains. In reality the transitions between the different domains are not brutal and the proposed threshold values should be treated as indicators of the order of magnitude (Mangiafico, 2014).

1.5.1 Linear viscoelasticity (LVE) of bituminous materials

To be defined as viscoelastic a material must show a complete stress recovery when subjected to the application of a constant strain for a certain interval of time (Figure 1.8).

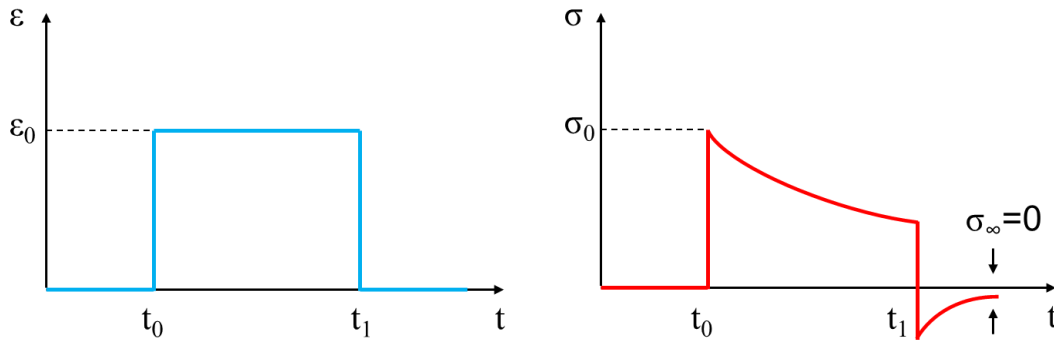


Figure 1.8 Typical response of a viscoelastic material. (Left) Applied strain. (Right) Response in terms of stress.

A viscoelastic material is characterised by a linear behaviour if it verifies the Boltzmann superposition principle, namely if its current response is equal to a superposition of the responses to each individual applied load (Salençon, 2016). In a more simple way, the relationship between stress and strain is linear at any time (Table 1.2).

Table 1.2 Boltzmann superposition principle.

Applied strain	Response
$\varepsilon_1(t)$	$\sigma_1(t)$
$\varepsilon_2(t)$	$\sigma_2(t)$
$\alpha \varepsilon_1(t) + \beta \varepsilon_2(t)$	$\alpha \sigma_1(t) + \beta \sigma_2(t)$

1.5.1.1 Creep and relaxation for a LVE material

Creep is defined as the characteristic of a material that undergoes increasing deformation under an instantaneous constant stress σ_0 applied at instant t_0 (Figure 1.9). If the applied stress is defined as:

$$\sigma(t) = \sigma_0 H(t - t_0) \quad (1.1)$$

Where

$$H(t - t_0) = \begin{cases} 0 & \text{if } t < 0 \\ 1 & \text{if } t \geq 0 \end{cases}$$

The material response in terms of strain can be expressed as:

$$\varepsilon(t) = \sigma_0 J(t_0, t) \quad (1.2)$$

Where $J(t_0, t)$ is the creep function that gives the material response at any time t for the stress σ_0 applied at the instant t_0 .

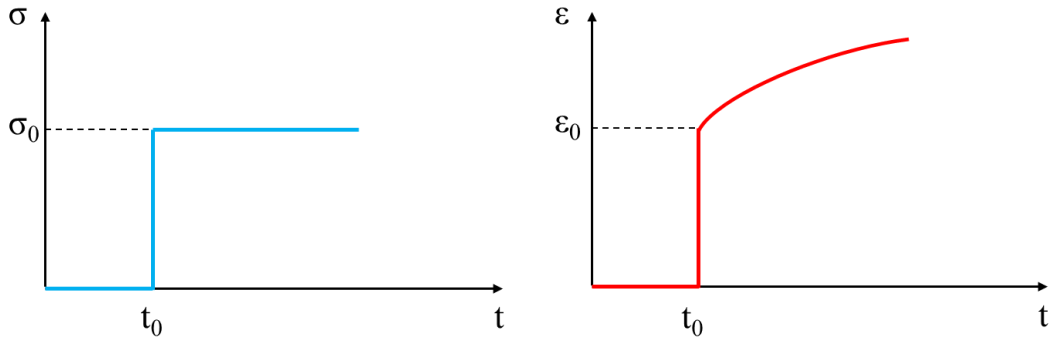


Figure 1.9 Creep test for a LVE material: (Left) applied stress; (Right) resulting strain.

If the applied stress is not constant but varies over time at a constant temperature, it is possible to use the incremental notation and define the strain variation $d\varepsilon(t)$ at the instant t for a stress variation $d\sigma(\tau)$ applied at the instant τ :

$$d\varepsilon(t) = d\sigma(\tau) J(\tau, t) \quad (1.3)$$

For a LVE material, by applying the Boltzmann superposition principle, the total strain response $\varepsilon(t)$ is equal to the sum of individual responses to each elementary stress variation:

$$\varepsilon(t) = \int_{t_0}^t J(\tau, t) d\sigma(\tau) \quad (1.4)$$

Relaxation, as the inverse of creep, is defined as the characteristic of a material that undergoes decreasing stress under an instantaneous constant strain ε_0 at instant t_0 (Figure 1.10). If the applied strain is defined as:

$$\varepsilon(t) = \varepsilon_0 H(t - t_0) \quad (1.5)$$

Where

$$H(t - t_0) = \begin{cases} 0 & \text{if } t < 0 \\ 1 & \text{if } t \geq 0 \end{cases}$$

The material response in terms of stress can be expressed as:

$$\sigma(t) = \varepsilon_0 R(t_0, t) \quad (1.6)$$

Where $R(t_0, t)$ is the relaxation function that gives the material response at any time t for the strain ε_0 applied at the instant t_0 .

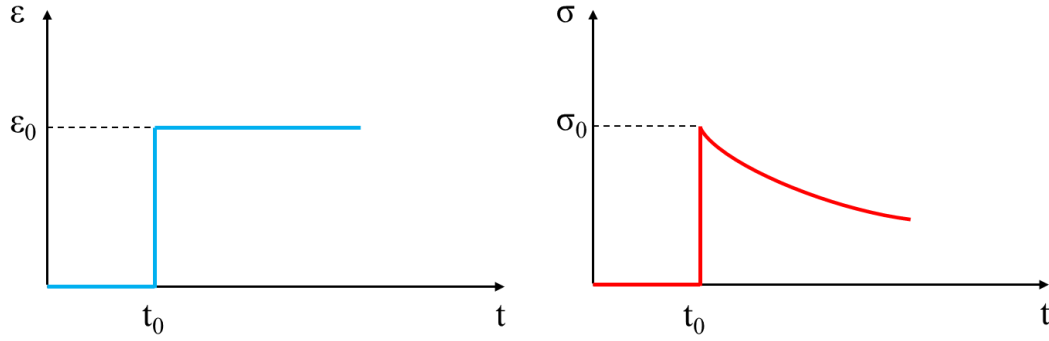


Figure 1.10 Relaxation test for a LVE material: (Left) applied strain; (Right) resulting stress.

If the applied strain is not constant but varies over time at a constant temperature, it is possible to use the incremental notation and define the stress variation $d\sigma(t)$ at the instant t for a strain variation $d\varepsilon(\tau)$ applied at the instant τ :

$$d\sigma(t) = d\varepsilon(\tau) R(\tau, t) \quad (1.7)$$

For a LVE material, by applying the Boltzmann superposition principle, the total stress response $\sigma(t)$ is equal to the sum of individual responses to each elementary strain variation:

$$\sigma(t) = \int_{t_0}^t R(\tau, t) d\varepsilon(\tau) \quad (1.8)$$

The integral equations (1.4) and (1.8) can be turned into algebraic (simplified) by applying the Laplace-Carson transform (Herve Di Benedetto & Corté, 2004). The Laplace-Carson transform \tilde{f} of a generic function $f(t)$, depending on time t , is defined as:

$$\tilde{f}(p) = p \int_0^{\infty} f(t) e^{-pt} dt \quad (1.9)$$

Where p is a complex variable corresponding to time in the transform domain.

Therefore, the equations (1.4) and (1.8) become similar to the equation of elasticity:

$$\tilde{\varepsilon}(p) = \tilde{J}(p) \tilde{\sigma}(p) \quad (1.10)$$

$$\tilde{\sigma}(p) = \tilde{R}(p) \tilde{\varepsilon}(p) \quad (1.11)$$

1.5.1.2 Definition of complex modulus and Poisson ratio

If a sinusoidal stress with a frequency f (equation (1.12)) is applied on a LVE material, its response in terms of strain will also be sinusoidal (equation (1.13)):

$$\sigma(t) = \sigma_0 \sin(\omega t) \quad (1.12)$$

$$\varepsilon(t) = \varepsilon_0 \sin(\omega t - \varphi) \quad (1.13)$$

Where $\omega=2\pi f$ and φ is the phase angle that indicates the phase lag between the two sinusoidal signals.

By using the complex notation, σ^* and ε^* can be defined as:

$$\sigma^*(t) = \sigma_0 e^{i\omega t} \text{ or } \sigma^*(t) = \text{Im}[\sigma^*(t)] \quad (1.14)$$

$$\varepsilon^*(t) = \varepsilon_0 e^{i(\omega t - \varphi)} \text{ or } \varepsilon^*(t) = \text{Im}[\varepsilon^*(t)] \quad (1.15)$$

Where Im is the imaginary part of the complex variable.

Equation (1.11) can then be written as:

$$\sigma^*(t) = \tilde{R}(i\omega)\varepsilon^*(t) \quad (1.16)$$

Therefore

$$E^*(\omega) = \tilde{R}(i\omega) = \frac{\sigma^*}{\varepsilon^*} \quad (1.17)$$

So that $E^*(\omega)$ is the complex modulus and is equal to the Laplace-Carson transform of the relaxation function calculated in $i\omega$. $E^*(\omega)$ can also be expressed as:

$$E^*(\omega) = \frac{\sigma_0 e^{i\omega t}}{\varepsilon_0 e^{i\omega t - \varphi}} = \frac{\sigma_0}{\varepsilon_0} e^{i\varphi} = |E^*| e^{i\varphi} \quad (1.18)$$

Where $|E^*|$ is the norm of the complex modulus.

Since E^* is complex, it is possible to isolate the real and imaginary parts:

$$E^* = E_1 + iE_2 = |E^*| \cos \varphi + i|E^*| \sin \varphi \quad (1.19)$$

E_1 is called "storage modulus" and represents the recoverable part of energy during loading, namely it is the elastic component of the LVE behaviour. E_2 is called "loss modulus" and represents the energy lost because of internal friction, namely it is the viscous component of the LVE behaviour. Equation (1.19) clearly shows how the phase angle characterizes the LVE behaviour. In fact, for $\varphi = 0$ the material is perfectly lineal elastic, for $\varphi = 90^\circ$ the material is purely viscous, for $0 < \varphi < 90^\circ$ the material is LVE (Herve Di Benedetto & Corté, 2004).

By analogy to E^* , the shear complex modulus can be defined as:

$$G^*(\omega) = \frac{\tau_0 e^{i\omega t}}{\gamma_0 e^{i\omega t - \varphi}} = \frac{\tau_0}{\gamma_0} e^{i\varphi} = |G^*| e^{i\varphi} = G_1 + iG_2 = |G^*| \cos \varphi + i|G^*| \sin \varphi \quad (1.20)$$

Where $\tau(t) = \tau_0 e^{i\omega t}$ is a sinusoidal shear stress of amplitude τ_0 and $\gamma(t) = \gamma_0 e^{i\omega t}$ is a sinusoidal shear strain of amplitude γ_0 .

If the hypothesis of isotropic material is valid, E^* and G^* are related:

$$G^* = \frac{E^*}{2(1 + \nu^*)} \quad (1.21)$$

Where ν^* is the complex Poisson's ratio.

The complex modulus (and its components $|E^*|$, E_1 , E_2 , and φ) varies with frequency and temperature. Results from laboratory tests (on bitumen and mixtures) are usually presented via some standardized plots:

- Isothermal curves are obtained by plotting the values of the norm of the complex modulus $|E^*|$ against frequency, for each temperature. Both axes are usually in logarithmic scale.
- Isochronal curves are obtained by plotting the values of the norm of the complex modulus $|E^*|$ against test temperatures, for each test frequency. Both axes are usually in logarithmic scale.
- The Cole-Cole plot displays the imaginary part of the complex modulus E_2 against the real part E_1 .
- The Black diagram displays the phase angle values against the complex modulus norm values. The x-axis is in logarithmic scale ($\log|E^*|$), while the y-axis is in real scale (φ).

1.5.1.3 Time Temperature Superposition Principle (TTSP)

As stated above, under the hypothesis of LVE behaviour, E^* and G^* depends on frequency and temperature. The representation of complex modulus test results via isothermal curves shows that the same value of $|E^*|$ can be attained for different frequency-temperature couples (equation (1.22)).

$$E^*(\omega_1, T_1) = E^*(\omega_2, T_2) \text{ with } (\omega_1, T_1) \neq (\omega_2, T_2) \quad (1.22)$$

This property is called time temperature superposition (TTSP) principle. Its validity can be also visualised in the Cole-Cole plot or the Black diagrams. As it was observed that for several LVE materials the test results tend to form a unique curve independently of test temperature and frequency (Ferry, 1980), materials showing this behaviour are called "thermorheologically simple" (Herve Di Benedetto & Corté, 2004). For this kind of materials the influence of temperature and frequency can be reduced to a single variable:

$$E^*(\omega, T) = E^*(\omega f(T)) = E^*(g(\omega)T) \quad (1.23)$$

The application of the TTSP implies the use of the isothermal curves to build a unique curve for a chosen reference temperature T_{ref} . This curve is obtained by shifting the isothermal curves along the x-axis ($\log(f)$) with respect to the isothermal T_{ref} , namely by multiplying the test frequencies by a shift factor a_T (equation (1.24)). The so modified frequencies are called "reduced frequencies".

$$E^*(\omega, T) = E^*(\omega a_T(T), T_{ref}) \quad (1.24)$$

The shift factor a_T depends on the temperature of the isothermal curve to shift and on the reference temperature T_{ref} , and it verifies the following properties:

$$a_T(T) = \frac{f(T)}{f(T_{ref})} \Rightarrow a_T(T_{ref}) = 1 \quad (1.25)$$

The unique curve thus obtained is called "master curve" and it allows to obtain $|E^*|$ values for inaccessible test temperatures or frequencies.

In this thesis, the Williams, Landel and Ferry (WLF) equation is used to fit the a_T values as a function of the temperature (Williams et al., 1955):

$$\log(a_T) = \frac{-C_1(T - T_{ref})}{C_2 + T - T_{ref}} \quad (1.26)$$

Where C_1 and C_2 are two constants. The form of the equation (1.26) is independent of the choice of T_{ref} (Chailleux et al., 2006) and it can be written with respect to another reference temperature T_{ref}^* , but associated with the constant C_{1^*} and C_{2^*} . The relations between the four constant are the following:

$$C_2 = C_{2^*} + T_{ref} - T_{ref}^* \quad (1.27)$$

$$C_1 = (C_{1^*} \cdot C_{2^*})/C_2 \quad (1.28)$$

1.5.2 Modelling LVE behaviour of bituminous materials

A LVE analogical model is a selected combination of springs and dashpots that provide a mathematical approximation of real mechanical behaviour of a LVE material (Herve Di Benedetto & Corté, 2004). The springs represent the elastic (recoverable) behaviour and the dashpots the Newtonian viscous behaviour (irrecoverable). Typically, the rheological models used to describe the LVE behaviour are those characterised by a continuous spectrum.

The simplest combinations of the springs and dashpots are the Maxwell and Kelvin-Voigt models, which cannot adequately describe the complex LVE behaviour of bituminous

materials, however they constitute the basic elements of more complex models, the generalized Maxwell and Kelvin-Voigt models. In fact, the latter consist of n Maxwell or Kelvin-Voigt elements assembled in series or in parallel. All the above mentioned models are characterised by a discrete relaxation spectrum, meaning that they have a finite number of elements (n) each one with a value of the modulus E_i corresponding to a relaxation time τ_i . Only if infinite elements are used ($n \rightarrow \infty$) it is possible to obtain a continuous relaxation spectrum (the modulus becomes a continuous function of relaxation time $E(\tau)$) (François Olard, 2003). However the more the elements number the bigger the computation time.

The models mainly used in this thesis are two continuous spectrum models, the Huet-Sayegh (Huet, 1965) (Sayegh, 1966) model and the 2S2P1D (2 Springs, 2 Parabolic elements, 1 dashpot) model (François Olard, 2003) (Hervé Di Benedetto, Olard, et al., 2004). The Huet-Sayegh model consist of two parallel branches (Figure 1.11). The first is made of a linear spring and two parabolic elements whose creep functions are expressed by Equation (1.29). The second is made of a second linear spring.

$$J_1 = a(t)^h; J_2 = b(t)^k \quad (1.29)$$

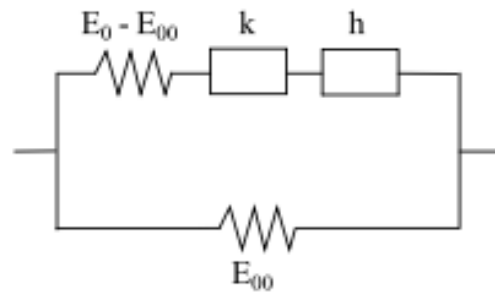


Figure 1.11 Representation of the Huet-Sayegh model.

Complex modulus is expressed by:

$$E^*(\omega) = E_{00} + \frac{E_0 - E_{00}}{1 + \delta(i\omega\tau)^{-k} + (i\omega\tau)^{-h}} \quad (1.30)$$

Where

- E_0 is the glassy modulus, which is associated to the behaviour at low temperatures and/or high frequencies;
- E_{00} is the static modulus, which is associated to the behaviour at high temperatures and low frequencies;
- k and h are constant defined such that $0 < k < h < 1$

- τ is a characteristic time that depends on temperature
- δ is a dimensionless constant

The Huet-Sayegh model fits well the behaviour of bituminous mixtures in the small strain domain at any temperature and frequency. However it cannot adequately describe pure bitumen behaviour at high temperatures and/or low frequencies (François Olard, 2003). This limit is overcome in the 2S2P1D model with the integration of a linear dashpot in series with the two parabolic elements (Figure 1.12) in order to take into account the purely viscous behaviour of pure bitumen at high temperatures and/or low frequencies.

Complex modulus is expressed by:

$$E^*(\omega) = E_{00} + \frac{E_0 - E_{00}}{1 + \delta(i\omega\tau)^{-k} + (i\omega\tau)^{-h} + (i\omega\beta\tau)^{-1}} \quad (1.31)$$

Where E_0 , E_{00} , k , h , τ and δ have the same meaning than in the Huet-Sayegh model and β is a dimensionless constant related to the Newtonian viscosity η by Equation (1.32).

$$\eta = (E_0 - E_{00})\beta\tau \quad (1.32)$$

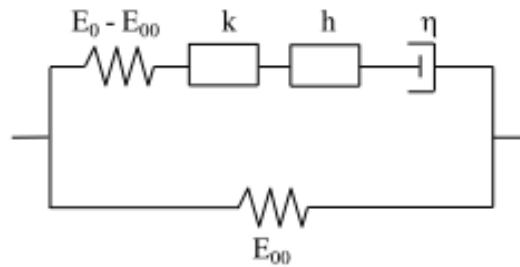


Figure 1.12 Representation of the 2S2P1D model (François Olard et al., 2003) (François Olard & Di Benedetto, 2003) (Hervé Di Benedetto, Sauzéat, et al., 2004).

Thus, the model is characterised by seven parameters, all having a physical meaning (Figure 1.13). Out of them, τ is the only one depending on temperature (as for the Huet-Sayegh model). It verifies the TTS principle as its evolution with temperature can be expressed by:

$$a_T = \frac{\tau}{\tau_0} \quad (1.33)$$

Where τ_0 is the characteristic time at reference temperature T_{ref} .

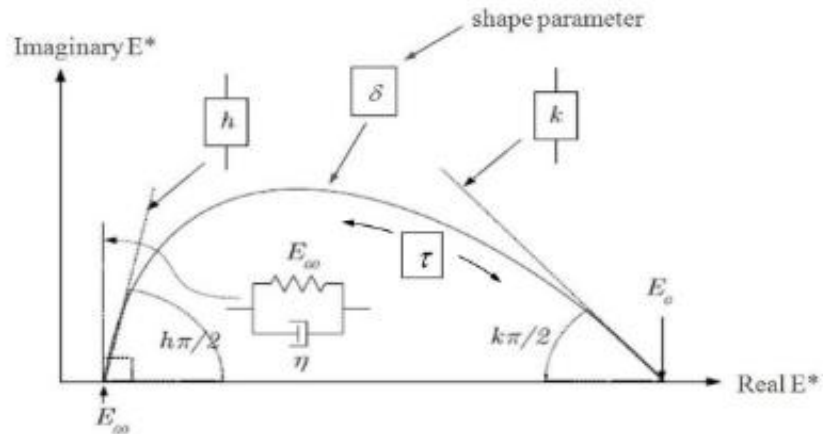


Figure 1.13 Representation of the 2S2P1D model parameters on the Cole-Cole plot.

1.6 Modelling and pavement design

1.6.1 Modelling of pavement mechanical behaviour

As for bituminous materials, the analysis of pavement mechanical behaviour requires the use of theoretical models for structural response. Various theoretical models have been developed, from analytical solutions based on elasticity to more complex models that take into account the viscoelastic behaviour of bituminous materials.

Boussinesq (Boussinesq, 1885) was the first to propose a series of equations to determine the response (in terms of strain, stress and deflections) of a semi-infinite homogeneous, isotropic, linear elastic medium, characterised by a modulus E and a Poisson's ratio ν , and subjected to a static point load. However, as described in Sections 1.3.1 and 1.3.2 road pavements consist of multiple layers having different mechanical properties, thus the Boussinesq model could be not very accurate. A better theory was developed by Burmister (Burmister, 1943), for two-layered elastic systems, which was then extended to a system composed of three and more (n) layers. This model is the most used in the mechanical pavement design methods. It is based on the following assumptions (Figure 1.14):

- The pavement is assimilated to a multi-layered medium. Each layer is homogeneous, isotropic, and linear elastic with a modulus of elasticity (E_i) and a Poisson's ratio (ν_i);
- Each layer has a finite thickness (h_i) and extends infinitely in the horizontal direction. The bottom layer extends infinitely downward.
- The load is uniformly distributed on a circular area with radius r . Multiple loads can be treated as summing the effects of individual loads;

- Interfaces are considered as either fully bonded (same displacement of the two layers at the interfaces) or frictionless (displacement of a layer independent of the other layer).

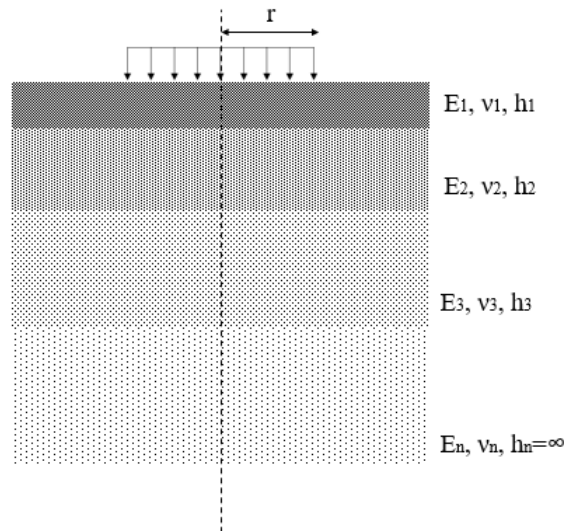


Figure 1.14 Burmister's multi layered system.

In this model stress and displacement are determined from the following stress function (PERRET, 2003):

$$\varphi_i = pa \int_0^{\infty} \frac{J_0(mr)J_1(ma)}{m} [A_i e^{mz} - B_i e^{-mz} + zC_i e^{mz} - zD_i e^{-mz}] dm \quad (1.34)$$

Where:

- a is the radius of the loading surface,
- p is the loading pressure uniformly distributed,
- r is the radial distance in cylindrical coordinates,
- z is the depth,
- A_i, B_i, C_i, D_i are unknown parameters determined by the boundary conditions,
- J_0 is the Bessel function of the first kind of order 0,
- J_1 is the Bessel function of the first kind of order 1,
- m is the integration parameter.

Many software have been developed based on the Burmister model. Two of them, used in this thesis, are described in the following sections, Alizé-LCPC (1.6.1.1) and Viscoroute© in which an adaptation to materials with viscoelastic behaviour was developed (1.6.1.2).

1.6.1.1 Alizé-LCPC

Alizé-LCPC (<http://www.alize-lcpc.com/fr/index.php>) is the reference software for pavement design in France. It implements the mechanist pavement design method developed by the LCPC (French acronym for "Laboratoire Central des Ponts et Chaussées" now become Université Gustave Eiffel) and the SETRA (French acronym for "Service d'Etudes Techniques des Routes et Autoroutes") (SETRA & LCPC, 1994). In Alizé-LCPC each layer is defined by its thickness (h), Young modulus (E, at 15 °C and 10 Hz), Poisson's ratio (ν , called "Nu"), and interface conditions. For the latter, the model includes three default options: fully bonded, semi-bonded, or frictionless. The "semi-bonded interface" option is recommended for a better characterisation of the interface between layers with materials treated with hydraulic binders. In this case the result is the average of two calculations: the first carried out with the hypothesis of fully bonded interfaces and the second with the hypothesis of frictionless interfaces. In addition Alizé-LCPC disposes of a library of standardized materials as defined by the French guides for pavement design (SETRA & LCPC, 1994) (SETRA; LCPC, 1998) or the European Standard NF P98-086 (AFNOR, 2019). Otherwise the user has the possibility to add a personalised material in the library.

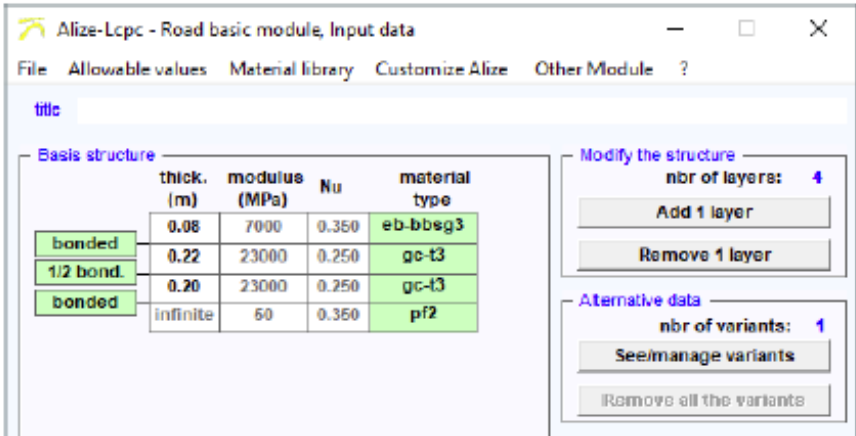


Figure 1.15 Example of structure composition in Alizé-LCPC (<https://www.alize-lcpc.com/documents/ALIZE-LCPC-MU-v1.5-EN.pdf>).

Alizé-LCPC has two main options for the definition of the bearing load: the reference loading condition and the special loading condition. The first loading pattern is a semi-axle with dual-wheel loaded to 65 kN. The geometry is detailed in Figure 1.16. The special

loading condition allows loading patterns from multi-axle vehicles and the setup of specific load characteristics (radius, weight, and pressure).

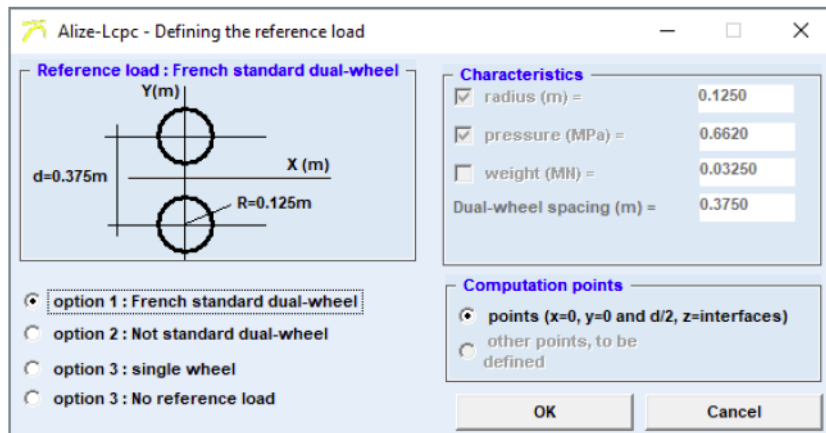


Figure 1.16 Standard loading condition in Alizé-LCPC (<https://www.alize-lcpc.com/documents/ALIZE-LCPC-MU-v1.5-EN.pdf>).

1.6.1.2 Viscoroute©

In Alizé-LCPC each layer of the pavement structure has a homogeneous and elastic behaviour. Viscoelastic effects are taken into account via an equivalent elastic modulus set at 15 °C (average temperature in France) and 10 Hz (frequency equivalent to the average vehicles speed in France, 72 km/h). However, for the analysis of pavement response in case of low heavy traffic and high temperatures the viscoelastic behaviour of bituminous materials is not negligible and has to be taken into account in order to have a good approximation in the results. The software Viscoroute© (Duhamel et al., 2005) (A Chabot et al., 2006) (A Chabot et al., 2010) allows to account for the viscoelastic behaviour of bituminous materials through the Huet-Sayegh model (described in Section 1.5.2). In this model the pavement structure is defined as "n" homogeneous horizontal layers infinite in the plan, having finite thickness (except for the bottom layer). The user can model the behaviour of each layer as elastic or viscoelastic (Figure 1.17). In the first case, the i^{th} layer is characterised by the Young modulus E^i and the Poisson's ratio ν^i . If the mechanical behaviour of the i^{th} layer is assumed to be viscoelastic, it will be characterised by five viscoelastic parameters (E_0^i , E_{00}^i , k_i , h_i , and δ_i) and three thermal coefficients (A_0^i , A_1^i , A_2^i) of the law $\tau(T) = \exp(A_0 + A_1 T + A_2 T^2)$ allowing to take into account the thermal susceptibility of the material. The above mentioned coefficients of the Huet-Sayegh model can be determined from experimental tests (complex modulus test) performed in the laboratory by using the free software Viscoanalyse (Chailleux et al., 2006).

The structure can be solicited by one or several moving loads that move in the x-direction at a constant speed V. The loading setup is defined by: the loading speed, the loading geometry, the applied load, and the number of computations to be performed (stress, strain, displacement) at a defined depth. Three geometries are available in Viscoroute©: punctual, rectangular, and elliptical. In the last two cases the parameters a and b have to be defined as in Figure 1.20.

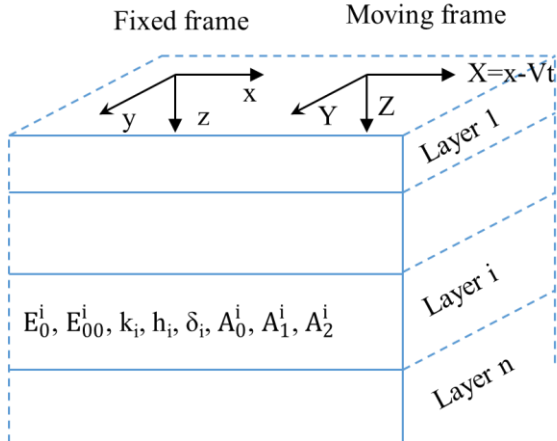


Figure 1.17 Modelling of the pavement under moving load in Viscoroute© (readapted from (A Chabot et al., 2010)).

ViscoRoute 2.0 (LCPC-ENPC)
 Fichier Outils Aide
 Structure | Chargement | Résultats |

Fichier structure non enregistré

Nb de couches: 3

	Z (m)	Epais. (m)	Module E (MPa)	Coef. de Poisson	Mas. Vol. (kg/m3)	Type de matériau	Comport.	Type de liaison	Module E0 (MPa)	T (°C)	k (loi H-S)	h (loi H-S)	delta (loi H-S)	A0	A1	A2
1	0.000	0.000	0.00000	0.000	0.000	autre	Viscoelastique	collée	0.00000	0.000	0.000	0.000	0.000	0.000	0.000	0.000000
2		0.000	0.00000	0.000	0.000	autre	Elastique	collée	0.00000	0.000	0.000	0.000	0.000	0.000	0.000	0.000000
3		infini	0.00000	0.000	0.000	autre	Elastique	collée	0.00000	0.000	0.000	0.000	0.000	0.000	0.000	0.000000

Figure 1.18 Example of the pavement structure composition in Viscoroute©.

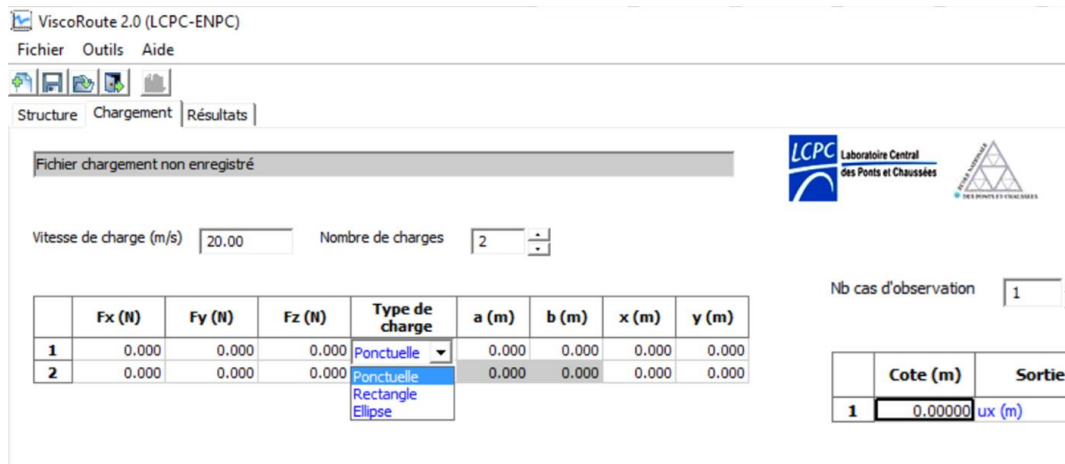


Figure 1.19 Example of loading setup in Viscoroute©.

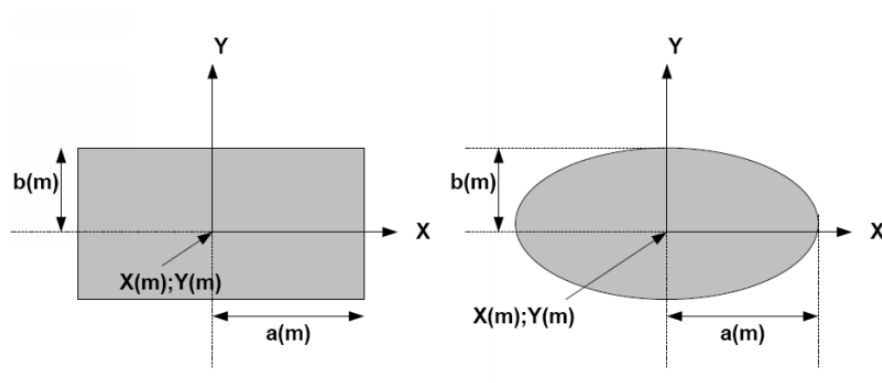


Figure 1.20 Loading geometries available in Viscoroute©: (Left) rectangular, (Right) elliptical.

1.6.2 Notions of pavement design

The goal of structural design is to determine the number, material composition and thickness of the different layers within a pavement structure required to accommodate a given loading regime. The first pavement design method, called "CBR (California Bearing Ratio) method" (Porter, 1943), was developed in 1928 by the California Division of Highways. The CBR method was an empirical design method, meaning that the relationships between design inputs (e.g., loads, materials, layer configurations and environment) and pavement failure were determined using experience, experimentation or a combination of both. Then the use of full-scale road tests saw the improvement of empirical methods. In particular the results of the AASHO (American Association of State Highway officials) road test were used to develop the AASHTO (American Association of State Highway and Transportation Officials) pavement design guide, first issued in 1961 (AASHTO, 1993).

With the arrival of the Burmister elastic model, another design approach was conceived, the mechanistic-empirical method. In this latter, the pavement response (in terms of stress,

strain, and deflections) to physical causes (loads and material properties) is described using a mathematical model. Empirical elements are used for the definition of the limit design values of pavement response (Pereira & Pais, 2017).

1.6.2.1 The ASSHTO pavement design guide

All versions of the ASSHTO pavement design guide are empirical methods based on field performance data measured at the AASHO Road Test in 1958-60. The various editions released from 1961 to 1998 have introduced several improved features for pavement design. The basic equation for flexible pavements developed at the AASHO Road Test is (AASHTO, 1993):

$$\log W_{18} = Z_R S_0 + 9.36 \log(SN + 1) - 0.20 + \frac{\log\left(\frac{\Delta PSI}{4.2 - 1.5}\right)}{0.40 + \frac{1094}{(SN + 1)^{5.19}}} + 2.32 \log(M_R) - 8.07 \quad (1.35)$$

Where:

- W_{18} is the number of 18 kip equivalent single axle loads (ESALs).
- $Z_R S_0$ is the reliability factor.
- SN is the structural number = $a_1 D_1 + a_2 D_2 + a_3 D_3$; where D_1 , D_2 , and D_3 are the thicknesses of the surfaces, base, and subbase layers, respectively, and a_1 , a_2 , and a_3 are the corresponding layer coefficients.
- ΔPSI is the difference between the initial design serviceability index, p_0 , and the design terminal serviceability index, p_t .
- M_R is the resilient modulus (psi).

The main limitation of this approach is that the empirical relationships cannot be applied to materials or structural configurations different from the test conditions from which they are inferred. The need for a mechanistically based pavement design procedure led to the development of a mechanistic empirical pavement design procedure under the NCHRP (National Cooperative Highway Research Program) Project 1-37A (sponsored by the AASHTO, the NCHRP and the Federal Highway Administration) which was first released in 2004. The approach provided in the MEPDG (Mechanistic Empirical Pavement Design Guide) consist of five main steps (AASHTO, 2008):

1. Select a trial design strategy.

2. Select the appropriate design performance indicator criteria and design reliability level for the project.
3. Obtain all inputs for the initial pavement design trial to run the software: general project information, design criteria, traffic, climate, structure composition, and material properties.
4. Run the MEPDG software, examine the inputs and outputs as well as whether the trial design has meet the performance indicator criteria and the design reliability level chosen for the project.
5. Revise the trial design if needed to correct anomalies.

1.6.2.2 The French pavement design guide

The French design method is an example of mechanistic-empirical method (SETRA & LCPC, 1994) (AFNOR, 2019) . It is based on the determination of the design thicknesses as a function of the design traffic for a certain service life. The design thicknesses are eventually modified for the verification of the frost/thaw behaviour and adjusted to account for practical conditions on the construction site. The method is based on the following general principles:

- The pavement response (in terms of stress and strain) induced by the reference load (dual-wheel axle loaded to 130 kN) is calculated using multi-layer elastic model (Alizé-LCPC);
- The calculated stress and strain are compared with limit design values which are function of design traffic (NE) and of material properties;
- The design traffic (NE) is expressed as a equivalent number of reference axles (dual-wheel axles loaded to 130 kN);
- Laboratory tests carried out on materials and are used to take into account materials properties in the design method.

Two failure mechanisms are considered for flexible pavement, fatigue at the base of the bituminous layers and rutting of the subgrade. Hence two criteria must be verified:

- The maximum tensile strain at the bottom of the bituminous layers must be lower that the limit tensile strain $\epsilon_{t,adm}$;
- The maximum vertical strain at the top of the subgrade must be lower than the limit vertical strain $\epsilon_{z,adm}$

The design traffic can be calculated as:

$$NE = N_{PL} \cdot CAM \quad (1.36)$$

Where CAM is the coefficient of average aggressiveness of a given traffic, and N is the number of heavy vehicles expected on the road.

The limit tensile strain at the basis of the bituminous layers is defined by:

$$\varepsilon_{t,adm} = \varepsilon_6(10^\circ\text{C}, 25\text{ Hz}) \sqrt{\frac{E(10^\circ\text{C}, 10\text{ Hz})}{E(15^\circ\text{C}, 10\text{ Hz})}} \left(\frac{NE}{10^6}\right)^b k_r k_s k_c \quad (1.37)$$

Where:

- $\varepsilon_6(10^\circ\text{C}, 25\text{ Hz})$ is the tensile strain leading to fatigue for 1 million load cycles, determined by the two point bending fatigue test (AFNOR, 2018a);
- b is the slope of the fatigue law of the bituminous material;
- $E(10^\circ\text{C}, 10\text{ Hz})$ and $E(15^\circ\text{C}, 10\text{ Hz})$ are the modulus measured in the lab respectively at 10°C and 10 Hz and 15°C and 10 Hz (AFNOR, 2012a);
- k_c is a calibration factor, function of the material used for the layer;
- k_s is a correction factor for subgrades of low bearing capacity;
- k_r is a risk coefficient;

The limit tensile strain at the basis of the bituminous layers is defined by:

$$\varepsilon_{z,adm} = A (NE)^b \quad (1.38)$$

Where A and b are parameters function of the traffic level, the material, and the structure.

1.7 In situ pavement monitoring with traditional technologies

Road pavements, as infrastructures in general, need adapted maintenance measures in order to ensure their efficiency and long-lasting operations. As mentioned in Section 1.1 the establishment of cost-effective asset management plans requires the assessment of pavement actual conditions and their evolution with time. A complete in situ-monitoring system is composed of three main elements: embedded sensing devices connected to an ad hoc data acquisition system; post-treatment of possibly massive data coming from the sensors; and, finally, a user-friendly interface showing the overall road network conditions and alerting in case of maintenance need (AASHTO, 2013). Thus, having a device that is compatible with the pavement itself is as important as developing a methodology for the inverse calculation of pavement mechanical performances. Considering the importance and the complexity of developing an operational in situ monitoring system for road pavement, a detailed review on

instrumentation for pavement is presented in the following sections. In Section 1.7.1, the most used embeddable solutions for in situ road pavement monitoring are described by focusing on their operating principles, as well as their installation requirements. Section 1.7.2 is a review of several instrumented sections in view of providing insight into the inverse calculation strategies for road structure, as well as the decision support tools.

1.7.1 Sensing solutions

1.7.1.1 Strain measurements

Strain measurements at different locations within the various pavement layers of the pavement are of great interest as they can be used to analyse pavement response with time under moving loads, as well as to verify the assumptions made during the design phase (Selvaraj, 2012). By recording the strain evolution within the pavement over time, it could be possible to predict the occurrence of fatigue or rutting phenomena (Section 1.3.3).

Horizontal asphalt strain gauges (H-gauges)

H-gauges are used to measure the magnitude of horizontal strains within pavement under dynamic load. They are usually placed at the bottom of the bituminous layers as this is the area where high tensile strains are concentrated and may give rise to fatigue events. A schematic representation of a horizontal asphalt strain gauge is given in Figure 1.21. The H shape of these sensors enhances their anchor in the asphalt medium. The sensitive part is actually in the central bar, which is made of a material and can contain between one and four active strain gauges connected in different configurations. Each edge of the central bar is connected to a metal strip.

As the pavement experiences strain, the movement of the anchors produces an elongation in the central bar. The subsequent resistance variation of the strain gauges can be translated into strain knowing the gauge factor (GF) which indicates the sensor sensitivity to strain:

$$GF = \frac{(\Delta R/R)}{\epsilon} \quad (1.39)$$

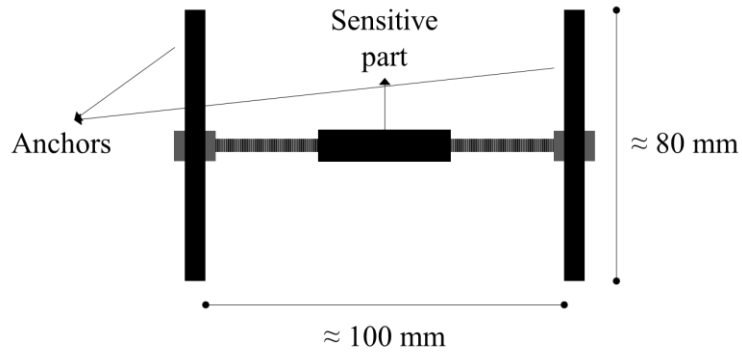


Figure 1.21 Schematics of an H-gauge (adapted from <http://www.jewellinstruments.com/>).

The H-gauges available on the market are waterproof and designed to withstand high temperatures and compaction loads associated with asphalt pavement construction procedures. In addition, their stiffness is of the same range of magnitude as the asphalt, thus permitting the measurement of the true strain within the pavement. Concerning the installation procedures, providers usually recommend to put some asphalt above and below the sensors before paving and compacting operations start. The purpose of this action is to protect the sensor itself and to guarantee bonding between the sensor and the surrounding structure, as well as longevity of the instrumentation (Weinmann et al., 2004). H-gauges are usually positioned in longitudinal and transverse direction with respect to traffic direction as shown in Figure 1.22.

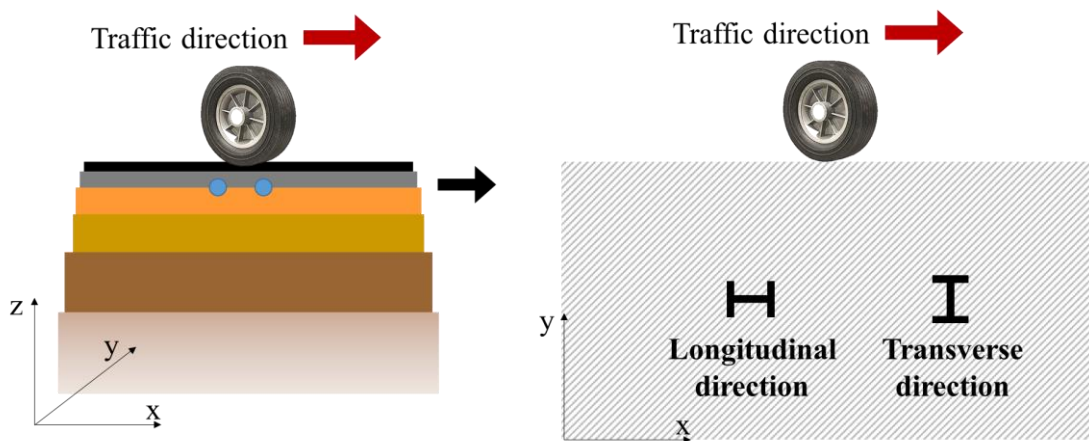


Figure 1.22 Schematics of H-gauges orientation with respect to traffic direction: longitudinal and transverse directions.

Some of the H-gauges available on the market are summarized in Table 1.3, where their specifications are compared. The sensors can provide accurate measurements (resolution of about $\pm 1 \mu\epsilon$) in a range that widely covers the level of strain felt by the pavement during the

construction process, as well as service life. The cost can go from 300 € to 700 € per transducer.

Table 1.3 Specifications of some H-gauges available on the market.

	Dynatest PAST	CTL ASG	Jewell ASG-3000-HT	TML KM-100HAS
Capacity	$\pm 1500 \mu\epsilon$	$\pm 1500 \mu\epsilon$	$\pm 3000 \mu\epsilon$	$\pm 5000 \mu\epsilon$
Temperature range	-30 to 150 °C	-34 to 204 °C	-34 to 200 °C	-20 to 180 °C
Resistance	120 Ω	350 Ω	350 Ω	350 Ω
Circuit	Quarter bridge	Full bridge	Full bridge	Full bridge
Modulus	2200 MPa	2340 MPa	<i>Not provided</i>	40 MPa

Vertical asphalt strain gauges

Similar to the H-gauges, the vertical asphalt strain gauges are composed of a sensitive part secured by two circular plates. The bottom plate has the function to keep the sensor in position, while the top plate transfers the load uniformly to the central bar. In addition, this type of sensor is equipped with a sharp stake to be inserted in the underlying layer. A scheme of a vertical asphalt strain gauge is given in Figure 1.23.

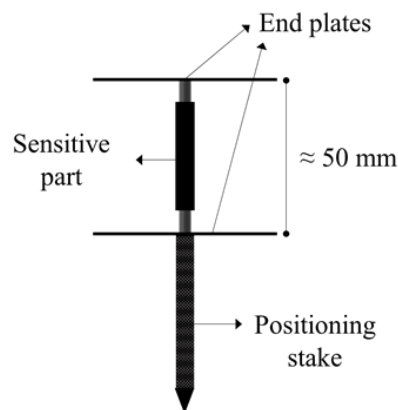


Figure 1.23 Schematics of a vertical asphalt strain gauge (adapted from <https://www.ctlgroup.com/>).

The operating principle and the compatibility with asphalt materials and construction phases are similar to the ones of H-gauges presented above (Islam & Tarefder, 2013). Concerning the installation, it requires the drilling of a hole to accommodate the positioning stake. Sand binder mixtures are applied to fill the hole and cover the surroundings. Thereafter, the sensor is delicately pressed into the hole until contact between the bottom plate and the surface is

attained. The providers generally suggest to first remove the top plate in order to apply the asphalt mix around the gauge and then replace it and cover the sensor with the mix. Then, it is possible to go forward with paving and compacting. Statistically, vertical asphalt strain gauges have a lower survival rate than H-gauges.

Fiber Optic Sensors (FOS)

A fiber optic sensor (FOS) is a device that uses an optical fiber connected to a light source as the sensing element to detect certain quantities (such as strain, temperature, pressure). FOSs represent a valuable technology to obtain crucial information about the pavement conditions due to their small size, flexibility, embeddability, and immunity to electromagnetic interference (Maeijer et al., 2020). In addition, FOSs allow high-precision (resolution of about $\pm 1 \mu\epsilon$) local or distributed strain measurements. Several types of FOSs are available on the market. They can be classified according to their sensing configuration: discrete, quasi-distributed, and distributed. Discrete measurements use the extrinsic Fabry-Perot (FP) interferometer principle (Rajibul Islam et al., 2014). The sensor consists of two semi-reflecting parallel mirrors placed at a distance. The variation of this distance is monitored by the system. It is attributed to the occurrence of an event (Choquet et al., 2000). Fiber Bragg gratings (FBGs) can be used for discrete measurements (Campanella et al., 2018). FBGs are made by modifying the refractive index of small portions of an optical fiber through an intense ultraviolet (UV) source, thus forming an interference pattern. This causes the reflection of a particular wavelength (called Bragg wavelength) and the transmission of all others. The application of strain to the modified part produces a shift in the Bragg wavelength (Figure 1.24).

Distributed fiber optic (DFO) sensing technologies enable continuous, real-time measurements along the entire length of a fiber optic cable, with high spatial resolution (up to 1 mm). The functioning principle of these devices for strain-sensing applications is based on two main techniques: Rayleigh and Brillouin scattering effects (Bao & Chen, 2012). What makes the difference between the two types is the relation between the measured strain and the change in optical properties of the scattered light (Glisic, 2011). In both cases the strain measurement must be compensated for by temperature variations.

FO sensors can be installed during the construction process or as a retrofit. However, the installation process is long and delicate, and very few studies provide technical details about the integration in asphalt pavements (Chapeleau et al., 2014) (Imai et al., 2014).

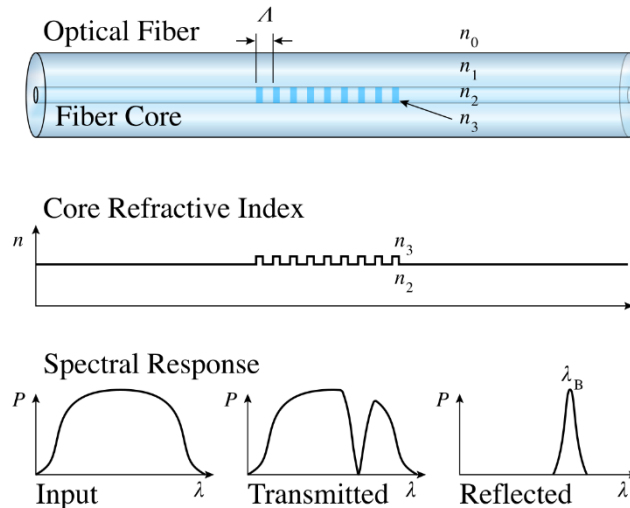


Figure 1.24 FBG functioning principle.

1.7.1.2 Deflection measurements

Pavement deflection measurements are a mean of evaluating overall pavement conditions. Many features of a flexible pavement can be determined by measuring its deflection response to load. For example, this quantity can be used for the inverse calculation of the pavement structural layer stiffness and the subgrade resilient modulus.

The most popular sensors for deflection measurements are linear variable differential transformers (LVDTs), accelerometers, and geophones (Tabatabaee & Sebaaly, 1990). The last two are less intrusive than LVDTs.

LVDTs

LVDTs are used to measure the actual vertical deflection of road pavement. These devices convert the relative displacement from a mechanical reference into an output voltage. A reference rod is anchored at a sufficient depth so that the deflection of that point due to surface loading is negligible. Single-layer deflectometers (SLDs - Figure 1.25) can measure the deflection of a given layer of the pavement, while the most sophisticated multi-depth deflectometers (MDDs) can measure deflection at multiple points of the pavement structure. The installation of LVDTs requires the execution of a core for the rod placement and sealing before the installation of the LVDT and the upper plate. Finally, the plate needs to be protected with some asphalt (Joshi, 2017) (Saevarsdottir et al., 2016). Such a device can provide highly accurate measurements.

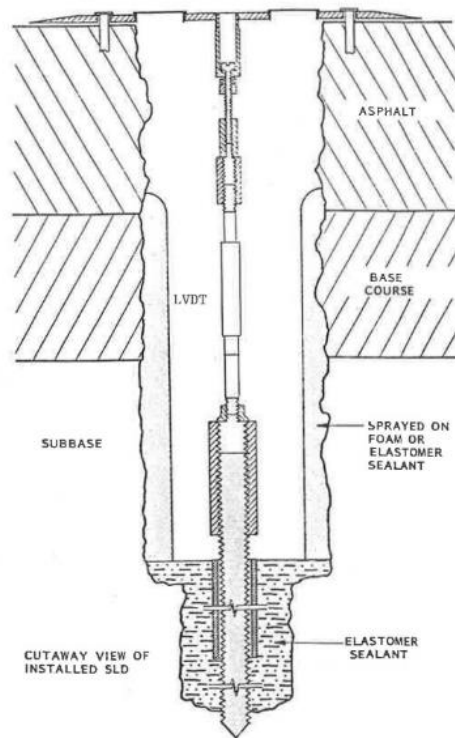


Figure 1.25 Schematics of LVDT single-layer deflectometer installed in a road pavement (reproduced from (Tabatabaee & Sebaaly, 1990)).

Accelerometers

An accelerometer is a device that measures velocity rate along one or multiple directions. By integrating the accelerometer signal twice, it is possible to obtain the pavement deflection. These devices do not need a reference point, as acceleration is an absolute value that refers to the state of rest. Thus, they can be installed on the surface or embedded at any depth in the pavement.

On a practical level, an accelerometer measures the acceleration of a mass connected on a spring. Under motion, the mass is accelerated due to the force applied on the spring. The displacement of the mass is then proportional to the acceleration (Levenberg, 2012).

Geophones

Geophones are sensors that measure the displacement velocity of the pavement under moving loads. Thus, by integrating the signal once, it is possible to obtain the deflection response. The device is composed of a mass attached to a spring and surrounded by a coil. A movement of the geophone produces a relative movement between coil and magnet (Figure 1.26). Thus, a voltage is induced in the coil that is proportional to the displacement velocity measured by the geophone (Nazarian & Bush III, 1989) (Liu et al., 2017). Geophones usually show a nonlinear response and an attenuation of the measured

displacement amplitude under the natural frequency; thus, measurements are possible only above a minimum frequency (Duong, Blanc, Hornych, Menant, et al., 2018).

Similar to accelerometers, these deflection sensors do not need any reference point, can be installed at any depth in the pavement structure, and can withstand the construction process phases.

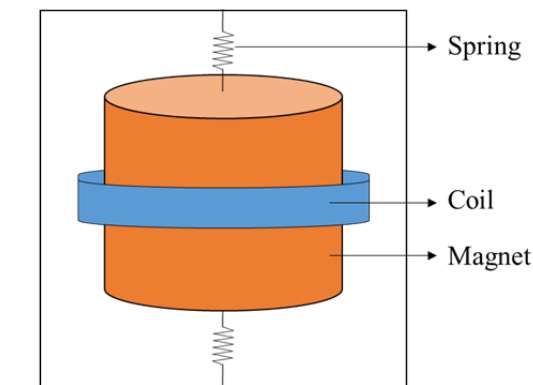


Figure 1.26 Geophone functioning principle.

1.7.1.3 Temperature measurements

Due to the intrinsic viscoelasticity of bituminous materials (Section 1.5) pavement response under loading depends on time and temperature. Temperature measurements strongly affect pavement structural response (Swett et al., 2008). Therefore, both strain and displacement measurements need to be coupled with temperature measurements within the pavement for an accurate interpretation and modelling of its mechanical behaviour. The most common temperature sensors are described in the sections below. All of them can be placed at different depths in the pavement structure. The installation procedures require cores (of a few millimetres) of the pavement layer for the insertion of the sensors that are then sealed with a resin in order to avoid the slipping off phenomenon.

Thermocouples

Thermocouples are the most used probes for temperature measurements within the pavement (Figure 1.27). Their operation is based on the Seebeck effect: the junction of two dissimilar metals yields a small voltage that varies with temperature. Thermocouple types K, E, or T can be used from subzero to very high temperatures, making them good candidate for embedding in the pavement, but they are less accurate than the following technologies (with accuracy 0.5 to 5 °C).



Figure 1.27 K-type thermocouple probes.

Resistance Temperature Detectors (RTDs)

RTDs are temperature-sensitive resistors. They usually consist of a fine wire (platinum, nickel, or copper) wrapped around a ceramic or glass core. The temperature range of use depends on the type of wire, but they can widely cover the temperature in the pavement during both construction and normal usage. In addition, they allow accurate (typically from 0.1 to 1 °C), stable, and repeatable measurements.

Thermistor sensors

Thermistors are sensors whose resistance is more strongly temperature-dependent than a standard resistor (Sangiorgi et al., 2018). They can be used in a smaller temperature range than the above-mentioned technologies, they allow for more accurate measurements (accuracy 0.05 to 1.5 °C) (Tabatabaee & Sebaaly, 1990).

1.7.1.4 Moisture measurements

It is demonstrated that an excess in moisture in the road structure results in the acceleration of pavement distress and, thus, speeds up the deterioration of the road-bearing capability. Therefore, there is a need to design and integrate drainage systems in the road that work efficiently during the lifetime of the pavement. To this respect, monitoring the moisture content at different depths in the road structure can give access to information concerning the drainage system and document pavement mechanical conditions (F. M. Fernandes & Pais, 2014) (Salour, 2015) (Arnold et al., 2017). The most used probes for moisture content measurements are TDR probes, whose functioning principle is based on the time-domain reflectometry. An electric pulse is sent through a waveguide. Its progression through the waveguide is a function of the moisture content in the pavement. When it reaches the end of the waveguide, the pulse is reflected and detected by a receiver. The intensity of the pulse is thus related to the moisture content (Salour, 2015). This device can measure between 0 and

100% water content, with an accuracy of $\pm 1\%$. Concerning the installation procedures, TDR probes can be installed in any orientation.

1.7.1.5 Pressure measurements

Pressure cells are used to measure the compressive stress in the road structure, notably in the unbound layers. The operating mode of these devices depends on their features. In fact, it is possible to distinguish mainly two types of pressure cells: hydraulic and diaphragm-based. The first consists of two steel plates configured in a way to form a cavity between them. This cavity is filled with a liquid. The induced liquid pressure is measured by strain gauges and is related to the applied load. The diaphragm cells are composed of a stiff ring that supports a diaphragm. The load application causes the deflection of the diaphragm that is measured by a strain gauge.

Concerning the installation, a procedure was suggested by Al-Qadi et al. (Al-Qadi et al., 2004). Once the sensor is placed in the excavation of the unbound layer, its levelling needs to be checked in order for the sensor to be in the horizontal position. Finally, the sensor is covered with the material previously excavated before construction operations start.

1.7.2 Instrumented sections

In this section we present some relatively recent instrumented pavement sections. The earliest examples of pavement instrumentation date back to the late 1980s (Cable et al., 1988).

1.7.2.1 The Virginia Smart Road (Al-Qadi et al., 2004)

The Virginia Smart Road (Al-Qadi et al., 2004) can be considered as a pioneering instrumented road. It demonstrates the feasibility of an instrumentation measuring flexible pavement responses to loading, and it is the first example of an end-to-end system for pavement in situ monitoring. The project started in 1998 and ended in November 1999, it was conducted by the Virginia Department of Transportation. It consisted of the construction of a 3.2-kilometer-long road. Over the entire length, 12 100-m-long sections were monitored by embedding different types of sensors at different depths. The instrumentation placement took place during the construction procedures. Strain gauges (H-shaped strain gauges and vibrating wire strain gauges), pressure cells, thermocouples, TDR probes, and resistivity probes were integrated (Figure 1.28).

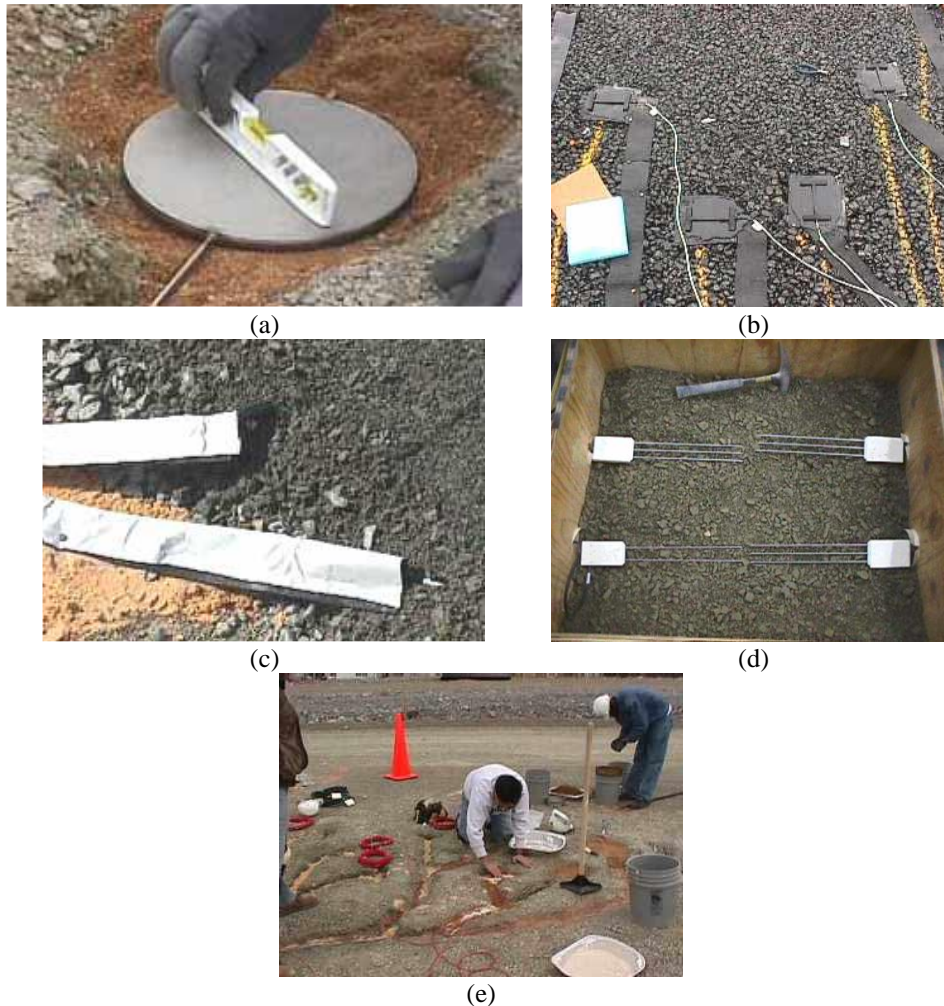


Figure 1.28 Sensor installation. (a) Pressure cells; (b) H-shaped asphalt strain gauges; (c) Thermocouples; (d) TDR probes; (e) Vibrating wire strain gauges (reproduced from (Al-Qadi et al., 2004)).

1.7.2.2 Test section in the State of Maine (Swett et al., 2008)

In 2005, the Maine Department of Transportation (DOT) built the first instrumented flexible pavement test section of the state of Maine (Swett et al., 2008). The instrumentation took place during reconstruction work for a damaged road. The sensors installed were: 12 asphalt strain gauges, 6 asphalt thermocouples, 4 soil strain gauges, 4 soil pressure cells, 6 soil moisture gauges, 24 soil thermocouples, and 2 frost resistivity probes (Figure 1.29). For each type of sensor was connected to its own data acquisition system. The systems allowed both dynamic and static data collection. This study showed that asphalt strain gauges installation is a very delicate process. In fact, among the 12 embedded sensors, 3 of them did not survive the construction phases.

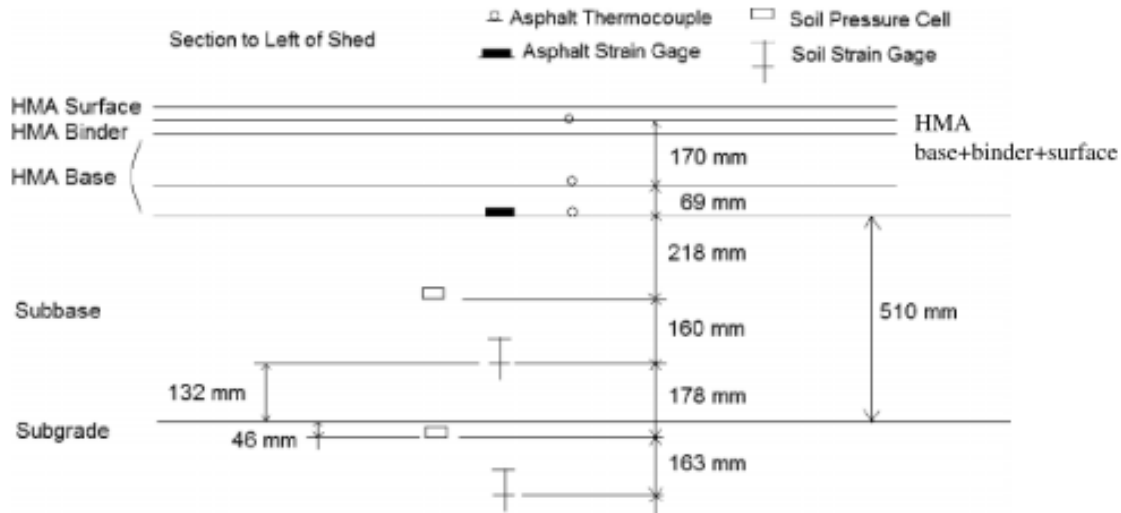


Figure 1.29 Layout of the instrumented section in the state of Maine (reproduced from (Swett et al., 2008)).

A model for subsurface temperature prediction was developed on the basis of temperature data collected over 5 months. Stress and strain data were collected over several passages of a truck with a known axle load. Three loading cases were considered. Each case included truck passages at five different speeds carried out in a short range of temperature in order to determine speed and temperature effect on pavement response. It was found that the time of loading (due to different speeds) does not vary at different depths (Figure 1.30), while speed variation has a significant impact on the measured strain. Finally, an elastic model (BISAR (JONG & L., 1979)) was used to model the experimental campaign. A good match between experimental and numerical results was obtained for low temperatures and speed levels.

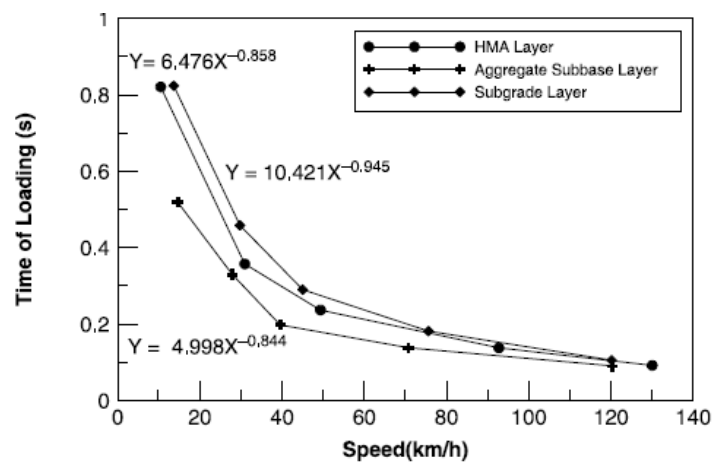


Figure 1.30 Test section in the state of Maine. Time of loading as a function of speed at different depths in the pavement structure (reproduced from (Swett et al., 2008)).

1.7.2.3 State of Virginia: instrumentation of Route 114 in Christiansburg (L. Wang et al., 2012)

In the state of Virginia at the Virginia Tech Transportation Department, a monitoring system was developed for the instrumentation of the Virginia State Route 114 and deployed in 2011 during the implementation of maintenance activities (L. Wang et al., 2012). The objective of this research project was the development of an inverse calculation methodology for weigh-in-motion (WIM), traffic classification, and monitoring of the pavement health conditions. An array of sensors was deployed for this instrumentation campaign: horizontal and vertical asphalt strain gauges, soil pressure gauges, thermocouples, and soil moisture probes. In addition, a wireless data logger was used to collect data from the sensors and transfer them to a laptop. Figure 1.31 is a representation of the sensor positioning in the pavement. The authors placed 5 horizontal strain gauges in the longitudinal direction (with respect to traffic direction) in order to estimate vehicle wandering. Indeed, inverse calculation of pavement mechanical conditions requires knowledge of the applied load, as well as its position with respect to the sensors locations. Finite element (FE) numerical simulations were performed with ABAQUS software in order to validate the proper operation of commercial sensors after installation and for inverse calculation and prediction of pavement distress. The initial objective was to determine the actual pavement modulus, by calculating the ratio between the measured vertical and horizontal strain. However, all the vertical asphalt strain gauges were damaged during construction. Therefore, the authors introduced the parameter R_{zx} :

$$R_{zx} = \sigma_z / \epsilon_x \quad (1.40)$$

Where σ_z is the measured vertical stress and ϵ_x is the measured longitudinal strain. By means of some FE calculations, the relation between R_{zx} and the pavement modulus was demonstrated; thus, R_{zx} was used for inverse calculation of the pavement's current viscoelastic properties. This process was integrated in a health monitoring system proposed by the authors and represented in Figure 1.32. The system includes periodic testing with a known loading truck for the determination of the actual pavement mechanical properties thus, for structure monitoring. Then time, these properties are implemented in a continuous model of the section for fatigue cracking and rutting distress predictions, based on the Mechanistic-Empirical Pavement Design Guide (MEPDG) models (AASHTO, 2008). In addition, the instrumentation was exploited for WIM and traffic classification. In particular, FE modelling of the pavement deformation due to a passing wheel was performed through

a bell-shaped Gaussian function, whose parameters were demonstrated to be related with wandering position, distance between wheels, width of tires, and axle loads. Finally, the signals from strain gauges were directly used to determine traffic volume and truck speed.

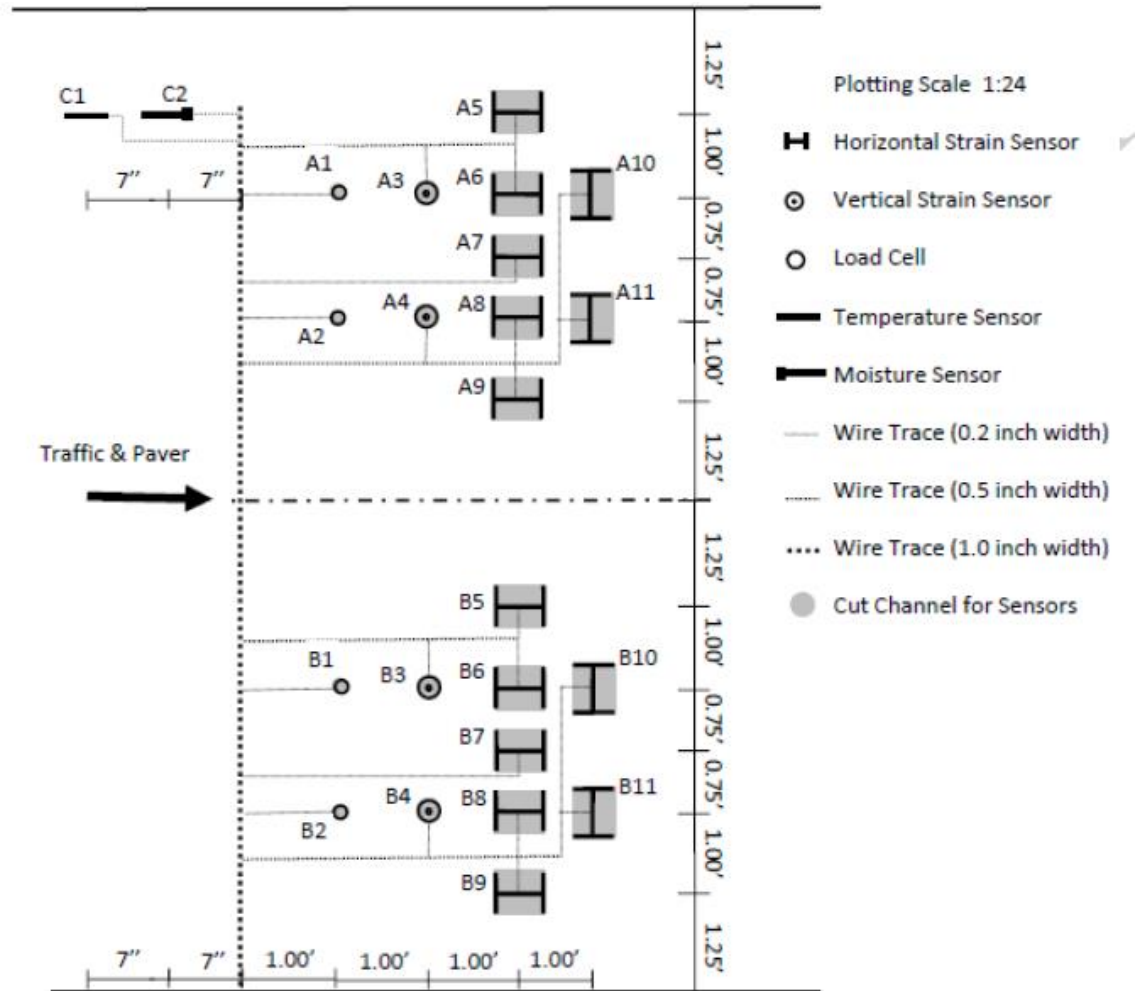


Figure 1.31 . Layout of the sensors in Route 114 (reproduced from (L. Wang et al., 2012)).

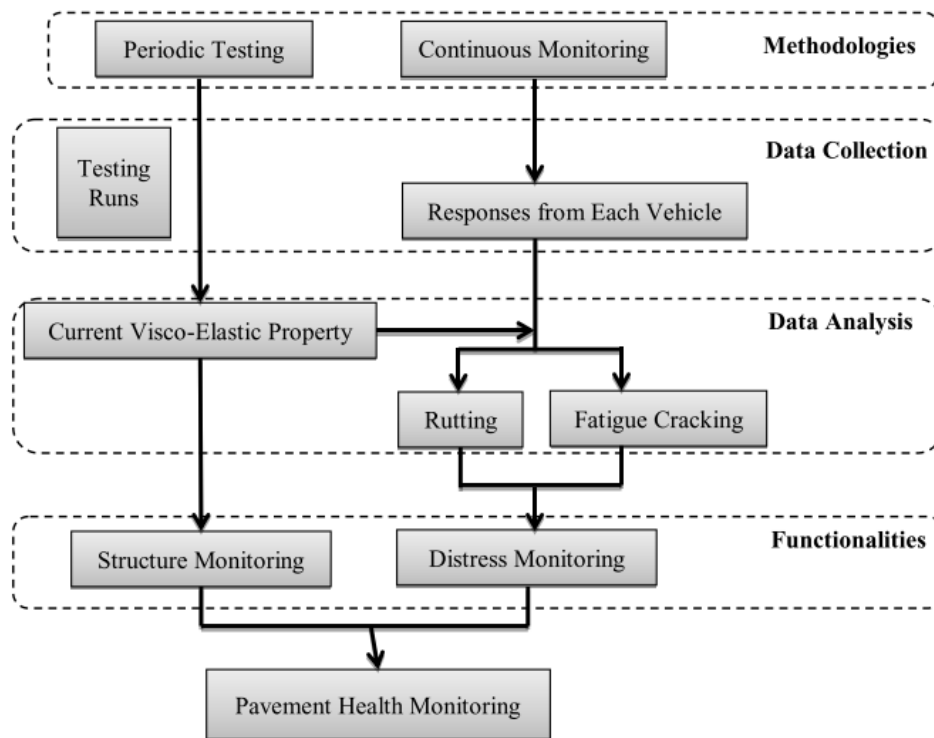


Figure 1.32 Pavement monitoring system designed for Route 114 in Christiansburg (reproduced from (L. Wang et al., 2012)).

1.7.2.4 The instrumentation of the A41N highway in France (Gaborit et al., 2014)

The instrumentation of the French highway A41N was part of a research project conducted in partnership between AREA, EIFFAGE, and the University of Lyon/ENTPE. The work was carried out in 2012 during maintenance operations (Gaborit et al., 2014). Two sections were instrumented with 47 strain gauges (horizontal and vertical asphalt strain gauges), 12 temperature probes, and 2 FBGs sensors. Sensors were located at different depths in the road structure so as to gain information about the wearing, base, and subbase course. The MGCplus data acquisition system provided by HBM was used with 5 acquisition modules. Measurements were acquired at 600 Hz. An in situ campaign of measurements with a truck of known load was carried out by performing passages at 3 different speeds (10 km/h, 50 km/h, and 90 km/h) and along 3 different trajectories (called “deltaD”) in order to assess structural pavement behaviour. No loss of sensors was observed in this study. The analysis of data acquired during the experimental campaign showed that, in flexible pavements, measured strains were strongly impacted by vehicle speed, as well as by truck trajectory (Figure 1.33).

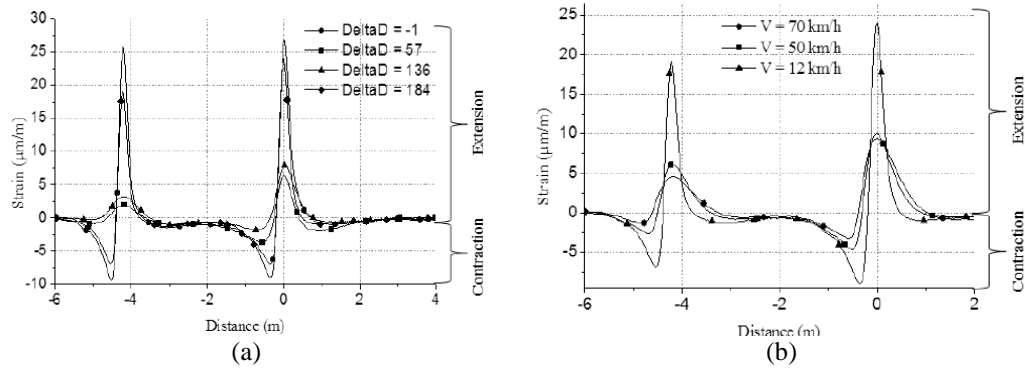


Figure 1.33 Instrumentation of the A41N highway in France. (a) Longitudinal strain in the subbase course for different truck trajectories ($V=12$ km/h, $T=20$ °C) and (b) longitudinal strain in the subbase for different speed (same trajectory, $T=23$ °C) (reproduced from (Gaborit et al., 2014)).

1.7.2.5 SMARTVIA®, the smart road (Pouteau et al., 2016)

The Smartvia concept, developed by the Eurovia Research Center, aims at onsite pavement monitoring and is based on sensor integration, electronics for real-time acquisition and data storage, and data post-processing for interpretation of pavement response (Pouteau et al., 2016). The first application in the field of this concept was performed in 2014 in the city of Lille (France), with the main objective to monitor the impact of trenches on new roads. The test section was composed of 7 instrumented nodes. A total of 98 sensing technologies were deployed: temperature sensors (PT100), strain gauges (H-gauges), moisture probes, and FBGs sensors. The data acquisition system (Figure 1.34) was composed by three data acquisition controllers. In addition, a digital camera was used for tracking every truck passing on the sensors. The data acquisition frequency was set at 1 kHz and triggers by events. Preliminary results documented the failure of almost all the H-gauges after 8 months due to corrosion, while a good feedback was obtained from the FBGs sensors.

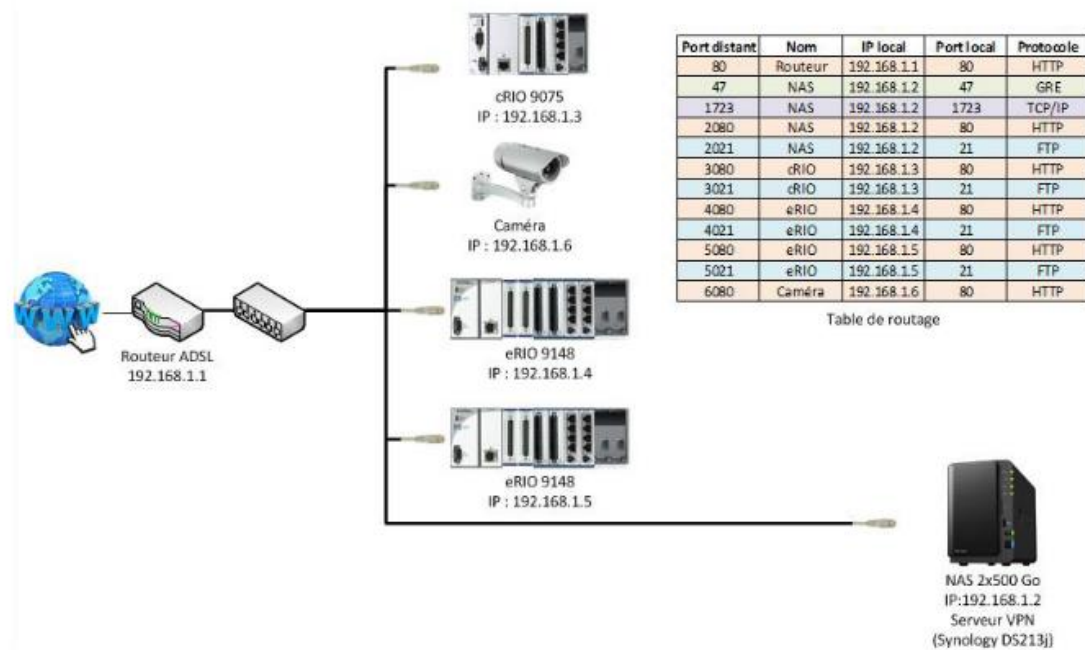


Figure 1.34 Architecture of the data acquisition system of SMARTVIA® (reproduced from (Pouteau et al., 2016)).

1.7.2.6 Instrumented test section in China (Ai et al., 2017)

In order to investigate the strain response of asphalt pavement under different axle configurations, axle loads, speeds, and pavement temperatures, a 900-m-long road was instrumented in China (Ai et al., 2017). A 4-lane and 2-way road was built using 3 types of pavement structures (semi-rigid, inverted, and compound asphalt pavement) for a length of 300 m each (Figure 1.35). Each section was instrumented with 4 asphalt strain gauges having 2 different orientations with respect to the traffic direction, as shown in Figure 1.35.

An experimental campaign was conducted with 2 trucks with different geometric configurations: single rear axle (truck 1) and tandem rear axle (truck 2). Three levels of axle loads were set: 98, 138, and 177 kN for truck 1 and 177, 255, and 334 kN for truck 2. Truck passages were conducted at three different temperatures (12, 21, and 43 °C) and two levels of speed:

- For the single axle load ≤ 138 kN and tandem axle axle load < 255 kN, 20, 40, 60, and 80 km/h
- For the single axle load > 138 kN and tandem axle axle load ≥ 255 kN, 20, 30, 40, and 60 km/h.

Results showed how strain increases with increased axle load, decreases with the increase of speed, and increases with the rise of temperature. Thus, a combination of high loading and

high temperatures could accelerate the occurrence of fatigue damage. In addition, the “truck 2” configuration generated higher strains than “truck 1”. Finally, a multivariate regression model was used to predict strain responses, and a good match between numerical and experimental results was found

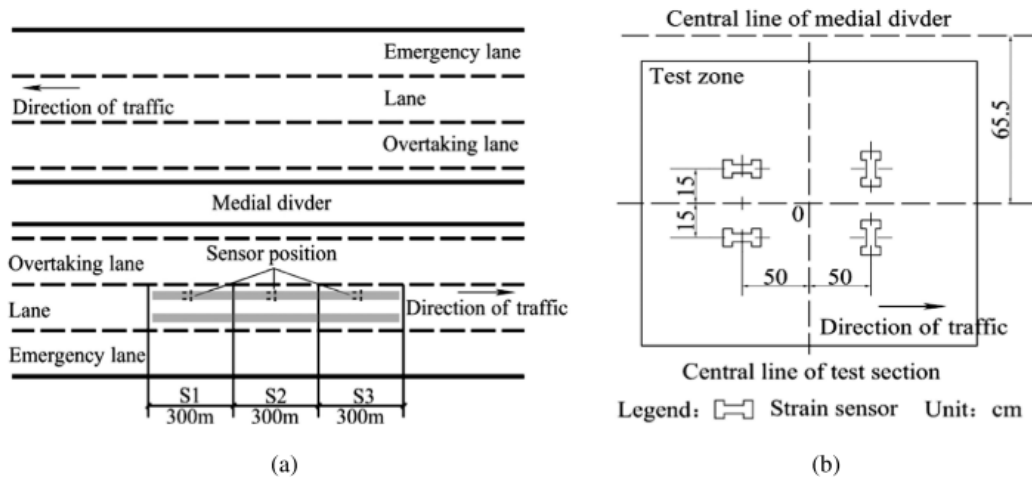


Figure 1.35 Instrumented section in China. (a) Layout of the instrumentation and (b) focus on the sensors (reproduced from (Ai et al., 2017)).

1.7.2.7 Monitoring of the motorway A10 in France (Juliette Blanc et al., 2017)

A part of the highway A10 in France was instrumented during the rebuilding of the slow vehicles lane (Juliette Blanc et al., 2017). The objective of this project was to evaluate the moduli of the pavement layers and monitor their evolution with time. Four sections (PR15+700, PR15+900, PR16+850, and PR17+100) were instrumented, with a total of 2 vertical ASGs and 5 horizontal ASGs per section. A fifth section (PR16+026) was instrumented with 2 geophones and 2 temperature probes. The pavement structure and the sensors layout are presented in Figure 1.36. A wireless data acquisition device, called PÉGASE, was used for remote monitoring. The PÉGASE device (developed by IFSTTAR and licenced to the company A3IP, France) permits data transfer from up to eight sensors (typically temperature and strain gauges in quarter, half, or full-bridge configuration) to a cloud-based supervisor and database (via 4G network) for further analyses. In addition, by integrating a low-power GPS receiver, the system allows accurate data dating and localization. An experimental campaign with two reference trucks (deflectograph and five-axle semi-trailer with tridem real axle) was conducted. Pavement calculations were performed to model the measurement campaign and inverse calculate the pavement moduli. The French software for pavement design, ALIZE, was used (Section 1.6.1.1). Good

agreement was found between numerical and experimental results. The moduli of the layers were calculated by fitting strain measurements within the pavement with the modelling data. This study also showed the good sensitivity and repeatability of geophone responses and suggested further investigation of this type of transducers for pavement monitoring.

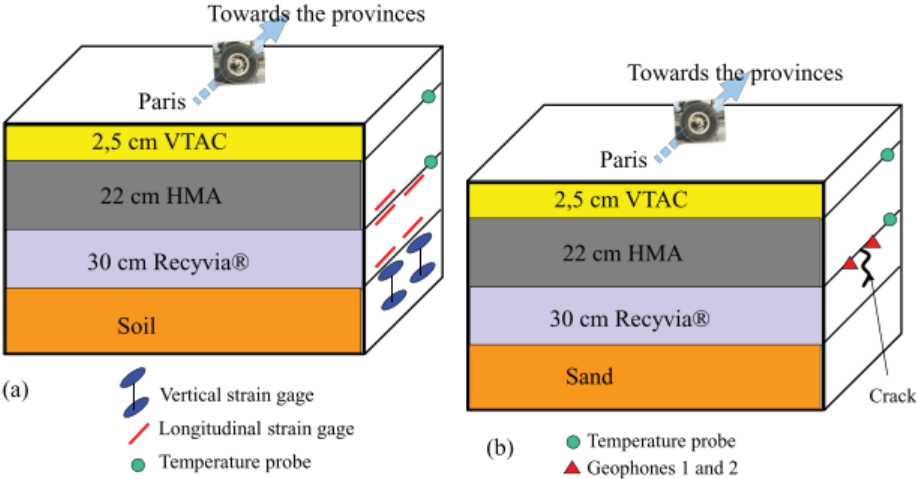


Figure 1.36 Road structure and sensors layout of the motorway A10 in France. (a) Sections PR15+700, PR15+900, PR16+850, and PR17+100 and (b) section PR16+026 (reproduced from (Juliette Blanc et al., 2017)).

1.7.2.8 Continuous monitoring by using geophones and ASGs (French motorway) (Duong, Blanc, Hornych, Bouveret, et al., 2018)

During the reconstruction of the slow lane of a French motorway, instrumentation was set up for continuous monitoring based on the coupling of ASGs with geophones and temperature probes (Duong, Blanc, Hornych, Bouveret, et al., 2018). The pavement structure and the sensors layout are shown in Figure 1.37. The PÉGASE Platform was used as the data acquisition system. Due to the impossibility to close the lane and perform measurements with a known truck, the acquisition was carried out under real traffic. Measurements show high sensitivity of strains to vehicle type and wandering. Thus, the authors developed a methodology to select a signal associated to heavy traffic passing right above the strain sensors by analysing the signal recorded by the geophones placed at different lateral positions (Figure 1.38). This showed the feasibility of pavement monitoring under real traffic.

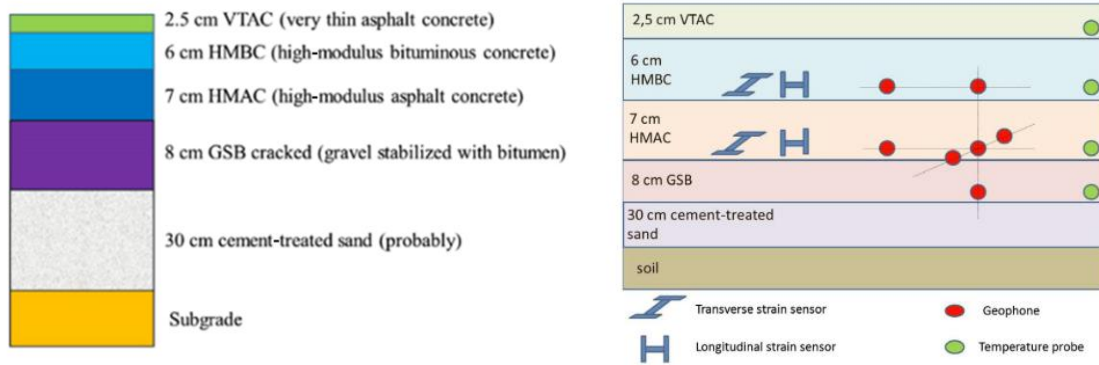


Figure 1.37 French motorway. (left) Pavement structure and (right) sensors layout (reproduced from (Duong, Blanc, Hornych, Bouveret, et al., 2018)).

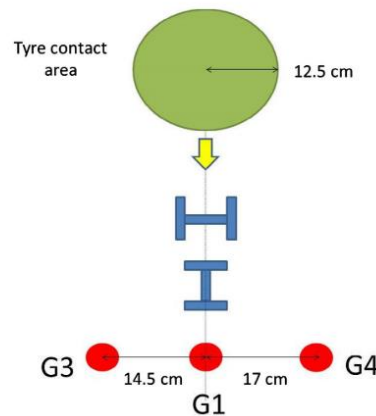


Figure 1.38 Lateral position of geophones G1, G3, and G4 installed on a French motorway (reproduced from (Duong, Blanc, Hornych, Bouveret, et al., 2018)).

Pavement calculations were performed by using the software ALIZE and Viscoroute© (Section 1.6.1.1 and Section 1.6.1.2). Results highlighted the importance to take into account the viscoelastic properties of bituminous materials and to consider the interface contribution for a better prediction of the pavement response under loading at high temperatures.

1.8 Potential of carbon nanomaterials (CNMs) for road pavement monitoring

As described in Section 1.7.1 various sensing technologies for road instrumentation are available on the market. These devices allow the assessment of pavement response in terms of stress, strain, deflection, temperature, and water content to moving loads and due to varying climate conditions. Sensors are designed to be asphalt-compatible and provide very accurate measurements. However, feedbacks from real applications (Section 1.7.2) have

shown some challenges (such as high intrusiveness, high cost, and short lifetime) and the need to pursue further research in this field.

A novel approach is based on nanotechnology and in particular on the use of carbon-based nanomaterials for civil engineering applications.

1.8.1 Carbon nanomaterials (CNMs): definition, structure and main properties

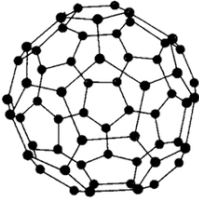
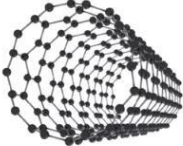
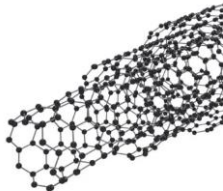
The most commonly accepted definition of nanotechnology is the one established by the National Nanotechnology Initiative (NNI) that defines nanotechnology as "*the understanding and control of matter at dimensions of roughly 1 to 100 nanometres, the size-scale between individual atoms and bulk materials, where unique phenomena enable novel applications*" (Sargent, 2014). In recent years nanomaterials (NMs) have attracted more and more attention as they exhibit unique characteristics compared to the same material without nanoscale features, such as increased strength, chemical reactivity, or conductivity. In fact, at this size range the behaviour and properties of the materials are ruled by two effects: the *surface effect* and the *quantum size effect* (Roduner, 2006). The first is related to the fact that when compared to the counterpart material in the bulk form the NMs have a higher fraction of atoms at the surface. These latter being less stabilized, make the material more chemically reactive and affect its strength and electrical properties. The *quantum size effect* becomes dominant for matter in the nanoscale, affecting the optical, electrical, and magnetic behaviour of materials.

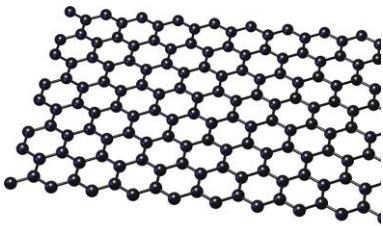
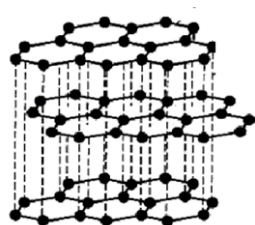
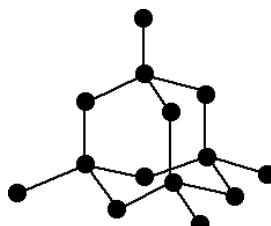
The nanotechnology industry has been seeing rapid growth in the last ten years and is expected to grow more. The "Global Nanotechnology Market (by Component and Applications), Funding & Investment, Patent Analysis and 27 Companies Profile & Recent Developments - Forecast to 2024" report estimates that the global nanotechnology market will exceed US\$ Billion by 2024. According to statistics, the 85% share of the global market is held by nanoparticles; and the top three applications of nanotechnology (electronics, energy and biomedical) together hold the 70 % share of the global market.

Nanotechnology has a significant impact in different fields, such as electronics, energy, biomedicine, automotive, textile, and agriculture among others. In particular, it also has an important role in civil engineering disciplines, including transportation, structural, geotechnical, water resources, and environmental engineering. The objective is to employ nanomaterial features to improve performance, resiliency, and longevity of traditional

construction materials and structural components. Overall the interest lies in incorporating new capabilities in civil engineering works (Lebental, 2010) (Mobasser & Firoozi, 2016). Compared to the other types of materials in the nanoscale, CNMs (especially graphene and carbon nanotubes) are some of the most promising ones as they exhibit attractive properties for technical applications (Lebental, 2016) (M. C. dos Santos et al., 2017). Carbon has the highest number of identified allotropes in the periodic table due to its various hybridization forms (Hu et al., 2016). CNMs can be categorized into four groups with respect to their structural dimension: in zero-dimensional (0D) NMs all the dimensions are measured in the nanoscale (no dimensions are larger than 100 nm); one-dimensional (1D) NMs have one dimension outside the nanoscale; in two-dimensional (2D) NMs two dimensions are outside the nanoscale; three-dimensional (3D) NMs generally consist of individual blocks which may be in the NMs or have features at the nanoscale (i.e. porosity, roughness) (Pokropivny & Skorokhod, 2007) (Fan et al., 2017). Following this classification, examples of carbon allotropes are reported in Table 1.4 (Barhoum et al., 2019). Concerning the fabrication process, several methods were developed for the synthesis of CNMs, among them arc-discharge, laser ablation, pyrolysis, and chemical vapour deposition (Cha et al., 2013).

Table 1.4 Examples of carbon allotropes structures: fullerene, single-walled carbon nanotubes, multi-walled carbon nanotubes, graphene, graphite, and diamond.

Structural dimension	Carbon allotrope	Picture
0D	Fullerene	
1D	Single-walled carbon nanotubes	
	Multi-walled carbon nanotubes	

Structural dimension	Carbon allotrope	Picture
2D	Graphene	
3D	Graphite	
	Diamond	

To give an idea about the remarkable properties of CNMs that make them attractive materials for civil engineering applications, let us focus on graphene and carbon nanotubes (CNTs) which have been heavily investigated. Both materials exhibit high flexibility as well as excellent mechanical properties. Graphene is the strongest material ever tested, with a tensile strength of 130 GPa and a Young's modulus of 1 TPa, five times bigger than that of steel (200 GPa). CNTs have a tensile strength between 11 and 63 GPa and a Young's modulus between 270-950 GPa. The electron mobility of graphene and CNTs reaches respectively, $\approx 100 \text{ cm}^2 \text{ V}^{-1} \text{ s}^{-1}$ and $200 \text{ cm}^2 \text{ V}^{-1} \text{ s}^{-1}$ compared to the $1400 \text{ cm}^2 \text{ V}^{-1} \text{ s}^{-1}$ for silicon (the most used semiconductor in electronics). The thermal conductivity of graphene is $5300 \text{ W m}^{-1} \text{ K}^{-1}$ and that of CNTs is $3500 \text{ W m}^{-1} \text{ K}^{-1}$, both higher than that of copper ($385 \text{ W m}^{-1} \text{ K}^{-1}$). For these reasons CNMs are promising materials for the improvement of common construction materials as well as the realisation of next-generation electronics (Ramsden, 2011) (Chae & Lee, 2014) (Lebental, 2016).

1.8.2 Applications in civil engineering

CNMs have attracted strong attention for civil engineering applications, and more specifically for strain monitoring, which is one of the major target quantities for monitoring

in this field. Indeed, they often feature piezoresistive behavior, either directly as raw material property (like semi-conducting single-walled carbon nanotubes) or by assembly into a percolating layer of conducting materials. In the latter case, when tensile (resp. compressive) strain is applied, the number of contact points between particles and the average distance between particles decreases (resp. increases). Hence the resistivity of the device increases (resp. decreases) (Obitayo & Liu, 2012) (Seppälä et al., 2010). An example of the piezoresistive behaviour of a percolating layer of conductive material under tensile and compressive stress is outlined in Figure 1.39.

Researchers have strongly focused on the development of self-sensing nanocomposite materials, made by mixing CNMs with traditional engineering materials such as concrete, bitumen or even polymers.

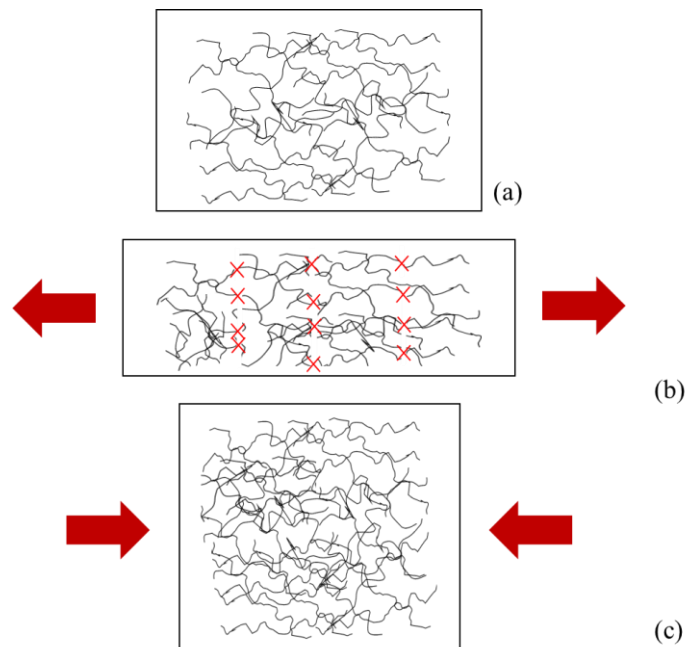


Figure 1.39 Outline of the piezoresistive behaviour of percolating layer of conducting material. (a) Resting configuration; (b) Application of tensile stress; (c) Application of compressive stress.

1.8.2.1 CNM-based composite materials

Introducing CNMs as filler material in traditional engineering materials was first proposed to enhance their durability and strength. Generally the addition of low portion of CNMs (less than 0.5 wt.%) to cement based materials is enough to significantly improve their mechanical properties. Konsta-Gdoutos et al. (Konsta-Gdoutos et al., 2010) reported a 45 % increase in the Young's modulus and a 25 % increase in the flexural resistance for small concentration of multi-walled CNTs (0.08 wt.% and 0.048 wt.%). They also highlighted the importance

of an effective dispersion of CNTs in the cement matrix; in this case it was achieved by applying ultrasonic energy and with the use of a surfactant. Later Li et al. (Xueguang Li et al., 2015) investigated the co-effect of single-walled CNTs (SWCNTs) and graphene oxide (GO) on the mechanical properties of cement. They showed an increase in bending strength of 72.7 %, higher than the improvement with only CNTs or GO.

Similar studies were carried out on binder and asphalt mixtures (Ashish & Singh, 2019). Ameri et al. (Ameri et al., 2016) found that the use of CNTs as binder modifier can promote fracture and fatigue resistance of asphalt mixtures. Different concentration of CNTs (0.2 %, 0.5 %, 0.8 %, 1.2 %, and 1.5 % of the weight of the base binder) were added to a 60/70 penetration grade bitumen. First they observed an improvement of the binder performances due to the increase of storage modulus and decrease of phase angle, especially for higher percentage of CNTs and higher frequencies (or lower temperatures). In addition the results obtained from semi-circular bending fracture test and flexural test showed an increase of the fracture resistance and fatigue life of the mixtures more pronounced for the highest CNTs concentrations. Similar improvement of binder performances were later observed by Goli et al. (Goli et al., 2017). The addition of different concentrations of CNTs (0.3, 0.6, 0.9, 1.2, 1.5 wt.%) to a PG 58-16 base binder resulted in the improvement of the complex modulus G^* and reduction of the phase angle δ (more important for concentrations > 1 wt.%), as well as the increase of the softening point of binder (from 53 °C to 61 °C for concentrations from 0.3 wt.% to 1.5 wt.%). The study also explored the influence of CNTs to SBS modified binders: an improvement of the storage stability was observed. Yang et al. (Yang et al., 2019) identified the optimum content of CNTs and graphene for bitumen binder, respectively 1.5 wt.% and 1 wt.%. They also found a better compatibility of graphene with bitumen probably due to its morphology (sheet-like surface) and larger specific area that make blending with bitumen molecules easier. In fact graphene modified bitumen are more performant than CNTs modified bitumen at the same concentrations. In a more recent study Yoo et al. (Yoo et al., 2019) found that the use on CNMs can enhance the self-healing capability of asphalt concrete. They evaluated how much the flexural strength of completely damaged asphalt concrete specimens (with and without carbon materials) was recovered by the induction heating process at the ambient temperature. They found a 40 % recovery of the original flexural strength for the mixture modified with 0.5 % of graphite nanofibers.

Besides the improvement of mechanical performances of construction materials, it was also shown that CNMs can endow them with piezoresistive capabilities (Banthia et al., 1992)

(Wen & Chung, 2000) (Loamrat et al., 2014) (Parmar et al., 2018). In fact the application of mechanical strain can alter the percolation paths between nanomaterials and thus the electrical resistance of the composite material. This aspect has attracted the curiosity of researchers who saw its potentiality in the development of self-sensing materials (Guo et al., 2019). Konsta-Gdoutos et al. (Konsta-Gdoutos & Aza, 2014) investigated the resistivity of CNT/cement and carbon nanofiber (CNF)/cement composites. The results obtained for neat cement paste (CP) were compared to those obtained for composites containing well-dispersed and "as received" nanomaterials. Obviously, the addition of nanomaterials resulted in a decrease of the electrical resistance with respect to neat CP. The best results were obtained with cement composite reinforced with well dispersed 0.1 wt.% CNTs (lower resistivity with good repeatability). In addition nanocomposites reinforced with 0.1 wt.% CNTs and CNFs under cyclic loading showed a higher change in resistivity ($\approx 5\%$) with respect to those reinforced with 0.3 wt.% CNTs or CNFs, meaning that the material exhibited a more pronounced sensitivity in recognizing the change in the applied stress. The possibility to use CNT/cement composite as crack detector was investigated by Lim et al. (Lim et al., 2017), who found that cracks could be detected by measuring a decrease in conductivity, though the latter was dependent on both crack width and moisture content. Yoo et al. (Yoo et al., 2017) reported on the sensing capacities of composites with various nanomaterials, namely multi walled CNTs (MWCNTs), graphite nanofibers (GNFs), and graphene (G) when incorporated to the cement paste with an identical volume fraction of 1 %. It emerged that MWCNTs were better than GNFs and G in providing the cement paste with self-sensing performances. In addition the MWCNT/cement composite exhibited a gauge factor (GF) of 113.2, much higher than commercially available strain gauges. A first attempt to use MWCNTs filled cement composite for developing piezoresistive sensors for traffic monitoring was made by Han et al. (Han et al., 2009). The CNT/cement composite was tested in the lab, under compressive loading and impulsive loading, as well as in the field, under vehicle loading (Figure 1.40). The tested sample is a 5.08 x 5.08 x 5.08 cm cube of Portland cement where a concentration of MWCNTs of 0.1 wt.% was added. Laboratory tests showed a regular response of electrical resistance of the composite under loading which indicated a good sensing capability. This latter was then confirmed in the field as the composite was sensitive to the passage of different vehicle types (passenger vehicles and minivan) indicating its possible use for vehicle detection and weigh in motion (WIM) applications (Figure 1.40). Similar studies were conducted in the field of asphalt materials. Rizvi et al. (Rizvi et al., 2016) found that CNFs can provide HMA (Hot Mix Asphalt) with

promising piezoresistive capabilities at different loading frequencies (Figure 1.41). Temperature impact on the sensing performances of the CNFs/asphalt composite was considered not relevant as sufficient change in resistivity with the change in load was observed at different temperatures (20 °C, 40 °C, and 60 °C).

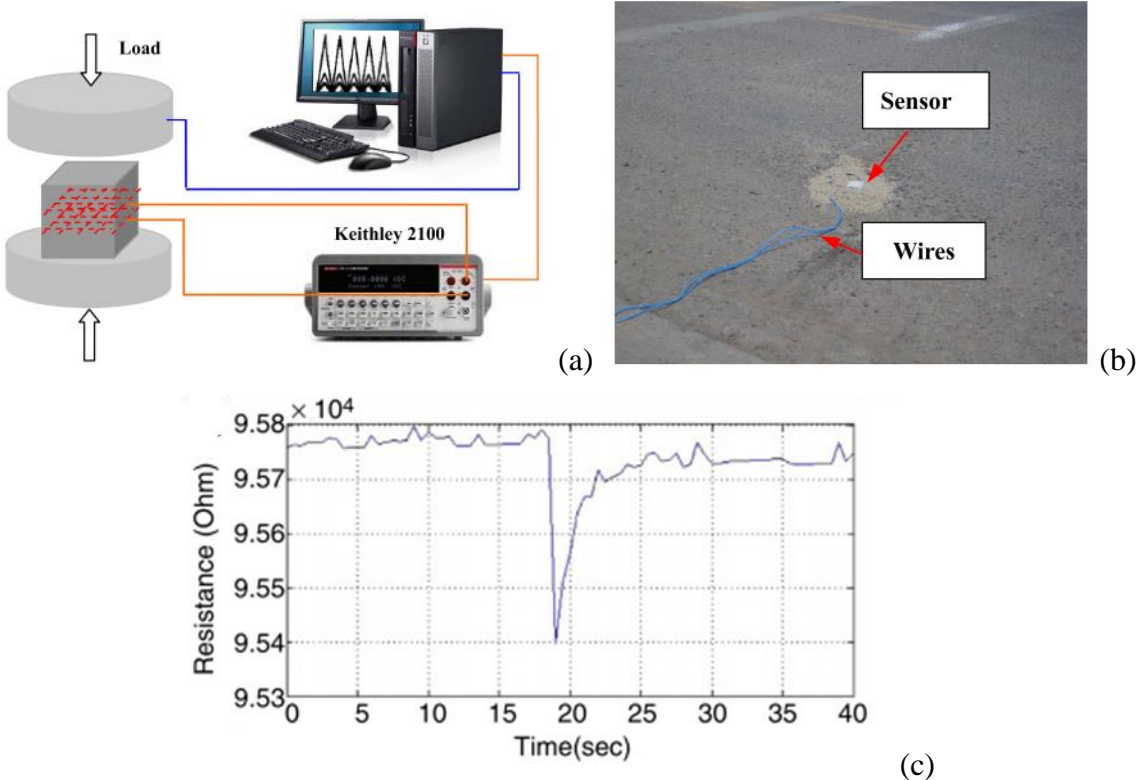


Figure 1.40 (a) Outline of the laboratory equipment used for compressive loading and impulse loading; (b) CNT/cement composite embedded in concrete pavement; (c) Response of the CNT/cement composite under the passage of a minivan (reproduced from (Han et al., 2009)).

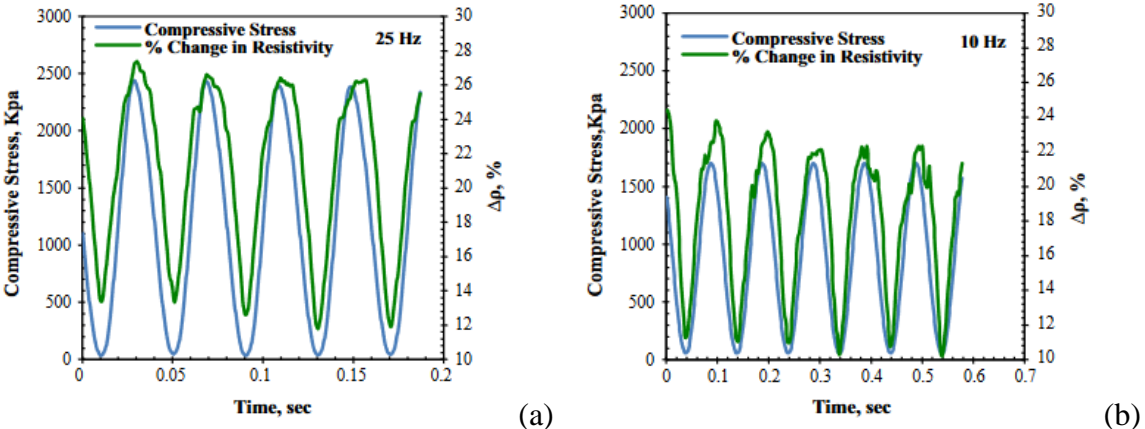


Figure 1.41 Resistivity response of 5.3 % CNFs/asphalt composite under compressive stress at (a) 25 Hz and (b) 10 Hz (reproduced from (Rizvi et al., 2016)).

However, this type of materials may not be the ideal solution for road monitoring. In fact a significant weight ratio of nanoparticles is needed to make asphalt conductive materials, which leads to unreasonable costs for the volume needed for self-sensing materials (Silvestre et al., 2016) (Du et al., 2020). In addition piezoresistivity requires very careful dispersion of CNMs in the construction materials, which is so far only suitable for prefabricated materials and thus not compatible with most use cases for road pavement monitoring solutions (Yang et al., 2019) (Du et al., 2020). Finally, having nanoparticles directly within the top road layer strongly raises the question of nanoparticles release in the environment during the lifetime of the road due to ageing (Silvestre et al., 2016).

1.8.2.2 CNM-based strain sensors

A strong alternative to such technologies lies in CNM-based strain sensors fabricated on flexible substrates as they are highly sensitive to the deformation of the substrate (Yee et al., 2019). CNM-based flexible strain sensors have been widely studied at a laboratory scale with the objective to improve their manufacturing process and understand their strain sensitivity (Vemuru et al., 2009) (Eswaraiah et al., 2011) (Karimov et al., 2012) (X. Wang et al., 2015) (Michelis et al., 2015) (A. Santos et al., 2019). All the aforementioned studies highlighted the interesting properties of CNM-based strain sensors, such as: high sensitivity, good stability and reproducibility, linear response, conformability (capability to follow the deformation of a structure), as well as the possibility to be deployed for static and high frequency signals. There have now been various advanced applications of these sensors in smart skin configuration, namely for surface-based motion monitoring: body motion (Yamada et al., 2011), plant growth (Tang et al., 2019), engineering and aerospace structures (Wincheski et al., 2019), as well as construction materials (Lebental, 2010) (Michelis, 2016). Loh et al. (Loh et al., 2005) developed a strain sensors for large-scale infrastructures monitoring based on a layer-by-layer film deposition using SWCNTs and polyelectrolyte (PE). The sensor, mounted on structural specimens, was tested in the lab under monotonic and cyclic load patterns. The graphs in Figure 1.42 show a good correlation between the sensor response and the change in resistance of the reference gauge. In addition, a GF of 4.52 was found.

Kang et al. (Kang et al., 2006) developed a MWCNT polymer composite continuous strain sensor, which is a low cost solution suitable for SHM. In fact the sensor is easy to apply to the structure with a spray-on technique and is able to detect crack propagation.

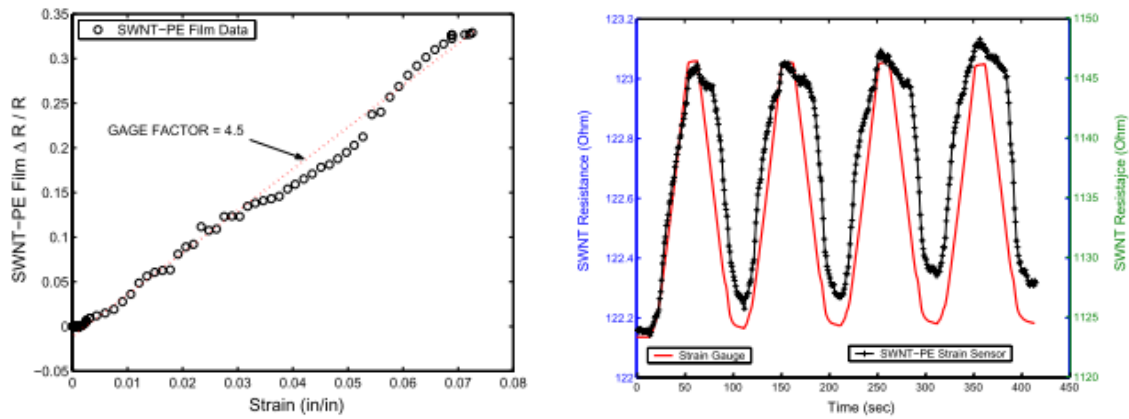


Figure 1.42 (Left) Change in resistance versus strain of the SWCNTs-PE sensor under monotonic loading (sensor mounted on the side of an aluminium coupon); (Right) Change in resistance of the SWCNTs-PE sensor and reference gauge under cyclic loading (sensors mounted on a cementitious plate) (reproduced from (Loh et al., 2005)).

In Burton et al. (Burton et al., 2016) a CNT polymer composite film fabricated with the layer-by-layer method was used to instrument a composite beam-column connection in the laboratory (Figure 1.43) and tested under quasi-static loading. The comparison between the sensor response and the response obtained from a strain gauge at the same location shows the proper operation of the sensor from the initial loading (Figure 1.44a) to the final failure of the structure (Figure 1.44b).

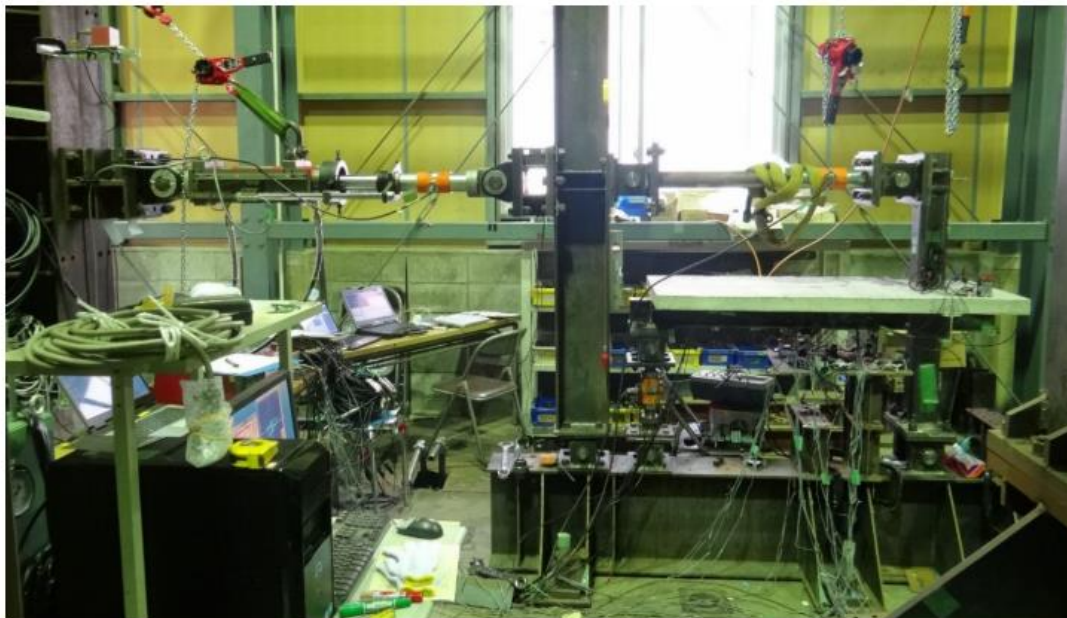


Figure 1.43 Composite beam-column connection in the laboratory (reproduced from (Burton et al., 2016)).

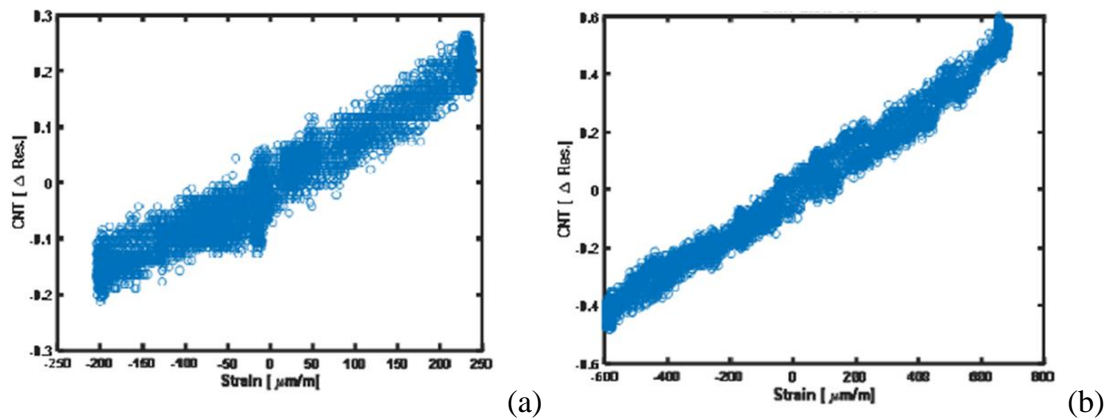


Figure 1.44 Strain-resistance response of CNT polymer composite film under quasi-static loading: initial loading (a) and failure of the structure (b) (reproduced from (Burton et al., 2016)).

Zymelka et al. (Zymelka et al., 2017) instrumented a metal girder of a highway bridge with a graphite-based flexible strain sensor. The sensor was able to detect all heavy vehicle passages (Figure 1.45), thus confirmed its potential use for traffic monitoring as well as for detection of occurring damage.

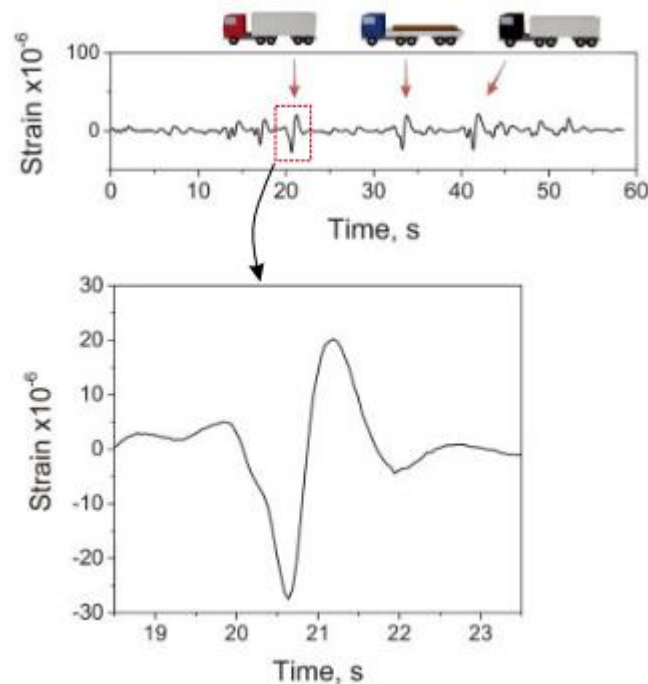


Figure 1.45 Data collected from a graphite-based flexible sensor attached to a metal girder of a highway bridge (reproduced from (Zymelka et al., 2017)).

More recently Nie et al. (Nie et al., 2019) developed a highly sensitive graphene-based strain sensor for monitoring of massive structures. The sensor was tested in the laboratory and

exhibited an excellent behaviour under tensile strain with GF values from 375 to 473 (Figure 1.46a), as well as a good stability over about 1000 cycles (Figure 1.46b).

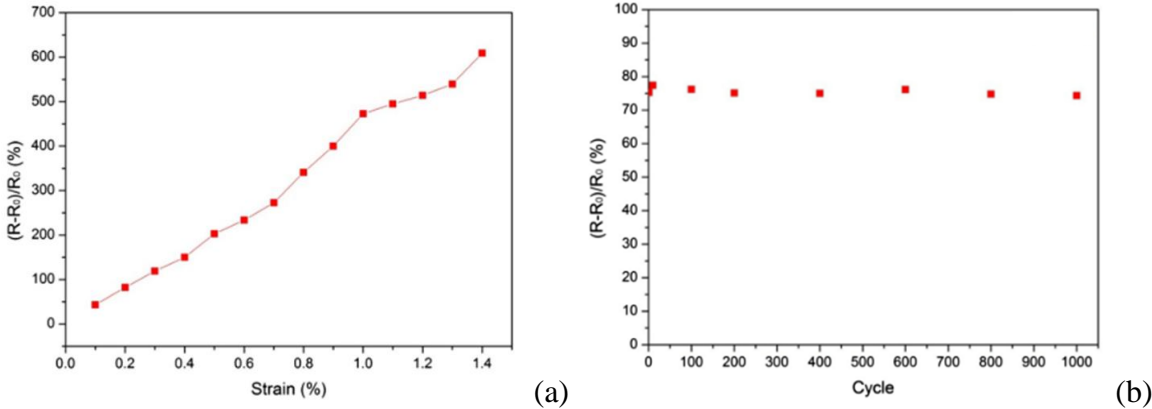


Figure 1.46 Laboratory test of graphene-based sensor. (a) Monotonic test: relative resistance change versus applied strain. (b) Cyclic test: relative resistance change with repeated tensile strain of 0.16 % (reproduced from (Nie et al., 2019)).

However, there has so far been very little work on embedded solutions, e.g. sensors embedded at the core of a construction material, though they are crucial notably for pavement monitoring applications as conditions of exploitation prevent the use of surface sensors: in (Michelis, 2016) a solution for embedded monitoring of concrete using ink-jet printed carbon-nanotube strain sensors was proposed and validated in the mortar foundation slab of a small house. After six months from pouring the CNT-based sensors exhibited a survival rate higher than the commercial ones, showing a higher adaptation to the harsh environment of concrete (Figure 1.47). A wireless version of the sensor was later proposed (Laheurte et al., 2016).

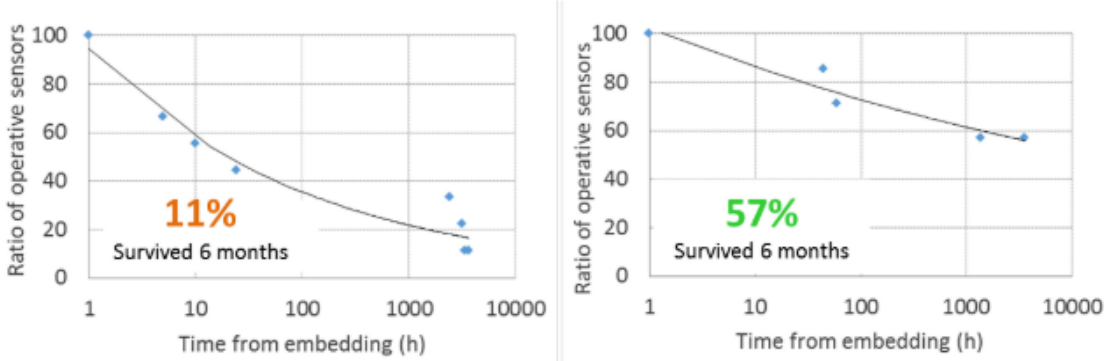


Figure 1.47 Survival rate of commercial strain gauges (left) and CNT-based ones (right) (reproduced from (Michelis, 2016)).

In Ghaddab et al. (Ghaddab et al., 2014) a weight sensor and crack monitoring solution directly lying at the interface between two bituminous mixture slabs (Figure 1.48) was proposed and validated at lab scale. It relied on directly fabricating at the slab surface a piezoresistive percolating layer out of a patented carbon-clay nanocomposite material (Lebental et al., 2014).

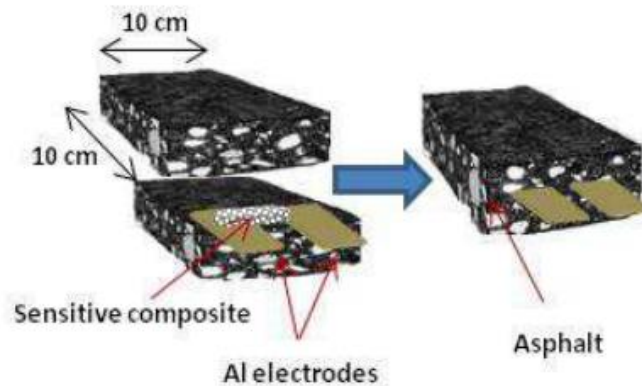


Figure 1.48 Outline of the specimen (reproduced from (Ghaddab et al., 2014)).

1.9 Conclusions

A road is typically composed of superimposed layers of processed materials having different thicknesses, where the loads are transferred from the top layer to the layer below (soil). Depending on the structure type, some of these layers consist of bituminous materials which are known for their viscoelastic behaviour and their temperature susceptibility, thus their response is a function of time and temperature. The analysis of the overall road pavement response can be performed with theoretical models based on the Burmister's multi-layered elastic model, such as Alizé-LPCP (reference software for pavement design in France) and Viscoroute©. The latter allows to account for viscoelasticity of materials through the Huet-Sayegh model.

In order to maintain the road network in good conditions road operators should establish cost-effective maintenance plans that require the evaluation of the road network for the assessment of its actual conditions. In this respect the use of embedded devices allows continuous and remote monitoring with no traffic disruption. Various sensing technologies for road instrumentation are available on the market, such as asphalt strain gauges (horizontal and vertical), fiber optic sensors, LVDTs, geophones, accelerometers,

thermocouples, resistance temperature detectors, thermistor sensors, moisture probes, and pressure cells. They allow the assessment of pavement response under moving loads and due to varying climate conditions in terms of strain, deflection, temperature, water content, and stress. Several road sections have been instrumented so far in order to investigate pavement response to load and temperature and follow its evolution with time. It emerged that the sensing technologies usually deployed in instrumentation projects may have some limitations in terms of survival rate at the installation phase, geometry, survivability, and costs. As expected, due to the complexity of bituminous materials, measurements within the pavement depend on multiple parameters, such as vehicle load, vehicle speed and temperature. A sufficient number of sensors (in order to account for sensor loss), as well as a full control of the load conditions is required for inverse calculation of pavement mechanical conditions.

With the aim of developing more advanced, embeddable sensing technologies, we focused on the deployment of the remarkable properties of carbon nanomaterials for road pavement applications. In this regard, most of the studies focused on the incorporation of CNMs in the asphalt mix to improve its mechanical properties and durability, as well as provide sensing features. It emerged that the major challenge associated to CNMs-asphalt composites is the poor dispersion of CNMs in the asphalt matrix. To this are added the high costs related to the amount of CNMs required to obtain a significant improvement of mechanical and/or sensing performances, as well as the problem of having nanoparticles directly at the surface of the road (dispersion in the environment).

In terms of strain sensing, a better application of CNMs to pavement monitoring lies on highly sensitive embeddable CNM-based strain sensors fabricated on flexible substrates.

While the community agrees that embedded pavement monitoring should be valuable, there is no proof yet that it is feasible in practical conditions. The overall goal of this thesis is to prove the feasibility of embedded pavement monitoring by demonstrating the exploitability of embedded sensor data to assess road ageing, and by providing a high performance, low intrusiveness technology. The thesis has three main goals:

1. Propose a methodology for sensor data interpretation to detect the occurring of damage in a road pavement. We analyse the occurrence of fatigue in a single layer of a road pavement under accelerated pavement testing.

1 Context: Road pavement monitoring and nanotechnologies

2. Propose a methodology to track the evolution of pavement conditions based on embedded sensing devices. To this purpose we work on the instrumentation of an existing road.
3. Investigate the benefits of using CNM-based strain sensors for pavement monitoring. Hence, the objective is the development of an embeddable nanotechnology that may overcome some of the drawbacks of existing sensing devices. We perform laboratory as well as full scale tests.

In the following chapters, we present the results that demonstrate the accomplishment of these goals.

2 DETECTION OF PAVEMENT AGEING BASED ON EMBEDDED SENSORS – ACCELERATED PAVEMENT TESTING

2.1 Introduction

We have seen in the introduction that the establishment of strategies for sensor data interpretation is crucial for pavement monitoring and damage detection. So here we consider the accelerated pavement testing (APT) of four sections having four different bituminous layers and we use embedded asphalt strain gauges and temperature probes to detect the occurrence of fatigue of the bituminous layers.

APT is a method used to assess full scale pavement performances in few weeks or months instead of the lifetime of a road (20-30 years) (Transportation Research Board, 2004, 2009). The APT facilities allow a better control of test conditions, namely the structure composition (materials; layer thickness, construction process), as well as axle load (applied value and point of application), loading speed and sensor locations. Different methods are used to track the evolution of pavement performances and evaluate how different loading configurations may influence the fatigue behaviour of road pavement. Notably, the sections are often instrumented with sensing devices that allow for measurement of pavement response to loading (see section 1).

APT is a perfect tool to test methodology to assess pavement ageing based on embedded sensors. We worked with a dataset provided by the full scale fatigue experiment conducted within the European project BioReparation (J Blanc, Chailleux, et al., 2019) (J Blanc, Hornych, et al., 2019) at the University Gustave Eiffel APT facility (also called fatigue carousel). We first compared strain measurements with measurements from traditional monitoring procedures, such as visual crack inspections, Benkelman's beam deflections, and

FWD deflections. Deflections measurements at the end of the fatigue test were used to inverse calculate the layer moduli of pavement. Based on this model, numerical strains are calculated and compared with sensor measurements. The analyses conducted proved that embedded asphalt strain gauges and temperature probes can be used valuably to assess pavement fatigue. Compared to previous studies carried out in (Timm et al., 2013), the analyses carried out in this thesis apply to greater level of damage and cracking. Finally, a procedure for temperature correction of strain measured within the pavement is presented as a tool improving sensor data interpretation.

2.2 Description of the full scale experiment and monitoring methods

2.2.1 The fatigue carousel facility

The fatigue carousel (Figure 2.1), located in Nantes (France), is an outdoor road traffic simulator designed for the assessment of real scale pavement behaviour under accelerated heavy traffic. The carousel has a perimeter of 120 m and is equipped of a central electro-hydraulic motor unit and 4 loading arms that can reproduce various loading configurations (single wheel, dual wheels, tandem, tridem). The arms can turn at the maximum speed of 100 km/h, their loads can vary between 40 and 150 kN and they feature the possibility of move transversely. Being outdoors, the fatigue carousel is subjected to climate variations, thus the different tests are carried out during the most suitable seasons. Usually fatigue tests are carried out during months with expected temperatures below 20 °C.



Figure 2.1 The University Gustave Eiffel fatigue carousel: four arms are controlled by a central electro-hydraulic motor unit. The perimeter is 120 m long.

2.2.2 Tested pavement sections

Four sections, having the structures presented in Figure 2.2-Right were tested simultaneously. The sections differ from each other by the asphalt mix used as surface layer:

- A reference material that is a high modulus asphalt mix (called EME2 in France, see Section 1.4.3), with 15/25 pen grade bitumen and 20 % of reclaimed asphalt.
- Three sections with the GB5® type mixes (F Olard, 2012; F Olard & Pouget, 2015a; Pouget et al., 2016) used in BioReparation containing respectively the performance additive SYLVAROADTM RP1000 provided by Kraton Chemical (in the following called Mix1), the bio-binder Biophalt® (Pouget & Loup, 2013) from Eiffage Route (in the following called Mix2), and the bio-based additive EMS (Epoxidized Soybean Soyate) from Iowa State University (in the following called Mix3).

The 9 cm-thick bituminous surface layer lays on a 76 cm-thick subbase layer of 0/31.5 mm unbound granular material, a 1.6 m-thick stone bed 50/120 mm (subgrade), a clay soil of low bearing capacity.

The reference section is 32 m long while the other three are 22 m long (Figure 2.2-Left). All the sections are 4.5 m wide. Another section of 22 m was tested but it is not included in this study (J Blanc, Chailleux, et al., 2019).

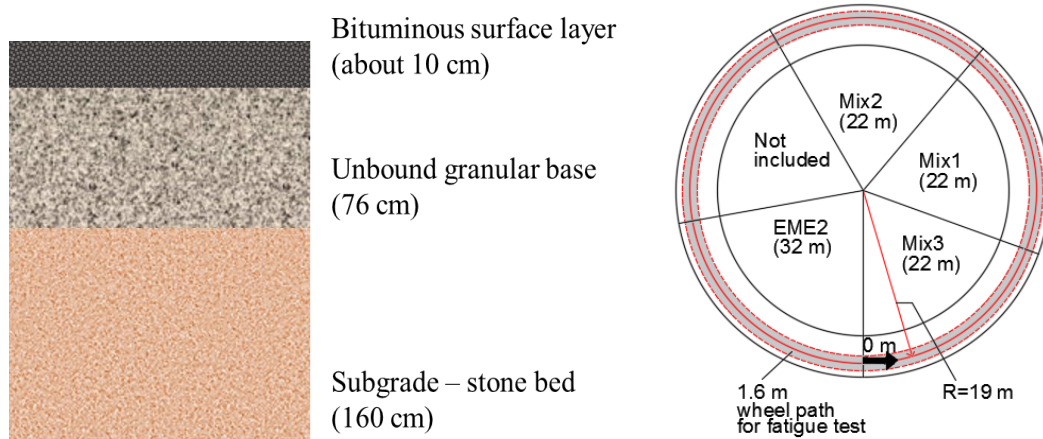


Figure 2.2 Sections on the APT. (Left) Pavement structure; (Right) layout of the test site.

2.2.3 Outline of the fatigue evaluation

The fatigue evaluation was carried out between November 2017 and March 2018. One million 65 kN dual wheel loads (corresponding to the French standard axle load) were applied at radius 19 m at 72 km/h. After this first phase no significant surface damage was observed on the four sections, therefore it was decided to continue with additional 400,000 75 kN dual wheel loads at 43 km/h. The loading conditions are summarised in Table 2.1 (J Blanc, Hornych, et al., 2019). No tests were performed outside the wheel path to separate fatigue damage (within the wheel path) from ageing (outside the wheel path). However binder evolution in the four sections was analysed using the non-destructive pavement micro-sampling technic as described in (J Blanc, Hornych, et al., 2019).

Table 2.1 Fatigue test loading conditions. 65 kN 1 million loads at 72 km/h followed by additional 75 kN 400,000 loads at 43 km/h.

N° of loads	Load	Speed	Transverse wandering	Mean temperature of the asphalt layer
1 million	65 kN	72 km/h	± 52 cm	9.4 °C (± 26 %)
400,000	75 kN	43 km/h	± 52 cm	13.8 °C (± 24 %)

2.2.4 Monitoring methods

The non-destructive monitoring procedures adopted for the assessment of pavement performances over the duration of the test are described in the following sections.

2.2.4.1 Visual crack inspections

A detailed visual inspection of pavement surface was conducted for all the sections in order to record crack appearance over the duration of the fatigue test. For a better identification cracks were painted with different colours according to different inspection times. Conventionally on the APT the extent of cracking is defined as the percentage of the pavement affected by cracks. For longitudinal cracks, the “cracked length” corresponds to the measured length of the cracks. For transversal cracks, a length of 50 cm is conventionally attributed to each crack (J Blanc, Hornych, et al., 2019).

2.2.4.2 Benkelman beam deflections

Pavement deflections were measured with the Benkelman beam (Figure 2.3) every 100,000 loads starting with the initial (pre load) configuration. The Benkelman beam provides punctual measurements of the pavement maximum deflection (AFNOR, 1992). The tip of the beam is placed exactly in the middle of the two wheels of the carousel arm (Figure 2.3). It measures the rebound of the pavement surface as the arm is moved away (at about 3 km/h). On each section measurements were spaced about every 4 m, which results in a total of 4 measurements on sections Mix1, Mix2 and Mix3 and 5 on section EME2 (J Blanc, Hornych, et al., 2019).

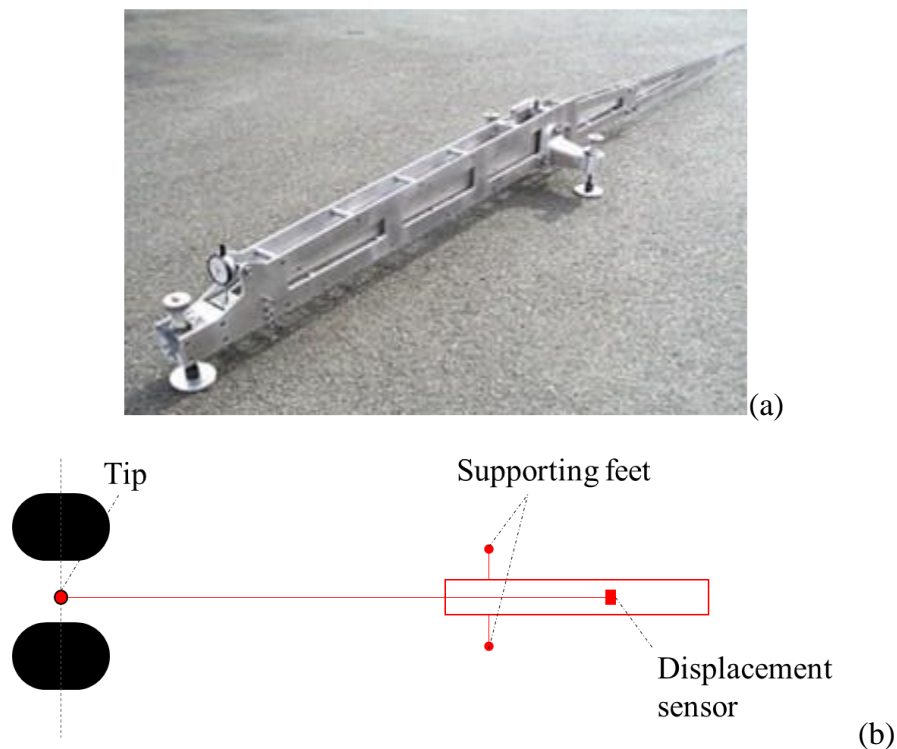


Figure 2.3 Benkelman beam (a) Photo; (b) Schematics.

2.2.4.3 Falling Weight Deflectometer (FWD) deflections

Pavement deflections were also measured with the Dynatest FWD apparatus in order to obtain the deflection semi-basin of the pavement (Henia & Braber, 2008). The 65 kN-load was applied through a load plate (diameter of 30 cm) and the pavement response was measured by 9 geophones as shown in Figure 2.4. The load application is such as to simulate the charging time of a truck at 70 km/h (33 ms-pulse loading corresponding to about 30 Hz). As shown in Figure 2.4 the maximum deflection is detected by the geophone D1 (under the point of application of load) and the minimum deflection is detected by the geophone D9 (the most distant from the point of application of load). It is demonstrated that the deflection measured by a geophone located at a distance D from the load is affected by pavement layers at a depths $H=D$ and higher (P Ullidtz, 1987) (Horak, 2008) (Horak & Emery, 2009). Measurements were performed every 500,000 loads from 0 to 1 million loads, and then every 100,000 loads until the end of the fatigue tests. On each section measurements were spaced about every 5 m at 0 and 500,000 loads and every meter from 1 million to 1.4 million loads (J Blanc, Hornych, et al., 2019).

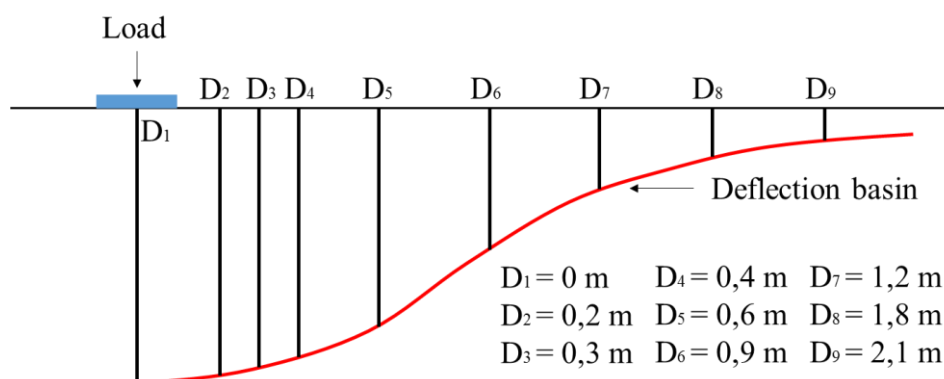


Figure 2.4 Outline of the FWD loading and measurement conditions. The load is applied with a load plate and the pavement response is measured by 9 geophones.

2.2.4.4 Pavement instrumentation

The response of the asphalt layer in terms of strain under moving loads was monitored through horizontal ASGs and temperature sensors (see Section 1.7.1).

The ASGs are located at the centre of the APT wheel path, namely at a radius of 19 m with respect to the centre of the carousel. The desire position is spray-painted on the bottom layer before placing the ASGs. Then the sensors and their cables are covered with some manually compacted asphalt mix in order to ensure protection before regular construction operation started. Each section is instrumented with four ASGs (KM-100HAS provided by Tokyo

Sokki Kenkyujo (Duong, 2017)) at the bottom of the bituminous layer, three in the longitudinal direction and one in the transverse direction. The layout of the instrumented areas in the fatigue carousel is reported in Figure 2.5. Sensors location for Mix1 and Mix3 sections is detailed in Figure 2.6. The Mix2 section is equipped with three additional sensors that are not part of this study as they are still research devices and their outputs were precisely being validated during the trial against ASGs (Figure 2.7) (Alavi et al., 2016) (Manosalvas-Paredes et al., 2020). For the same reasons the EME2 section is equipped with 13 additional sensors; among them only the sensors CTL1 and CTL2 (from CTL Group) and Dyn1 and Dyn2 (from Dynatest) are part of this study (Figure 2.8). Measurements were performed approximately every 20,000 loads (1,200 Hz acquisition frequency).

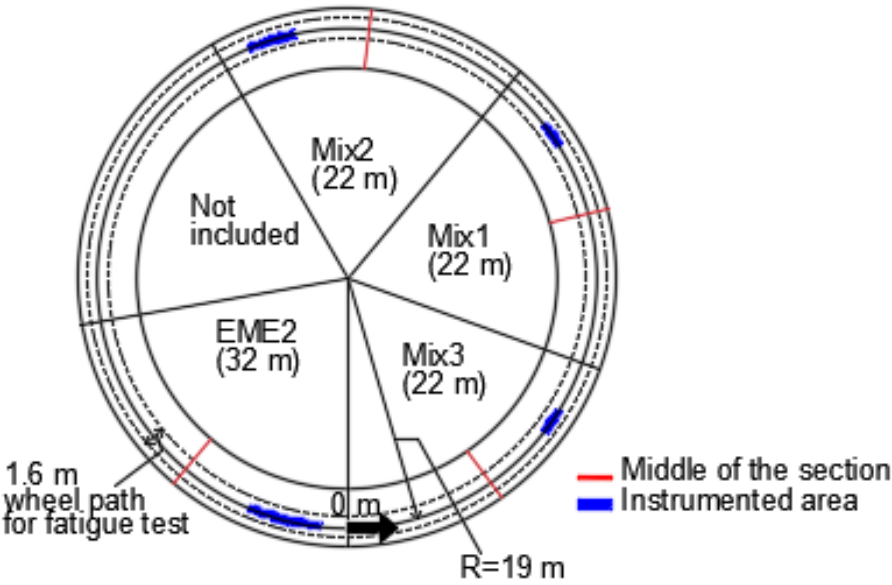


Figure 2.5 Plan of the location of instrumented areas in the fatigue carousel.

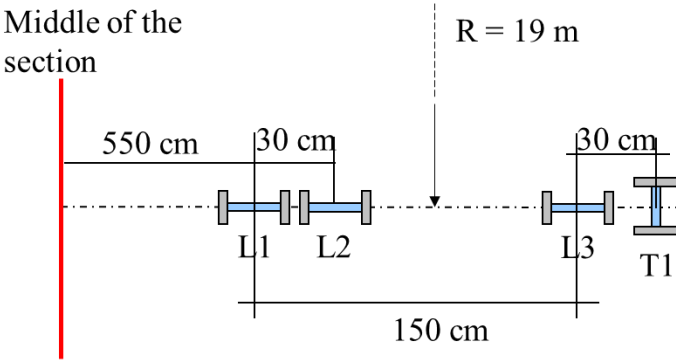


Figure 2.6 Outline of Mix1 and Mix3: ASGs locations.

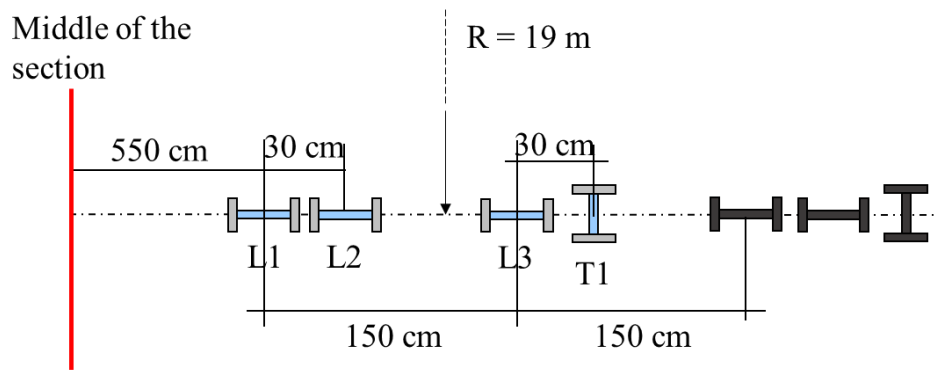


Figure 2.7 Outline of Mix2: ASGs locations. Sensors L1, L2, L3, and T1 are part of this study.

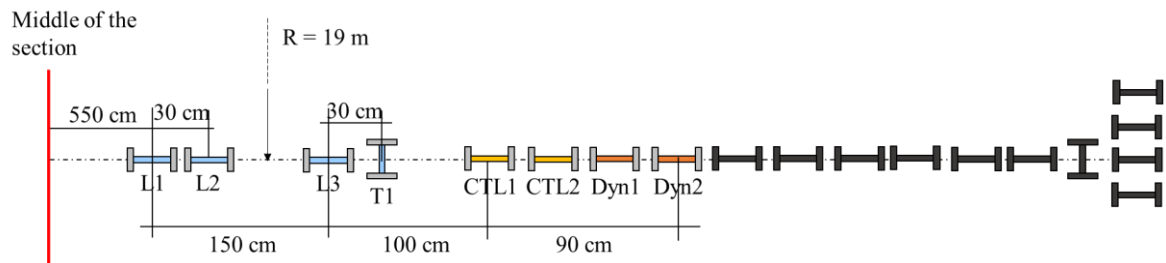


Figure 2.8 Outline of EME2: ASGs locations. Sensors L1, L2, L3, T1, CTL1, CTL2, Dyn1 and Dyn2 are part of this study.

Temperature evolution within the pavement was measured with three temperature probes PT100 placed at the top, middle (- 5 cm) and bottom (- 10 cm) of the bituminous layer in Mix2 section. Temperatures were measured at 10 min intervals. The average of the three measurements is considered as the temperature of the bituminous layers.

2.3 Comparison between traditional monitoring methods and embedded sensors

In section 2.3.1 we summarize results from (J Blanc, Hornych, et al., 2019) (J Blanc, Chailleux, et al., 2019) focusing more on a descriptive analysis of experimental results. Then in sections 2.3.2 and 2.3.3, we provide new contents deepening the analyses of results from embedded sensors as well as comparison with other monitoring methods.

2.3.1 Traditional monitoring methods

2.3.1.1 Visual crack inspections

By the end of the test two sections exhibited cracks, Mix 3 and EME2 (Figure 2.9). The first cracks were observed on section EME2 at about 900,000 loads. On this section cracking

increased consistently and at 1.4 million loads the extent of cracking reached 28 % (see section 2.2.4.1 for the calculation of the extent of cracking). On section Mix 3 the first cracks were observed after 1 million loads and at 1.4 million loads the extent of cracking reached 10 % (J Blanc, Hornych, et al., 2019). No cracks were observed on section Mix 1 and Mix 2. In all cases cracks were transversal with respect to the traffic direction. Please note that a deeper analysis of the crack pattern is carried out in section 2.3.3.

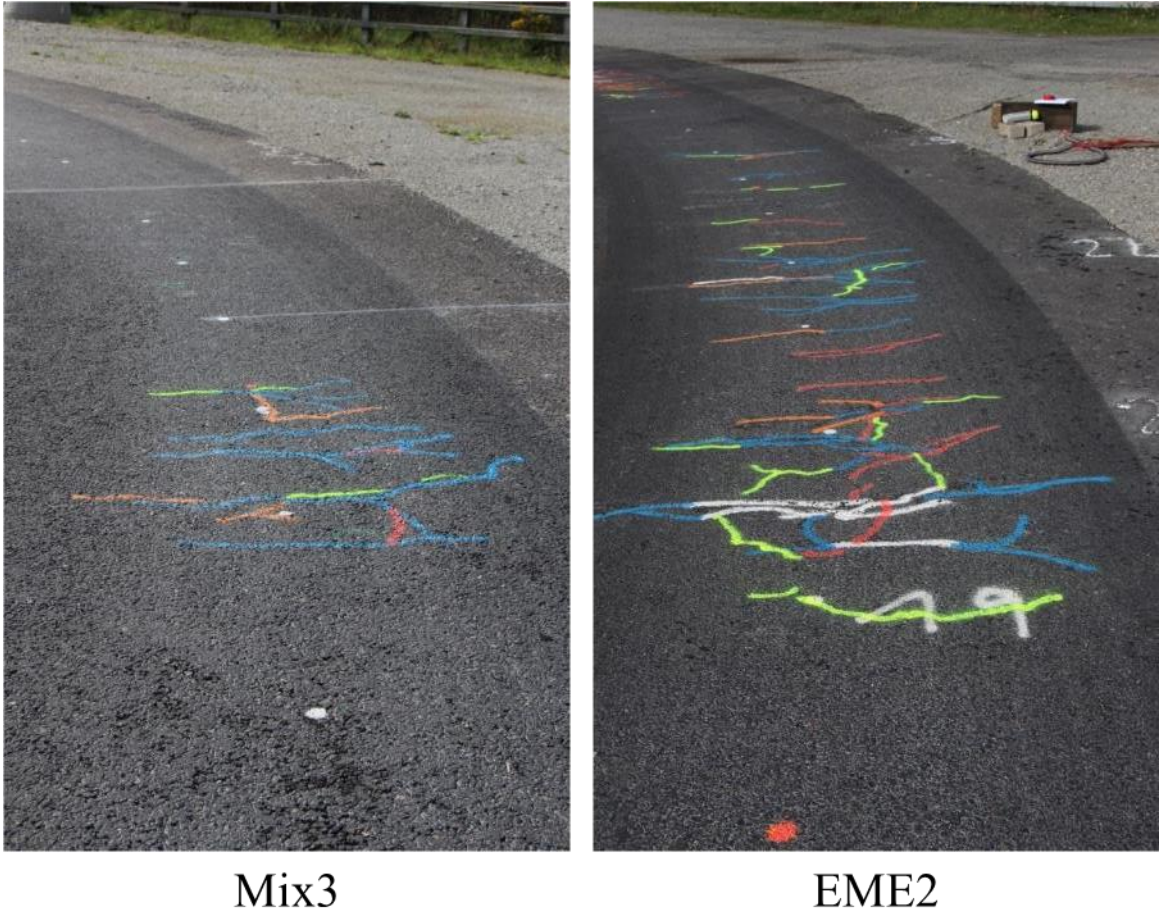


Figure 2.9 Pictures of the damaged sections at the end of the test (1.4 million loads). (Left) Mix3 section; (Right) EME2 section.

2.3.1.2 Benkelman beam deflections

In Figure 2.10 the deflection measured with the Benkelman beam are plotted as a function of the distance on the track. In particular, the graph displays measurements recorded at 0, 500,000, 1 million, 1.1 million, 1.2 million, 1.3 million and 1.4 million loads, as well as the mean temperature in the asphalt layer recorded during each measurement campaign.

Table 2.2 reports the mean deflections calculated at each loading stage, representative of the behaviour of the entire sections.

2 Detection of pavement ageing based on embedded sensors – Accelerated Pavement Testing

As it can be observed between 0 and 500,000 loads deflections decrease probably due to post-compaction effects and temperature decrease (J Blanc, Hornych, et al., 2019). At this stage deflections are quite similar for the four sections. From 1 million to 1.4 million loads the appearance of peaks indicate the occurring of some damaged areas. In fact, the first cracks were observed on sections Mix3 and EME2 at about 1 million loads (see section 2.3.1.1) consistently with the increase of deflections. At 1.4 million loads the highest peak values are obtained on sections EME2 and Mix3 (respectively 96 mm/100 and 90 mm/100), followed by 76 mm/100 for section Mix1, while the deflections measured in section Mix2 are still quite stable. This is consistent with the fact that by the end of the test no cracks were observed on sections Mix1 and Mix2 (see section 2.3.1.1).

With respect to the mean deflection measured at 500,000 loads, sections Mix3 and EME2 gained respectively the 63% and 73%, followed by section Mix1 and Mix2 with 49% and 55%. This means that, as expected, by the end of the test the sections experienced an overall reduction of their bearing capacity. This phenomenon is stronger for sections Mix3 and EME2 where the highest deflections peaks were measured indicating a more important damage.

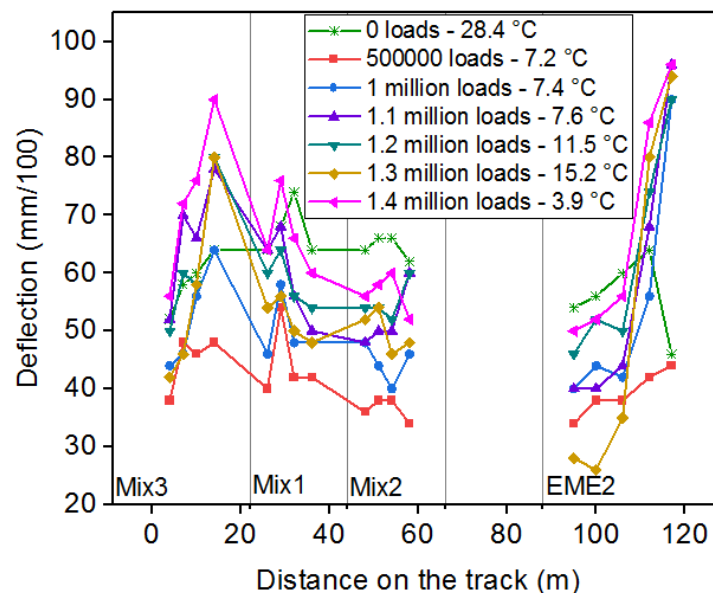


Figure 2.10 Deflection measured with the Benkelman beam on the four sections. Measurements are spaced about every 4 m. The mean temperature in the bituminous layers is recorded.

Table 2.2 Mean Benkelman beam deflections recorded at 0, 500,000, 1 million, 1.1 million, 1.2 million, 1.3 million and 1.4 million loads on the four sections. The mean temperature in the asphalt layer is also reported.

Loads	Mean deflection (mm/100)				T (°C)
	Mix 1	Mix 2	Mix 3	EME2	
0	68	65	59	56	28.4
500,000	45	37	45	39	7.2
1 million	50	45	53	54	7.4
1.1 million	60	52	67	58	7.6
1.2 million	59	55	62	62	11.5
1.3 million	52	50	57	53	15.2
1.4 million	67	57	74	68	3.9

2.3.1.3 Falling Weight Deflectometer (FWD) deflections

In order to evaluate in details the evolution of deflections over the fatigue test, for each measurement campaign a basin representative of the behaviour of the overall sections was calculated from geophone measurements (see section 2.2.4.3). For each section it is defined as the real measured basin which is closest to the mean basin (average of the measured deflections) and is calculated at 0, 500,000, 1 million, 1.1 million, 1.2 million, 1.3 million and 1.4 million loads. The obtained deflection basins are shown in Figure 2.11 where the mean temperature measured within the asphalt layer is also indicated but no temperature correction is applied to the measurements. Indeed, the fatigue test was carried out over a relatively small period of time during which temperature variations were very small (see section 2.2.3) and it was decided not to apply any temperature correction.

A difference between the 0 loads basin and the 500,000 loads basin can be observed for all sections (consistently with Benkelman beam measurements reported in section 2.3.1.2). This is not *a priori* a sign of damage, it can be explained by post compaction effect as well as temperature decrease (J Blanc, Horny, et al., 2019). This is also supported by the evolution of deflections measured by the geophone D1 as a function of the distance on the track reported in Figure 2.12, where measurements recorded at 500,000 loads look quite stable for all sections and do not show any peaks as is the case at higher loads.

From 1 million to 1.4 million loads deflection basins become steeper in the area close to the load indicating that fatigue damage is occurring in the asphalt layer (see section 2.2.4.3). As measurements recorded from more distant geophones are stable, it can be deduced that lower layers are not featuring any damage. With respect to the basin calculated at 500,000 loads, maximum deflections at 1.4 million loads increase of 19% and 15% for sections Mix 1 and Mix 2 respectively, and 32% and 39% for sections Mix 3 and EME2 respectively

2 Detection of pavement ageing based on embedded sensors – Accelerated Pavement Testing

(Figure 2.11). This confirms the fact that the last two sections experience far more significant damage. This is also supported by the evolution of deflections recorded by geophone D1 reported in Figure 2.12, as from 1 million loads measurements exhibit peaks of considerable magnitude right in section Mix 3 and EME2 where the cracks were observed (see Section 2.3.1.1).

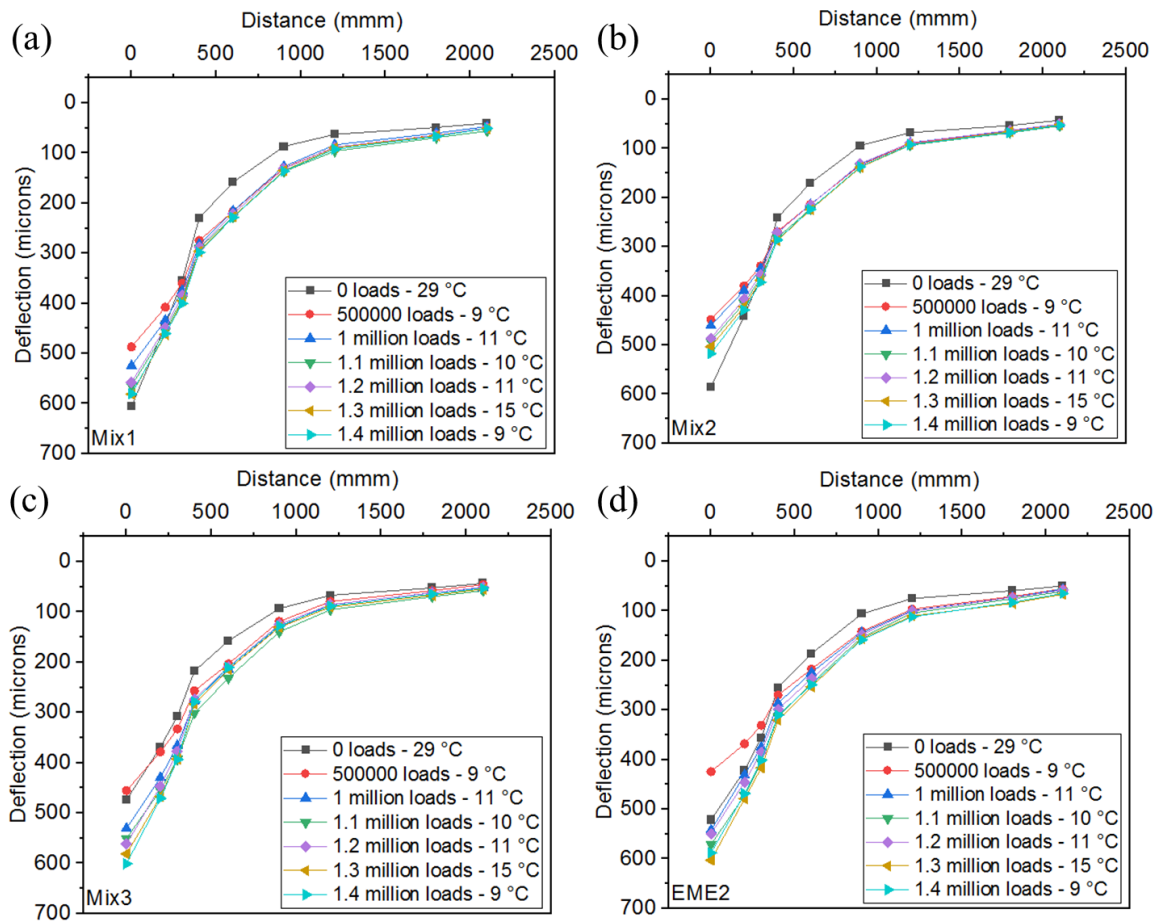


Figure 2.11 Basin representative of the behaviour of the overall section calculated at 0, 500,000, 1 million, 1.1 million, 1.2 million, 1.3 million and 1.4 million loads. (a) Mix 1, (b) Mix 2, (c) Mix 3, (d) EME2.

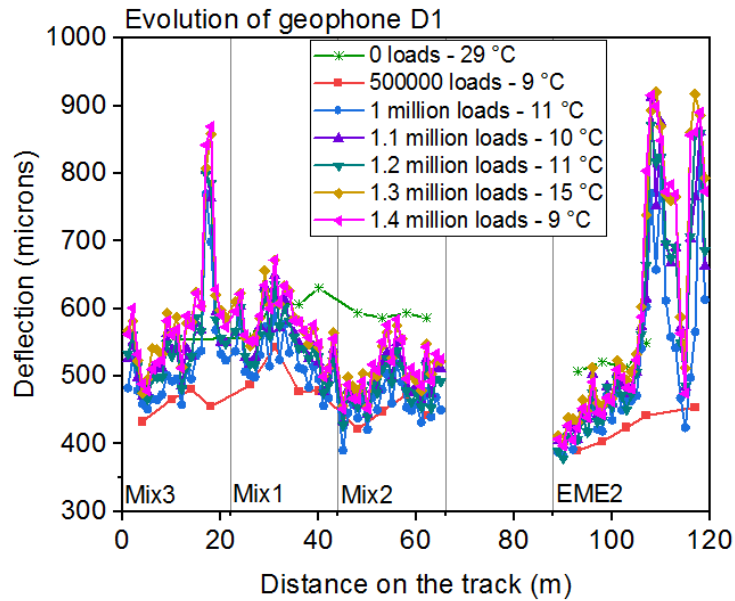


Figure 2.12 Deflection measured by geophone D1 of the FWD on the four sections. At 0 and 500,000 loads, measurements are spaced about every 5 meters; from 1 million to 1.4 million loads measurements are spaced about every 1 meter. The mean temperature in the bituminous layers is recorded.

2.3.2 Monitoring based on embedded sensors

2.3.2.1 Survival rate to installation

Overall, the survival rate of horizontal ASGs (longitudinal and transversal) to installation is higher than 60%. The accurate installation procedures adopted by the team of the APT (J. Blanc et al., 2016) guaranteed a good protection of the gauges to construction (paving and compaction, the latter being the most delicate phase undergone by embedded devices as discussed in section 1.7). The survival rate for each section is detailed in Table 2.3. This statistics only refer to devices that are part of this study, as indicated in Section 2.2.4.4.

Table 2.3 Survival rate of ASGs to installation for each section.

Section	Survival rate
Mix 1	50%
Mix 2	75%
Mix 3	50%
EME2	70%

The following analyses are based on the strain measurements recorded by the longitudinal ASGs that survived the construction process, namely Mix1-L1, Mix1-L2, Mix2-L2, Mix2-L3, Mix3-L1, EME2-L1, EME2-L2, EME2-Dyn2.

2.3.2.2 Definition of signal shape parameters

A common practice on the APT is to define a strain signal as the average of the four loading arms passages in order to avoid small load variations between the arms (J Blanc, Chailleux, et al., 2019). The raw sensor measurement is shown in Figure 2.13-Left where one can clearly see the four arms rolling on the sensor. Once the four signals are averaged, a time-to-distance transformation of the x-axis is carried out through the equation $x = vt$ by using the arms rolling speed. Figure 2.13-Right shows the calculated average signal characterised by alternating compression (negative strain)-tension (positive strain)-compression pattern. The abscissa $x = 0$ m corresponds to the maximum peak in extension, when the centre of the dual-wheel is on the top of the sensor. Negative distances correspond to pavement response when the load approaches while positive distances correspond to pavement response when the load moves away.

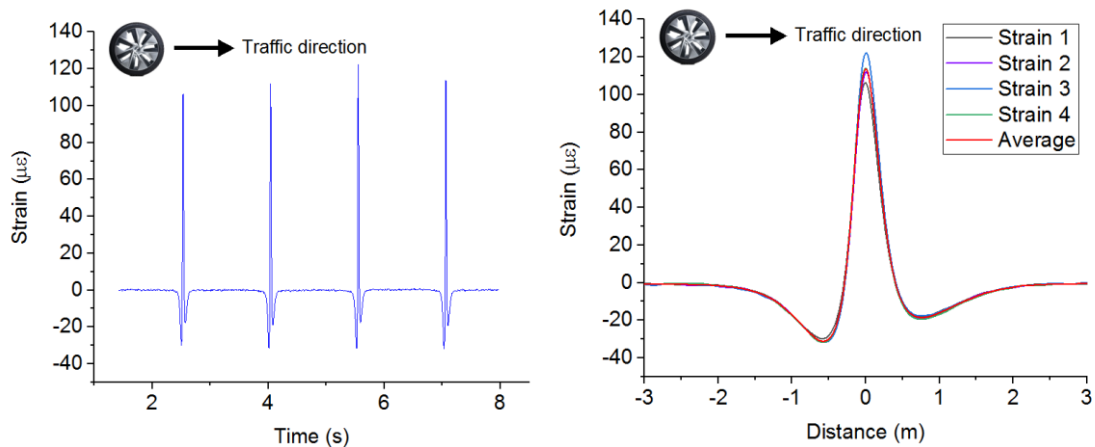


Figure 2.13 Signal treatment process on the APT. (Left) 4 arms passages. (Right) Average of the 4 arms passages and time-to-distance transformation of the x-axis.

In order to analyse the occurring fatigue damage through the evolution of strain signals a set of shape parameters can be defined (Figure 2.14) (Homsı, 2011), namely:

- the maximum strain in extension, ϵ_{\max} ,
- the first peak in contraction, $\epsilon_{\min,1}$,
- the second peak in contraction, $\epsilon_{\min,2}$,
- the difference between ϵ_{\max} and $\epsilon_{\min,1}$ ($\epsilon_{\max} - \epsilon_{\min,1}$), A_1 ,
- the difference between ϵ_{\max} and $\epsilon_{\min,2}$ ($\epsilon_{\max} - \epsilon_{\min,2}$), A_2 ,
- the distance between the $\epsilon_{\min,1}$ x-coordinate and the ϵ_{\max} x-coordinate ($|\mathbf{X}_{\epsilon_{\min,1}} - \mathbf{X}_{\epsilon_{\max}}|$), d_1 ,

- the distance between the $\epsilon_{\min,2}$ x-coordinate and the ϵ_{\max} x-coordinate ($|X_{\epsilon_{\min,2}} - X_{\epsilon_{\max}}|$), d_2 ,
- the total width of the peak, the sum of d_1 and d_2 ($d_1 + d_2$), d_{tot} .

In particular the parameters ϵ_{\max} , $\epsilon_{\min,1}$, $\epsilon_{\min,2}$, A_1 and A_2 characterise the pavement response to load in terms of strain, while d_1 , d_2 and d_{tot} characterise the pavement area mostly influenced by the load in terms of distance.

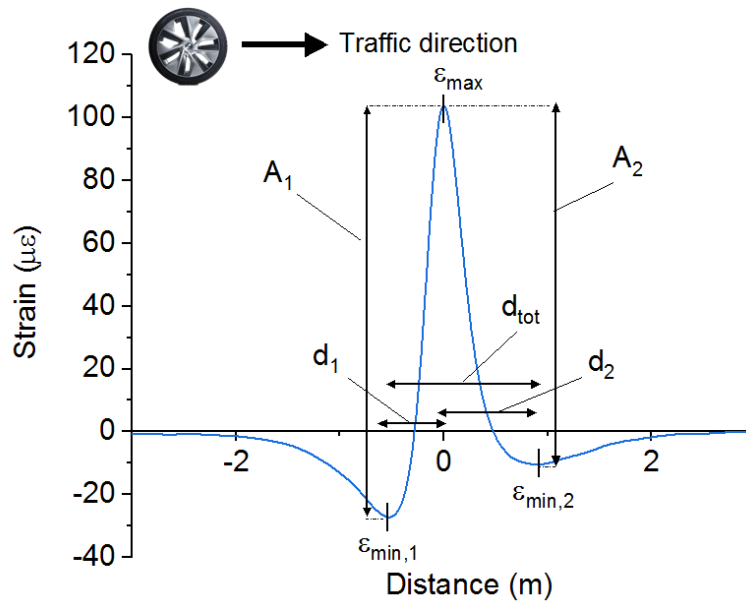


Figure 2.14 Definition of the signal shape parameters.

2.3.2.3 Evolution of the maximum longitudinal strain

First, the evolution of the maximum longitudinal strain (ϵ_{\max}) at the bottom of the asphalt layer over the duration of the experiment is analysed. Indeed the repeated occurrence horizontal strains at the basis of the bituminous layer is known to be responsible for fatigue degradation and to lead to crack propagation (see Sections 1.3.3 and 1.6.2). Figure 2.15 reports the evolution of ϵ_{\max} as well as the temperature measured within the asphalt layer. Figure 2.15-Left shows the evolution of ϵ_{\max} for each section obtained by averaging the response of the sensors reported in Figure 2.15-Right. As can be seen, in the beginning the responses of the sensors are of the same magnitude and follow the same trend. At about 200,000 loads the response of sensor EME2-L2 starts to drift upward of the other sensors, followed by the responses of sensor Mix3-L1 at about 400,000 loads and of sensor EME2-Dyn2 at about 600,000 loads. This is a strong clue pointing toward the occurrence of fatigue damage in sections Mix3 and EME2, confirmed by the observation of the first cracks at about 1million loads. By contrast, the other sensors located in the other two sections do not

2 Detection of pavement ageing based on embedded sensors – Accelerated Pavement Testing

show significant drift and no crack was observed at the end of the test. These results are confirmed by deflections measurements (sections 2.3.1.2 and 2.3.1.3) and visual cracks inspections (section 2.3.1.1). Interestingly the responses of the three sensors in section EME2 are quite different, in particular, those of sensors EME2-L1 and EME2-L2 placed at a distance of 30 cm from each other. It is probable that a crack appears nearby or rather in correspondence of sensor EME2-L2 which explains such high strain levels. It is surprising that the response of sensor EME-L1 seems to be not perturbed by this event. This may suggest a problem in sensor orientation or anchoring or even the occurring of local interlayer deboning associated to crack manifestation.

As expected, due to the new loading conditions after 1 million loads (see section 2.2.3) an increase of ϵ_{\max} is observed in all the sections.

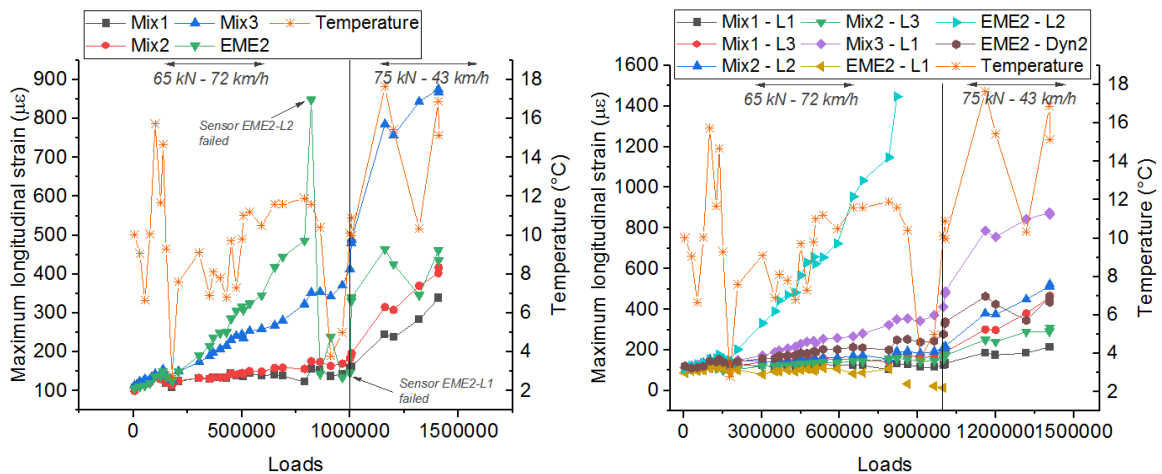


Figure 2.15 Evolution of the maximum longitudinal strain (ϵ_{\max}) at the bottom of the asphalt layer over the duration of the fatigue test. (Left) Response for each section obtained by averaging the response of the sensors. (Right) Response of each sensor.

2.3.2.4 Signal shape evolution

Figure 2.17 reports the evolution of the shape parameters A_1 , A_2 and d_{tot} (see section 2.3.2.2) as a function of the number of loads for one sensor per section, namely sensors Mix1-L3, Mix2-L2, Mix3-L1 and EME2-Dyn2. Plots for the other sensors are reported in Appendix 1. All signals feature differences between the parameters A_1 and A_2 since the beginning of the experiment until its end. In other words, the response to loads exhibits asymmetry. This phenomenon is attributed to the orientation of the anchorage of the sensors in the mix rather than directly to a mix viscous behaviours of the different mix, as those are expected to occur only at significantly higher temperatures (J Blanc, Chailleux, et al., 2019) (see also section

3.6). A study was performed on the evolution of the asymmetry throughout the experiment. For this purpose an asymmetry factor (F) was calculated with the following equation:

$$F = \left(\frac{A_1 - A_2}{A_1} \right) * 100 \tag{2.1}$$

Figure 2.16 shows the evolution of F for all the sensors, while the mean value calculated over 1.4 million loads is reported in Table 2.4 along with the standard deviation. As it can be observed, values of F are between 0% and 15% and remain roughly constant over the duration of the test independently from temperature or fatigue. This suggests this is not related to the thermo-viscoelastic properties of the mixes. Interestingly higher oscillations are observed for sensors Mix2-L3, Mix3-L1, EME2-L1 and EME2-L2 which suggests that, though the initial asymmetry is not due to viscous effects, this asymmetry (indicative of viscous effect) may be impacted by fatigue.

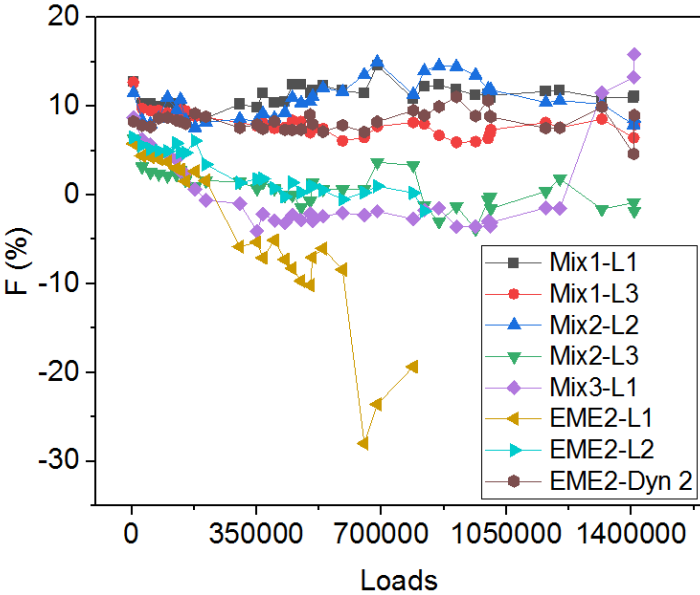


Figure 2.16 Evolution of the asymmetry factor F for all the sensors over the duration of the fatigue test.

Table 2.4 Mean value of the asymmetry factor F calculated over 1.4 million loads along with the standard deviation. The coefficient of variation is calculated as the ration between the standard deviation and the mean.

Sensor	Mean value (%)	Coefficient of variation (%)
Mix1-L1	11	11
Mix1-L3	8	17

Mix2-L2	11	20
Mix2-L3	1	291
Mix3-L1	1	832
EME2-L1	-5	186
EME2-L2	2	101
EME2-Dyn2	8	14

With the increase of number of loads and with the occurrence of fatigue A_1 and A_2 increase (with the same trend) and d_{tot} , decreases. This is more evident for Mix3 and EME2 sections (Figure 2.17-b and c) which exhibit the first cracks at about 1 million loads showing that the pavement is in fatigue regime. This is consistent with the fact that that fatigue is associated with a reduction of the material stiffness that results in an increase in strain level (compressive and extensive) and reduction in response area for the same load. Hence, the parameters A_1 and A_2 and d_{tot} can be considered as real-time indicators of fatigue damage.

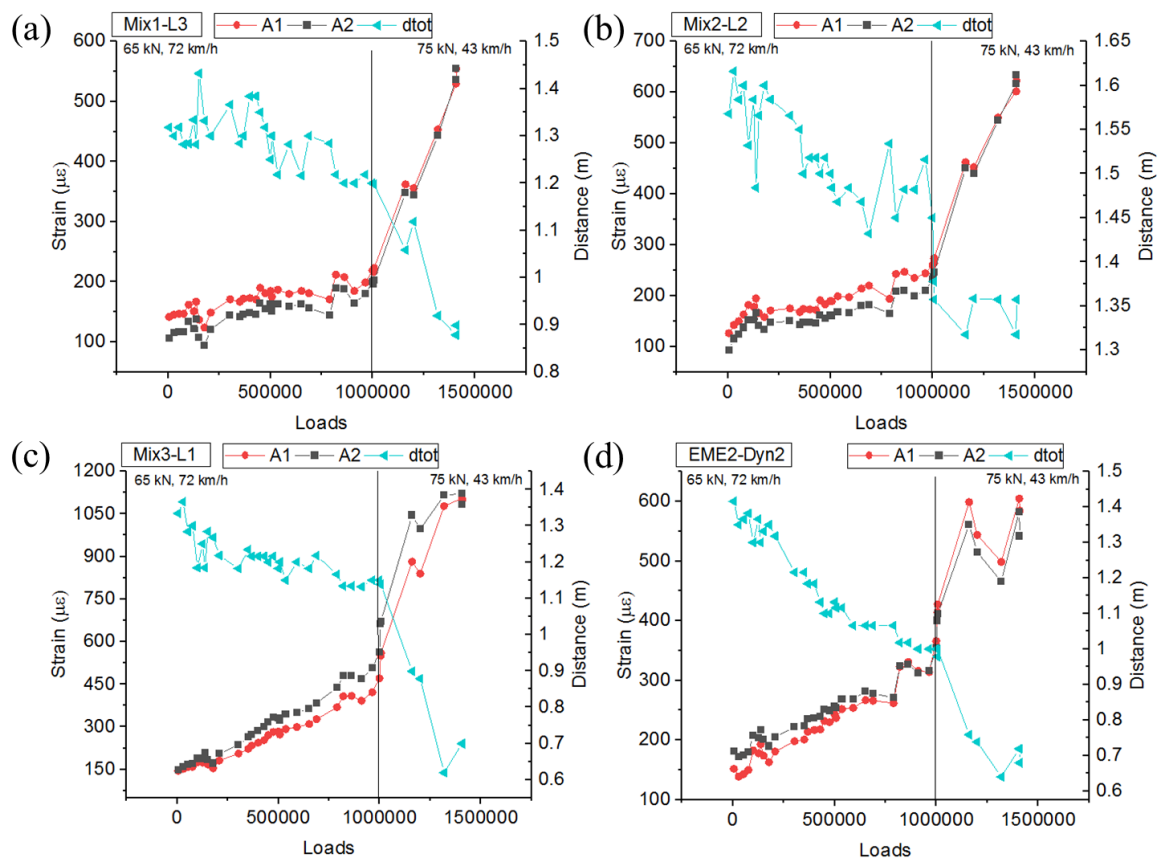


Figure 2.17 Evolution of the shape parameters A_1 , A_2 and d_{tot} with the increase of the number of loads. Sensors: (a) Mix1-L3, (b) Mix2-L2, (c) Mix3-L1, (d) EME2-Dyn2.

In details, the parameters A_1 , A_2 and d_{tot} do not change independently from each other and their relation can be considered linear with a good approximation, as shown by the coefficients of determination R^2 reported in Table 2.5. These coefficients are obtained by plotting the mean value between A_1 and A_2 as a function of d_{tot} for all sensors. Interestingly sensors EME2-L1 and EME2-L2 present the smaller R^2 coefficients. That can be probably explained by a disruption caused by the occurrence of nearby cracking. Overall A_1 and A_2 vary linearly with ε_{max} , $\varepsilon_{min,1}$, and $\varepsilon_{min,2}$, as shown in Table 2.6 where coefficients of determination R^2 are obtained by plotting the mean value between A_1 and A_2 as a function of ε_{max} , $\varepsilon_{min,1}$, and $\varepsilon_{min,2}$ for all sensors.

Table 2.5 Correlation between A_1 , A_2 and d_{tot} . R^2 is obtained by plotting the mean value between A_1 and A_2 as a function of d_{tot} for all sensors.

Sensor	R^2
Mix1-L1	0.46
Mix1-L3	0.87
Mix2-L2	0.68
Mix2-L3	0.74
Mix3-L1	0.91
EME2-L1	0.21
EME2-L2	0.21
EME2-Dyn2	0.89

Table 2.6 Correlation between A_1 , A_2 and ε_{max} , $\varepsilon_{min,1}$ and $\varepsilon_{min,2}$. R^2 is obtained by plotting the mean value between A_1 and A_2 as a function of ε_{max} , $\varepsilon_{min,1}$ and $\varepsilon_{min,2}$ for all sensors.

Sensor	Correlation to ε_{max} -	Correlation to $\varepsilon_{min,1}$ -	Correlation to $\varepsilon_{min,2}$ -
	R^2	R^2	R^2
Mix1-L1	1.00	0.94	0.93
Mix1-L3	1.00	0.95	0.96
Mix2-L2	1.00	0.93	0.96
Mix2-L3	1.00	0.48	0.86
Mix3-L1	1.00	0.81	0.75
EME2-L1	0.98	0.50	0.24
EME2-L2	1.00	0.97	0.98

EME2-			
Dyn2	1.00	0.95	0.93

2.3.3 Discussion

The evolution of ASGs measurements is consistent with the other monitoring methods. This validates the use of ASGs as effective method for road pavement monitoring and damage prediction. In fact the sensor measurements are not only in good agreement with deflection measurements and cracks visual inspections but the sensors seem to be able to detect in advance the occurring of damage. The responses of sensor EME2-L2, EME2-Dyn2 and Mix3-L1 start to derive well before the visualization of the first cracks on the pavement surface, as well as the detection of deflection peaks. It would therefore seems that these sensors detect a bottom-up cracking phenomenon. For further confirmation of these assumptions a study of sensor locations with respect to FWD deflection measurements and the crack pattern was conducted. In Figure 2.18 sensor locations are plotted on the "FWD deflection – distance on the track" plots for all sections. In Figure 2.19 sensor locations are represented on the crack pattern produced until 1.1 million loads. As can be observed, sensors detecting the occurrence of damage in the asphalt layer are located in the areas showing (later) deflection peaks with FWD (Figure 2.18-c and d) and where the first cracks arose (Figure 2.19). Damaged areas are those where sensors are placed indicating that they may create weakness points in the asphalt layer where the cracks will initiate. Nevertheless, sensors do not always cause cracking. Indeed, no cracks appear on sections Mix1 and Mix2, although in the latter the sensor density is higher than in Mix3 section where some cracks are observed at about 1 million loads.

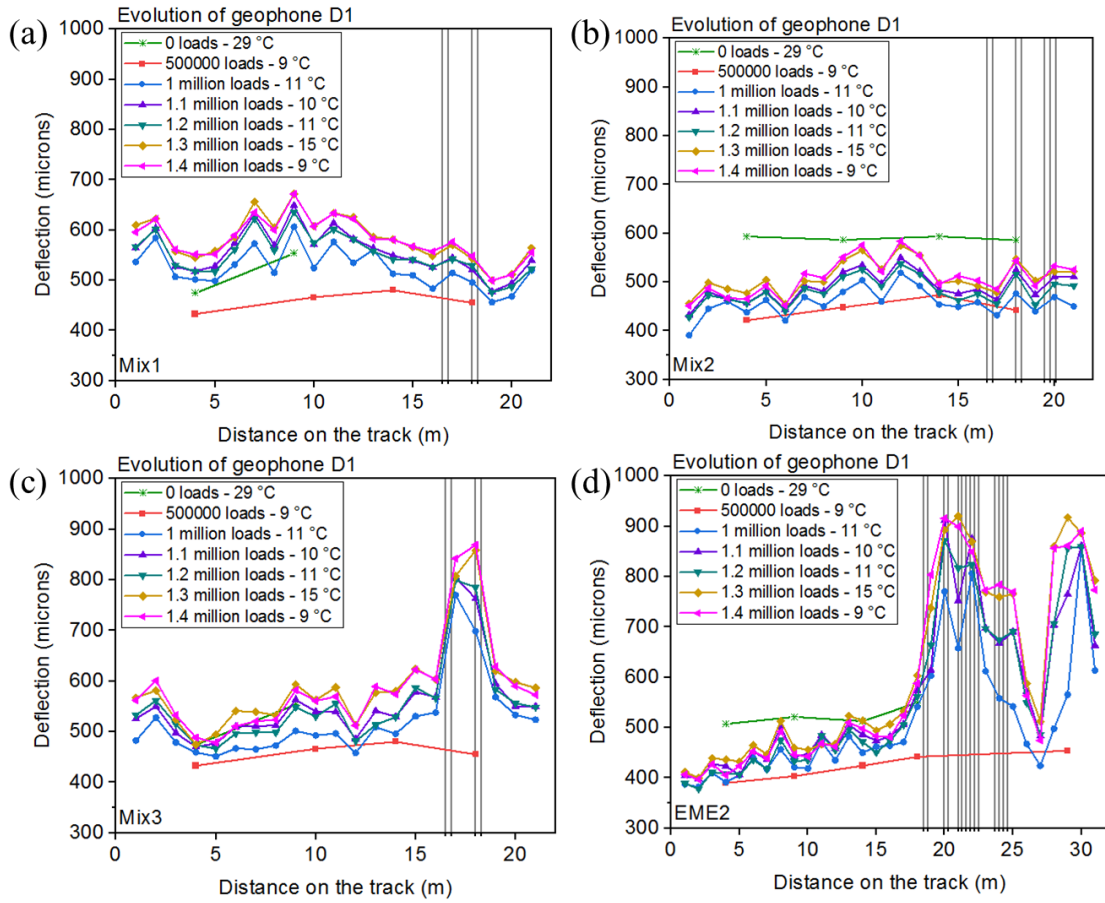


Figure 2.18 Representation of sensors location on the plots " FWD deflection - distance on the track": (a) section Mix1, (b) section Mix2, (c) section Mix3 and (d) section EME2.

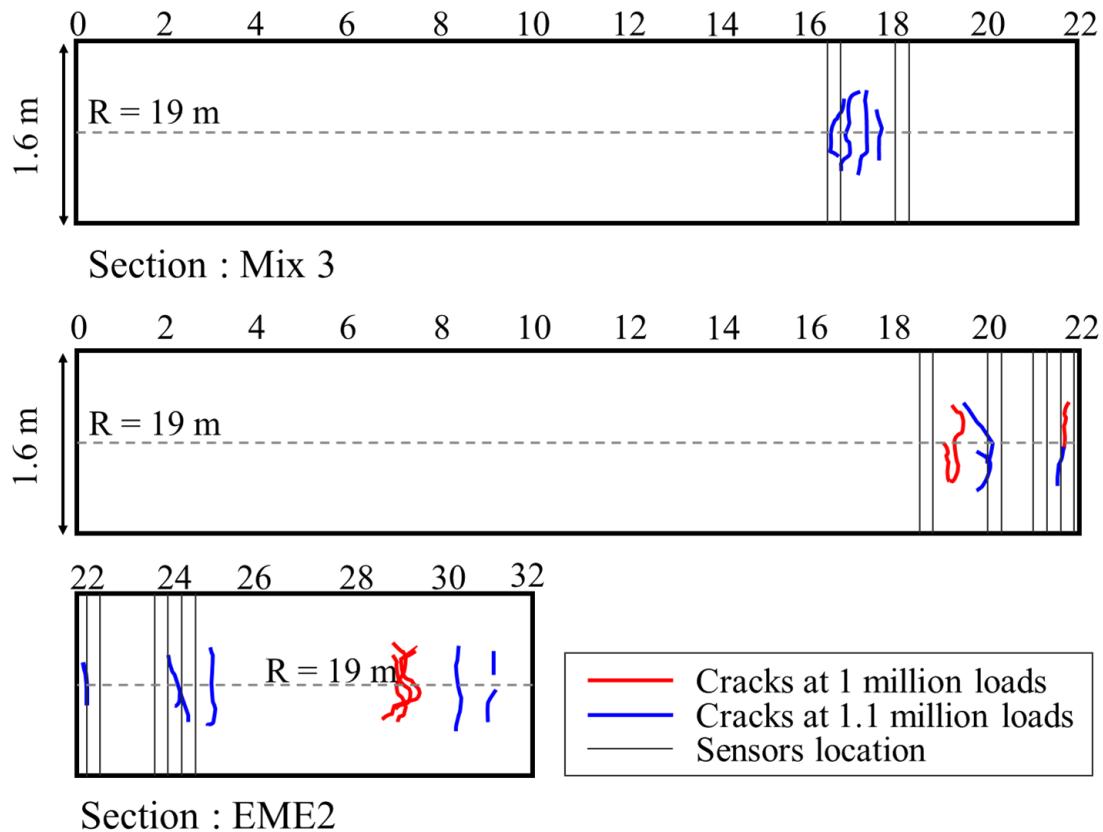


Figure 2.19 Representation of sensors location on the crack pattern produced for sections Mix3 (top) and EME2 (bottom). The crack pattern reports the cracks observed at 1 million and 1.1 million loads. Sensors are located in the areas where the first cracks arose.

2.4 Comparison between field measured strain and inverse calculated strain

2.4.1 Assessment of pavement conditions via inverse calculation of FWD measurements: methodology

The deflection basins obtained through the FWD can be used to carry out an inverse calculation of the actual stiffness of each layer of the monitored structure and estimate the remaining service life. The software Alizé (see section 1.6.1.1) has a module dedicated to the computation of the elastic moduli of the whole or of some layers of a pavement structure from the deflection basin. This inverse calculation is based on the minimization of the difference between the measured and the calculated deflection basins. It yields as output the layer moduli that provide best fit between measured basin and computed basin. The number of layers, their thickness, their Poisson's ratio, the interfaces conditions, as well as the type of loading are considered fixed.

In order to compare the performances of the four sections at the end of the fatigue experiment as well as compare the performances of damaged and non-damaged areas on the same section, three inverse analyses are conducted for each section:

- Inverse calculation from the 1 million loads basin representative of the whole structure.
- Inverse calculation from the 1 million loads basin representative of the non-damaged zone.
- Inverse calculation from the 1 million loads basin representative of the damaged zone.

The last two analyses are carried out on sections Mix3 and EME2 only as sections Mix1 and Mix2 do not exhibit any damaged zone.

The methodology used for inverse calculation of the actual stiffness of each layer of the structure is outlined in Figure 2.20. The initial set of moduli, called "initial structure" in Figure 2.20, comes from field controls made during and after construction as indicated in Blanc et al. (J Blanc, Chailleux, et al., 2019) (see also section 2.5). In details the initial structure refers to:

- E_i , the initial modulus of the bituminous layer,
- $E_{UGB,i}$, the initial modulus of the unbound granular base layer,
- $E_{subgrade,i}$, the initial modulus of the subgrade.

In particular, for the bituminous layers the equivalent elastic moduli $E_i(11\text{ }^\circ\text{C}, 30\text{ Hz})$ at $11\text{ }^\circ\text{C}$ (mean temperature of the asphalt layer during FWD measurements) and 30 Hz (loading frequency during FWD measurements) are used. They are lab-measured using complex modulus test carried out on field-produced mixes.

The set of re-calculated layer moduli is called "intermediate structure" in Figure 2.20 and consists of:

- E_r , the recalculated modulus of the bituminous layer,
- $E_{UGB,r}$, the recalculated modulus of the unbound granular base layer,
- $E_{subgrade,r}$, the recalculated modulus of the subgrade.

It is known that due to the dynamic nature of the FWD, static inverse calculation produces errors in the estimation of the subgrade modulus associated with the neglect of dynamic effects (Per Ullidtz et al., 2006) (Grenier, 2007) (Broutin et al., 2019). Usually a correction factor between 30% and 70% (as a function of the type of soil) should be applied to the

obtained value to determine the real modulus of the subgrade. For this reason it was decided re-calculate the moduli of the subgrade using the deflections measured with the Benkelman beam. In particular, the mean deflection values between measurements at 800,000 and 1 million loads are considered. For this latter computation in Alizé the equivalent elastic modulus at 8.4 °C (mean temperature of the asphalt layer during Benkelman beam measurements at 800,000 and 1 million loads) and 2 Hz (loading frequency), $E_r(8.4 \text{ °C}, 2 \text{ Hz})$, is considered for the asphalt layers, as indicated in the following equation:

$$E_r(8.4 \text{ °C}, 2 \text{ Hz}) = E_r(11 \text{ °C}, 30 \text{ Hz}) * \frac{E_i(8.4 \text{ °C}, 2 \text{ Hz})}{E_i(11 \text{ °C}, 30 \text{ Hz})} \quad (2.2)$$

Where

- $E_r(11 \text{ °C}, 30 \text{ Hz})$ is the modulus at 11 °C and 30 Hz calculated in Alizé by fitting the deflection basin measured with the FWD.
- $E_i(8.4 \text{ °C}, 2 \text{ Hz})$ is the initial modulus at 8.4 °C and 2 Hz determined in the laboratory at the beginning of the test by performing the complex modulus test on field produced mixes.
- $E_i(11 \text{ °C}, 30 \text{ Hz})$ is the initial modulus at 11 °C and 30 Hz determined in the laboratory at the beginning of the test by performing the complex modulus test on field produced mixes.

The final set of moduli, called "final inverse calculated structure", in Figure 2.20 consists of:

- E_r , the modulus of the bituminous layer previously calculated,
- $E_{UGB,r}$, the modulus of the unbound granular base layer previously calculated,
- $E_{subgrade,f}$, the modulus of the subgrade resulting from the last computation.

A further elastic calculation is carried out in Alizé to determine the numerical strain at the bottom of the asphalt layer by using for this latter the modulus $E_i(10 \text{ °C}, 10 \text{ Hz})$ at 10 °C (mean temperature in the asphalt layer at 1 million loads) and 10 Hz (loading frequency) calculated with the equation:

$$E_r(10 \text{ °C}, 10 \text{ Hz}) = E_r(11 \text{ °C}, 30 \text{ Hz}) * \frac{E_i(10 \text{ °C}, 10 \text{ Hz})}{E_i(11 \text{ °C}, 30 \text{ Hz})} \quad (2.3)$$

Where

- $E_r(11 \text{ °C}, 30 \text{ Hz})$ is the modulus at 11 °C and 30 Hz calculated in Alizé by fitting the deflection basin measured with the FWD.

- $E_i(10^\circ\text{C}, 10\text{ Hz})$ is the initial modulus at 10°C and 10 Hz determined in the laboratory at the beginning of the test by performing the complex modulus test on field produced mixes.
- $E_i(11^\circ\text{C}, 30\text{ Hz})$ is the initial modulus at 11°C and 30 Hz determined in the laboratory at the beginning of the test by performing the complex modulus test on field produced mixes.

The computed strains are compared with measurements obtained from strain sensors (see section 2.4.2).

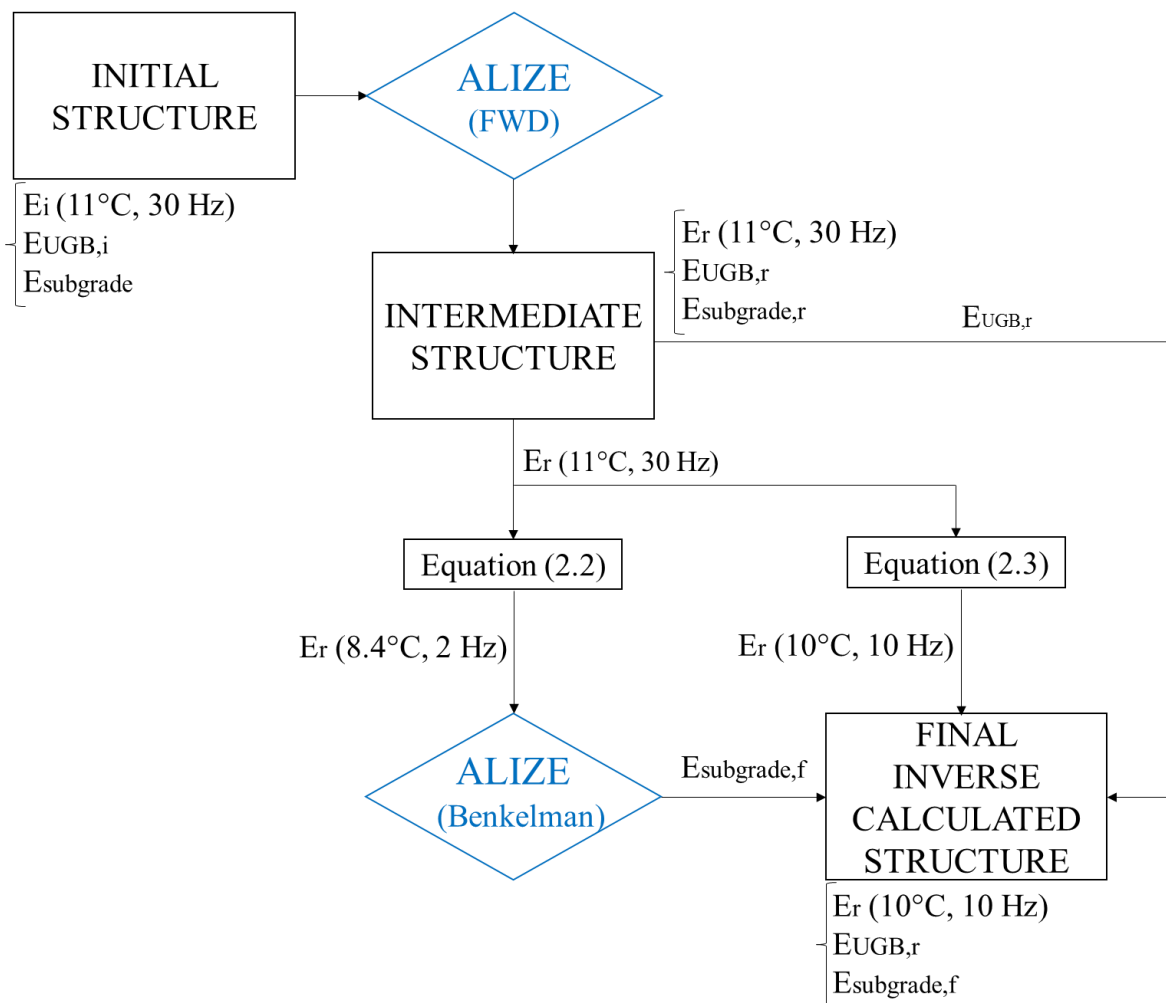


Figure 2.20 Outline of the adopted inverse calculation methodology.

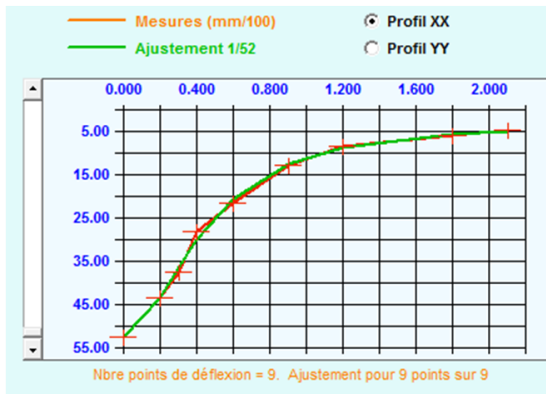
2.4.1.1 Inverse calculation from representative basin

The representative basin is defined as the real measured basin which is closest to the mean basin (average of the measured deflections – see also section 2.3.1.3). Figure 2.21 reports the results obtained in Alizé by performing an inverse calculation from the measured basins:

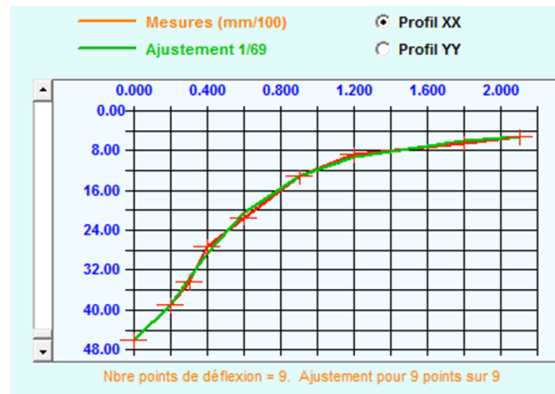
the superposition between measured (red) and calculated (green) deflection basin shows that the prediction is good for the four sections. Deflections measured with the Benkelman beam and deflections calculated in Alize are reported in Table 2.7, and even then the prediction is good. A comparison between the initial structure and the final structure is reported in Table 2.8 for sections Mix1 and Mix2 and Table 2.9 for sections Mix3 and EME2. The following conclusions can be drawn:

- The stiffness of the subgrade did not variate. The differences between the final and initial moduli can be considered negligible. Indeed, the accelerated fatigue test reproduces a very high number of loads in a small time period with relatively stable weather conditions. Thus a variation of the subgrade modulus is unlikely except for some post compacting effects occurring in the beginning of the experiment (J Blanc, Hornych, et al., 2019). The small differences observed can be attributed to the precision of measures, especially for the Benkelman beam measurements.
- Similar observations can be done for the stiffness of the unbound granular base course. The differences between the final and initial moduli can be considered not significant.
- The highest variations are found for the bituminous layers of sections Mix3 and EME2, respectively 60% and 40% of the initial modulus, meaning that the fatigue criterion is satisfied, as the applied loading is such that the modulus is almost halved after 1 million cycles. 86% and 87% of the initial moduli is found for sections Mix1 and Mix2: these small decreases in modulus do not induce cracking.

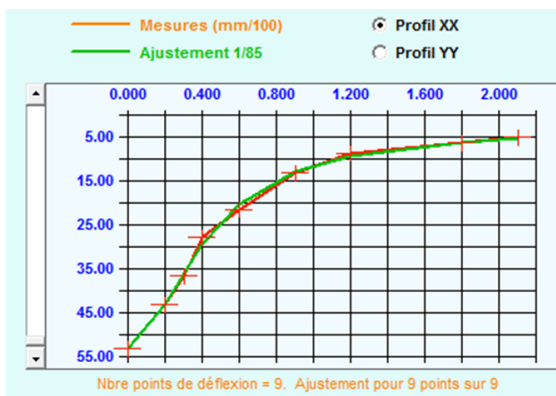
Mix 1



Mix 2



Mix 3



EME2

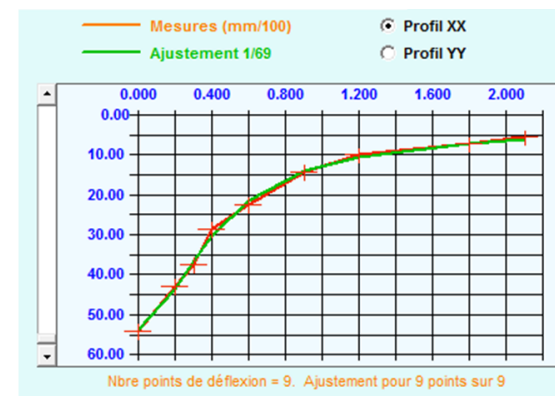


Figure 2.21 Results obtained in Alizé by performing an inverse calculation from the measured basins representative of the whole structures: (top-left) Mix1, (top-right) Mix2, (bottom-left) Mix3 and (bottom-right) EME2. The measured basins are well predicted by the model.

Table 2.7 Comparison between Benkelman beam measured deflections (average between 800,000 and 1 million loads) and deflections calculated in Alizé.

	Mix 1	Mix 2	Mix 3	EME2
Measured deflection (mm/100)	50.0	44.5	51.3	51.8
Calculated deflection (mm/100)	50.7	44.0	50.7	49.6
Relative difference (%)	1.4	1.1	1.2	4.3

Table 2.8 Comparison between mechanical properties of the structure at the beginning and at the end of the test. Sections Mix1 and Mix2. The moduli of bituminous layers are considered at 10 °C and 10 Hz.

Layer	Mix 1			Mix 2		
	Initial (MPa)	Final (MPa)	Final/Initial (%)	Initial (MPa)	Final (MPa)	Final/Initial (%)

2 Detection of pavement ageing based on embedded sensors – Accelerated Pavement Testing

1	18555	15913	86%	21147	18303	87%
2	160	155	97%	160	168	105%
3	90	90	100%	95	95	100%

Table 2.9 Comparison between mechanical properties of the structure at the beginning and at the end of the test. Sections Mix3 and EME2. The moduli of bituminous layers are considered at 10 °C and 10 Hz.

Layer	Mix 3			EME2		
	Initial (MPa)	Final (MPa)	Final/Initial (%)	Initial (MPa)	Final (MPa)	Final/Initial (%)
1	20018	11956	60%	20177	8370	41%
2	160	172	108%	160	185	115%
3	90	80	89%	85	75	88%

2.4.1.2 Inverse calculation from basin in non-damaged zone

For section Mix3 the deflection basin representative of the non-damaged zone was calculated as the average of measurements between 1 and 13 m (Figure 2.22), while for the Benkelman beam the average of at 4, 7 and 10 m (Figure 2.22) was considered. For section EME2 the deflection basin representative of the non-damaged zone was calculated as the average of measurements between 1 and 17 m (Figure 2.23), while for the Benkelman beam the average of at 7 and 12 m (Figure 2.23) was considered.

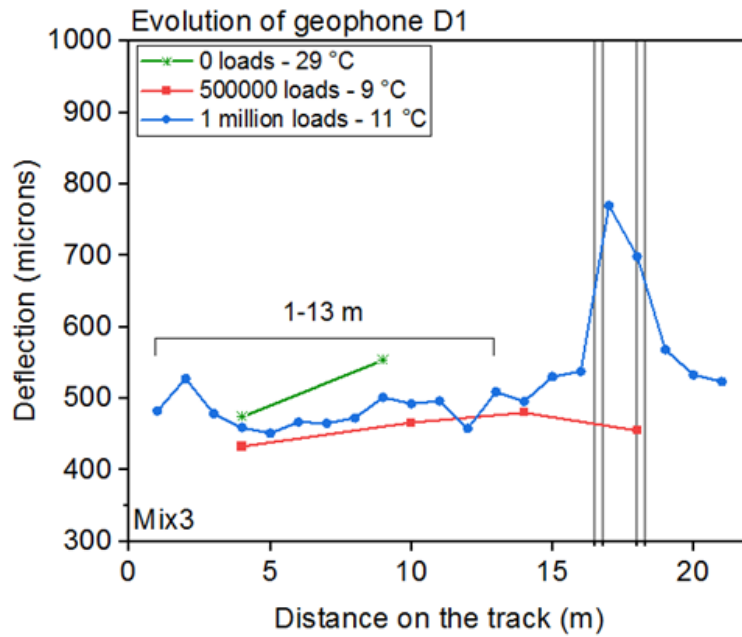


Figure 2.22 Mix 3 section, FWD deflection measured by geophone D1 at 1 million loads as a function of the distance on the track. The bracket indicates the range of FWD measurements taken into account for the calculation of deflection basin representative of the non-damaged zone.

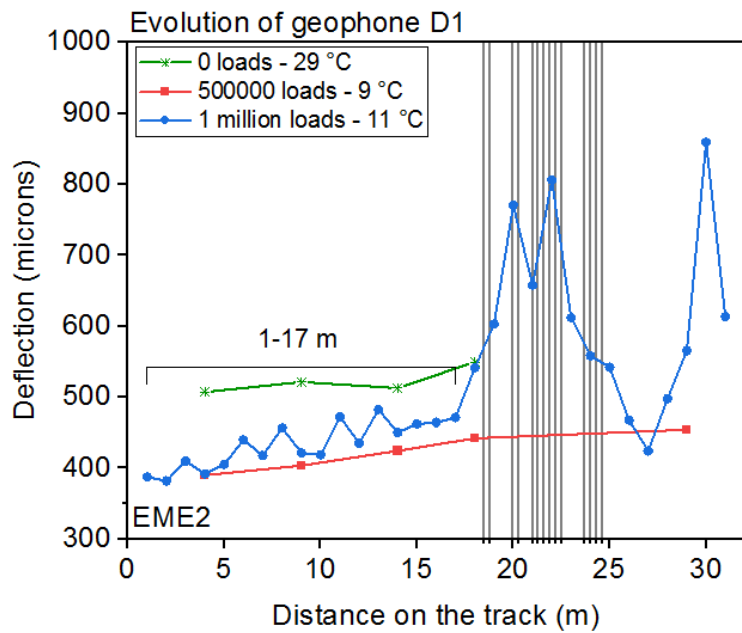


Figure 2.23 EME2 section, FWD deflection measured by geophone D1 at 1 million loads as a function of the distance on the track. The bracket indicates the range of FWD measurements taken into account for the calculation of deflection basin representative of the non-damaged zone.

Figure 2.24 reports the results obtained in Alizé by performing an inverse calculation from the measured basins: the superposition between measured (red) and calculated (green) deflection basin show that the prediction is good for the four sections. Deflections measured with the Benkelman beam and calculated deflections in Alize are reported in Table 2.10, and

2 Detection of pavement ageing based on embedded sensors – Accelerated Pavement Testing

even then the prediction is good. A comparison between the initial structure and the final structure is reported in Table 2.11 for the two sections. The same considerations as in section 2.4.1.1 can be made for the subgrade and unbound granular base moduli, the variations are negligible. Interestingly, the performances of the asphalt layers in the non-damaged zone remain almost unchanged for both the bituminous reference material (EME2) and the bio-recycled asphalt mix (Mix 3).

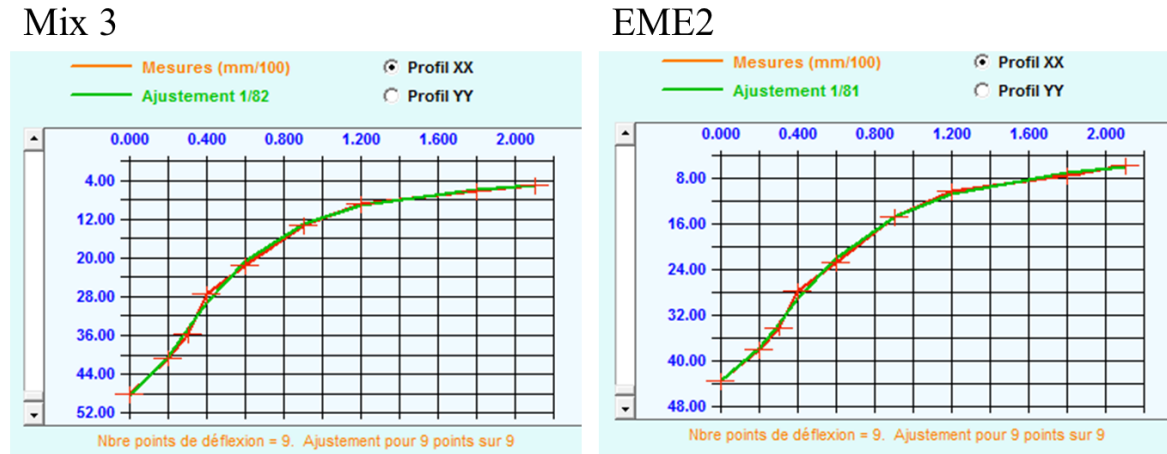


Figure 2.24 Results obtained in Alizé by performing an inverse calculation from the measured basins representative of the non-damaged zone: (left) Mix3, (right) EME2. The measured basins are well predicted by the model.

Table 2.10 Comparison between Benkelman beam deflections measured in the non-damaged zone (average between 800,000 and 1 million loads) and deflections calculated in Alizé.

	Mix 3	EME2
Measured deflection (mm/100)	48.3	42.0
Calculated deflection (mm/100)	48.2	41.7
Relative difference (%)	0.2	0.7

Table 2.11 Comparison between mechanical properties of the structure in the non-damaged zone at the beginning and at the end of the test. Sections Mix3 and EME2. The moduli of bituminous layers are considered at 10 °C and 10 Hz.

Layer	Mix 3			EME2		
	Initial (MPa)	Final (MPa)	Final/Initial (%)	Initial (MPa)	Final (MPa)	Final/Initial (%)
1	20018	17796	89%	20177	20595	102%

2	160	164	103%	160	169	105%
3	90	80	89%	85	85	100%

2.4.1.3 Inverse calculation from basin in damaged zone

For section Mix3 the deflection basin representative of the damaged zone was calculated as the average of measurements at 17 and 18 m (Figure 2.25), while for the Benkelman beam the measurement at 14 m was considered as it was the only available measurement closest to the damaged zone (Figure 2.25). For section EME2 the deflection basin representative of the non-damaged zone was calculated as the average of measurements between 20 and 22 m (Figure 2.26), while for the Benkelman beam the average of at 18, 24 and 29 m (Figure 2.26) was considered.

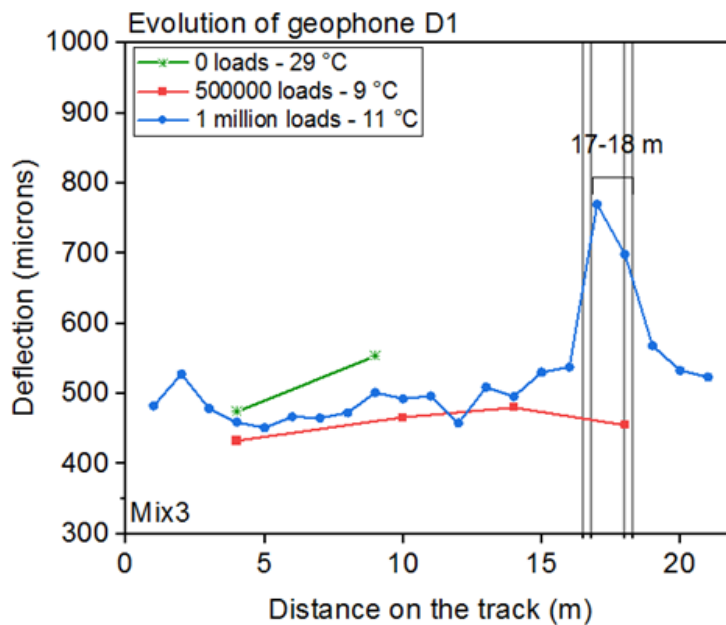


Figure 2.25 Mix 3 section, FWD deflection measured by geophone D1 at 1 million loads as a function of the distance on the track. The bracket indicates the range of FWD measurements taken into account for the calculation of deflection basin representative of the non-damaged zone.

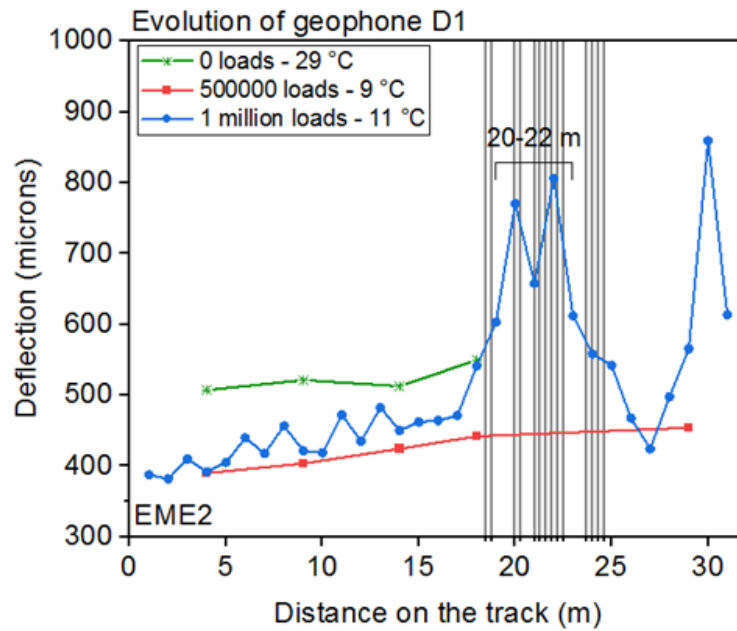


Figure 2.26 EME2 section, FWD deflection measured by geophone D1 at 1 million loads as a function of the distance on the track. The bracket indicates the range of FWD measurements taken into account for the calculation of deflection basin representative of the non-damaged zone.

Figure 2.27 reports the results obtained in Alizé by performing an inverse calculation from the measured basins: the superposition between measured (red) and calculated (green) deflection basin show that the prediction is good for the four sections. Deflections measured with the Benkelman beam and calculated deflections in Alize are reported in Table 2.12, and even then the prediction is good. A comparison between the initial structure and the final structure is reported in Table 2.13 for the two sections. The same considerations as in section 2.4.1.1 can be made for the subgrade and unbound granular base moduli, the variations are negligible. The same considerations as the previous can be made for the subgrade and unbound granular base moduli, the variations are negligible. As expected, the performances of the asphalt layers in the damaged zone are far worse than those in non-damaged zone: only 21% and 22% of the initial moduli of Mix 3 and EME2 sections are obtained respectively. Interestingly the levels of degradation of both sections are similar, confirming that the bio-recycled mix (Mix 3) performs similarly to the bituminous reference material (EME 2).

Mix 3



EME2



Figure 2.27 Results obtained in Alizé by performing an inverse calculation from the measured basins representative of the damaged zone: (left) Mix3, (right) EME2. The measured basins are well predicted by the model.

Table 2.12 Comparison between Benkelman beam deflections measured in the damaged zone (average between 800,000 and 1 million loads) and deflections calculated in Alizé.

	Mix 3	EME2
Measured deflection (mm/100)	60.0	58.3
Calculated deflection (mm/100)	62.0	62.4
Relative difference (%)	3.3	7.0

Table 2.13 Comparison between mechanical properties of the structure in the damaged zone at the beginning and at the end of the test. Sections Mix3 and EME2. Sections Mix3 and EME2. The moduli of bituminous layers are considered at 10 °C and 10 Hz.

Layer	Mix 3			EME2		
	Initial (MPa)	Final (MPa)	Final/Initial (%)	Initial (MPa)	Final (MPa)	Final/Initial (%)
1	20018	4232	21%	20177	4527	22%
2	160	151	95%	160	137	85%
3	90	90	100%	85	85	100%

2.4.2 Comparison between numerical and experimental strains at the bottom of the bituminous layers

The maximum strains at the bottom of the bituminous layers are calculated considering the structures obtained by inverse analysis as in sections 2.4.1.1, 2.4.1.2 and 2.4.1.3 in order to

make a comparison with strain measured with the ASGs (see section 2.3.2.3). An elastic computation is performed in Alizé by considering for the unbound granular base and the subgrade the initial moduli and for the asphalt layers the moduli inverse calculated from the FWD deflection basins adjusted in temperature and frequency as in the equation (2.3). The load was modelled as 65 kN dual wheel and the wheel-to-pavement surface area was considered as circular. The computed strains as well as the measured strains (obtained by averaging the response of the ASGs for each section at 999,200, 1,005,200 and 1,006,400 loads), are reported in Table 2.14. The mean temperature in the asphalt layers is 10 °C.

As it can be seen sensors response is very close to the calculated strain for Mix1 (relative variation of 6 %). For Mix2 the experimental strain measured in the field is higher than the numerical strain (relative variation of 38 %). As expected the measured strains in sections Mix3 and EME2 are closer to those calculated from the FWD basin representative of the damage zone where the sensors are located (relative variation of 42 % and 1 % respectively). Overall, the study shows a very good agreement between sensor measurements and computed strains for both damaged and non-damaged sections. The relative variation goes from 1 % to 40 %, which is an excellent result and suggests once again that asphalt strain gauges can be considered as a valuable method for pavement monitoring.

Table 2.14 Maximum strain at the bottom of the asphalt layer calculated in Alizé considering the structures inverse calculated from FWD deflection basins at 1 million loads and strains measured with ASGs.

Section	Maximum strain at the bottom of the asphalt layer ($\mu\epsilon$)			
	Inverse calculation	Inverse calculation	Inverse calculation	ASGs measurements
	from basin	from basin	from basin	
	representative of	representative of	representative of	
the whole structure	non-damaged zone	damaged zone		
Mix1	170	-	-	160
Mix2	138	-	-	190
Mix3	185	148	324	461
EME2	199	122	313	316

2.5 Development of a procedure for temperature correction of measured strains

Due to the intrinsic viscoelastic behaviour of bituminous materials (see Section 11), pavement responses under moving loads are influenced also by the temperature evolution within the pavement. Indeed temperature variations have a large influence on flexible

pavements structural response (Swett et al., 2008). The use of ASGs for pavement monitoring may require more advanced tool for data interpretation. Here a methodology for temperature correction of strain measurements in the road pavement to a reference temperature (10 °C) is proposed. The purpose is to separate the temperature-induced changes in pavement stiffness from those associated to damage occurrence. Please note that since temperature variation during the fatigue experiment at the APT were fairly moderate the procedure outlined in this section was not applied to the analyses presented in the previous section. In addition, in the previous section we considered strain measurements at 10 °C which is the reference temperature adopted for the procedure.

As shown in Section 2.3.2.3, at the beginning of the test, the maximum longitudinal strains at the bottom of the surface bituminous layer are of the same magnitude (100 ÷ 130 $\mu\epsilon$). At about 200,000 loads the response of some sensors start to derive indicating that cracking or damage is occurring near the sensors. In order to avoid confusing the impact of temperature with the impact of damage propagation in the pavement, the analyses are limited to the data recorded in the first 136,800 loadings where it is reasonable to assume that the materials mechanical performances have not undergone any change. As it can be observed from Figure 2.28, in this phase the sensors have pretty much the same trend.

The establishment of a methodology for temperature correction of strain measurements to a reference temperature (10 °C) requires the assessment of structure-to-temperature sensitivity. Thus, the theoretical $\mu\epsilon$ - °C law was determined for each mix; where " $\mu\epsilon$ " is the response in terms of strain at the bottom of the surface layer. For this purpose some viscoelastic calculations were carried out by using the Viscoroute© software (see Section 1.6.1.2) (A Chabot et al., 2010). The characteristics of the pavement structures used in the model come from field controls. The viscoelastic parameters entered in Viscoroute© for the surfaces layers are listed in Table 2.15; while Table 2.16 reports the parameters considered for the base and subgrade layers for each section. The load was modelled as 65 kN dual wheel and the wheel-to-pavement surface area was considered as circular. Calculations were performed in a temperature range between -10 and 40 °C.

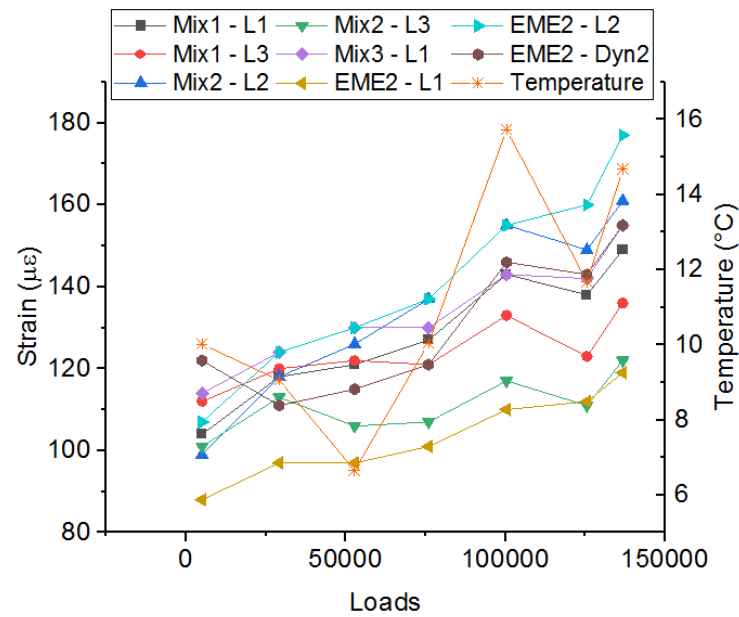


Figure 2.28 Fig. 5 Longitudinal maximum strain evolution in the first 136,800 loads.

Table 2.15 Surface layers viscoelastic parameters entered in Viscoroute©

	Thickness (cm)	E_{∞} (MPa)	ν	E_0 (MPa)	k	h	δ	A_0	A_1	A_2
Mix1	8.6	38167	0.35	0.209	0.209	0.637	2.271	3.337	-0.368	0.001604
Mix2	9.5	36321	0.35	0.215	0.215	0.659	1.426	3.029	-0.381	0.001675
Mix3	9.1	37172	0.35	0.193	0.193	0.605	2.25	4.692	-0.382	0.001610
EME2	10.2	35284	0.35	0.183	0.183	0.580	2.312	5.899	-0.400	0.001581

Table 2.16 Unbouncing granular base and subgrade parameters entered in Viscoroute©

	Mix1	Mix2	Mix3	EME2
E_{UGB} (MPa)	160	160	160	160
ν_{UGB}	0.35	0.35	0.35	0.35
$E_{subgrade}$ (MPa)	90	95	90	85
$\nu_{subgrade}$	0.35	0.35	0.35	0.35

Figure 2.29 shows a clear non-linear temperature dependency for all the mixes considered in this study. The maximum longitudinal strain increases significantly with increasing temperature. A polynomial function of the 3rd order is chosen as it gives the best fit for the numerical results:

$$S = A_3T^3 + A_2T^2 + A_1T + A_0 \quad (2.4)$$

Where S is the strain in expressed $\mu\epsilon$, T is the temperature expressed in $^{\circ}\text{C}$, A_3 , A_2 , A_1 , A_0 are coefficients and they are listed in Table 2.17 for all the mixes.

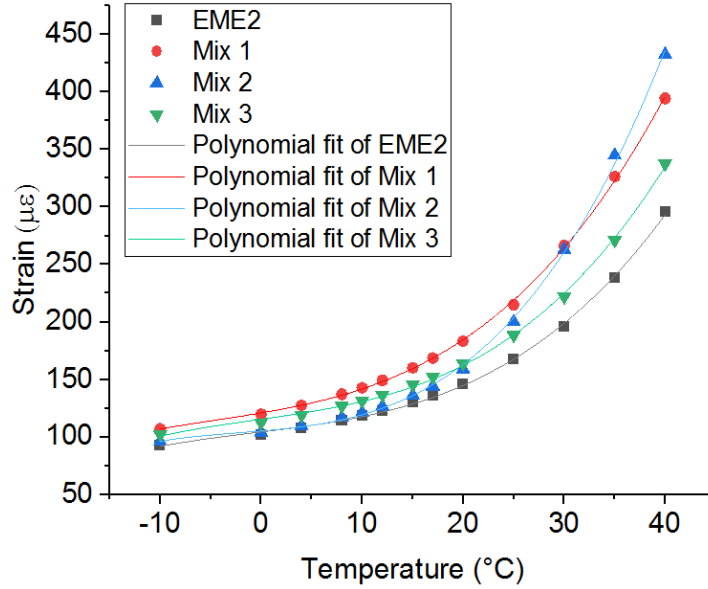


Figure 2.29 Strain ($\mu\epsilon$)-Temperature ($^{\circ}\text{C}$) numerical relations and polynomial fits.

Table 2.17 Coefficients of the polynomial functions used to fit the numerical results.

Section	A_3 ($\mu\epsilon / ^{\circ}\text{C}^3$)	A_2 ($\mu\epsilon / ^{\circ}\text{C}^2$)	A_1 ($\mu\epsilon / ^{\circ}\text{C}$)	A_0 ($\mu\epsilon$)
Mix 1	2.50E-03	3.46E-02	1.50E+00	1.21E+02
Mix 2	4.10E-03	2.65E-02	7.51E-01	1.05E+02
Mix 3	2.60E-03	2.90E-03	1.26E+00	1.15E+02
EME2	2.20E-03	3.50E-03	1.08E+00	1.04E+02

Once the structure-to-temperature sensitivity is known, the temperature-correction factor (CF) is defined as follows:

$$\text{CF}(T) = -\epsilon_{\text{th}}(T_{\text{ref}}) + \epsilon_{\text{th}}(T) \quad (2.5)$$

Where $\epsilon_{\text{th}}(T_{\text{ref}})$ and $\epsilon_{\text{th}}(T)$ are the numerical strains (determined by the method described above) respectively at the reference temperature and at the temperature T measured in the pavement; T_{ref} is selected to be 10°C .

Using this definition of $\text{CF}(T)$, the equivalent strain at temperature T, $\epsilon_e(T)$, is expressed as:

2 Detection of pavement ageing based on embedded sensors – Accelerated Pavement Testing

$$\varepsilon_e(T) = \varepsilon_m(T) - CF(T) \quad (2.6)$$

Where $\varepsilon_m(T)$ is the measured deformation at the temperature T.

Figure 2.30 shows the equivalent maximal longitudinal strain at the reference temperature of 10 °C for one sensor per section, the others are reported in Appendix 2. Before correction, the graphs show an overall increase of strain with number of loads for all sensors and all mixes. This is not expected as, at the early stage of loadings, no degradation is expected in the pavement, especially not for all mixes. After correction, the graphs all show a reduction of the strain to time slope. This latter can be better visualized in the bar graph in Figure 2.31, where the slopes of the linear strain-to-loading trendlines fitting the measured and equivalent strains are compared. The application of the temperature correction generates the decrease of the slopes consistently for all the sensors (about 50% on average).

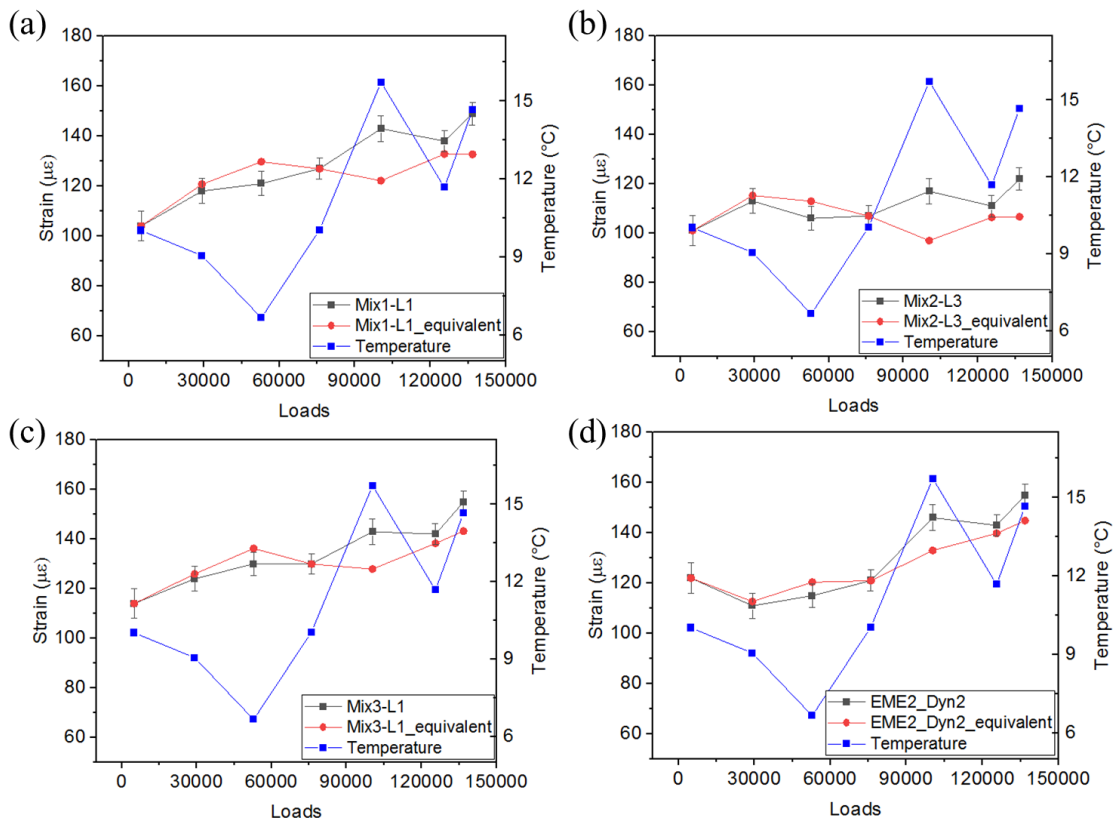


Figure 2.30 Equivalent maximum longitudinal strain at the reference temperature of 10 °C for sensors (a) Mix1-L1, (b) Mix2-L3, (c) Mix1-L3 and (d) EME2-Dyn2. Correction applied in the first 136,800 loads.

This suggests that the correction method proposed here works well. As it can be noticed in the graphs in Figure 2.30, let us add that the larger the temperature variation ($|T_{ref} - T|$), the stronger the strain correction ($|\varepsilon_e(T) - \varepsilon_m(T)|$). It suggests that the methodology would be even more useful in a context of stronger temperature variations.

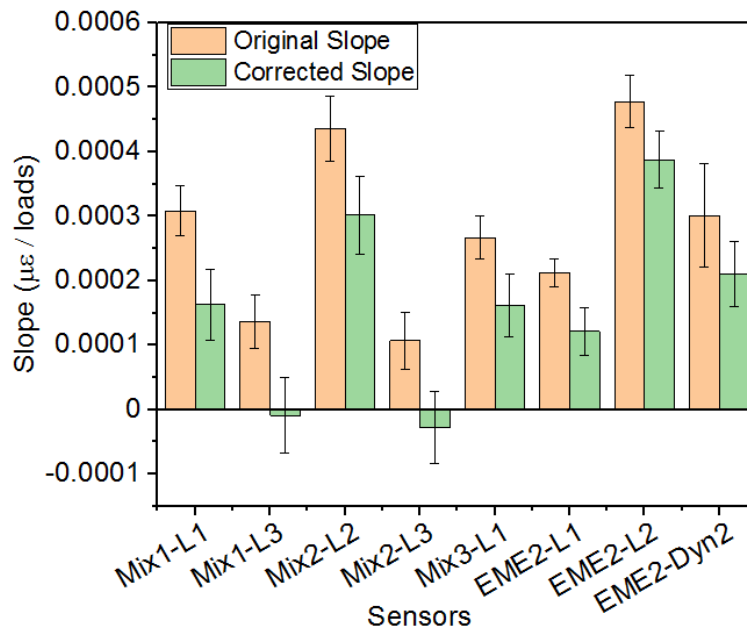


Figure 2.31 Comparison between the slopes of the trendlines fitting the measured and the equivalent strain values. Correction applied in the first 136,800 loads.

In order to validate the approach, the proposed methodology is applied to a wider loading range (from 178,000 to 500,000 loads) where similar temperature oscillations are recorded ($\Delta T = 8 \text{ }^\circ\text{C}$) within the bituminous layer. In this phase, only sensors in sections Mix1 and Mix2 are considered as it is demonstrated that for these sections materials did not show any degradation of mechanical properties (see Section 2.4).

As it can be observed from Figure 3.26 in this phase the sensors have pretty much the same trend. The plots in Figure 2.33 and the bar graph in Figure 2.34 show that the application of the temperature correction generates the decrease of the slopes consistently for all the sensors (about 40% on average), hence they validate the procedure.

These results show that the proposed approach works well with different pavement structures, opening the ways toward replication of the method for real cases of pavement in-situ monitoring.

2 Detection of pavement ageing based on embedded sensors – Accelerated Pavement Testing

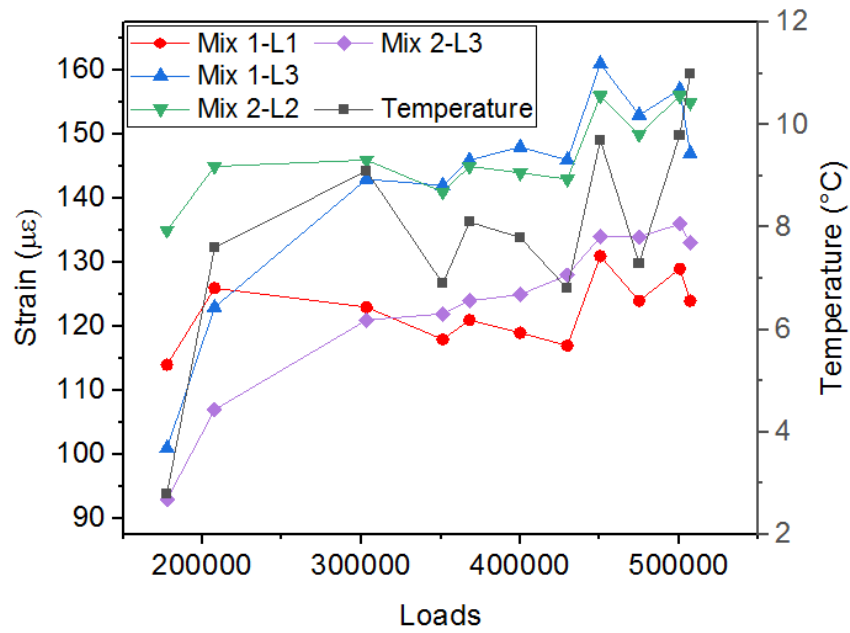


Figure 2.32 Longitudinal maximum strain evolution from 178,000 to 500,000 loads.

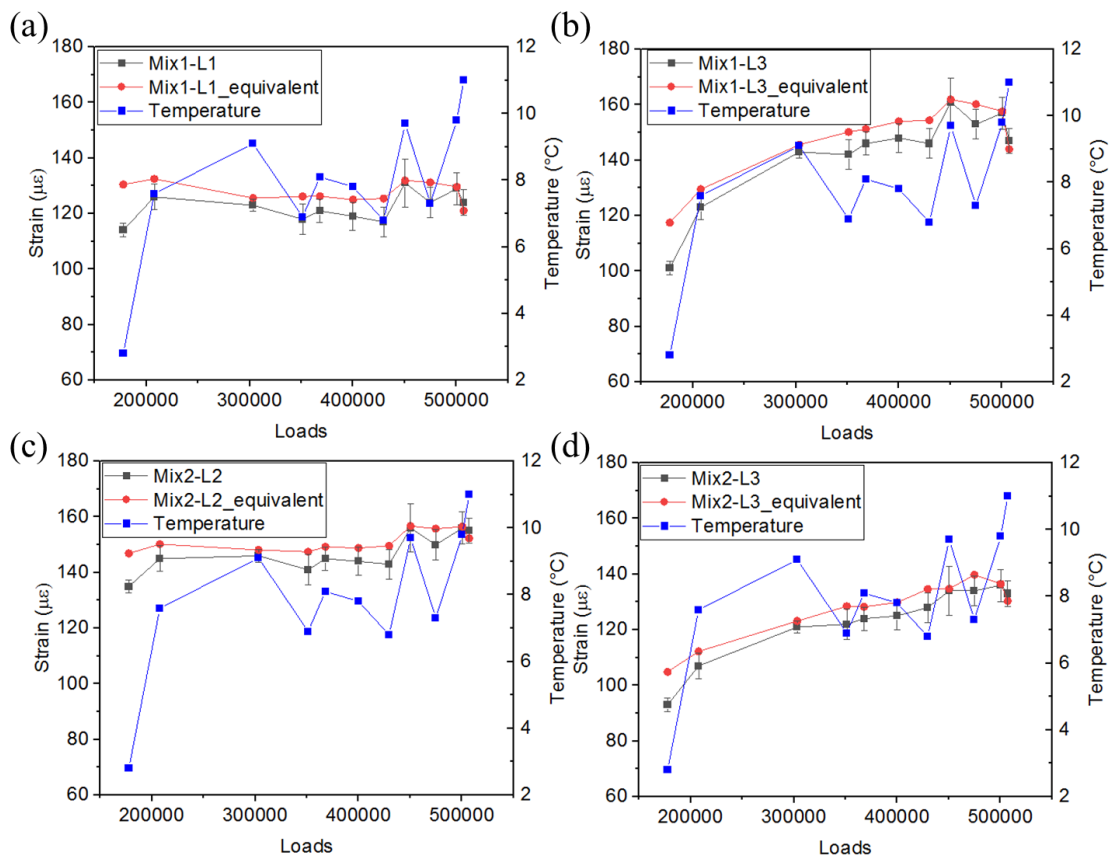


Figure 2.33 Equivalent maximum longitudinal strain at the reference temperature of 10 °C for sensors (a) Mix1-L1, (b) Mix1-L3, (c) Mix2-L2 and (d) Mix2-L3. Loading range: 178,000 – 500,000 loads

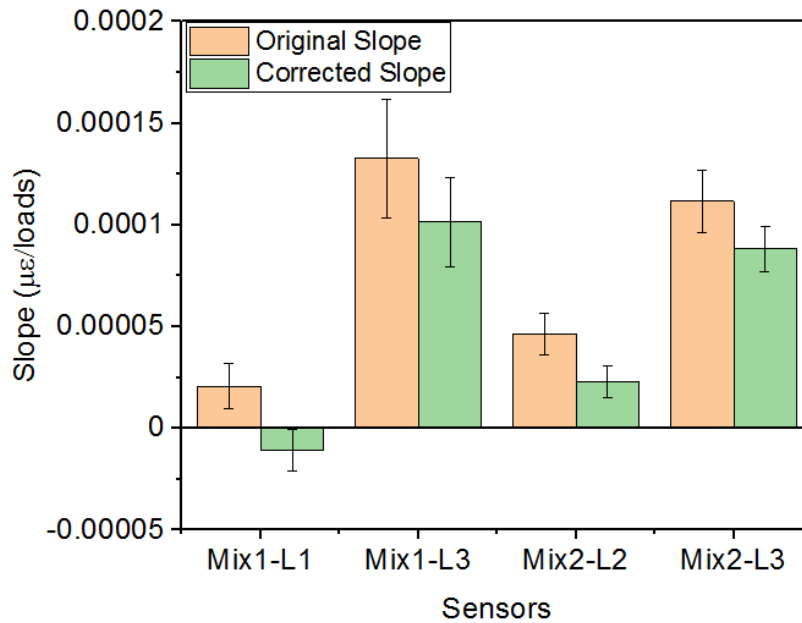


Figure 2.34 Comparison between the slopes of the trendlines fitting the measured and the equivalent strain values. Loading range: 178,000 – 500,000 loads.

2.6 Conclusions

This chapter presents the results of the analyses performed on a set of data collected from the University Gustave Eiffel asphalt pavement testing facility with the purpose to detect pavement ageing based on embedded strain gauges. The data were generated during the fatigue experiment carried out within the European project BioReparation finalised at assessing the performances of three bio-recycled asphalt mixes. Four section were tested simultaneously, the three innovative mixes (sections Mix1, Mix2 and Mix3) and a reference section (EME2) which is a high performance reference material for base layers. A total of 1.4 million loads were applied in two loading configurations: 65 kN 1 million loads at 72 km/h and additional 75 kN 400,000 loads at 43 km/h. In order to track the evolution of mechanical performances of the four sections different non-destructive monitoring methods were used:

- Traditional monitoring methods, such as visual inspection, Benkelman beam deflections and FWD deflections.
- Instrumentation based on the use of embedded horizontal asphalt strain gauges and temperature probes located at the bottom of the bituminous layer.

The first cracks were observed on Mix 3 and EME2 sections at about 1 million loads, while sections Mix 1 and Mix 2 did not show any damage. An increase of maximum strain

2 Detection of pavement ageing based on embedded sensors – Accelerated Pavement Testing

measured at the bottom of the bituminous layer was recorded by AGSs installed in Mix 3 and EME2 sections, consistently with crack visual inspections and deflection measurements. In addition, the sensors showed a quite localized response as sensors installed in the same section can possibly exhibit different evolutions (see sensors EME2-L1 and EME2-L2).

Furthermore, ASGs were able to detect the occurrence of fatigue damage earlier than the other monitoring tools. In fact the response of some sensors (see sensors Mix3-L1, and EME2-L2) started to derive well before crack visualization or detection of deflection peaks by the Benkelman beam and the FWD.

The analyses of the superposition of FWD measurements, sensor localization, and cracking pattern suggested that the sensors may represent a weakness point in the pavement from where cracks originate. However, the presence of embedded technologies is not responsible for damage in the pavement as Mix 1 and Mix 2 sections did not exhibit any cracks despite the fact that they were instrumented as well.

For further investigation, strain measurements were compared with numerical strains obtained from the inverse analysis of layer moduli based on FWD deflection basins measured at 1 million loads. The dedicated Alizé module was used at this purpose. The study showed that damaged is concentrated in the surface bituminous layers. At 1 million loads, the initial moduli are halved. In addition, the comparison of performances of non-damaged and damaged areas highlights that fatigue damage is a localised phenomenon as suggested by the ASGs signal analysis. Overall a very good agreement was found between inverse calculated and measured strain at the bottom of the bituminous layer which strongly point towards the use of ASGs as effective monitoring method able to provide information about the current status of pavement conditions.

Finally a monitoring tool to improve the interpretation of strain sensor data is developed. It concerns a methodology for temperature correction of strain measured within the pavement. It means that equivalent strains are calculated as if the temperature is the reference one, allowing to account for temperature influence on strain measurement.

In this chapter, we demonstrate for the first time the feasibility of detecting fatigue occurrence in different bituminous layers based on sensor data. Thus, we show the interest of instrumentation as monitoring method as well as the eventual limitations related to the geometry of the sensing devices.

In the following section we investigate how instrumentation can be deployed on a real road for inverse calculation of its mechanical conditions, and we propose a first validation of an innovative sensing device.

3 INVERSE CALCULATION OF PAVEMENT RESPONSE BASED ON EMBEDDED SENSORS – CORBAS TRIAL SECTION

3.1 Introduction

In the previous chapter, we proved that asphalt strain gauges and temperature probes can be deployed to detect the occurrence of fatigue in the road pavement by focusing on the damage of a single layer of a road prototype. In this chapter we want to investigate the utility of embedded sensors to inverse analyse the conditions of materials and their response on a real road. We present the efforts undertaken to embed a set of sensors in an existing road pavement on an industrial site of Eiffage Route used to develop and validate an inverse model for the derivation of the pavement mechanical behaviour (both modulus and viscous properties). Hence, the chapter presents our selected approach towards road modelling (direct and inverse) based in Viscoroute© software.

We describe the sensor network, the installation procedures, and the connection to data acquisition system for remote monitoring. We present the coring campaign and the laboratory characterization of each layer of the road pavement. We illustrate the 2 day-measurement campaign performed with a truck of known load at different temperatures, speeds, and trajectories. We finally compare experimental and numerical results and we use the model to study the pavement response at high temperatures and in particular the contribution of the interface between layers.

In this chapter, we also introduce a first step towards the development of an innovative, sensing device for pavement monitoring. The objective was to finally propose a prototype of a solution that can overcome some of the drawbacks identified with commercial sensing

devices. In this chapter, we validate the geometry of the system and its resilience to the construction phase. Please note that, the instrumentation was initially designed to further validate the system via comparison with asphalt strain gauges, here considered as the reference solution. Finally, due to some issues encountered we did not explore this aspect. Further insights are presented in chapter 4.

3.2 Description of the trial section

The trial section object of this study was instrumented with a sensor network composed of six asphalt strain gauges and an innovative sensing device. The whole installation process, such as the sensor location and the connection to the data acquisition system, are described in details below.

3.2.1 Experimental site

The experimental site is an industrial site of Eiffage Route located in Corbas (France) with an area of 6.4 m×30 m. A 5 cm-thick wearing course made of BBSG (see Section 1.4.3 for more details on this bituminous mix) was paved over a pre-existing road pavement after the application of a tack coat emulsion with a distributor truck (see Section 1.3.2 for more details on its role). The exact stratification of the road was initially unknown.

3.2.2 Sensors installation

The section was instrumented by placing the sensors on the top of the existing pavement. The tack coat emulsion was first manually applied under and around the sensors; a second application was executed with a distributor truck over the total area before paving the 5-cm-thick wearing course. The employed sensors are an InTRACK device provided by Altaroad (<https://www.altaroad.com/>) and six ASGs provided by CTL Group (<https://www.ctlgroup.com/>).

- The InTRACK solution is a multi-sensor connected device crossing the width of a lane (Figure 3.1). The system collects real time road and traffic data for processing by advanced algorithms. Embedding over 30 sensors inside one lane, it measures deformations of the road in multiple directions, as well as temperature evolution within the road. Packaged in an easy to deploy and bitumen-compatible material, the system is composed by a sensing band of 12 cm x 250 cm x 0.4 cm and a road side unit located in a dedicated inspection sump. The InTRACK is placed in the transverse

3 Inverse calculation of pavement response based on embedded sensors – Corbas trial section

direction with respect to traffic direction. The final implementation is invisible for a passer-by.



Figure 3.1 Altaroad's InTrack solution during installation on experimental construction site (October 2017).

- The ASGs (Figure 3.2) are designed to withstand the high temperatures and compaction loads associated with asphalt pavement construction. Each ASGs is composed of 4 active strain gauges with nominal resistance of 350Ω mounted in full-bridge configuration. Three horizontal measurement directions were chosen for the ASGs, longitudinal, transversal, and at 45° angle. The use of two sensors for each direction, instead of only one, was motivated by the wish to implement redundancy, namely to have at least one measurement per direction if one sensor fails in time.

The sensors were widely spaced in order to reduce cross perturbation; in particular, the spacing in the y-direction of ASGs is such as to match the width of a truck. All wires were collected in an inspection sump on the roadside. The outline of sensors configuration in the experimental site is shown in Figure 3.3.

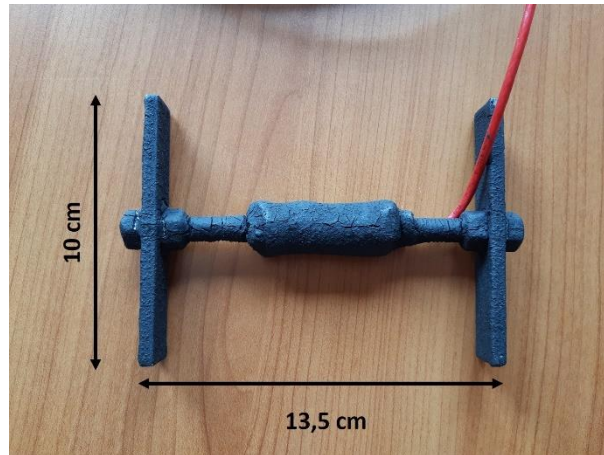


Figure 3.2 ASGs provided by CTL Group employed for the instrumentation of the section. The sensors are characterised by an H-shape measuring 10 cm x 13 cm with a thickness of 2 cm.

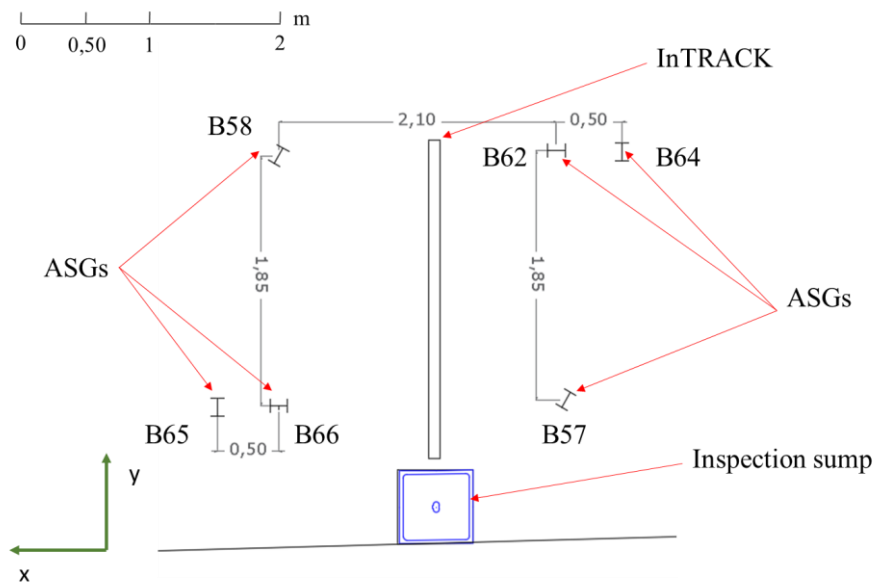


Figure 3.3 Sensors configuration in the experimental site. The sensors are located on the top of the existing pavement. Two types of sensors are employed: ASGs from CTL Group and Altaroad InTRACK system. All wired are collected in the inspection sump.

3.2.3 Data acquisition system

The wires collected in the inspection sump were driven up to an external box (Figure 3.4) and connected to a remote data acquisition system called PÉGASE (<http://Pégase-instrumentation.com/>). The PÉGASE is a wireless platform for sensor acquisition developed by the University Gustave Eiffel and licenced to the company A3IP. PÉGASE permits data transfer from up to eight sensors (typically temperature and strain gauges in quarter, half, or full bridge configuration) to a cloud-based supervisor and database (via 4G network) for

3 Inverse calculation of pavement response based on embedded sensors – Corbas trial section

further analyses. In addition, by integrating a low-power GPS receiver, the system allows accurate data dating and localisation.



Figure 3.4 Experimental site: location of the external box and the inspection sump.

3.2.4 Measurement campaign

As stated in the introduction, the overall goal of this work is to confront in-situ experimental data to modelling data (from Viscoroute©) to derive pavement mechanical behaviour via inverse calculation. It is well-known (see Section 1.7) that such inverse methodology requires a fine-grained knowledge of the loading parameters. For this purpose, an experimental campaign was performed over a 2-day period on 17th and 18th July 2018 on the trial section. The maximum air temperature reached during the campaign was 30°C. The surface temperature of the asphalt pavement was recorded during the two days of tests with an infrared thermometer (Testo 830-T2 - <https://www.testo.com>) and, as expected, it reached over 50°C (Figure 3.5). This results in low stiffness and high deformability of the road pavement. In this section, we present the geometry of the truck used for the measurement campaign, as well as its main trajectories and speeds.

3.2.4.1 Geometry of the truck used for the measurement campaign

The loading truck has three axles and its geometry is shown in Figure 3.6. The weight by axle is checked before the tests and the wheel-prints were taken by spray-painting them on some papers.

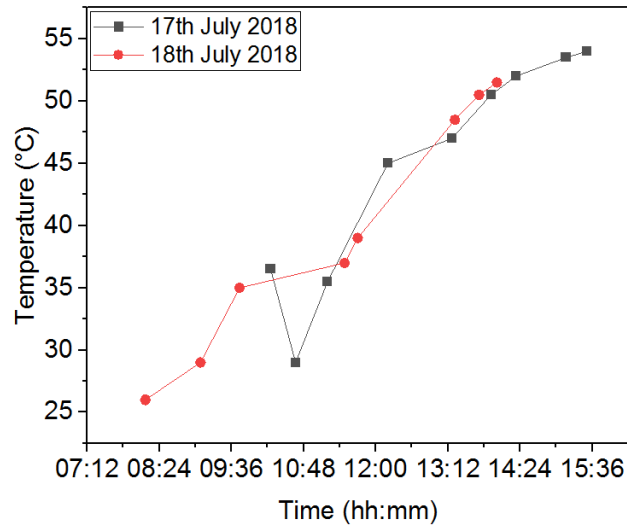


Figure 3.5 Temperature measurements at the surfaces of the road pavement recorded the 17th and 18th July 2018.

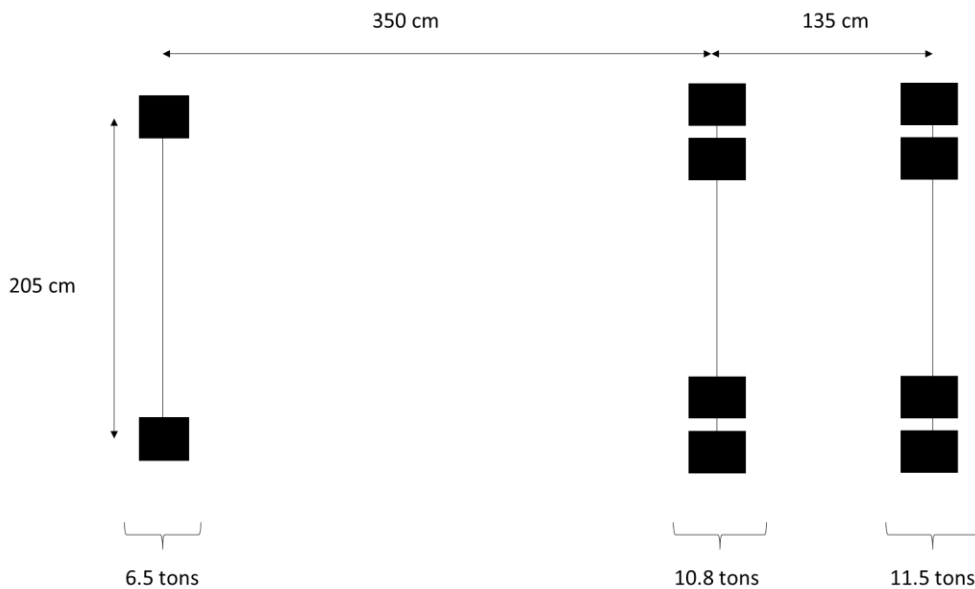


Figure 3.6 Geometry of the loading truck used for the measurement campaign.

3.2.4.2 Definition of truck trajectories

The campaign was based on a series of passages of the same truck. Two types of truck trajectories were defined, the first mostly on top of the sensors, the second 30 cm to the side. As there was a significant variability in the trajectory actually achieved by the truck, the actual transverse position of the truck was recorded at each passage. To do this, a sand strip (Gaborit, 2015) was placed on the top of the road pavement, as shown in Figure 3.7. If we define $\Delta D_{y,ref}$ as the distance between the roadside and the projection of reference sensor (circled in Figure 3.7) on the sand strip, we can state that ΔD_y is the measured distance on

3 Inverse calculation of pavement response based on embedded sensors – Corbas trial section

the sand strip between the roadside and the middle of the rear left axle. Thus the trajectory T0 is defined as $\Delta D_{y,ref} = \Delta D_y$, while the trajectory T1 is defined as $\Delta D_y - \Delta D_{y,ref} = 30$ cm. The two trajectories can be better visualized in Figure 6.9 in Appendix 3.

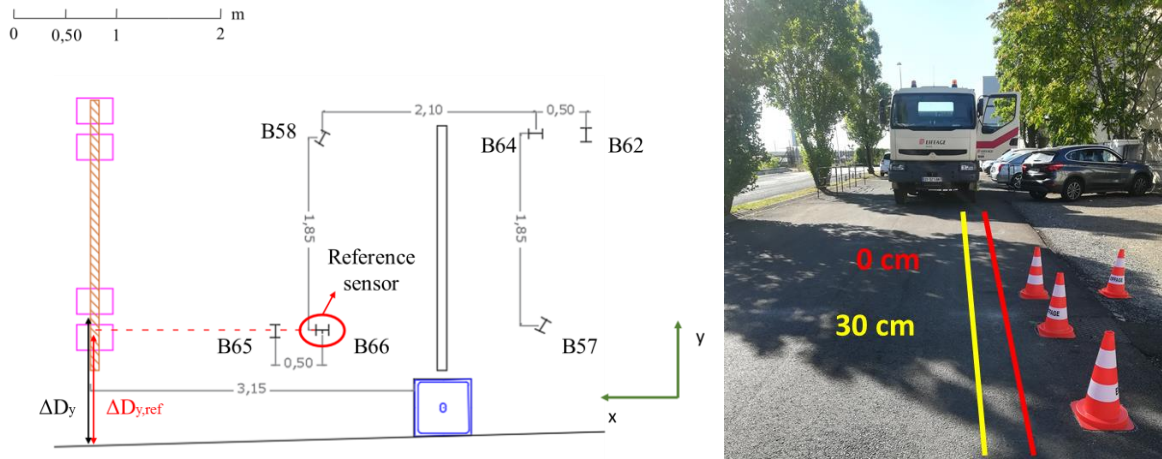


Figure 3.7 Truck trajectory: (Left) sand strip placed on the top of the asphalt layer for the identification of the $\Delta D_{y,ref}$ and ΔD_y parameters, (Right) visualisation of the two trajectories in the field.

3.2.4.3 Truck speed

Two truck speeds were chosen for the experimental campaign, 10 and 20 km/h. The loading conditions over the two days of tests are summarised in Table 3.1.

Table 3.1 Loading conditions during the measurement campaign.

	T0	10 km/h	20 km/h	T1	10 km/h	20 km/h
Day 1	X	X	X			
Day 2	X		X	X	X	

3.2.5 Modelling in Viscoroute©

With the purpose to simulate the response of the instrumented section, pavement calculations were carried out by using Viscoroute©. As mentioned in Section 1.6.1.2, Viscoroute© considers by default fully bonded layers. To address more complex, and expectedly more realistic, configurations with Viscoroute©, thin (2 mm) layers are added at the interfaces between the layers (Duong, 2017).

3.3 Feedback from the InTRACK solution

As stated in section the introduction of the chapter, the InTRACK was integrated in the trial section with the aim of testing its geometry, its adaptability to the road environment and in

particular to the construction phase. The on-site experimentation followed up a series of preliminary lab studies carried out at the Research Center of Eiffage Route aimed at selecting the best encapsulation material for the sensor network. Multiple asphalt specimens (slabs) integrating different encapsulation materials were fabricated and tested under 11,000 stress cycles at different temperatures. At the end of the experimental campaign the material preserving a good bonding at the interface with asphalt was retained. In this section we present some preliminary results.

3.3.1 Resilience to construction phase

Continuous acquisition (0.1 Hz) of data during and right after construction process allowed to assess proper operation of the sensors within the road after this step. First of all, all the sensors withstand the installation phase (exposure to high temperatures and high compaction efforts) without interruption or degradation of the signal quality. By analysing the response of 8 sensors (Figure 3.8) of the Altaroad solution one can clearly visualize all the phases of the construction process: hot mix asphalt placement, compaction and cooling down period of asphalt before regular operation started. Similar curves are obtained for the other sensors. Hence, the system can operate in the hostile road environment.

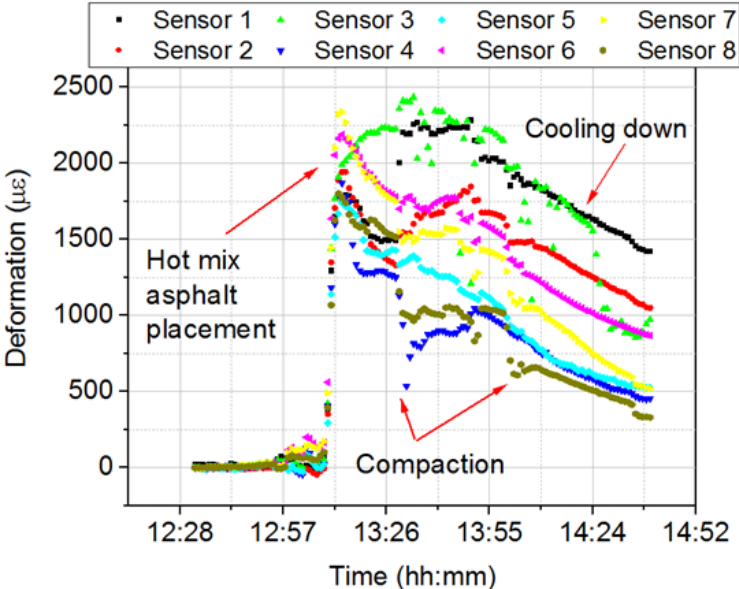


Figure 3.8 Response of one of the sensors of the Altaroad's InTrack during the construction process (acquisition frequency of 0.1 Hz). The different phases of the installation can be clearly recognised: hot mix asphalt paving, compaction, cooling down.

3.3.2 Quality of interface and impact on the road pavement

The extraction of cores at the location of the InTRACK allowed to assess the quality of the interfaces between the system and the asphalt layers as well as its impact on the road pavement. The observation of the core samples confirmed very good bonding of the InTrack/asphalt interfaces (Figure 3.9). In addition, after 36 months from the installation the pavement did not show any cracking related to the embedded sensing technologies. Hence, in this context (relatively low traffic, relatively short duration), this innovative technology has no negative impact on the road.



Figure 3.9 Sample cored on the trial section 2 months after the installation: very good bonding at the interfaces InTrack/asphalt.

3.3.3 Discussion

The test conducted on the Altaroad's InTRACK solution represented the basis for the development of a novel technology for pavement monitoring. The preliminary results analysed in this section show the potential of the system in terms of:

- Geometry. Thanks to its geometry, the system can integrate a large number of sensors, both strain sensors and temperature sensors, and cover the width of a lane.
- Adaptability to the road environment. Thanks to its design, the system can withstand the construction phase and is less intrusive for the road pavement.

The results of the InTRACK could not be exploited and compared with ASGs during the measurements campaign with the truck due to an issue in the waterproofing of the system. However the first feedback obtained from the trial section served as the basis for the upgrading of the device as presented in chapter 4.

3.4 Laboratory characterizations of the pavement structure

In most of the studies available in the literature, the instrumentation takes usually place on a highway, either within the construction of a new structure, or within maintenance works that involve the rebuilding of some bituminous layers (see Section 1.7.2). This implies that either all or a significant proportion of the structure and its material properties is well known. As mentioned in Section 3.2, the instrumentation object of this study involved a pre-existing road and the implementation of an additional layer. The uncertainty on the underlying structure made it necessary to carry out a coring campaign followed by an experimental lab campaign for materials characterisation (carried out at the Research Centre of Eiffage Route). In this section we describe the experimental procedures carried out on materials to characterise their linear viscoelastic behaviour (see Section 1.5.1) and the obtained results. 2S2P1D model (see Section 1.5.2) was used to fit experimental data both for binders and mixes in order to simulate their LVE behaviour.

3.4.1 Coring campaign

Four samples were cored on the experimental site (according to the plan reported in Appendix 4) at a sufficient distance from the sensors to not impact their measurements. A coring drill with a diameter of 230 mm was applied down to a depth of about 200 mm. Below this threshold, the subgrade, apparently made of sand and small size stones, was clearly visible and it was decided not to drill any deeper. Details about the cores are given in Appendix 4. As can be seen on one of the cores shown in Figure 3.10, the road structure is unexpectedly complex: it is actually divided in five bituminous layers, as summarised in Table 3.2.

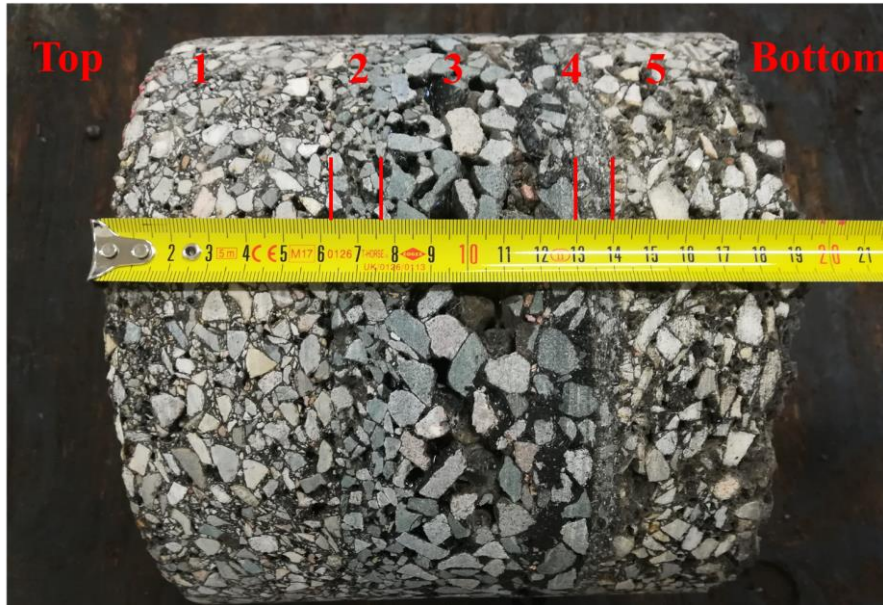


Figure 3.10 Sample cored in the experimental site: the road structure is composed of 5 bituminous layers.

Table 3.2 Structure of the pavement derived from the cores extracted in the field.

Layer no.	Thickness (mm)
1	≈ 50
2	≈ 10
3	≈ 60
4	≈ 10
5	≈ 50

3.4.2 Characterization of the bitumen of the tack coat emulsion

As specified in Section 3.2 a tack coat emulsion was used at the interface between the existing and the new asphalt layers. This layer is usually applied to ensure proper bonding between pavement layers and so have the completed structure acting as a single unit (see Section 1.3.2). In this specific case, the emulsion was also used to promote the optimal adhesion between the sensors and the road structure. After a first manual application under and around the sensors, a second one was executed with a tack coat distributor truck. The bitumen used for the emulsion had a penetration grade of 70/100.

3.4.2.1 Complex modulus test: procedure description

The complex modulus test was performed using the DSR (Dynamic Shear Rheometer) apparatus (EC-Twist 502 manufactured by Anton-Paar and shown in Appendix 5) of the Eiffage Route Research Centre according to the European Standard NF EN 14470 (AFNOR,

2012b). Loading was performed in strain control mode (0,1%) over a range of temperatures from -20°C to 70°C and a range of frequencies ranging from 0.01 Hz to 10 Hz as shown in Appendix 5 (Section 6.5.1). For temperatures between 30°C and 70°C a 25 mm diameter sample was used (Figure 3.11-Left), while for temperatures between -20°C and 40°C , a 8 mm diameter sample was used (Figure 3.11-Right). At lower temperatures the bitumen becomes more brittle, thus the geometry was adapted in order to avoid excessive stress on the sample. In both cases, the sample thickness was 2 mm.

3.4.2.2 Complex modulus test: analysis of results

As the behaviour is supposed isotropic, the complex modulus E^* was calculated from the shear complex modulus G^* (see Section 1.5.1.2) using the following equation:

$$G^* = \frac{E^*}{2 \cdot (1 + \nu^*)} \Rightarrow E^* = 3 \cdot G^* \quad (3.1)$$

where the Poisson's ratio was arbitrary assumed equal to 0.5 (incompressibility) (Pouget et al., 2010). DSR complex modulus test results were modelled with the 2S2P1D model, which parameters (see Section 1.5.2) are listed in Table 6.3 in Appendix 5. The model accurately fits experimental data. Complex modulus master curve ($T_{\text{ref}} = 15^{\circ}\text{C}$) and Cole-Cole curve are shown in Figure 3.12.

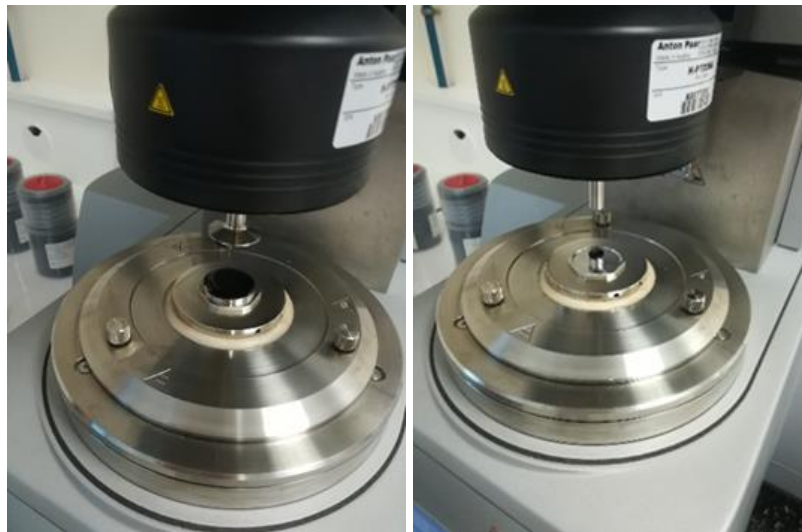


Figure 3.11 Samples used to perform the complex modulus test on the bitumen of the tack coat emulsion: (Left) 25 mm test sample; (Right) 8 mm test sample.

3 Inverse calculation of pavement response based on embedded sensors – Corbas trial section

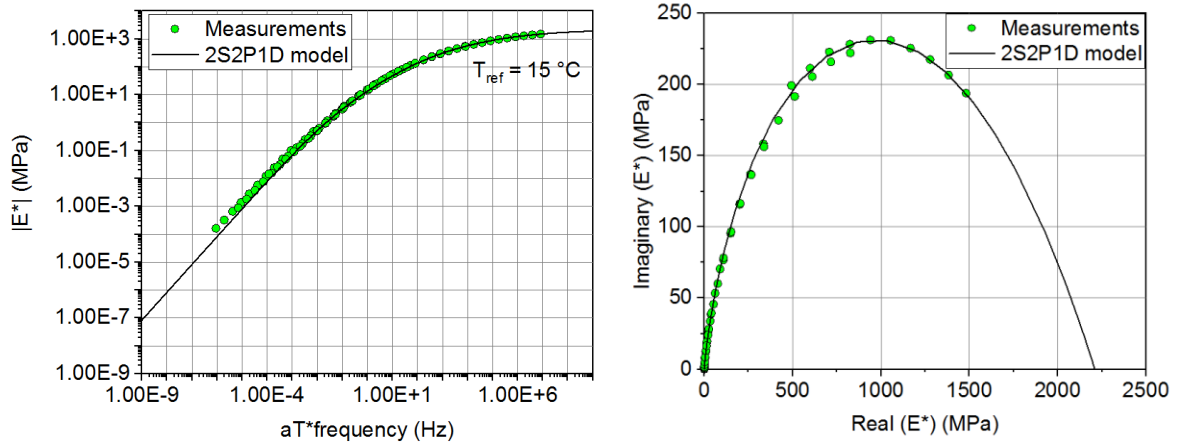


Figure 3.12 2S2P1D model fitting for bitumen 70/100 tested with DSR (from -20 °C to 70 °C and from 0.01 Hz to 10 Hz): (Left) master curve ($T_{ref} = 15\text{ °C}$), (Right) Cole-Cole diagram.

3.4.3 Asphalt mixes

The asphalt mix used for the realisation of the new wearing course in the experimental site is a BBSG 2 0/10–35/50 with the composition reported in Section 6.5.2 (Appendix 5). The mix was tested under different test modes. The Cyclic Indirect Tensile Test (CITT) and the Modal Test (MT) were chosen for the characterisation of samples cored in the field, while the Direct Tension-Compression Test (DTCT) for samples manufactured in the laboratory by reproducing the same mix used for Layer 1 in the trial section. The air void contents of the tested samples was previously determined by gamma rays according to the European Standards (AFNOR, 2021). All tests are summarised in Table 3.3 and described in details in the following sections.

Table 3.3 Summary of all tests performed on the mix BBSG 2 0/10-35/50.

Test	Size	Temperatures (°C)	Frequencies (Hz)
CITT	Disk	From -25 to 35	From 0.03 to 10
MT	Beam	17, 35, 50	-
DTCT	Cylinder	From -20 to 50	From 0.01 to 20

3.4.3.1 Cyclic Indirect Tensile Test (CITT): procedure and results

The CIT test is one of the test modes set out in the NF EN 12697-26 (AFNOR, 2018b) that enables the measurement of the modulus of small field core specimens (François Olard et al., 2006). The test was performed by using a hydraulic press MTS equipped with the thermal chamber MTS 651 (as shown in Figure 6.12 in Appendix 5). The sinusoidal load was applied

along the vertical diametric plane of the specimen (height = ≈ 50 mm, diameter = ≈ 100 mm). The cited European Standard imposes test temperatures ranging between -10 °C and 20 °C, and load frequencies in a range between 0.1 and 10 Hz. For research purposes, it was decided to try the test over a temperature range of -25 °C to 35 °C and a frequency range of 0.03 and 10 Hz. This choice led to the cores break under low temperatures (-25 °C). At this stage, being the asphalt very rigid, in order to maintain the horizontal strain in the specimen centre in a range between 25 $\mu\epsilon$ and 50 $\mu\epsilon$, a higher load was required. The application of a high load on a small area (loading strips) might cause a very high stress that led to rupture (Figure 3.13). For this reason, in order to complete all the desired measurements, it was decided to use a first sample for the low temperatures range and another sample (of the same layer) for the high temperature range. The obtained results are modelled with 2S2P1D which parameters are summarised in Table 6.5 (Appendix 5). The model accurately fits the measurements. Complex modulus master curve ($T_{ref} = 15$ °C) and the Cole–Cole curve are reported in Figure 3.14.

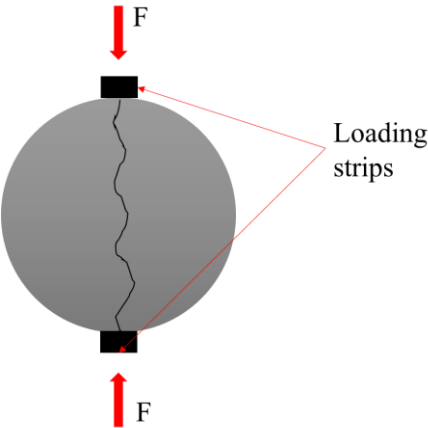


Figure 3.13 Cyclic indirect tensile test on BBSG 2 0/10-35/50. Loading application and failure mechanism.

3 Inverse calculation of pavement response based on embedded sensors – Corbas trial section

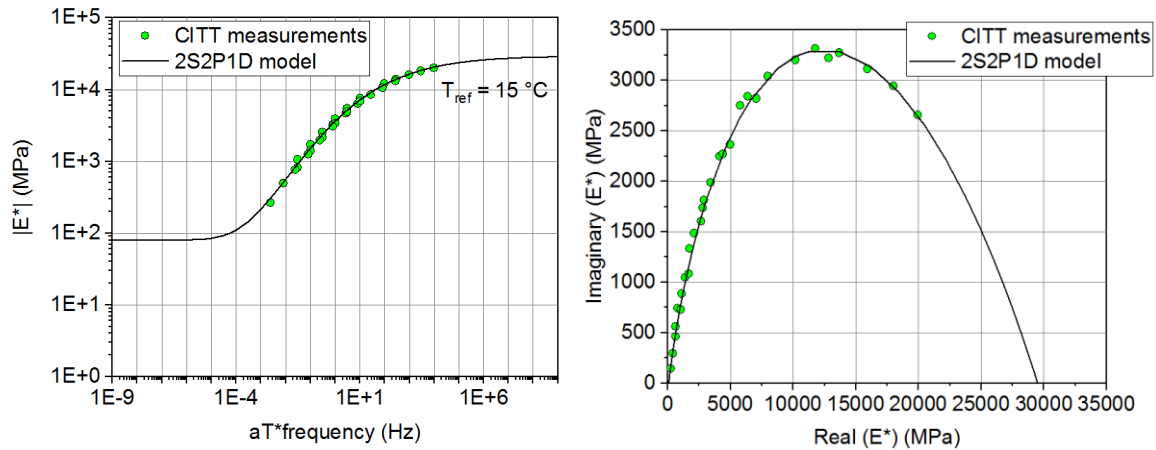


Figure 3.14 2S2P1D model fitting for BBSG 2 0/10-35/50 tested under CITT test (from -25 °C to 30 °C and from 0.031 Hz to 10 Hz): (Left) master curve ($T_{ref} = 15 \text{ }^{\circ}\text{C}$), (Right) Cole-Cole diagram.

3.4.3.2 Modal Test (MT): procedure and results

The Modal Test is a novel non-destructive laboratory test method to characterise asphalt concrete (Gudmarsson, 2014). This approach allows the determination of the viscoelastic properties of asphalt concrete through the resonance frequencies of a specimen in free boundary conditions. The resonance frequencies are determined by measuring the vibrations generated by an excitation. As shown in Figure 3.15, the load is applied with an automated impact hammer (PCB model 086E80) and the vibrations are measured with an accelerometer (PCB model 35B10) screwed on a mounting base glued to the specimen. Both are connected to a signal conditioner (PCB model 480B21) for preparation and eventual amplification of the signal. The signal conditioner is connected to the data acquisition device (NI USB-6251 M Series) for analog to digital conversion of the signals, and this latter is connected to a laptop through a USB cable where a toolbox in MATLAB® is used to record and process the measurements.

The frequency response functions (FRFs) are determined with the following equation:

$$H(f) = \frac{Y(f) \cdot X^*(f)}{X(f) \cdot X^*(f)} \quad (3.2)$$

Where $H(f)$ is the frequency response function, $Y(f)$ is the measured acceleration, $X(f)$ is the measured applied force and $X^*(f)$ is the complex conjugate of the applied force (Gudmarsson, 2014). A finite element method is then applied in order to determine iteratively the properties of the specimen over a wide frequency range by fitting theoretical FRFs with measured FRFs (Gudmarsson et al., 2012). The 2S2P1D model is implemented in the finite element calculations.

Beam-shaped specimens sawn out from the cores extracted in the field (dimensions 35*35*210 mm) were excited in the longitudinal mode of vibration (as shown in Figure 3.15). Other studies demonstrate that the best results in terms of test repeatability and reproducibility are obtained with this configuration (Carret, 2018). The test was performed at three temperatures (as suggested in (Carret, 2018)): 17 °C, 35 °C and 50 °C. According to (Gudmarsson, 2014) and (Carret, 2018) the strain level attained during the modal test are of around 10^{-7} (below) and this is expected to lead to slightly higher values of $|E^*|$. The results obtained for Layer 1, modelled with 2S2P1D model, are shown in Figure 3.16 (master curve and Cole-Cole curve). The 2S2P1D parameters are reported in Table 6.5 (Appendix 5).

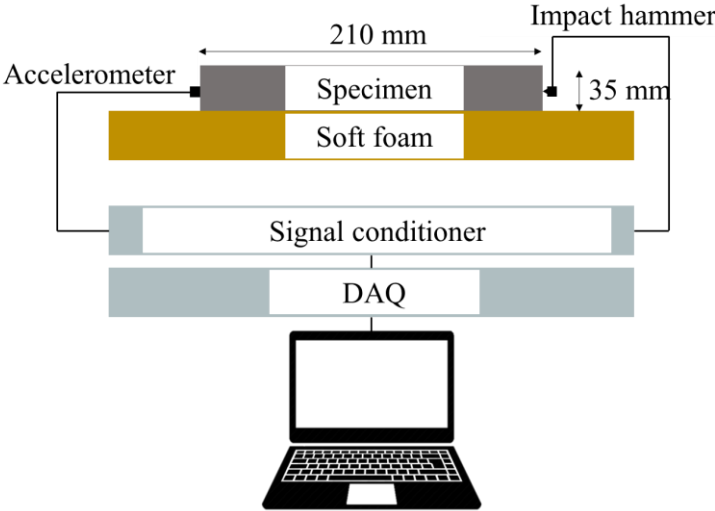


Figure 3.15 Equipment and test set-up for the modal test: the impact hammer and the accelerometer are connected to a signal conditioner, which is connected to a data acquisition device, which is connected to a laptop.

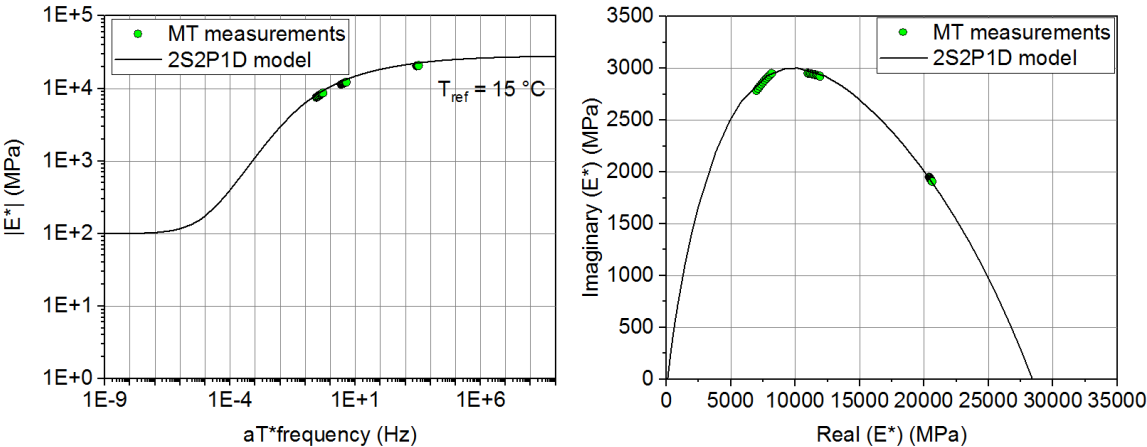


Figure 3.16 2S2P1D model fitting for BBSG 2 0/10-35/50 tested under modal test (at 17 °C, 35 °C and 50 °C): (Left) master curve ($T_{ref} = 15 \text{ }^\circ\text{C}$), (Right) Cole-Cole diagram.

3.4.3.3 Direct Tension-Compression Test (DTCT): procedure and results

Complex modulus test in tension-compression mode was carried out on cylindrical specimens manufactured in the laboratory by reproducing the same mix used for Layer 1 (BBSG 2 0/10-35/50) in the experimental site. Samples (diameter = 64 mm, height = 140 mm) were cored from slabs (400*600*150 mm) compacted using a French wheel compactor according to the NF EN 12697-26 (AFNOR, 2018b). Two coring directions were chosen, the vertical direction (II) and the horizontal direction (I) as indicated in Figure 3.17.

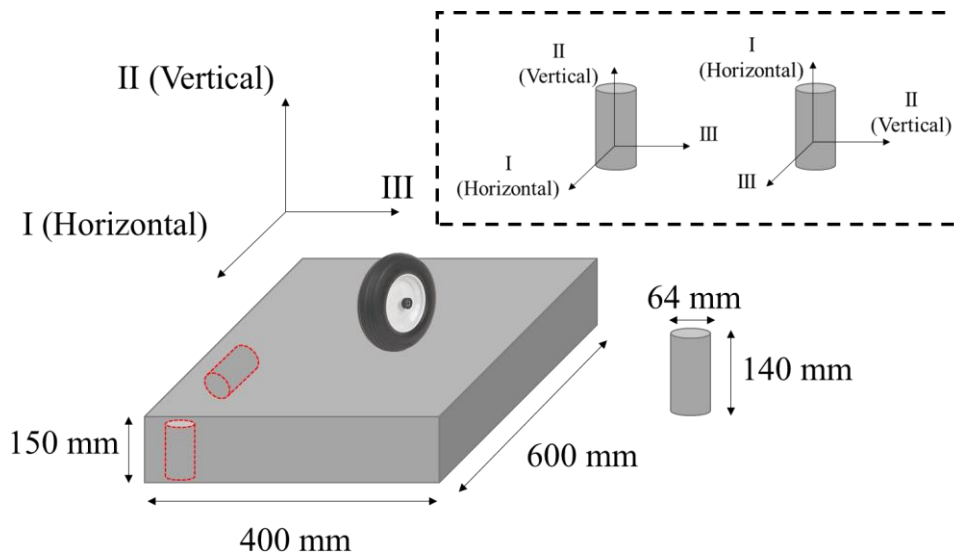


Figure 3.17 Slab are compacted using a French wheel compactor. Samples are cored in two directions, the vertical direction (II) and the horizontal direction (I).

Tests were performed with a MTS hydraulic press (same apparatus as in Section 3.4.3.1) by applying cyclic sinusoidal loading in strain-controlled mode. The maximum strain amplitude was $25 \mu\epsilon$ in order to stay in the linear domain (see Section 1.5). The axial stress was obtained from a load cell, while the considered axial strain value was the average of three strain measured from the three extensometers placed at 120° distance (Figure 3.18). The results obtained for the two directions are well fitted by the 2S2P1D model and are presented in Figure 3.19 (master curve and Cole-Cole diagram). The 2S2P1D parameters are summarised in Table 6.5 (Appendix 5). The measurements look consistent with previous studies concerning the anisotropy of bituminous mixes (Clec'h, 2010). This justifies, in first approximation, the assumption of isotropic behaviour of in situ materials taken into account in the calculations. Even though a bigger discrepancy was expected with respect to the parameter E_0 of the 2S2P1D model, the obtained result can be justified by the lower air

voids content of the cylinder cored in direction II (6.8%) with respect to the one cored in the direction I (7.5 %).

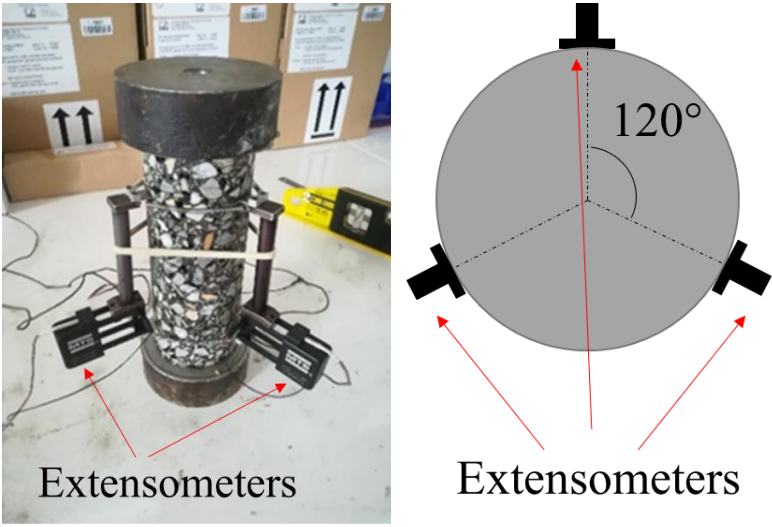


Figure 3.18 (Left) instrumented sample before the test; (Right) visualization of the three extensometers used to measure the axial deformation.

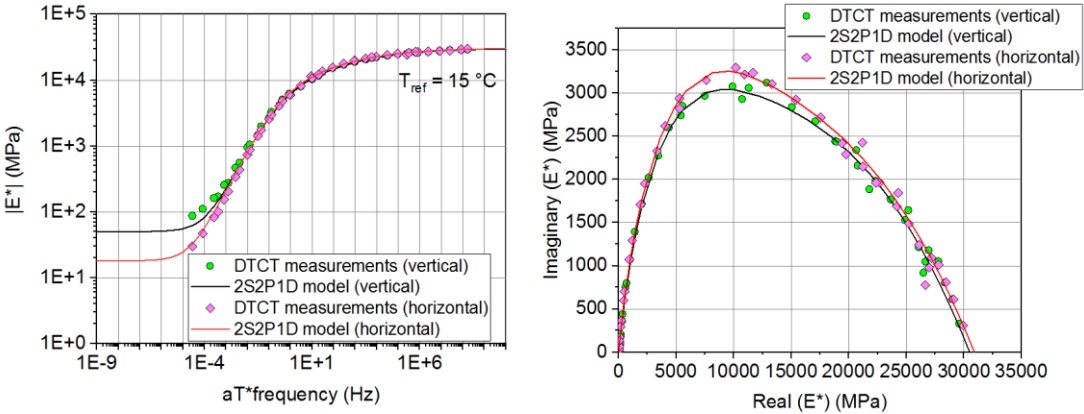


Figure 3.19 2S2P1D model fitting for BBSG 2 0/10-35/50 tested under direct tension-compression test (from -20 °C to 50 °C and from 0.01 Hz to 20 Hz): (Left) master curves ($T_{ref} = 15\text{ °C}$), (Right) Cole-Cole diagrams.

3.4.3.4 Comparison of results and comments

A superposition of the fitted models for all the tests described above is shown in Figure 3.20 pointing out the values at 15 °C and 10 Hz for Layer 1. The comparison highlights a good agreement between the DTCT and the MT, while the curve related to the CITT differs from the others and shows an underestimation of the modulus at 15 °C and 10 Hz. A slight higher modulus at 15 °C and 10 Hz evaluated from MT was expected with respect to the modulus evaluated from DTCT (see Section 3.4.3.2). The obtained result can be justified by the higher

3 Inverse calculation of pavement response based on embedded sensors – Corbas trial section

air voids content of the sample cored in the field (13.1 %) with respect to the ones manufactured in the lab (7.5 % and 6.8 %). This reinforces the good consistency of the modal test on beam-shaped specimens in predicting the mechanical behaviour of the mixes. As regards the characterisation of the other layers, tests are conducted on specimens from the field only with the procedure summarised in Table 3.4 and the results are reported in Section 6.5.2 in Appendix 5.

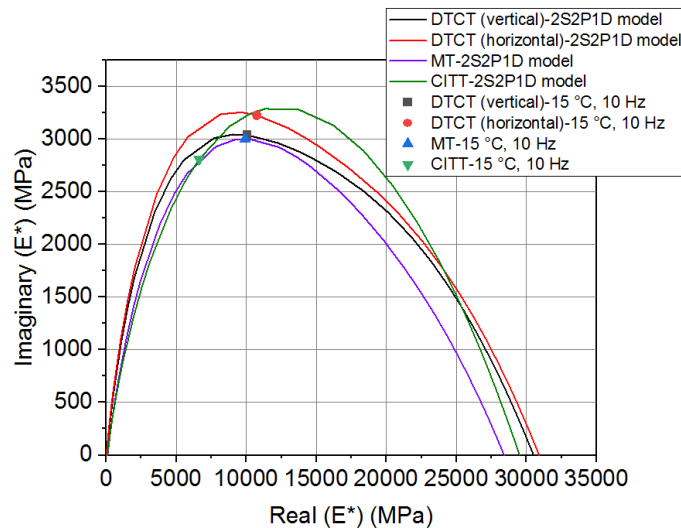


Figure 3.20 Superposition of the 2S2P1D models fitted for the cyclic indirect tensile test, the modal test, and the direct tension-compression test performed on the BBSG 2 0/10-35/50 (Layer 1 in the experimental site).

Table 3.4 Summary of all tests performed on the road structure of the experimental site.

	Material	Field (F) / Lab (L)	CITT	MT	DTCT
Layer 1	BBSG 2 0/10-35/50	F, L	X	X	X
Layer 3	Unknown	F	X		
Layer 5	Unknown	F		X	

3.5 Measurement campaign: results

The details concerning all the truck passages, the theoretical loading configuration, as well as the measured surface temperature (see Section 3.2.4) the actual truck trajectory (determined as indicated in Section 3.2.4.2) and truck speed are reported in Table 6.8 in Appendix 6. In particular knowing the geometry of the passing truck (see Section 3.2.4.1),

the actual speed can be calculated with the time interval of the two peaks caused by two axles as indicated in (L. Wang et al., 2012):

$$v = \frac{d_{axles}}{t_2 - t_1} \tag{3.3}$$

Where v is the actual speed in, d_{axles} is the distance between the first and the second axle of the truck, and t_2 and t_1 are respectively the time coordinates of the second and first peaks (see Figure 3.21).

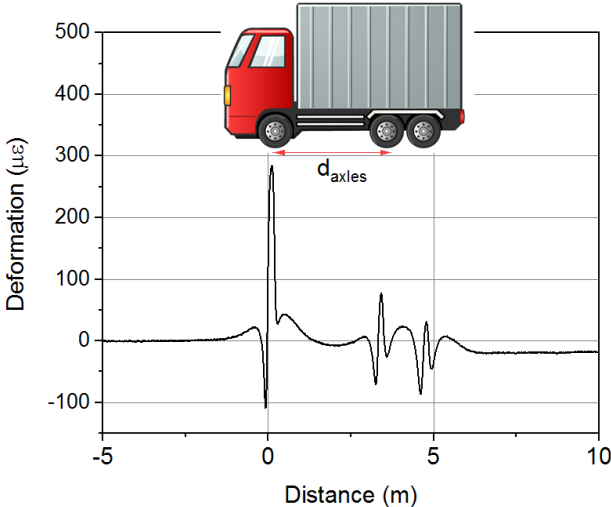


Figure 3.21 Example of a signal collected during the campaign of measurements. Knowing the geometry of the passing truck, the actual speed can be determined with the time interval of the two peaks caused by two axles. The abscissa $x = 0$ m identifies the passage of the front axle.

For each truck passage, the pavement response was recorded and stored in the cloud to be analysed afterwards. The calibration factor provided by the manufacturer are used to convert the measured voltage into strain. The strain signals are expressed as a function of time. In order to make a comparison between passages at different truck speeds, a time-to-distance transformation of the x-axis was made. Knowing the geometry of the truck axles and the time lapse between the axles passages (identified by peaks), we can calculate the actual speed and multiply it by the time for the time-to-distance conversion. Finally the abscissa $x = 0$ m identifies the passage of the front axle.

The methodology used to analyse and present sensor data is outlined in Figure 3.22. Each strain signal is characterised by three peaks (extension or compression) corresponding to the three axles of the truck. Positive values correspond to strain in extension. For each peak, the maximum horizontal deformation ($\epsilon_{max,1}$, $\epsilon_{max,2}$, and $\epsilon_{max,3}$) is derived as shown in Figure 3.22-top left. All measurements of the same sensor recorded at the same main truck speed

3 Inverse calculation of pavement response based on embedded sensors – Corbas trial section

and trajectory are then grouped in a graph as shown in Figure 3.22-top right. The nomenclature used to identify the different truck passages is the same used in Table 6.8 in Appendix 6. In order to better visualise the measurements variability in terms of maximum horizontal deformation for the same theoretical loading configuration, ϵ_{\max} is grouped by truck passage and by axle in a histogram as shown in Figure 3.22-bottom. In addition the coefficients of variation (CV) of $\epsilon_{\max,1}$, $\epsilon_{\max,2}$, and $\epsilon_{\max,3}$ are calculated, as shown in Figure 3.22-bottom.

Table 3.5 reports some of the measurements recorded the 17th July when the passing truck moved at 10 km/h on the trajectory T0, while Table 3.6 reports the some of the measurements recorded the 18th July when the passing truck moved at 10 km/h on the trajectory T1. The graphs in the left column group together the signals for each sensor, while in the histograms in the right column data are grouped by axle and by passage. All the other recordings are reported in Table 6.9 and Table 6.10 in Appendix 6.

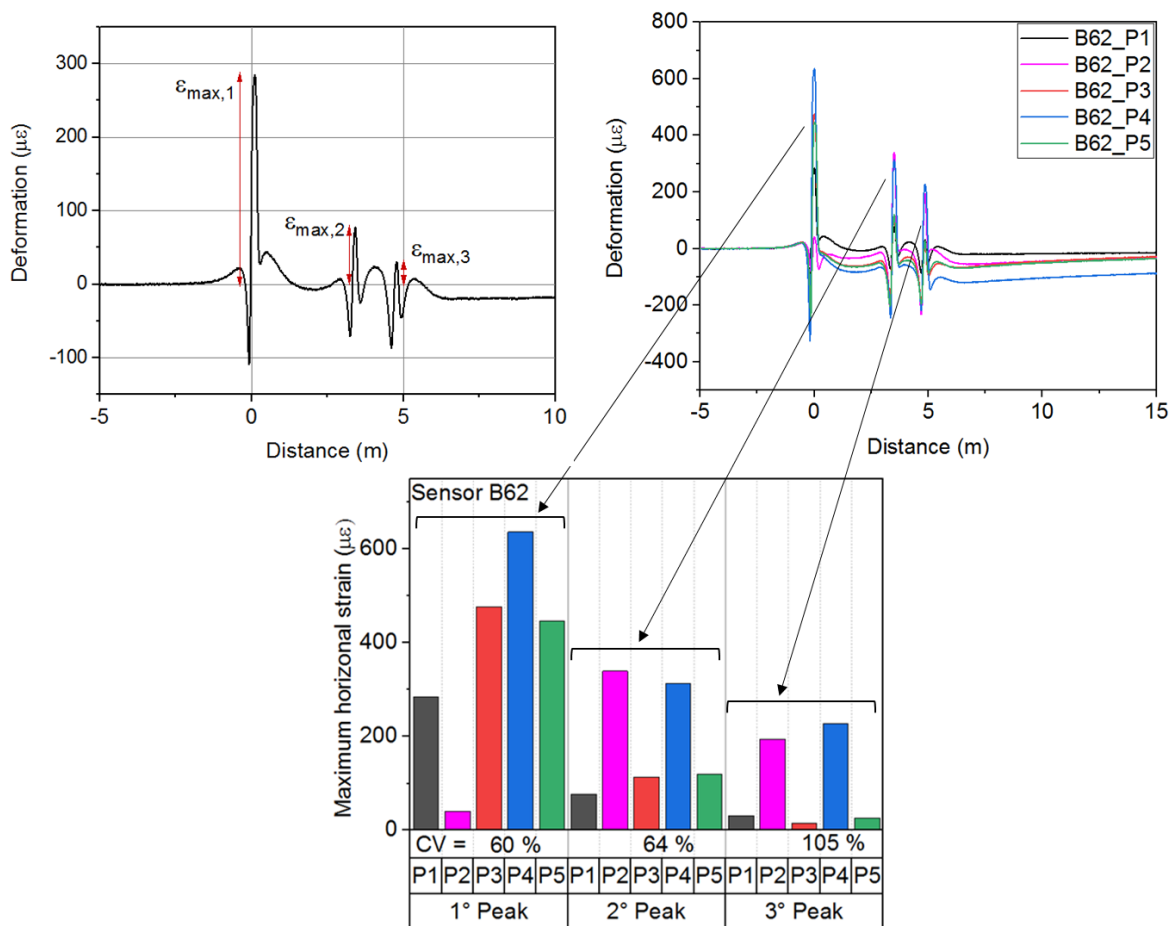
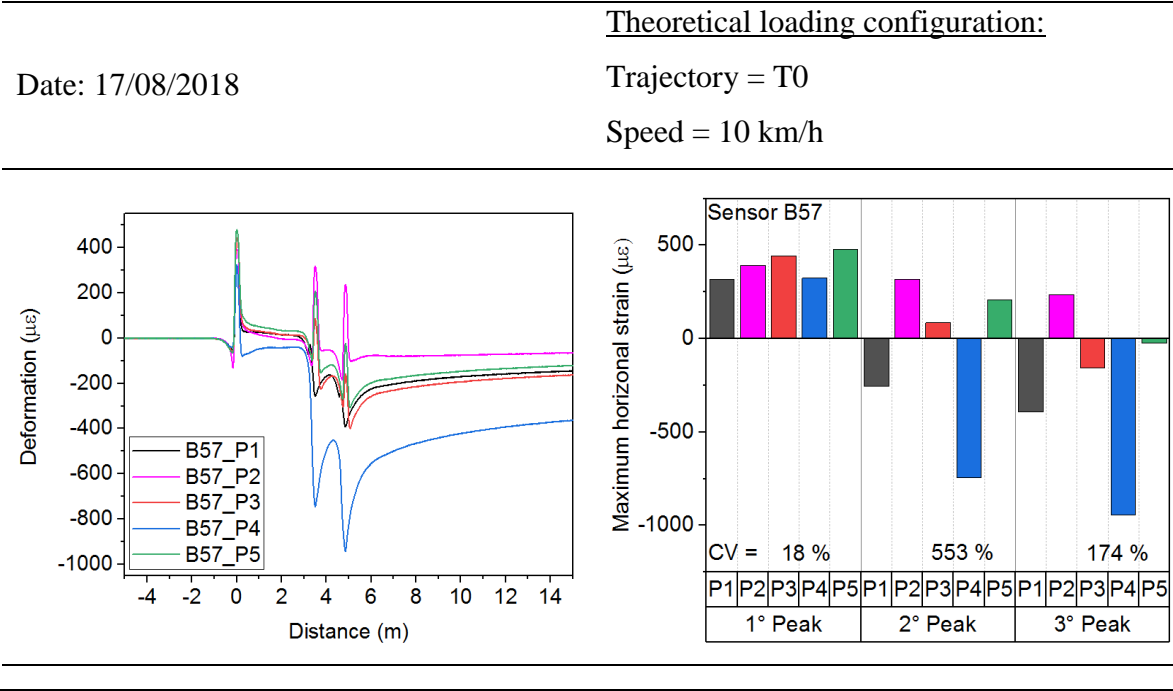


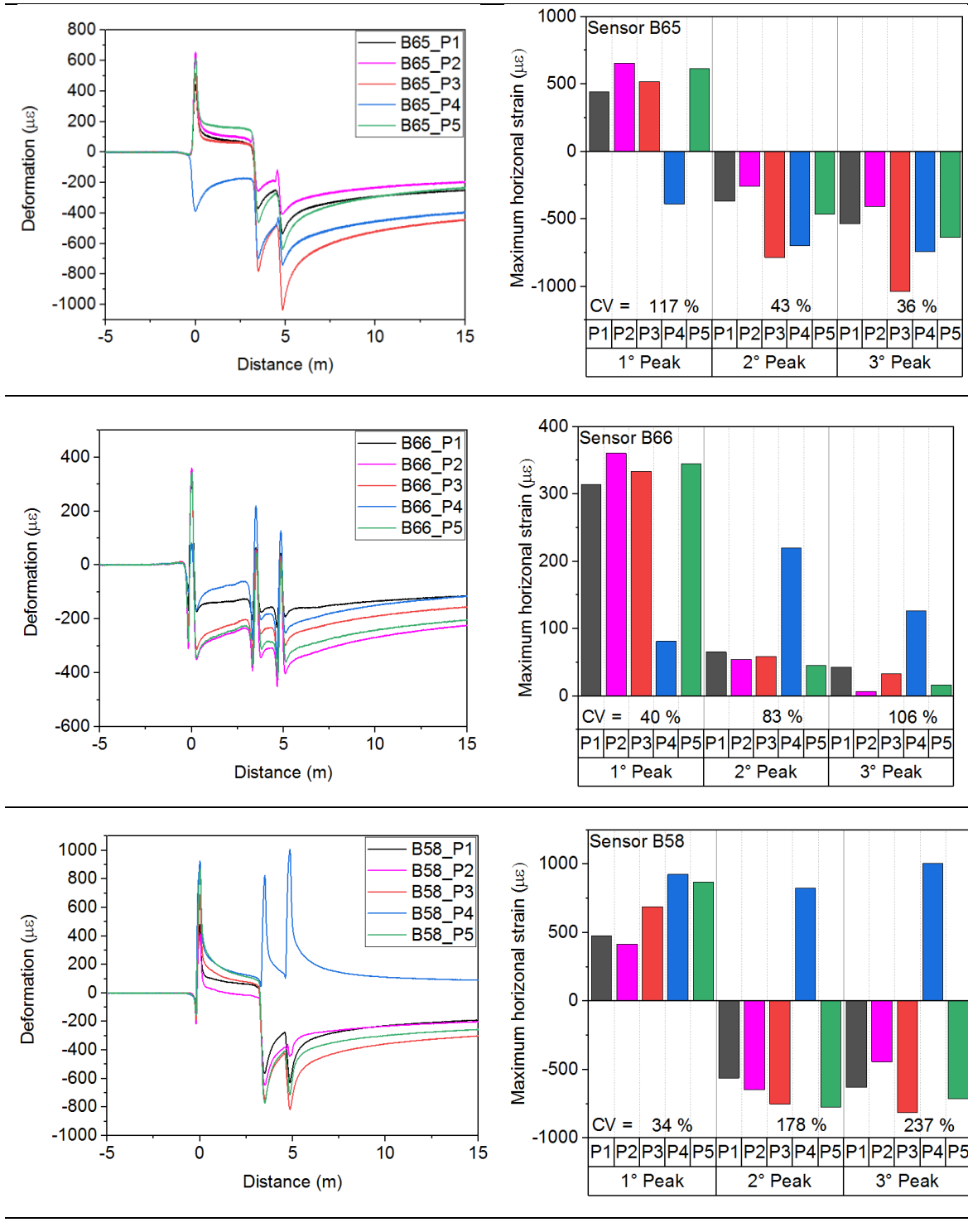
Figure 3.22 Methodology used to analyse sensor data. (Top left) Definition of the maximum longitudinal strain ϵ_{\max} for each peak corresponding to the truck axles. (Top right) Grouping of all measurements (P1 to P5) of the same sensor (B62) recorded at the same main truck speed and trajectory. (Bottom) Visualization of ϵ_{\max} by passage (P1 to P5) and by axle and calculation of the coefficients of variation (CV).

Interestingly the experimental results clearly show the high sensitivity of the strain to the transverse position of the truck, even when this latter varies of few centimetres (see Table 6.8). This phenomenon can be better visualised by consulting the histograms reported in the right column of Table 3.5 and Table 3.6. Let us remark that not only the magnitude of the peaks is impacted by the trajectory, but also the shape of the signals. For instance, compared to the other passages, passage P2 (Table 3.5) features inverted strains (extension instead of contraction and vice versa) on sensor B64 (transverse), and different structure of the first peak on sensors B62 (longitudinal). The same considerations can be made for passage P4 on sensors B57 and B58 (45° direction), B65 and B64 (transverse). This suggest that, due to the linear viscoelastic behaviour of bituminous materials, at high temperatures the pavement response under moving loads is more localised, thus it can variate significantly with the transverse position of the passing vehicle. This is confirmed by the measurements reported in Table 3.6 when the truck follows the T1 trajectory at 10 km/h, still the magnitude of the peaks and the signal shapes are impacted.

Table 3.5 Deformations measured on the experimental site during the campaign of measurements with a truck: surface temperature from 50 °C to 54 °C, $\Delta D_y - \Delta D_{y,ref} = 0$ cm (trajectory T0), speed = 10 km/h. The signals are grouped per sensors. Positive values correspond to extension.



3 Inverse calculation of pavement response based on embedded sensors – Corbas trial section



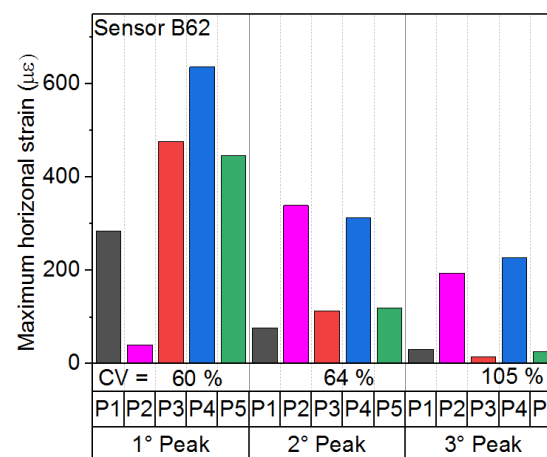
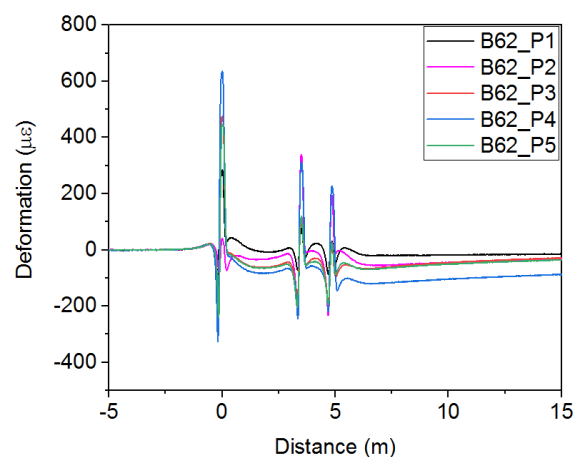
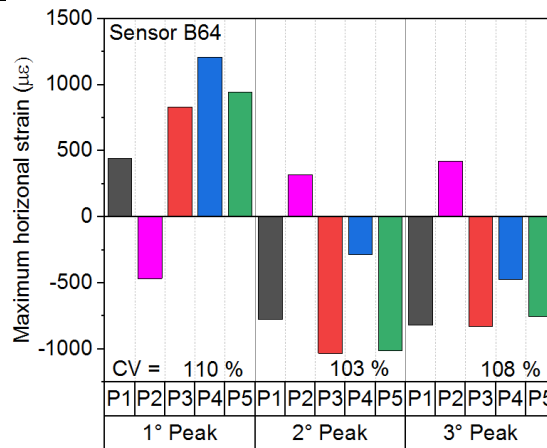
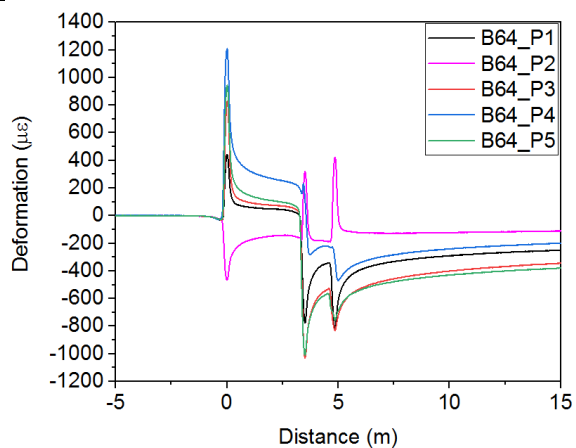


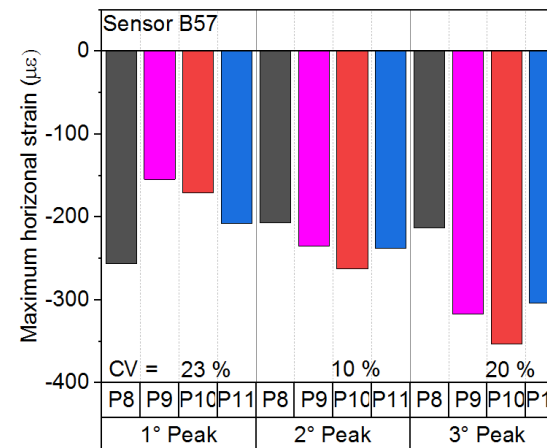
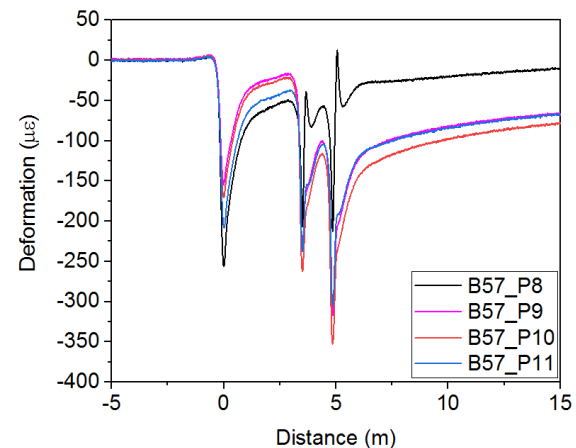
Table 3.6 Deformations measured on the experimental site during the campaign of measurements with a truck: surface temperature = 50 °C, $\Delta D_y - \Delta D_{y,ref} = 30$ cm (trajectory T1), speed = 10 km/h. The signals are grouped per sensors. Positive values correspond to extension.

Theoretical loading configuration:

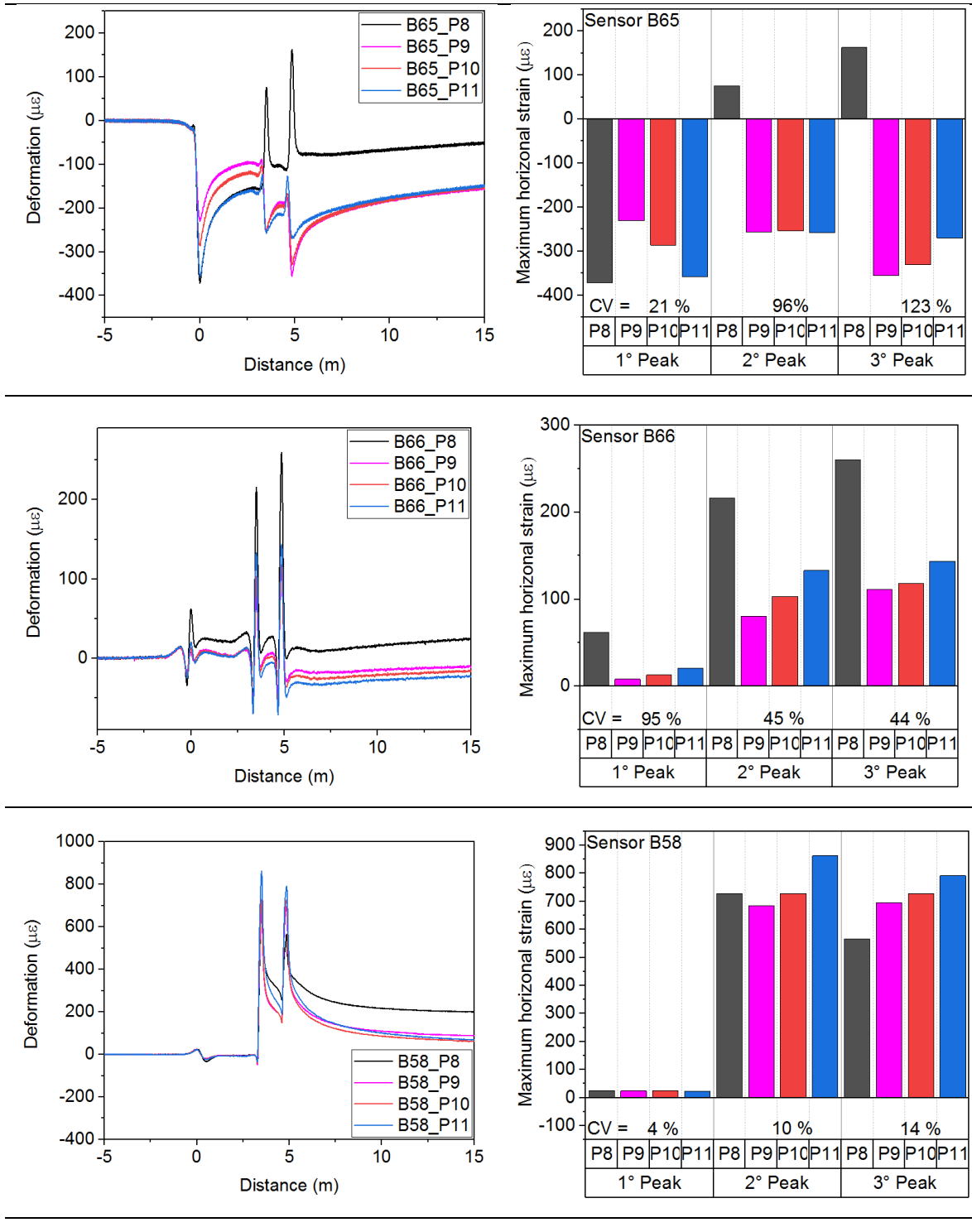
Date: 18/08/2018

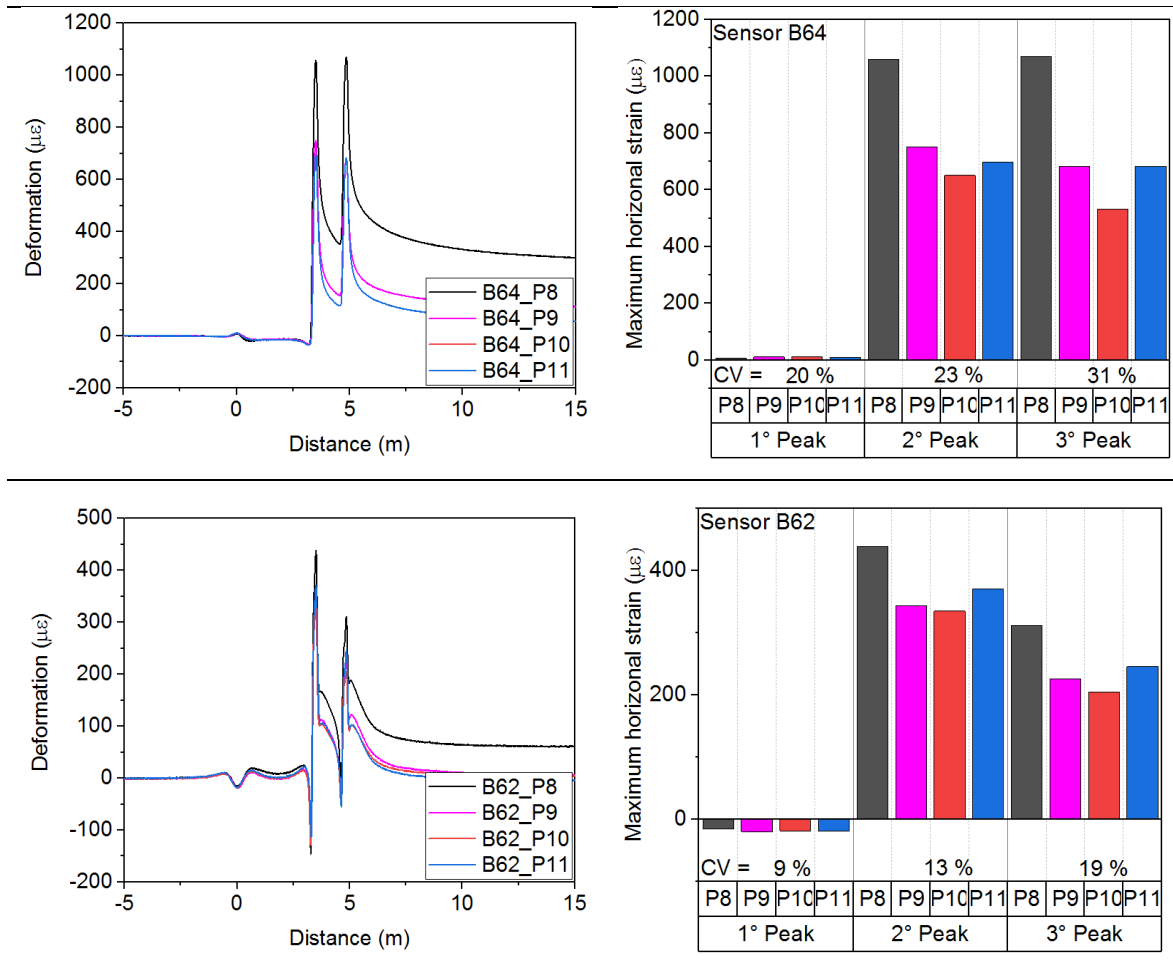
Trajectory = T1

Speed = 10 km/h



3 Inverse calculation of pavement response based on embedded sensors – Corbas trial section





Interestingly, despite the high temperatures, small speed variations seem to have negligible impact on the magnitude of the peak, as shown in Figure 3.23. To distinguish from the effect of the varying trajectories, this graph shows the average of all passages at roughly the same speed and temperature for a given sensor with the same "main" trajectory.

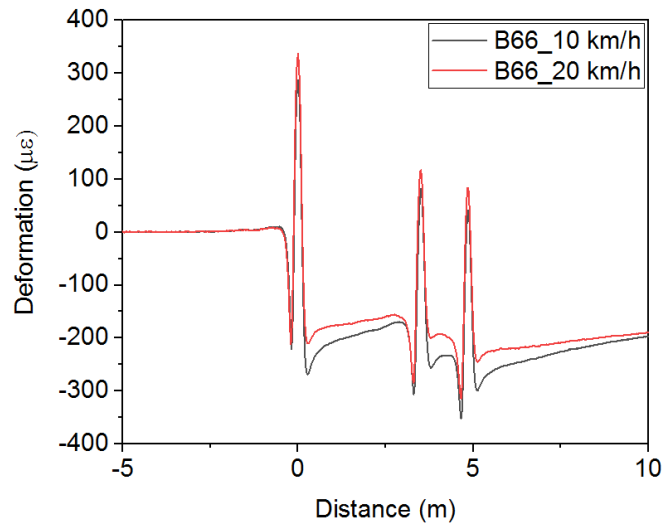


Figure 3.23 Average of strain measurements recorded for sensor B66 (longitudinal) on 17th July. The black curve is the average of passages from P1 to P5, while the red curve is the average of passages P6 and P7.

As expected, as shown in Figure 3.24, the strain as well as the viscous effects are drastically smaller when temperature decreases. As it can be observed, the order of magnitude of temperature effect on the signal shape and the magnitude of the peaks is almost the same than the effect of scattering transverse position of the truck.

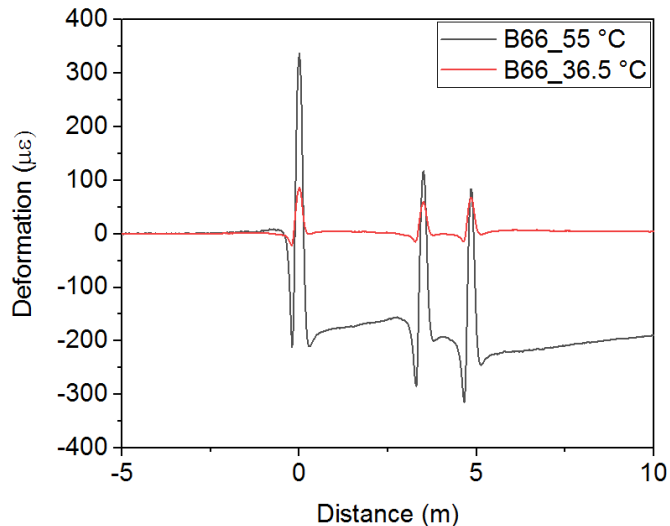


Figure 3.24 Average of strain measurements recorded for sensor B66 (longitudinal) on 17th July and 18th July. The black curve is the average of passages P6 and P7, while the red curve is the average of passages from P12 to P17.

3.6 Modelling in Viscoroute©: results

We compared three scenarios whose parameters are summarised in Table 3.7: linear elastic structure with fully bonded interfaces, viscoelastic structure with fully bonded interfaces, and viscoelastic structure with viscoelastic interfaces modelled as 2-mm thick thin layers

(Duong, 2017). The nomenclature of the layers in Table 3.7 follows that shown in Figure 3.10 and Table 3.2. In all the models Layer 2 and Layer 4 of the cores were considered part of the underlying layer, and Layer 3 was modelled as an elastic layer because of the impossibility to have reliable test results over an adequate range of temperatures and frequencies (see Section 6.5.2). The last two layers in Table 3.7 are assumed to be sandy gravel and subgrade as this is the most common French road structures. For the elastic calculations the pavement layer moduli are determined from the test results presented in Section 3.3 at the chosen temperature and loading frequency. For the viscoelastic calculations, the parameters are determined by fitting the experimental test results with the 2S2P1D model. In fact, with respect to the mixes the Huet-Sayegh and the 2S2P1D models are analogous. With regard to the interfaces, since the Huet-Sayegh model does not take into account the pure viscous behaviour of the bitumen at high temperature, the parameter E_0 has to be set different from zero. Due to the lack of information, Interface 2 is considered similar to Interface 1. All measurements recorded the 17th July from sensors B62 (longitudinal) and B64 (transverse) in the first loading configuration (T0 trajectory and 10 km/h speed) are modelled. The calculation is performed under wheels load, moving horizontally along the x-axis at the actual truck speed. The wheel-to-pavement contact area is considered as elliptical. An example of a loading configuration entered in Viscoroute© is shown in Figure 3.25. Concerning the temperature evolution, a decrease by 10°C is assumed between the surface and the bottom of the wearing course; the layers below are hypothesised to be at 25°C. An example of the pavement structure entered in Viscoroute© is reported in Table 3.8.

Table 3.7 Characteristic of the structure implemented in Viscoroute©.

	Name	Material	Linear elastic model, fully bonded interfaces	Viscoelastic model, fully bonded interfaces	Viscoelastic model, viscoelastic interfaces
1	Layer 1	BBSG 2 0/10-35/50	Elastic	Viscoelastic	Viscoelastic
2	Interface 1	Emulsion (70/100)	None	None	Viscoelastic
3	Layer 3	Unknown	Elastic	Elastic	Elastic
4	Interface 2	Unknown	None	None	Viscoelastic
5	Layer 5	Unknown	Elastic	Viscoelastic	Viscoelastic

3 Inverse calculation of pavement response based on embedded sensors – Corbas trial section

6	Sandy gravel	H_p	Elastic	Elastic	Elastic
7	Subgrade	H_p	Elastic	Elastic	Elastic

Vitesse de charge (m/s) Nombre de charges

	F _x (N)	F _y (N)	F _z (N)	Type de charge	a (m)	b (m)	x (m)	y (m)
1	0.000	0.000	32700.000	Ellipse	0.150	0.125	0.000	-1.020
2	0.000	0.000	26900.000	Ellipse	0.150	0.125	3.500	-0.750
3	0.000	0.000	26900.000	Ellipse	0.175	0.125	3.500	-1.100
4	0.000	0.000	28650.000	Ellipse	0.175	0.125	4.850	-0.750
5	0.000	0.000	28650.000	Ellipse	0.175	0.125	4.850	-1.100
6	0.000	0.000	32700.000	Ellipse	0.175	0.125	0.000	1.020
7	0.000	0.000	26900.000	Ellipse	0.175	0.125	3.500	0.750
8	0.000	0.000	26900.000	Ellipse	0.175	0.125	3.500	1.100
9	0.000	0.000	28650.000	Ellipse	0.175	0.125	4.850	0.750
10	0.000	0.000	28650.000	Ellipse	0.175	0.125	4.850	1.100

Figure 3.25 Example of a loading configuration entered in Viscoroute©. The wheels load moves horizontally along the x-axis at the actual truck speed. The wheel-to-pavement contact area is considered as elliptical.

Table 3.8 Example of the pavement layers parameters used for the viscoelastic calculation in Viscoroute©.

Name	Thickness (mm)	E ₀₀ (MPa)	ν	E ₀ (MPa)	k	h	δ	A ₀	A ₁	A ₂
1 Layer 1	0.06	30500	0.35	50	0.213	0.21	2.2	3.291	-0.405	0.0019
2 Interface 1	0.002	2250	0.50	2.2	0.22	0.22	2.1	-8.298	-0.371	0.0018
3 Layer 3	0.07	4000	0.35	-	-	-	-	-	-	-
4 Interface 2	0.002	2250	0.50	2.2	0.22	0.22	2.1	-8.298	-0.371	0.0018
5 Layer 5	0.06	10000	0.35	100	0.28	0.35	1.9	1.3	-0.265	0.0018
6 Sandy gravel	0.5	100	0.20	-	-	-	-	-	-	-
7 Subgrade	∞	100000	0.20	-	-	-	-	-	-	-

The elastic model with fully bonded interfaces and the viscoelastic model with fully bonded interfaces give similar results. Both the calculations provide a not realistic strain profile. It emerged that the contribution of the interfaces has a significant impact in this sense. In fact, the viscoelastic calculation with viscoelastic interfaces allows a better prediction not only of

the peak values (as indicated in similar analyses carried out in (Duong, 2017)) but also of the strain signal shape (in terms of tension-compression sequence, see Table 3.9). At the very high temperatures experienced during the measurement campaign the hypotheses of linear elastic behaviour and fully bonded interfaces are not realistic and lead to a wrong estimation of the strain profile, as shown for the longitudinal and transverse sensors presented in Table 3.9. The obtained results rather show that sliding is occurring at the interface and that its mechanical behaviour depends on the temperature and loading frequency. These results are important and need to be taken into account to define a framework for sensor data interpretation.

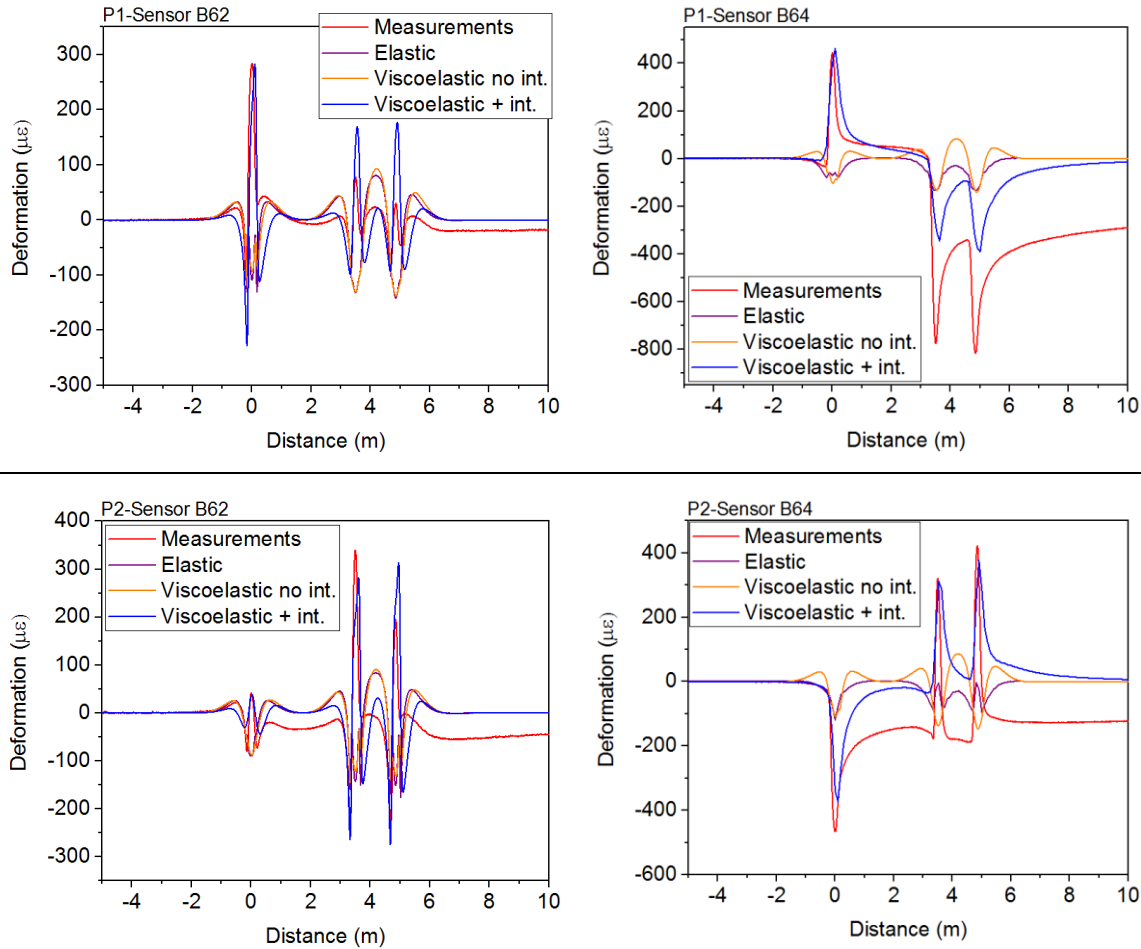
Table 3.9 Comparison between experimental and model data based on pavement response in terms of horizontal (longitudinal and transverse) strain. Red curves are measured strains. Purple curves are results obtained from elastic model with fully bonded interfaces. Orange curves are results obtained from viscoelastic model with fully bonded interfaces. Blue curves are results obtained from viscoelastic model with viscoelastic interfaces.

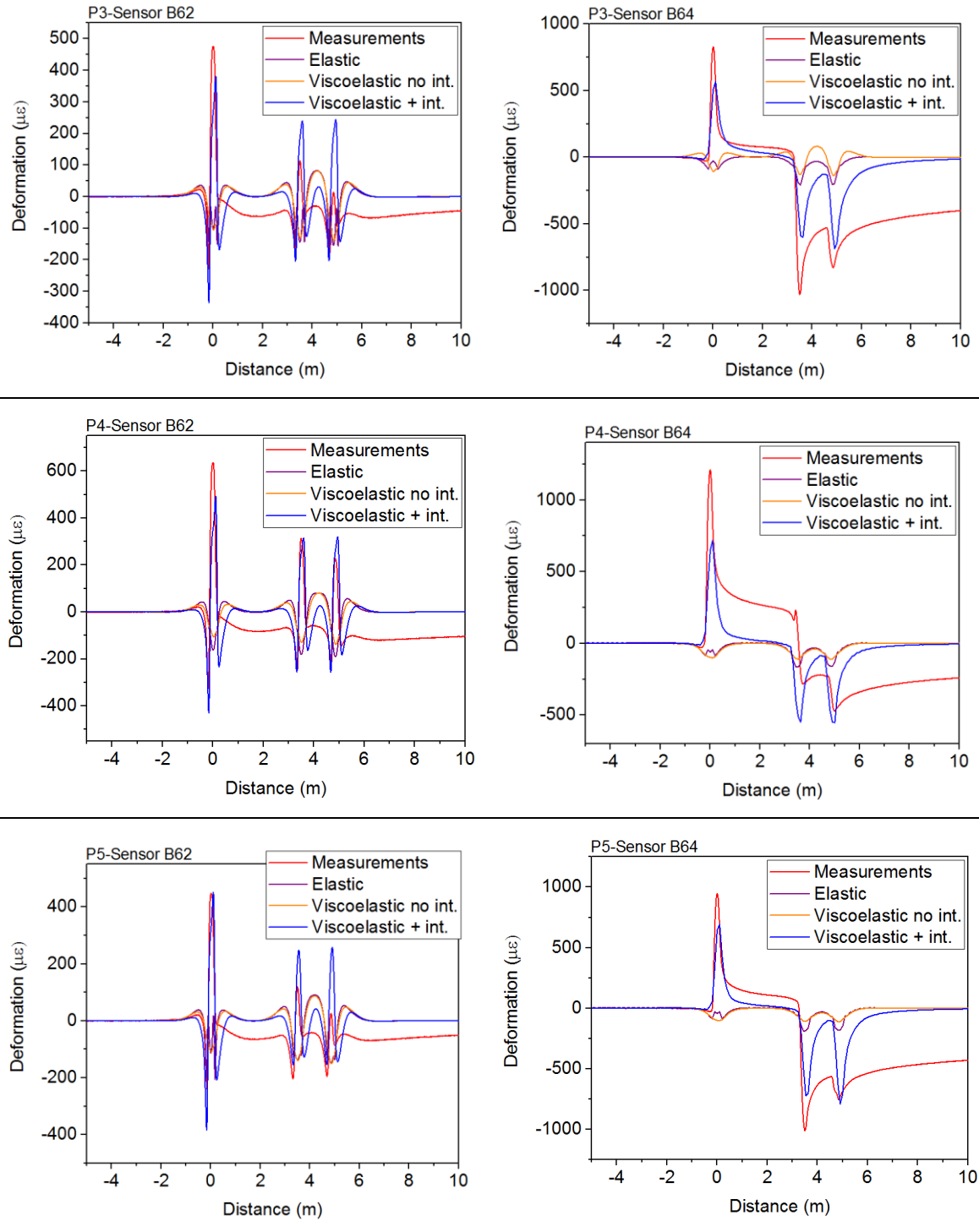
Theoretical loading configuration:

Date: 17/08/2018

Trajectory = T0

Speed = 10 km/h





3.7 Conclusions

In this chapter, we explore further the use of embedded strain sensors for health monitoring of road pavement. We present the instrumentation of an existing road on an industrial site of Eiffage Route located in Corbas (France). The trial section was instrumented with six asphalt strain gauges provided by CTL group and the Altaroad's solution.

We present our methodology for the assessment of the structure composition, the mechanical conditions of in-situ materials, and the pavement response. A coring campaign was carried out in order to investigate the road pavement stratification, followed by lab tests for the assessment of materials mechanical behaviour. A truck with a known load was employed for the measurement sessions. Passages were performed at two speeds (10 km/h and 20 km/h) and two trajectories (called in the text T0 and T1). Three scenarios were modelled by using the Viscoroute© software: linear elastic model with fully bonded interfaces, viscoelastic model with fully bonded interfaces, and viscoelastic model with viscoelastic interfaces. The models were built by using the results of the laboratory characterization of the different layers.

The analyses of strain profiles recorded by ASGs during the truck passages showed the sensitivity of sensor measurements to temperature, truck speed, and truck transverse position. For structural monitoring purposes the assessment of these parameters as well as the structure composition is fundamental. In fact, it emerged that at high temperatures, due to the amplification of viscous effects, the road pavement response to a passing vehicle is more localised. This results in a high sensitivity of the strain to scattering transverse positions of the truck, even when this latter varies of few centimetres. Sometimes this is of the same order of magnitude than temperature effect.

The numerical study pointed out that at high temperatures a viscoelastic model of the road pavement with viscoelastic interfaces allows a better prediction of strain profiles. In addition, the hypothesis of fully bonded interfaces is not realistic and leads to a wrong prediction of the pavement response under moving loads.

Important results were obtained despite the complexity of the road structure. They point towards the importance of establishing a framework for sensor data interpretation that takes into account the influence of loading parameters (truck weight, truck speed, and track trajectory) and temperature on pavement response. Concerning the measurements sensitivity to load position, the use of a sensor network with higher sensor density in the transverse direction (with respect to traffic direction) could be the optimal solution to account for scattering load transverse positions.

In this sense, the preliminary results obtained from the Altaroad's InTRACK solution seemed very promising. In fact the system design allows the integration of a large number of sensors (both strain and temperature sensors) over the width of a lane. In addition, it responded well to the installation procedures and showed good bonding at the interfaces with old and new

3 Inverse calculation of pavement response based on embedded sensors – Corbas trial section

asphalt layers. These reasons motivated the study presented in the following chapter aimed at improving the device by exploiting the properties of carbon nanomaterials.

4 DEVELOPMENT AND DEPLOYMENT OF AN EMBEDDABLE NANO-CARBON BASED STRAIN TECHNOLOGY

4.1 Introduction

In the previous chapters, we proved how embedded sensing technologies can be used to foreshadow future crack/distress manifestation as well as to inverse analyse pavement mechanical conditions. Hence, strain and temperature measurements can provide valuable information for the implementation of advanced management systems tailored to respond to in-situ requirements. In this regard, technological development is leading to new possibilities. Indeed the improvement of existing technologies as well as the development of more advanced devices is essential to achieve better performances terms of connectivity, efficiency and durability of the road network. The challenges that still need to be addressed are:

- High costs. Devices should be available at cost compatible with deployment in large number throughout the road network.
- Intrusiveness. It emerged that although in-roadway sensing solutions allow remote monitoring with no traffic disruption, they are intrusive elements that may introduce weakness points in the road itself from which distresses may originate.
- Number. A large number of sensors is needed to in order to have sufficient information at disposal for the analysis. In particular it emerged that sensor density in the transverse direction (with respect to traffic direction) can enable more accurate information concerning the vehicle position and trajectory.

4 Development and deployment of an embeddable nano-carbon based strain technology

- Installation and maintenance. The technology must withstand the pavement construction process (high compression and temperature), maintain performances during the full lifetime of the road, and be compatible with road maintenance actions.

In this sense based on the promising results obtained with the Altaroad's InTRACK presented in chapter 3, we propose a sensing technology that can overcome the above mentioned drawbacks. As discussed in the introduction (section 1.8) CNM-based strain sensors become interesting for road pavement applications, thanks to their interesting sensing properties.

A hysteresis-free, high-stability, embeddable nanocarbon-based strain sensor is fabricated and its relevance for pavement monitoring is validated with accelerated pavement testing. Thanks to its design the system can embed a large number of sensors, its geometry less intrusive for the road pavement, and it provide higher sensitivity with respect to commercial strain gauges.

We use a carbon-clay nanocomposite active material to fabricate piezoresistive sensors on E-glass and polyimide substrate. The devices on polyimide are further encapsulated between two bitumen-compatible thermoplastic sheets and then integrated into pavement using regular pavement construction process. The resulting structure is tested using an accelerated pavement testing facility. The results clearly prove the suitability of the nanosensors for use in real-life pavement monitoring conditions.

In this work we do not address specifically the questions of costs of the devices. However, the increasing market of carbon and graphene families and the technology development associated to the use of this materials is likely to lead to a decrease in their price. This will make CNMs even more appealing for road pavement monitoring.

Please note that some of the results reported and discussed in this section are part of a research carried out before this thesis work. In particular, the active material preparation was conducted at the Materials Science Institute of Madrid, CSIC. The active material morphology analysis was carried out at LPICM by Bérengère Lebental. The study on devices with E-glass substrate comes from Eduardo Milana's internship at LPICM (French acronym for Laboratoire de Physique des Interfaces et des Couches Minces – joint research between Ecole Polytechnique and CNRS). The research on devices with polyimide substrate was conducted in collaboration with Altaroad. I worked on the laboratory characterization on

devices on polyimide substrate, their encapsulation and integration for full-scale testing, and the interpretation of data from the full-scale test.

4.2 Device fabrication process

In this section, we present the fabrication process of the device.

4.2.1 Materials: Carbon-clay nanocomposite

The active material is a carbon-clay nanocomposite composed of graphene-like material supported on sepiolite (fibrous clay mineral with $\text{Mg}_4\text{Si}_6\text{O}_{15}(\text{OH})_2 \cdot 6\text{H}_2\text{O}$ as ideal formula) mixed with multi-walled carbon nanotubes (MWCNT), in short C/Sep-MWCNT.

The C/Sep-MWCNT material is prepared as follows: Pangel® S9 commercial sepiolite supplied by Tolsa SA is mixed with MWCNTs (0.1 to 0.5 wt%) and water. Homogenization of the system is reached by sonomechanical treatment using Sonics Vibracell VCX750 equipment with a Ti-Al-V tip 13 mm in diameter, operating at a resonant frequency of 20 kHz, with 4.4 kJ (94 J/g) energy applied by 10 s pulses on/off (Francisco M. Fernandes & Ruiz-Hitzky, 2014). The dispersion is partially dried at around 60-70 °C overnight. Liquid caramel (Royal™, 80% provided by Kraft) is added to the sepiolite-MWCNT mixture at 2:1 caramel-sepiolite weight ratio. The homogenization is realized by kneading. The resulting mixture of sepiolite-MWNT-caramel is again partially dried at 60-70 °C overnight, and then heated up from room temperature to 800 °C under nitrogen flux at a rate of 5 °C/min. The material is kept to 800 °C for 1 h, transforming the caramel into a conducting carbonaceous compound containing graphene-like structures and supported by the sepiolite fibers (Ruiz-Hitzky et al., 2011). The resulting material takes the form of a black powder composed of micro and nanoparticles of the C/Sep-MWCNT nanocomposite.

4.2.2 Water based ink formulation

The C/Sep-MWNT powder is dispersed at 0.5 wt% in water with optionally 0.1 wt% of sodium dodecyl benzene sulfonate (SDBS, technical grade, provided by Sigma Aldrich) as surfactant. When the surfactant is needed (which depends on the sensor substrate; see next section), it is first mixed with water using a magnetic stirrer for 5 min. The C/Sep-MWNTs powder is added to the resulting solution, which is stirred for 1 h then sonicated for 1 h, thus forming a homogeneous black solution. When not used directly after fabrication, the ink is sonicated for 1 h before use.

4.2.3 Device design, ink deposition and encapsulation

4.2.3.1 For layer morphology analysis

For layer morphology analysis (profilometry, SEM and AFM), the ink is deposited by drop casting (approx. 10 μL /drop) on Si wafer with 100 nm SiO_2 insulating layer. During deposition, the substrate is heated at 100 $^\circ\text{C}$. Each drop is deposited only after the previous one has dried (about 5 min).

4.2.3.2 For electrical, thermal and electromechanical characterizations in the lab

The main substrate used for laboratory characterization is a 300 μm thick layer of E-Glass from Goodfellow Inc.. It is a composite material made of borosilicate glass fibers in an epoxy matrix. Each device is made on top of a E-Glass substrate of size 120 mm x 60 mm rinsed with ethanol before deposition. This size is selected to be compatible with the available set-up for 4-point bending. A square of size 40 mm x 40 mm is marked in the middle of the rectangle to mark the area where the ink will be drop cast.

To form the electrodes, two small pieces of copper tape are attached with a cyanoacrylate adhesive 5 mm away from the two sides of the square, perpendicularly to the longest side of the substrate. The 5 mm are then painted with Conductive Epoxy paste charged with silver particles. The Conductive Epoxy is a bicomponent paste provided by Circuitworks. The two components are mixed for 5 min in equal parts before use. The schematics of the prepared substrate with electrodes is provided in Figure 4.1-left. This dual electrode material strategy (copper tape covered with silver paste) was selected to achieve stable electrical response under mechanical strain. Indeed, copper tape alone tends to delaminate under bending, while the wires soldered directly on top of silver paste (and not on copper tape) tend to break.

The prepared substrate is then fixed on a metallic plate warmed up at 70 $^\circ\text{C}$. The ink (with SDBS surfactant) is drop cast on the square area. The deposition overlaps on the electrodes on purpose. For a deposition area of 40 mm x 40 mm, a first layer is formed by 600 μL of solution poured drop by drop with a 100 μL syringe. It is dried on the hot plate for 10 min then a new layer is deposited in the same manner. The number of layers in the devices reported here is 15. During the deposition of the first layers, as the E-glass is hydrophobic, the drops do not spread properly on the yet uncovered area. Thus, the drops are spread manually using the syringe head. Figure 4.1-right shows an image of the resulting device.

4 Development and deployment of an embeddable nano-carbon based strain technology

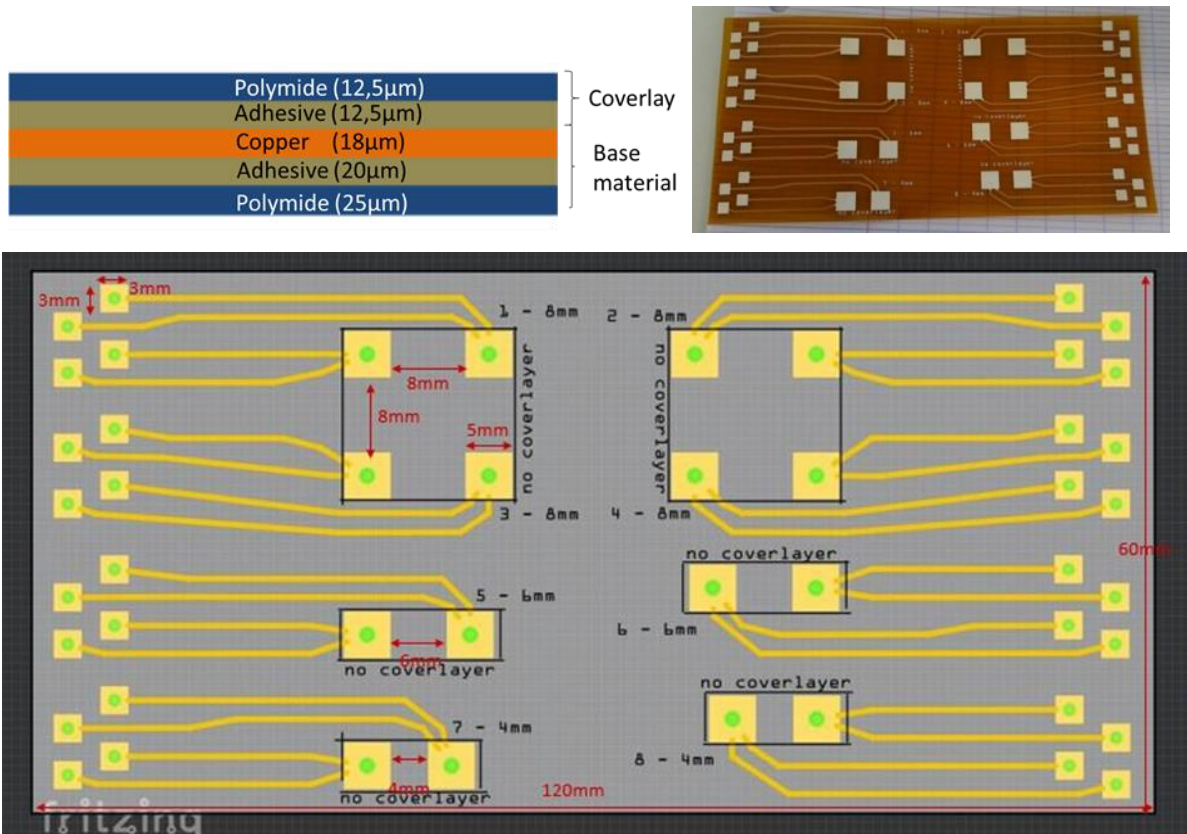


Figure 4.2 Top left - composition of the substrate. Top right - image of the substrate. Bottom - Geometry of the substrate.

On this substrate, the use of SDBS as surfactant in the ink leads to poor electrical conductivity. Thus, inks without SDBS are used. During deposition, the foil is kept on a heated plate at 90 °C. The C/Sep-MWCNT ink is deposited by 20 μ L-drop casting. Like in the previous section, enough drops are put to cover the deposition area, then the sample rests on the heated plate for 5 min before a new deposition starts. After fabrication the foil is left on the heated plate at 50 °C for about 15 h to ensure complete water evaporation. A total volume of about 560 μ L is needed to reach a resistance in the range of 1 M Ω (which is the target to allow electrical measurement in the field). Figure 4.3 shows four devices right after fabrication.

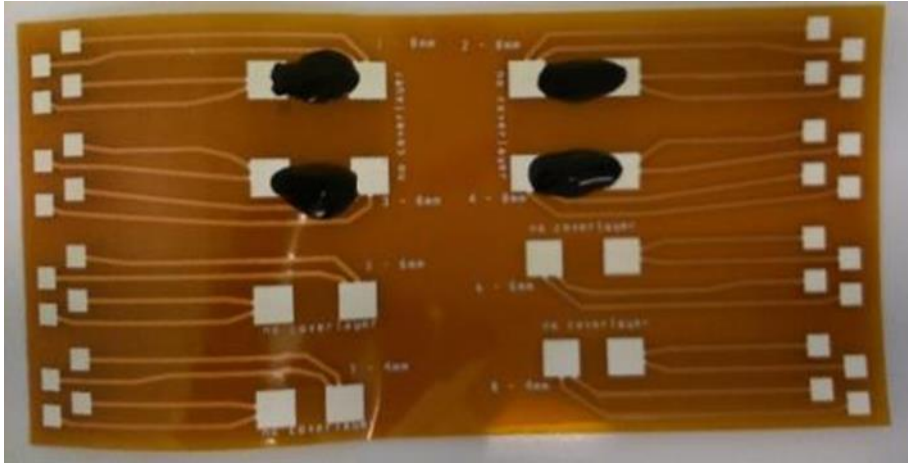


Figure 4.3 Four devices after fabrication.

As discussed in section 4.4, mechanical characterizations show a significant variation of resistance, attributed to the loss of particles from the active area. Henceforth, two methods of encapsulation of the particles were tested, Kapton tape (tesa® 51408) and silicone (LOCTITE® SI 5366TM). Figure 4.4 shows example of sensors after encapsulation.

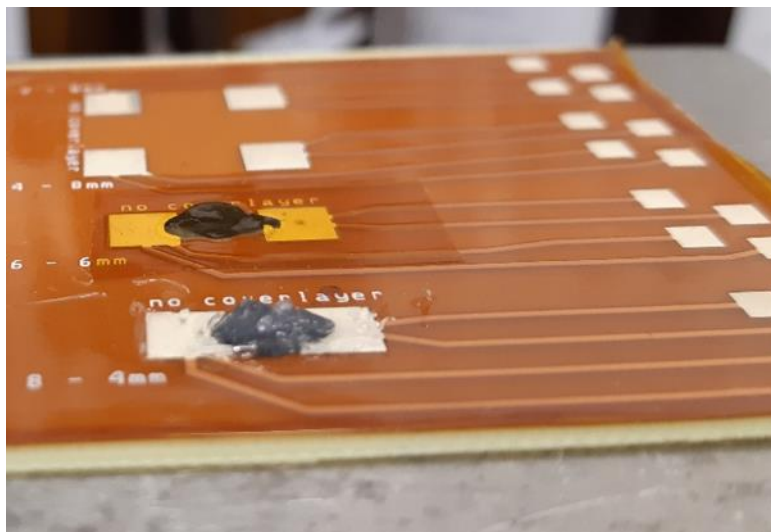


Figure 4.4 Sensors after encapsulation: Kapton tape on top and silicon on bottom.

Measurement of the electrical resistance before and after encapsulation shows that silicon encapsulation leads to the most stable devices. Figure 4.5 reports on the electrical resistance evolution from last drop deposition (0 hours) to encapsulation (44 hours). Please note that Kapton tape was used for Sensor 6 and silicon for Sensor 8. Due to water evaporation, both devices experience a rise in resistance after resting 15 hours on the heated plate at 50 °C. Resistance variation occurring from 15 hours to 44 hours could be associated to sensors stabilization. Right after encapsulation measurements show that the application of Kapton

4 Development and deployment of an embeddable nano-carbon based strain technology

tape results in an increase in resistance of 6.8 M Ω with respect to the previous measurement, while 0.38 M Ω was observed after the silicon application.

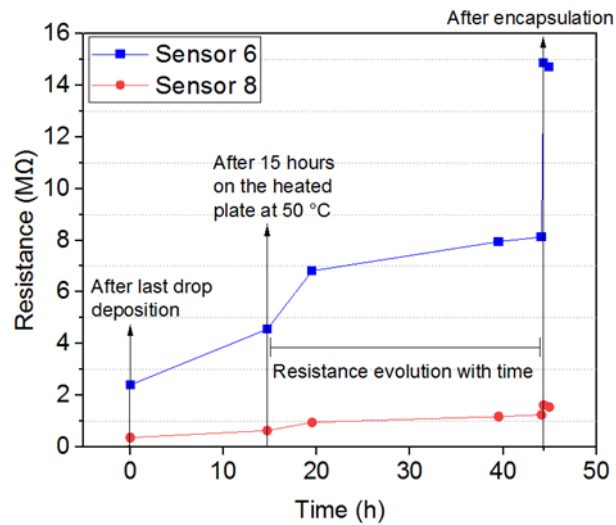


Figure 4.5 Resistance measurements of two sensors encapsulated with Kapton tape (Sensor 6) and silicon (Sensor 8).

4.2.4 Deployment in the pavement

For integration into pavement, a second stage of encapsulation is needed. As reported in chapter 3, Altaroad's breakthrough InTrack solution allows to embed a large number of flexible strain and temperature sensors into pavement (see Figure 3.1). The approach consists in gluing a sensing layer (made of thin flexible PCB material, such as the polyimide foils described above) between two thin (2 mm), large (12 cm x 250 cm) sheets of thermoplastic polymers. The sheets are sealed together with the sensing layer inside by application of heat on the side of the polymer, which melts the two sheets together (Villette et al., 2014).

Adapting this strategy to the devices on polyimide described above, 6 sensors were cut out of the polyimide foils after their encapsulation with silicone. They were glued to a thermoplastic sheet of size 10 cm x 100 cm x 2 mm with strain gage adhesive (M-bond 200 provided by Micro Measurements), together with commercial strain gauges (model RS Pro Single Strain Gauges), as depicted in Figure 4.6. Commercial sensors are used for comparison purposes. Then tinned copper wires (1.2 mm in diameter) were soldered and shielded with self-adhesive tin-plated copper-mesh tape (RS Pro Adhesive Zip Mesh). Finally, a top thermoplastic sheet was glued to the bottom sheet via thermo-fusion. Figure 4.7 shows the assembled system before inclusion in pavement.

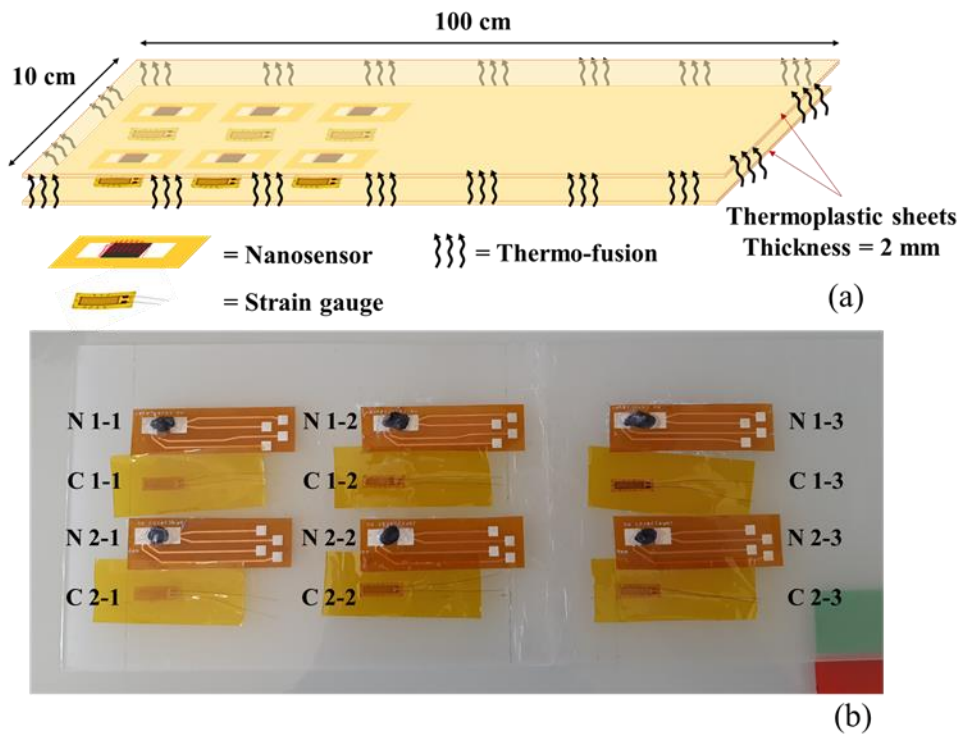


Figure 4.6 (a) Layout of sensing layer assembly process; (b) Nanosensors and strain gauges glued to thermoplastic sheet.

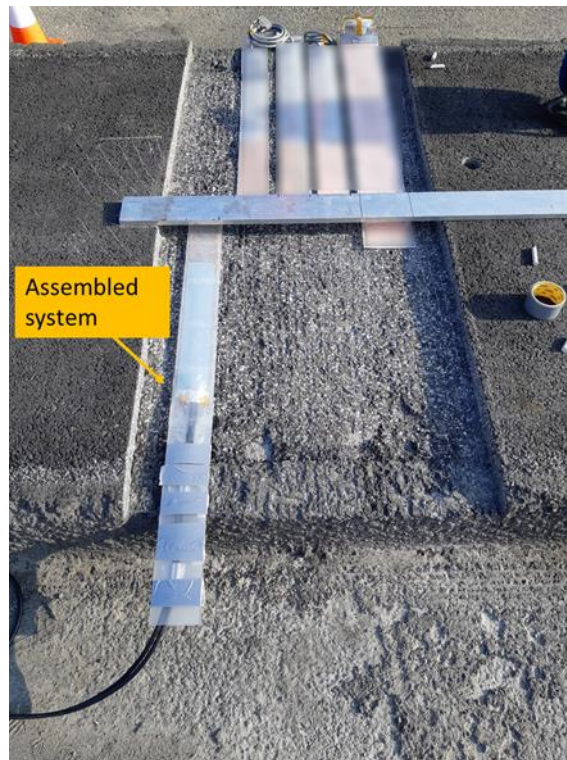


Figure 4.7 The left bar is the assembled system before inclusion in the pavement. The four bars to the right are Altaroad's regular InTrack solutions.

4 Development and deployment of an embeddable nano-carbon based strain technology

The assembled system is then deployed in pavement. The structure of the test track, presented in Figure 4.8-left, had the following composition:

- 8 cm of BBME 0/10, that is a common used asphalt mix in France for surface layer (see section 1.4.3)
- 25 cm of bituminous base course
- 20 cm of cement treated base course
- 25 cm of unbound granular base course

The track was prepared for the instrumentation by excavating an area of 80 cm x 185 cm to a depth of 4 cm (Figure 4.8-right). The sensing device was then located on the top of the remaining structure and covered with bitumen mix after application of a tack coat bituminous emulsion. The latter was used in order to ensure the adequate bonding between pavement layers as well as the optimal adhesion between the sensing layer and the structure. Figure 4.9 shows the different phases of the construction process, namely: tack-coat emulsion application before and after positioning the assembled system, paving and compacting.

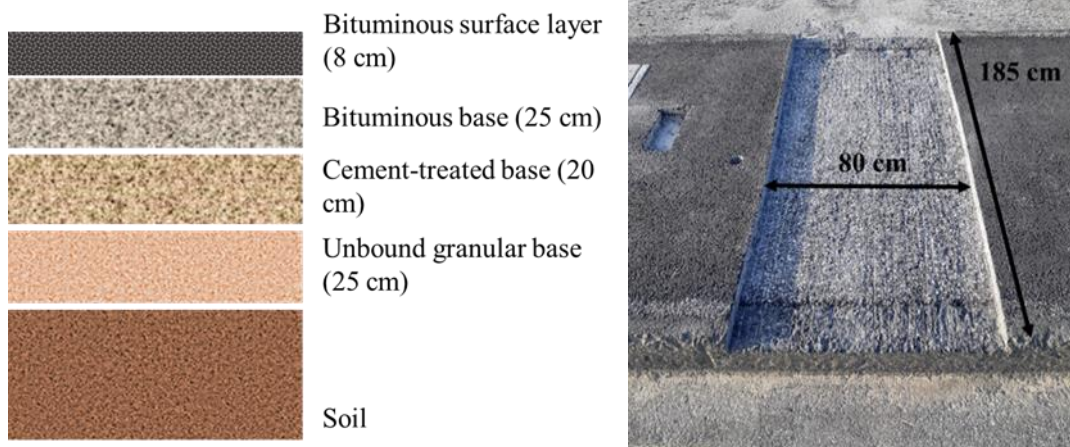


Figure 4.8 Pavement structure (Left); test track (Right).



Figure 4.9 Different phases of the construction process: tack-coat emulsion application (top left), paving (top right), 1st compaction (bottom left), and 2nd compaction (bottom right).

4.3 Device characterizations

4.3.1 Laboratory characterization

The microstructure is imaged using a Philips XL-30S scanning electron microscope (SEM) in the secondary electron image mode between 10 kV and 20 kV. Atomic Force Microscopy (AFM) measurements are conducted in tapping mode using a Dimension 10000 AFM from Veeco Instruments. The average layer thickness is measured over a 3 mm long line using a DEKTAK IIA profilometer. Confocal imaging (Leica DCM8) is also used for fast imaging of the depositions as well as non-quantitative analysis of vertical material distribution.

Resistance measurements along the fabrication process are done via digital multimeter (velleman® DVM894). During electromechanical tests a Keithley 6221 current source and a NI9210 voltage acquisition system are used, with a LabView-programmed acquisition software running on computer. Acquisition frequency is 50 Hz. Electromechanical tests are done using a four-point bending system shown in Figure 4.10-left. Testing of the devices on E-glass was done at room temperature. For the testing of the devices on polyimide, the four-point bending system was integrated into an environmental chamber (Dycometal) enabling control of temperature between -40 °C and 150 °C (Figure 4.10-right).

4 Development and deployment of an embeddable nano-carbon based strain technology

The devices on E-glass are tested following three modes: under increasing then decreasing strain up to 0.06% strain at slow speed (0.1 mm/s – 0.002 %/s); under cyclic strain up to 0.06% strain at 0.05 Hz (0.15 mm/s – 0.003 %/s) and under stepwise displacement (by 500 μm – 0.01% - 1 min step) of the traction jaw. The response of the devices is compared to the response of a commercial strain gauge glued to the same E-glass substrate (the strain being constant over the surface by design of four-point bending – see Appendix 7-section 6.7.1).

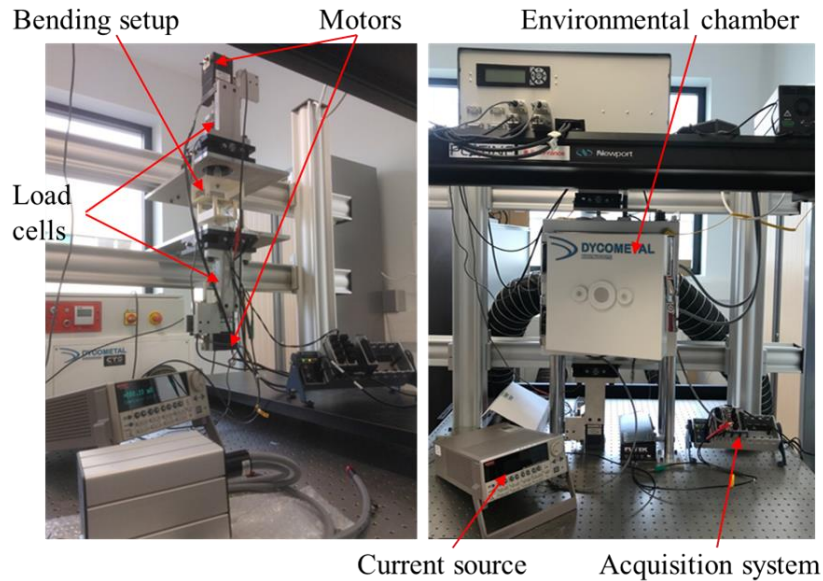


Figure 4.10 Multiphysics bench enabling four-point bending with or without temperature control. (Left) Bending setup, motors and load cells with current source and acquisition cards. (Right) Bending setup mounted within the environmental chamber enabling temperature and relative humidity control.

For mechanical characterization in the laboratory of devices on polyimide, the foils are glued (with LOCTITE SUPER GLUE-3®) on FR-4 support (isola® DE156) 10 h before starting fabrication. Then the fabrication proceeds as described in section 4.2.3.2. The devices are tested under cyclic strain up to 0.06 % at 2 mHz (0.001 mm/s – 0.00005 %/s). The test is performed under displacement control. Knowing the Young's modulus of the FR-4 support, the strain applied on the sample is calculated using the formula reported in Appendix 7-section 6.7.1.

4.3.2 Field characterization

4.3.2.1 Accelerated pavement test

To evaluate the response of the sensors within pavement, the test section undergoes accelerated pavement test using the FABAC machine from the University Gustave Eiffel (<https://www.lames.ifsttar.fr/en/the-institute/mast/laboratories/lames/equipments/the->

[fabac-machines/](#)). The FABAC machine (Figure 4.11) is a small-size outdoor heavy-traffic simulator. It has four load modules carried by a chain to apply the load over a solicitation area of 2 m without lateral wandering. Two loading configurations are possible: single wheel and dual wheel. The maximum load frequency is 50 loads per minute. In particular the load can vary between 30 and 75 kN, and the wheel speed between 0.5 and 7 km/h. The machine can reproduce up to 300000 loadings weekly. Table 4.1 shows the loading conditions that were actually carried out during the experimental campaign, which took place in April 2019 over one week. A total of 80,700 loadings were applied with 5 different loading configurations. The temperature in pavement at the depth of the sensors was collected by one of the Altaroad's InTrack devices tested simultaneously (Figure 4.7).

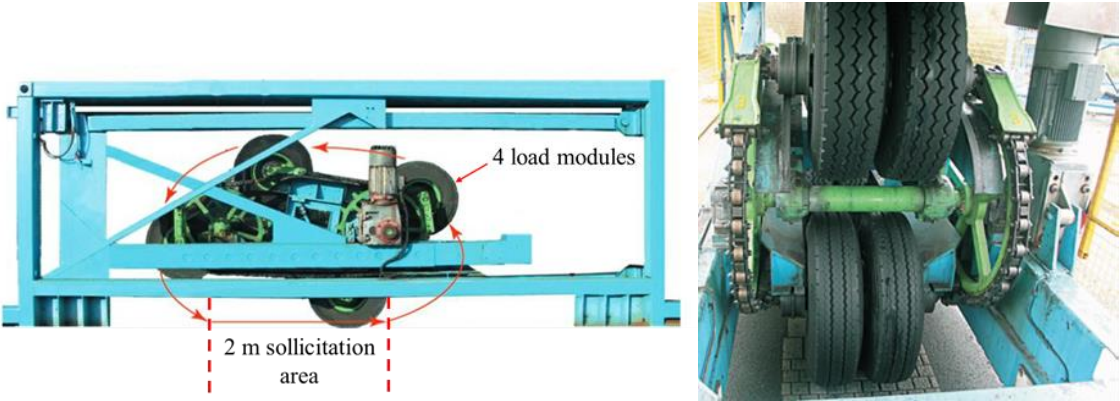


Figure 4.11 FABAC machine from University Gustave Eiffel: (Left) functioning principle, (Right) zoom of wheels and chain while turning.

Table 4.1 Loading cases description: 5 loading configurations.

Loading case	Load (t)	Speed (km/h)	Temperature at -4 cm (°C)
I	5.5	0.5	10.2
II	5.5	1.5	14.1
III	6.5	1.5	9.6
IV	6.5	2.5	11.9
V	7.5	3	12.2

4.3.2.2 Acquisition system

After embedding in pavement, the devices are connected using a PÉGASE version 1 acquisition station (<http://Pégase-instrumentation.com/>) already described in section 3.2.3. Two PEGASE boxes were used for the connection of the 8 sensors, 4 per box in 3-wire

4 Development and deployment of an embeddable nano-carbon based strain technology

quarter bridge configuration (4 nanosensors and 4 commercial strain gauges detailed in section 4.2.4) in 3-wire quarter bridge configuration. Three acquisition modes are used during the test:

- 0.1 Hz during the construction process to assess sensors survival.
- 1 Hz continuously throughout the test to record the sensors static response.
- 100 Hz punctually throughout the test to record the sensors dynamic response to wheel passage; from 1 to 3 periods of acquisition of 5 to 10 min each are acquired for each loading configuration (as described in Table 2), corresponding to 25 to 40 wheel passages per period. Note that monitoring at 100 Hz continuously was not possible as the volume of data was too large from proper data transmission.

4.3.2.3 Data post-processing

Each wheel passage yields a peak in the 100 Hz signal of the sensors. However, the processing and exploitation of each peak is challenging because of a high level of noise (about 3 V peak-to-peak) observed despite the shielding of the wires and attributed to the running of various large motorized apparatuses in the vicinity of the test site, including the FABAC machine itself. Thus, a low-pass filter (5 Hz for nanosensors and 1 Hz for commercial strain gauges) is applied to all the signals. For each period of 100 Hz data acquisition (between 25 and 40 peaks), 10 peaks are randomly selected and averaged. The resulting peak is centered at zero on the time-axis. Finally, the resulting peaks corresponding to the same loading configuration are averaged. This process is schematized in Figure 4.12 for a nanosensor. Note that the output signal is a voltage. In order to calculate the GFs, the output signal is converted to resistance by using the conversion factor reported in Appendix -section 6.7.2.

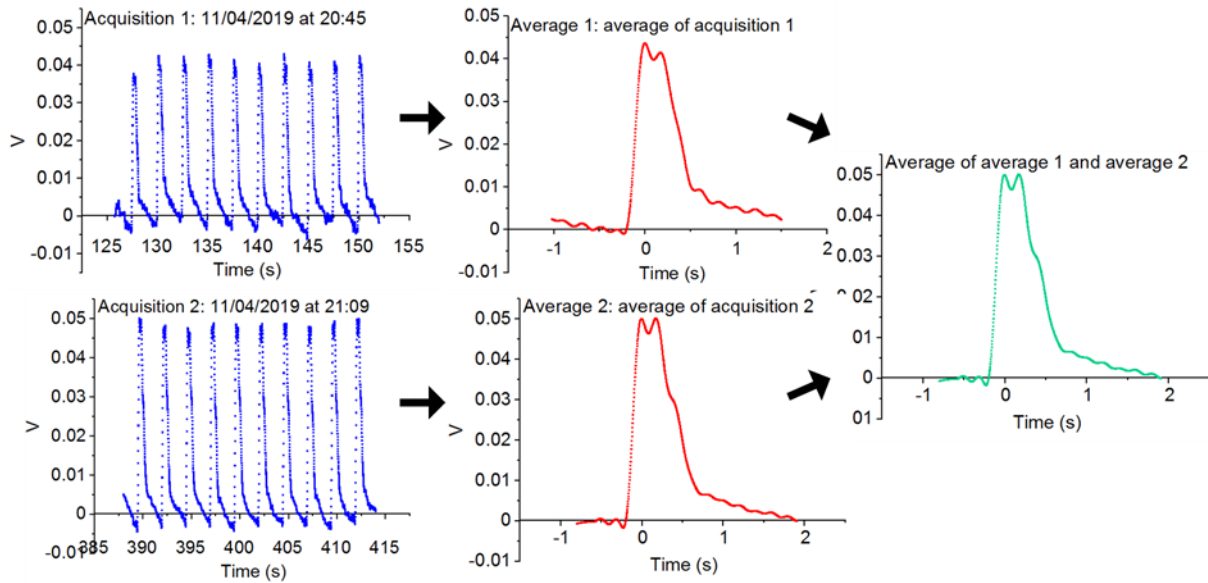


Figure 4.12 Signal treatment process of two data acquisitions from a nanosensor. Loading case V: 7.5 t at 3 m/s; temperature recorded at -4 cm below pavement equal to 14.3 °C.

4.4 Performances of C/Sep-MWCNT-bases strain sensors

4.4.1 Morphology and electrical properties of the C/Sep-MWCNT material

Figure 4.13 shows typical SEM images of C/Sep-MWCNT particles. The size of the particles varies widely, with a characteristic size ranging from a fraction of micrometers to tens of micrometers. The particles feature porosity at various scales (micro and nano) as well as surface nanostructuring. Well separated MWCNTs and sepiolite fibers can be identified and appear encased into a porous and disordered carbon matrix acting as connectors or scaffold structure. A single-drop layer is 940 ± 100 nm thick as measured by profilometry. It is non-continuous, showing separate particles with thickness ranging from 0.5 nm to 2 μm .

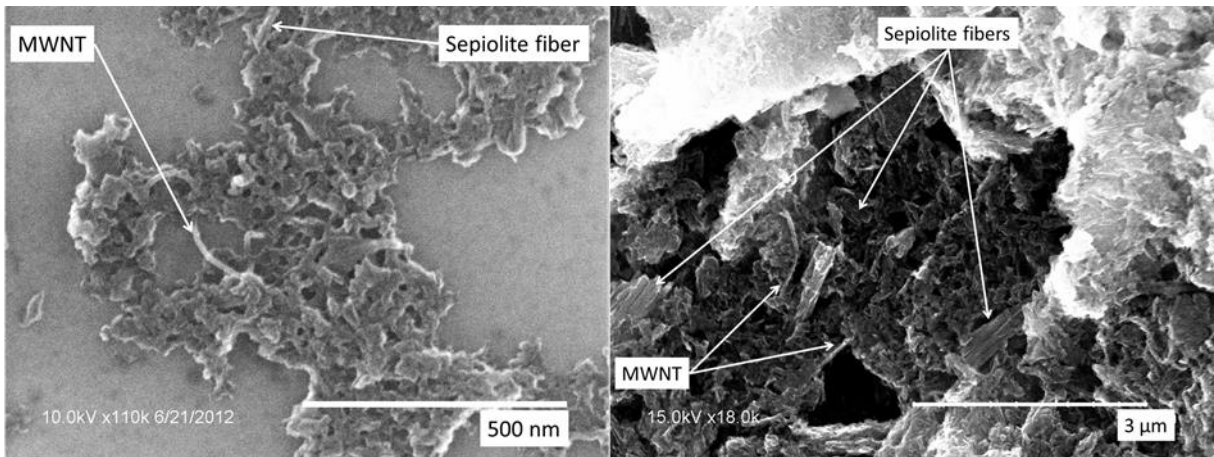


Figure 4.13 SEM images of C/Sep-MWCNT particles (0.5 % wt MWCNTs) at different scales. Well separated MWNTs and sepiolite fibers are encased in a disordered, porous carbon matrix.

Figure 4.14 shows at different scale the morphology of a deposition of 30 10 μ L-drops. Observed with SEM at the millimeter scale, the layer remains porous, with large ridges of C/Sep-MWCNT materials (Figure 4.14-a). Within each ridge, at submillimeter scale, the layer appears continuous though highly disordered (Figure 4.14-b and c). Its roughness reaches 30 nm as measured over a 10 μ m by 10 μ m AFM image (Figure 4.14-d).

Up to 30 drops, the layer thickness (measured with profilometry) increases linearly, with average increase of layer thickness of $h_a=310$ nm/drop (Figure 4.15-left). This value is significantly lower than the average thickness of a single drop ($h_d=940$ nm), indicating that the layer progressively densifies until it reaches approx. 3 times the density of a single drop (see Appendix 7-section 6.7.3 for the calculation of the densification). This densification is expected, as particles in each additional drop fill in the pores of the previous layer.

A single-drop layer is not conducting (resistance above 1 G Ω); from 5 drops upward, the layer is conducting and its resistance decreases exponentially with the thickness (Figure 4.15-right), which is typical for a percolating layer.

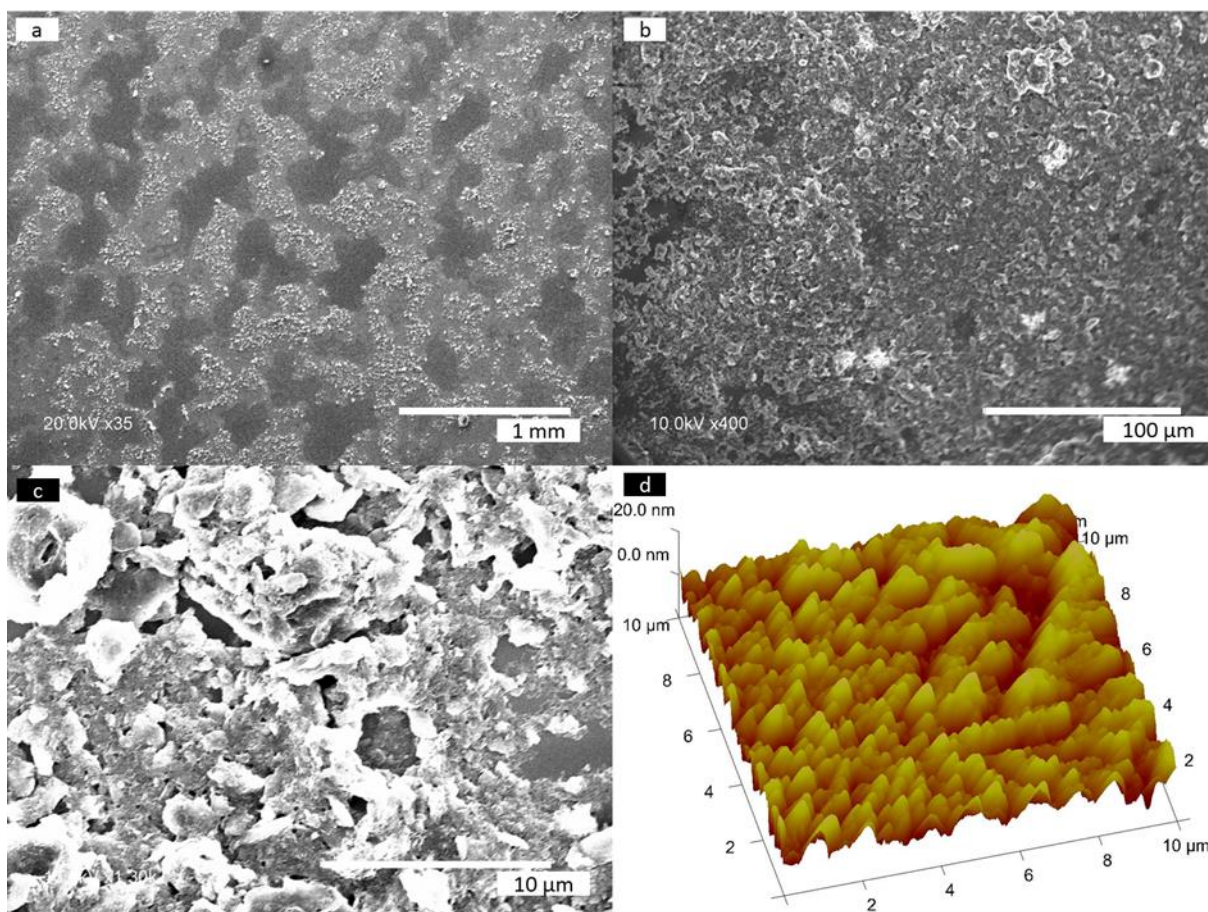


Figure 4.14 SEM (a-c) and AFM (d) images of a 30-drop C/Sep-MWNT layer at different scales. a) The layer surface is characterized by marked valleys and ridges, while at lower scales (b-c), the material appear continuous and very disordered. d) AFM estimated roughness.

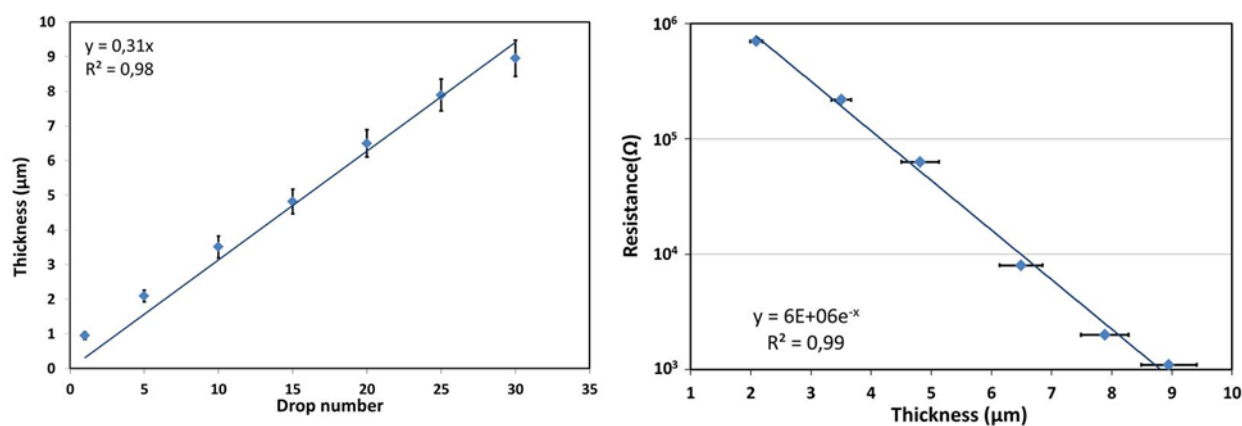


Figure 4.15 Relationship between thickness of the C/Sep-MWCNTs layer, resistance and drop number.

4.4.2 Device variability on E-glass

The average resistance of a 8-device batch on E-glass for a 15-drop layer is $34 \text{ k}\Omega \pm 9,5 \text{ k}\Omega$.

There is only 28 % relative standard deviation on the resistance over this batch (called B34

4 Development and deployment of an embeddable nano-carbon based strain technology

in the following), which corresponds to a good stability for a drop-casting based process (traditionally lacking reproducibility). The details on resistances values and variability as a function of the number of drops for batch B34 are provided in Appendix 7-section 6.7.4. The results show that both the resistance and the relative standard deviation on the resistance (the device-to-device variability) decrease with increasing number of drops, which is expected for a percolating network of nanoparticles (Michelis, 2016). The batch reproducibility can be further improved by adjusting the number of drops to reach the target resistance. By this admittedly time-consuming approach the relative standard deviations of two 6-device batches with respectively 30 k Ω and 22 k Ω average resistances, called in the rest B30 and B22, were lowered down to 3 % and 12 % only. The low variability of batch B30 at 3 % is a very good result compared to the state of the art of drop casting of nanocarbon-based materials. For instance, in (Shintake et al., 2018), 13 % was achieved for six devices obtained by film casting (layer-by-layer fabrication process) using carbon black-filled elastomer composite and silicone elastomer. The same performance, 13 %, was achieved for three films obtained by drop casting of colloidal suspensions of multilayer graphene nanoplatelets (MLG) in 1-propanol (Rinaldi et al., 2014). It is on par with best performances achieved on small batches of nanocarbon-based devices with ink-jet printing, a process lauded for its reproducibility, for instance less than 4 % in (Kim et al., 2009) and (Benchirouf et al., 2012).

4.4.3 Strain sensors on E-glass

Figure 4.16-c shows the response of a typical device of batch B34 to a ramp-wise loading up to 0.06 % strain. While the response in extension follows very closely the loading, during unloading there is a small delay in response. The extension and unloading ramps can be exploited to derive the gauge factor GF (Figure 4.16-b and c), namely the slope of the curve linking relative resistance variation and strain. The linearity is very good in extension, slightly degraded during unloading especially at higher strain levels. There is a slight hysteresis in the GF between extension and unloading, between 3.7 % and 16 % of the GF depending on device.

Over batches B30, B34 and B22 (resistance respectively 30 k Ω \pm 3 %, 34 k Ω \pm 28 %, and 22 k Ω \pm 12 %), the average GF in extension was found to be respectively 78 \pm 44 %, 61 \pm 16 % and 80 \pm 15 %. The highest GF reaches up to 137 at 29 k Ω within batch B30. In average over the 3 batches, the GF is 73 \pm 22 %. Interestingly, the variability in GF of batch B22 and B34 are much lower (resp. 15 % and 16 %) than that of batch B30 (44 %) while the variability in baseline resistance of B30 is much lower (3 %) than the other batches. This is advantageous

because it means that the time-consuming sensor-by-sensor adjustment of device resistance carried out by drop casting to achieve the remarkably low device-to-device variability of batch 30 is actually not required to achieve low variability in strain sensors.

To assess the impacts of dynamic effects on the GF, the gauge factor is also estimated over strain steps (static) and strain cycles. The discrepancy between ramp-wise and step-wise extension GF estimate is 6 % only. Results during strain cycles are also consistent with ramp-wise and step-wise data and provided in Appendix 7-section 6.7.6.

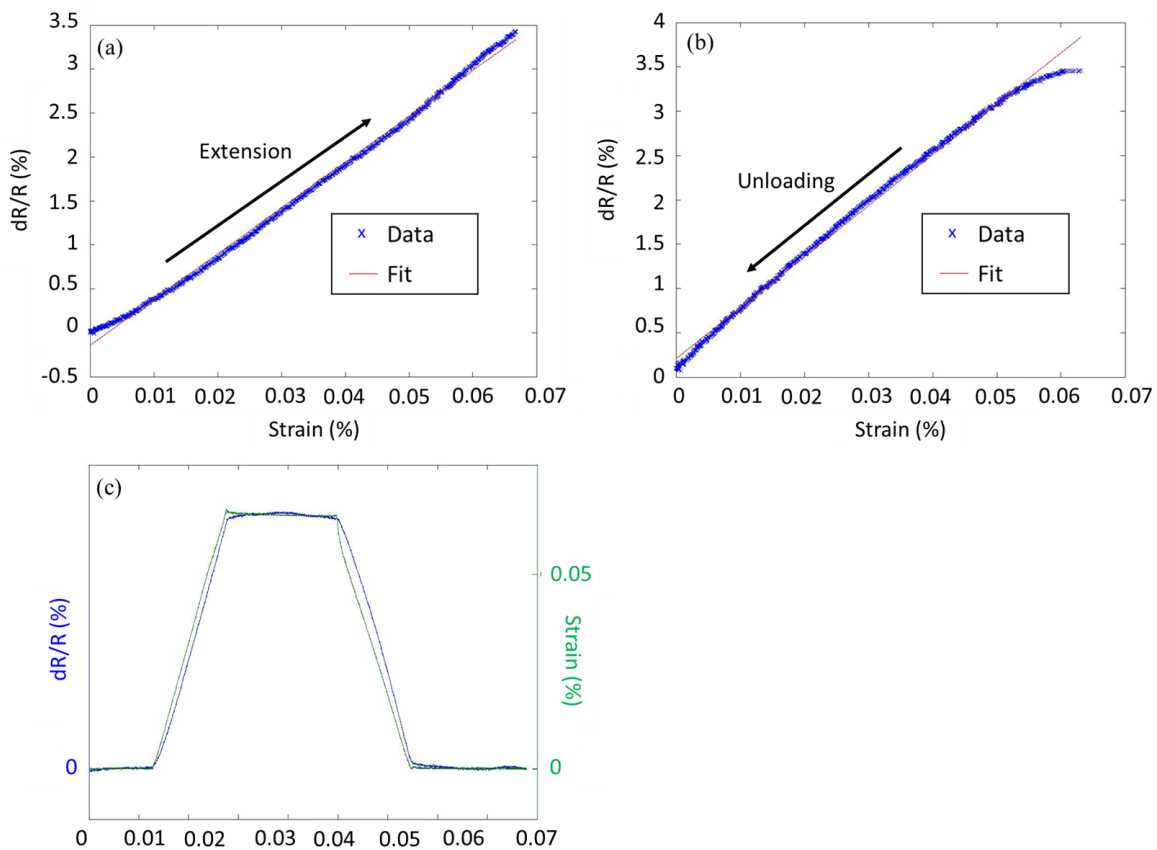


Figure 4.16 Response of E-glass device NA32 of batch B34 to a ramp-wise loading up to 0.06 % strain; (a) extension ramp; (b) unloading ramp; (c) time response.

Let us point out that the GF found here are remarkably high compared to commercial and research state of the art. In extension, the sensitivity is already 30 times higher than commercial devices based on metal foils (around 2 – (RS PRO, 2018) (OMEGA, n.d.) (Micro Measurements, 2010)), and even twice higher than the only commercial technology relying on percolating nanoparticles (<https://www.nanolike.com/fr/>). It is also higher than most recent results reported in the literature (notably 3.37 in (Shintake et al., 2018) for a strain sensor based on carbon black-filled elastomer composite, 1.5 in (Giffney et al., 2017) for a carbon nanotube/silicone rubber piezoresistive sensor, 42.2 in (Chun et al., 2017) for

4 Development and deployment of an embeddable nano-carbon based strain technology

an all-graphene strain sensor, 13.1 in (Zheng et al., 2018) for a strain sensor based on hybrid carbon nanofillers/polydimethylsiloxane composite, 78.13 in (Dongzhi Zhang et al., 2018) for a graphene/poly (diallyldimethylammonium chloride) film strain sensor), while it is based on a fabrication process which is much lower cost than those commercial and research devices. Moreover, the approach does not face the traditional hurdle of devices based on drop casting, the high device-to-device variability in gauge factor: the variability is as low as 16 % in (extension) gauge factor (batch B34). It is actually comparable with best results achieved for inkjet printing, for instance those on carbon nanotubes strain sensors reported in (Michelis et al., 2015).

4.4.4 Strain sensors on PI PCBs

Several batches were fabricated: a 3-device batch (25 drop layer, called P1), a 4-device batch (21 drop layer, called P2), a 8-device batch (30 drop layer, called P3), a 8-device batch (28 drop layer, called P5) and a 6-device batch (28 drop layer, called P6), with respectively 30 $k\Omega \pm 84$ %, 891 $k\Omega \pm 38$ %, 33 $k\Omega \pm 45$ %, 1.28 $M\Omega \pm 87$ % and 1.98 $M\Omega \pm 31$ % average resistances. Expectedly (because the width is 8 times smaller and the gap between electrodes is different from E-glass sensors), the resistance is significantly higher than the resistance found for E-glass devices. The variability for a constant number of drops is also higher. We attribute the higher variability to the coffee ring effect (Deegan et al., 1997): indeed, as can be seen in Appendix 7-section 6.7.7, the size of the coffee ring is comparable to the size of the device (unlike for devices in E-glass that are much larger than the coffee ring).

Figure 4.17 shows the response of sensor c5 out of P1 batch (average resistance 30 $k\Omega \pm 84$ %) to cyclic loading up to 0.06 % strain for 13 cycles (sensor c7 of the same batch provided similar results as reported in Appendix 7-section 6.7.6). While the linear range is slightly reduced compared to E-glass devices (up to 0.04 % instead of 0.06 %), the GFs derived for devices c5 and c7 are on average 132 ± 4 % and 205 ± 4 % respectively in extension, and 137 ± 1 % and 225 ± 2 % respectively in unloading, the standard deviation being calculated over the 13 cycles. The GF values are remarkably stable over the loading cycles (less than 4.5 % over 13 cycles), with a slight hysteresis between extension and unloading (4 % for c5, 9 % for c7) and higher GF than E-glass devices (c7's GF is 1.5 times larger than the E-glass device with highest GF – 137; the average extension GF of c5 and c7 is 168, 2.3 higher than the E-glass devices average). Besides being remarkable compared to the state of the art, these results indicate the possibility to obtain the same sensitivity with considerably less conductive

volume of conductive materials and smaller surface area, reducing the costs of the devices and enabling the monitoring of much more localized strain.

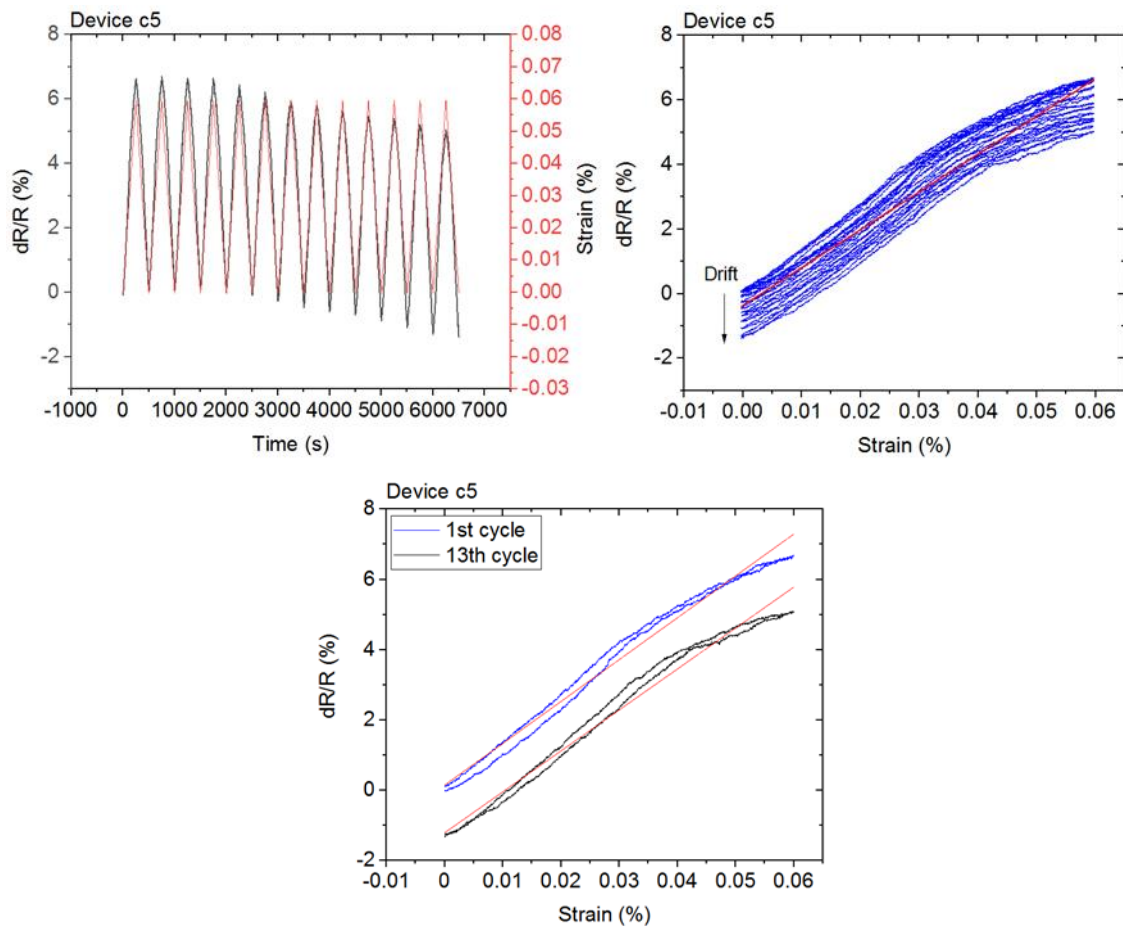


Figure 4.17 Device c5 resistance variation under strain cycles up to 0.06% strain at 2 mHz: (top left) time response, (top right) resistance-strain curve, (bottom) resistance-strain curve, zoom on the 1st and 13th cycle.

Based on these results, the PI sensors are even more promising than E-glass devices for pavement monitoring (the reduction of the linear range down to 0.04 % strain being not restrictive compared to typical pavement strains expected in the field, namely below 0.03 %). A slight drawback compared to E-glass, the cycles feature however a slight downward baseline shift (-0.14 % dR/R/s and -0.20 % dR/R/s for devices c5 and c7) absent in E-glass devices. This is not an issue for the pavement application, as the main focus lies in the dynamic response to wheel passage, obtained by subtraction of the baseline.

Based on this, 4 sensors were selected for embedding in pavement out of batches P5 (1.28 M Ω ±87 %) and P6 (1.98 M Ω ±31 %) whose fabrication was split into two days using the same ink. The selected 4 devices feature an average resistance for of 0.84 M Ω ±58 % which is higher compared to the resistance of devices tested in the lab. Hence, we expect higher sensitivity to strain as we are closer to the percolation threshold. Table 6.12 in Appendix 7-

section 6.7.7 provides their geometry and resistance values, while Figure 6.19 in the same section shows a confocal image of the 4 devices.

4.5 Performances of C/Sep-MWCNT-bases strain sensors under accelerated pavement testing

4.5.1 Resilience to the construction phase

The installation procedures of the sensors in the pavement consisted in the following steps: emulsion application, sensors placement on the top of the road, another emulsion application, paving, and compaction (Figure 4.18). Installation is one of the most critical phases of a pavement instrumentation project, as the sensors undergo high temperatures (about 160 °C for about 10 minutes) during asphalt application and high compression efforts during compaction (for about 5 minutes). Continuous acquisition (0.1 Hz) of data during and right after construction process allows to assess proper operation of the sensors after this step.

First of all, all the sensors (commercial and nano) withstand the installation phase without interruption degradation of the signal quality and without discontinuity in resistance values, as can be seen in Figure 4.18. This validates the nanosensor design, the choice of packaging material as well as the wiring and soldering strategy. In more details, Figure 4.18 shows the output of one of the nanosensors. One clearly recognizes the different phases of installation from the peaks in the sensor output. This means that our solution could be used first to monitor the quality of the construction phase (for instance useful in the context of performance based contracting (Stankevich et al., 2009)). A baseline variation of the sensor output before (approx. -1.4 V) and after (approx. -1 V) construction is observed. This may indicate either post compaction effects in the pavement or irreversible degradation of the sensors. As all the sensors keep operating throughout the experiment it is more likely to be the former. Indeed, degradations that lead to such a range of magnitude of variation tend to lead to rapid failure of the sensors, which did not occur after 20500 loading cycles.

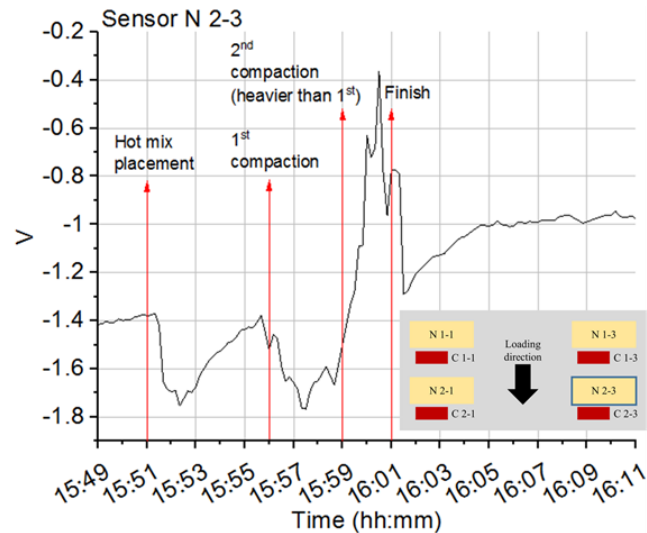


Figure 4.18 Response of nanosensor N 2-3 during the construction process (acquisition frequency of 0.1 Hz). The different phases of the installation can be clearly recognised: hot mix asphalt placement, 1st compaction and 2nd compaction (heavier than the 1st).

4.5.2 Resilience to the accelerated pavement testing

Low frequency acquisition (1 Hz) was performed throughout the test in order to globally monitor the nanosensors fatigue through their baseline resistance. The graphs reported in Figure 4.19 show that all the nanosensors survived 80700 loadings. They show an increase of the baseline voltage over the duration of the test, which does not occur for commercial strain gauges (Figure 4.19). This corresponds to an increase in resistance by 133 %, 24 %, 21 %, 37 % respectively for sensor N 1-1, N 1-3, N 2-1, N 2-3. It suggests that sensors N 1-3, N 2-1, N 2-3 are little impacted by fatigue, or are actually displaying the evolution of strain of the pavement section; while sensor N 1-1 is undergoing fatigue. In details, the response of sensor N1-1 is characterized by multiple fluctuations and baseline jumps, which might be caused by delamination phenomena occurring between the sensor and the bottom layer of the casing, or fatigue of the sensor, or instability of the electrical contacts.

4 Development and deployment of an embeddable nano-carbon based strain technology

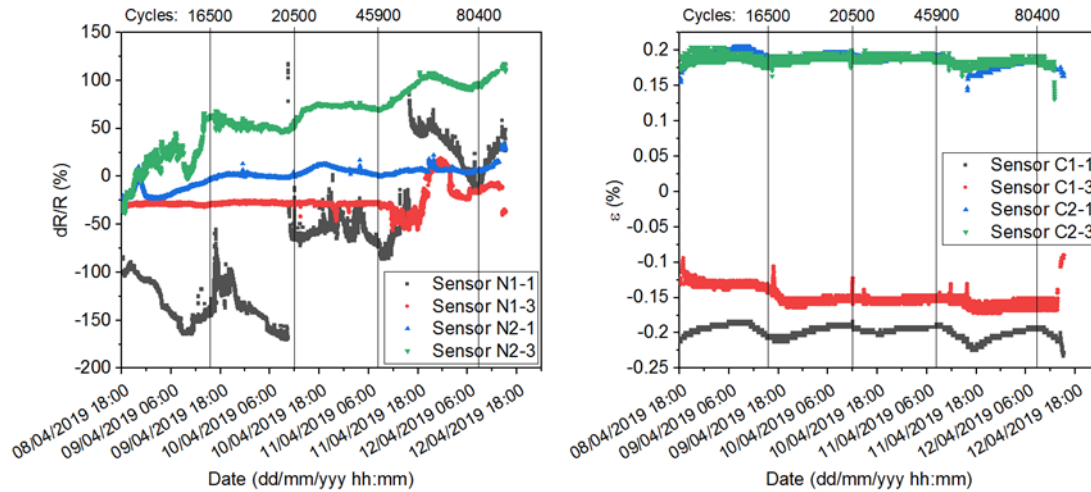


Figure 4.19 Low frequency (1 Hz) acquisition over the duration of the test (1 week). (Left) dR/R evolution for nanosensors. (Right) strain (%) evolution for commercial strain gauges.

4.5.3 Sensitivity to wheel passage

High frequency acquisition (100 Hz) of sensors data allows to analyse the on-site dynamic sensor responses to different loading configurations. Due to the high level of noise experienced on the site (see section 4.3.2.3), the measurements of nanosensors N 1-3 and N 2-1 could not be exploited. The rest of the analysis focuses on sensors N 1-1 and N 2-3. Please note that the data processing of high frequency data removes the baseline, so the results can be analysed independently from the baseline drift. We discuss below whether the dynamic response is impacted by fatigue or delamination.

Three sets of 100 Hz acquisitions of sensors N 2-3 and C 2-3 in loading configuration I (5.5 t – 0.5 km/h – 9.5 °C), III (6.5 t – 1.5 km/h – 9.5 °C), and IV (6.5t – 2.5 km/h – 10.1 °C) were used to calculate and track the sensitivity to wheel passage. The first response is shown in Figure 4.20-left, the others two are reported in Appendix 7-section 6.7.8. The relative variation of resistance for each sensor is plotted against the strain measured by the commercial strain gauge, as can be seen in Figure 4.20-rigth. The first strain response of the nanosensor, shown in Figure 4.20, is characterized by very low sensitivity at lower strain (below 0.003 %), then high, linear sensitivity in the 0.003% to 0.006 % range, saturation effect above 0.006 %. The second and third responses, reported in Appendix 7-section 6.7.8 are characterised by linear sensitivity in the 0.005 % to 0.009 % range and 0.006 % to 0.008 % range respectively, and no saturation effect is observed.

For each cycle the GF was calculated in the linear range. The results obtained are impressive: the on-site GFs are respectively $1.7e03 \pm 23\%$, $1.2e03 \pm 12\%$, $1.6e03 \pm 37\%$, which suggest an on-site sensitivity already 625 times bigger than commercial strain gauges and 6.1 times

bigger than the best result obtained in the lab for devices on polyimide (see section 4.4.4). In average, the GF over the three loading configurations is $1.5e03 \pm 16\%$. The standard deviation by cycle and by loading configuration observed on-site is slightly higher than lab results. However, the results are remarkable and suggest that the proposed technology is stable and even more appealing for pavement applications despite the bulky packaging, the challenging installation conditions and the large number of truck passages.

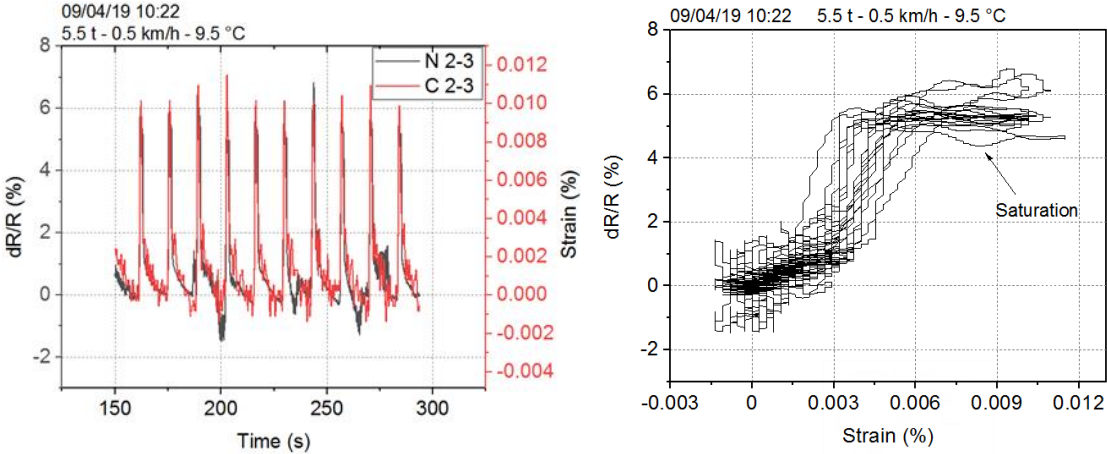


Figure 4.20 Sensors N 2-3 and C 2-3: 100 Hz acquisition on 09/04/2019 at 10:22. Load = 5.5 t, speed = 0.5 km/h, and temperature = 9.5 °C. (Left) time-response. (Right) resistance-strain response. Sensor N 2-3 features saturation.

Despite the very high sensitivity observed here, to fully prove the relevance of the solution, one also needs to prove that the sensors outputs are correlated with the loading conditions. In Figure 4.21, the maximum peak values are displayed for each speed and loading configuration described in Table 4.1, for sensors N 1-1 and C 1-1, and N 2-3 and C 2-3. The strains on sensor C 2-3 are more intense than on sensor C 1-1 due to the different positioning of the sensors with respect to the twinned wheels of the FABAC machine. The comparison between the trends shows that sensor N 2-3 behaves consistently with sensor C 2-3 for the entire duration of the test. On the other end, sensor N 1-1 experiences some delamination or fatigue phenomena at about 20500 loadings when it starts to inverse its response (from positive to negative peak values). This is consistent with the jump in voltage value observed in Figure 4.19 on 10/04/2020 after 12:00, which is indicative of degradation of the sensors. Finally, in view of proving that the sensors embedded in pavement provide representative information on pavement loading, the correlation between the maximum peak values evolution and the different loading configurations (load and speed changing) was evaluated. The effect of temperature oscillations on pavement response is considered negligible (below 5°C). Thus the response was considered only load and speed-dependent, and a multiple linear

4 Development and deployment of an embeddable nano-carbon based strain technology

regression was carried out. The correlation yielded a coefficient of determination (R^2) of 0.73 for sensor N 2-3, which is of the same order of magnitude of the coefficient R^2 obtained for sensor C 2-3, equal to 0.78 (see Appendix 7-section 6.7.9 for regression statistics and coefficients). Note that the correlation was only tested on sensor N2-3 as there are data available (without suspicion of delamination) for all the load configurations. The availability of this correlation for both sensors shows that the strategy of sensor embedding in pavement is valid and can lead useful information on pavement status. The fact that the correlation coefficient are similar shows that the nanosensors proposed in this paper are an acceptable alternative to commercial sensors for this specific application. Moreover, with their much higher sensitivity, they are expected to have much better sensitivity to loading, and thus to provide access to finer-grained strain evolutions in pavement.

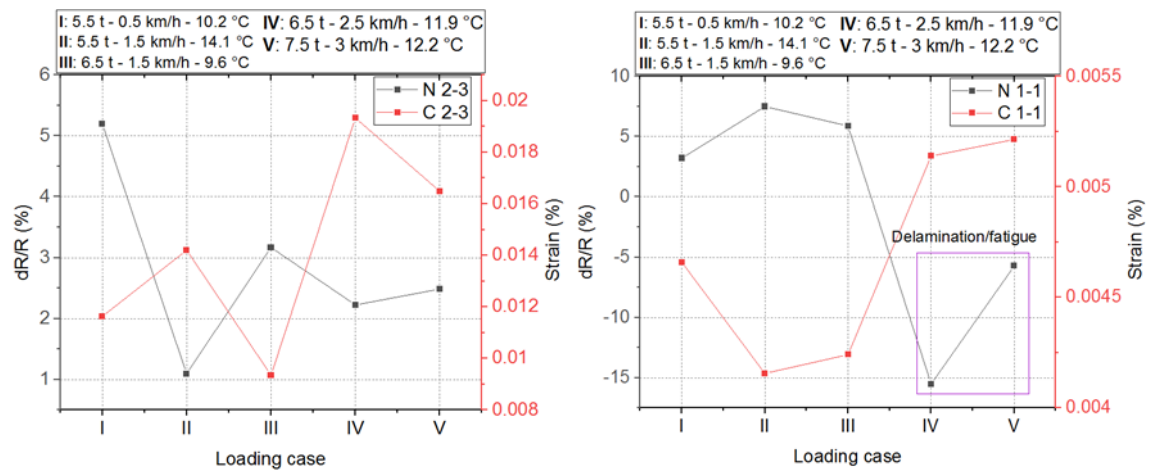


Figure 4.21 Maximum peak values evolution over the duration of the test. Left: sensors N 2-3 and C 2-3. Right: sensors N 1-1 and C 1-1

4.5.4 Quality of interface and impact on the road

In order to investigate the quality of the interface between the assembled sensing system and the asphalt, two cores are extracted in the field following the coring plan reported in Figure 4.22 Quality of the interface between the assembled sensing system and the asphalt: two cores extracted in the field.. In details, the cores have a diameter of 100 mm and are spaced of about 200 mm (center-to-center) distance. Core 5 is extracted so as to partially cover the assembled system (half of the interface), while the interface of core 2 is characterised by the tack-coat emulsion used during installation. Core 2 is used as comparative. The two samples are shown in Figure 4.22 Quality of the interface between the assembled sensing system and the asphalt: two cores extracted in the field.. A slight debonding of the interface is observed in core 5, as indicated by the red arrow in Figure 4.22 Quality of the interface between the

assembled sensing system and the asphalt: two cores extracted in the field., which does not occur in core 2. The fact that a relatively small area is instrumented with a total of 5 sensing devices (see Figure 4.7) may be the origin of a non-perfect bonding at the interfaces. Or else the detachment may have occurred during coring operation itself. Indeed the feedback obtained from a device of the same type previously installed on a larger section (see Figure 3.3) along with other sensing devices properly spaced, exhibits very good adhesion at the interfaces. Thus, considering the two field experiences it can be concluded that proposed technology is not intrusive for the road.

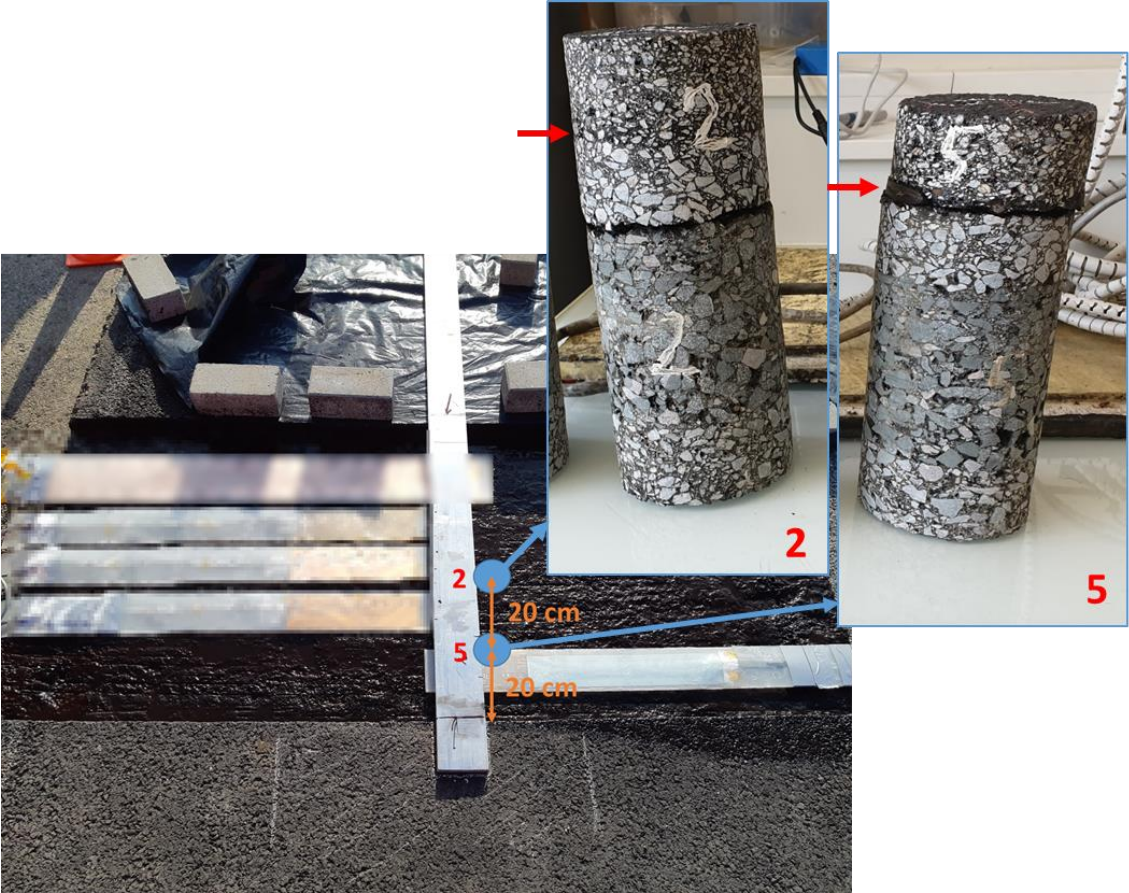


Figure 4.22 Quality of the interface between the assembled sensing system and the asphalt: two cores extracted in the field.

4.6 Conclusions

In this chapter, we demonstrate that the sensing properties CNM-based sensors can be exploited in the field for road monitoring. We propose a high-sensitive, hysteresis-free, embeddable sensor for traffic classification and monitoring of pavement health conditions. The devices are fabricated by drop-casting of the conductive mix (a carbon-clay nanocomposite active material) on E-glass substrate and polyimide substrate, as this latter

4 Development and deployment of an embeddable nano-carbon based strain technology

was identified as most appropriate substrate for integration within a pavement structure. Sensors sensitivity to strain was explored under cyclic strain up to 0.06 %. Devices on E-glass exhibit average gauge factor already 30 times bigger than commercial strain gauges based on metal foils. Even better performances are obtained for devices on polyimide with an average gauge factor 1.2 times higher than the best results obtained for devices on E-glass.

For integration in the pavement the devices on polyimide are encapsulated between two bitumen compatible sheets of thermoplastic polymer together with commercial strain gauges for comparison. This approach comes from the Altaroad's breakthrough InTrack solution. The assembled system is embedded in the road pavement and tested under the FABAC accelerated pavement testing machine (University Gustave Eiffel facility). Remote monitoring is carried out via connection to the PÉGASE data acquisition system. The on-site performance of the proposed sensing technology is very promising. The sensors withstand the high temperatures and high compression efforts typical of the installation without degradation proving to be appropriate to monitor the quality of the construction phases. The sensors remain operational after 80700 dual-wheel loadings despite an increase of the baseline resistance. The dynamic sensor responses to different loading configurations is investigated and the on-site sensitivity to strain is enhanced by a factor of 600 with respect to commercial strain gauges. This suggests that the system could provide meaningful information even when positioned deeper in a road pavement, where measured strain could be smaller than 0.01 %.

Overall, the proposed technology represents a promising solution for traffic and pavement health conditions monitoring. The assembled device is thin and bitumen compatible and features high sensitivity enabling the use for precise measurements even at lower layers in the road structure. Thanks to its geometry the system can cover the width of a lane and embed more than 30 sensors.

This is the first time such a demonstration is made, high sensitivity and reasonable lifetime is shown for a technology that surpasses any commercial options and most research results.

5 CONCLUSIONS AND PERSPECTIVES

5.1 Conclusions

This thesis aimed at demonstrating the feasibility of pavement monitoring based on embedded sensing technologies. We showed the advantages of using sensor data to track pavement conditions and we propose an innovative embeddable nanotechnology.

The bibliographic review showed a growing interest in the use of embedded sensing technologies to track actual pavement conditions and their evolution with time. Through the connection to adapted data acquisition systems, these devices can measure pavement response to load and to climatic variations remotely, continuously, and with no traffic disruption. These aspects make instrumentation more appealing with respect to traditional ex-situ monitoring methods, such as visual inspection and deflection measurements. Indeed, the integration of sensors in the road pavement allows the assessment of the complete history of pavement conditions, starting from sensor installation. Collecting this information is expected to help road managers to define cost-effective asset management plans. Hence, the establishment of framework for sensor data interpretation is crucial.

We provided a descriptive analysis of several sensing technologies available on the market, in terms of operating principle, accuracy of measurement, and requirements for the embedment in the road pavement. Some of these devices were deployed in test sections for the development of strategies for data interpretation and inverse calculation. It emerged that installation is the most critical phase in the lifetime of in-roadway devices due to the high temperatures of the asphalt mix, as well as rolling and vibrations generated during compaction. In addition, the high costs of marketed sensing devices, as well as their geometry, may be a limitation in the implementation of a suitable sensor network in terms of number of embedded devices.

Due to the thermo-viscoelastic behaviour of bituminous materials, pavement response depends on multiple parameters, such as applied load, loading frequency, load trajectory,

and temperature. Hence, strategies for data interpretation have to include procedures to take into account the influence of the listed variables on measurements.

Overall, the analyses revealed a lack of strategies for pavement distress prediction based on embedded sensors, as well as, some limitations to sensors deployment in the field, due to their poor adaptability to the harsh road environment (construction phase and service life). In this respect, we explored the use of carbon nanomaterials for road pavement application. Nanometer-sized particles have unique properties which cannot be found in their relative bulk counterparts. In most of the studies they were incorporated to the asphalt mixes to improve their mechanical performances and/or endow them with piezoresistive capabilities. However, the fabrication of these composite materials presented some limitations. For example, the important quantity of nanoparticles required to make asphalt mixes more resistant and/or turn them into conductive materials resulted in unaffordable costs for real scale applications.

From the point of view of strain sensing, some studies demonstrated that a strong alternative to such composite materials relies CNM-based strain sensors fabricated on thin flexible substrates.

The thesis proposes, via an accelerated pavement test, a validation of asphalt strain gauges as monitoring method for fatigue prediction in a road pavement. Thus, we further explored the use of embedded sensors for inverse calculation of pavement mechanical conditions via the instrumentation of an existing road with a network of asphalt strain gauges. The same trial section was the environment for a first validation of a novel sensing technology based on the use of carbon-based flexible strain sensors, later tested under an accelerated pavement test. Thereby we demonstrated how the proposed nanotechnology can overcome some of the drawbacks of existing sensing devices in terms of geometry, compatibility with the road environment, sensitivity and costs.

First, we investigated the use of asphalt strain gauges for detection of damage of a single layer of road pavement. To this end, we worked on a dataset collected on the accelerated pavement testing facility of the University Gustave Eiffel within the European project BioReparation. A fatigue test was carried out on four sections with different bituminous surface layers. The performances of all sections were monitored regularly by using traditional monitoring methods (such as Benkelman beam deflections, FWD deflections, and

visual inspection) and instrumentation (such as asphalt strain gauges and temperature probes).

The comparison of field measurements revealed that sensor measurements, besides being consistent with the observation of the first cracks and deflection measurements, were able to detect the occurrence of fatigue well before traditional monitoring methods. This was also validated by the analysis of sensor locations with respect to FWD deflection measurements and the crack pattern. It highlighted that the sensors alerting for damage occurrence were actually in the areas where cracks were observed. At the same time it emerged that sensors may create weakness points in the road pavement from where cracks may originate.

Furthermore, the accuracy of sensor measurements was evaluated via the comparison between strains measured at 1 million loads with numerical strains obtained from calculations based on pavement moduli inverse calculated from deflection measurements. Relative low differences were found between field and computed strains, confirming that asphalt strain gauges can provide reliable information about pavement mechanical conditions. The model also showed the localized nature of the fatigue phenomenon. In fact, for the same section, the inverse calculated modulus of the bituminous layer of the damaged zone (showing cracks) halved its initial value, while on the non-damaged zone the modulus remains almost unaffected.

Finally, we provided a strategy for sensor data interpretation, namely a methodology to account for temperature influence on strain measurements within a road.

As a result of this experimentation, we used asphalt strain gauges for the instrumentation of an existing road and we focused on the inverse calculation of pavement mechanical conditions as well as on the analysis of interface contribution at high temperatures. A trial section was built by instrumenting an existing road with six asphalt strain gauges and the InTRACK solution. The sensors were placed on the top of the existing surface layer after the application of a tack-coat emulsion. Then, a 5 cm-thick layer of BBSG was paved and compacted. Remote acquisition was carried out via connection to the data acquisition system.

The InTRACK gave very promising results in terms of design (integration of a large number of sensors), possibility to embed both temperature and strain sensors, adaptability of the system to the road environment (construction phase and service life). The system underwent waterproofing issues, hence it could not be exploited in the following phases of the experimental work and we focused on the exploitation of ASGs only.

As the composition of the existing road was unknown, a coring campaign was carried out. We studied in the lab the viscoelastic behaviour of the bitumen used for the tack coat emulsion (DSR apparatus) as well as of the different asphalt layers (cyclic indirect tensile test, complex modulus test, modal test). Test results were modelled with the 2S2P1D model. We performed a measurements campaign with a truck of known load, at two different speeds and two different trajectories. The analyses of experimental results confirmed the influence of temperature and speed on pavement response. Moreover, it emerged that, at high temperatures, the sensitivity of sensor measurements to the truck transverse position with respect to the sensor location was very high. In fact, strain profiles recorded at the same main speed and main trajectory presented non negligible differences not only in the peak values but also in tension-compression sequence. This underlined the need of a large number of sensors in the transverse direction to track vehicle trajectory.

Finally a model was built in Viscoroute© to fit measured strain profiles and determine the pavement mechanical conditions. In particular, we focused on the contribution of interfaces on the pavement response. For the characterisation of the asphalt layers we used the results of the test campaign performed in the lab. We modelled the interfaces as 2 mm-thick layers having the mechanical properties of the bitumen of the tack-coat emulsion. We compared three models, elastic with fully bonded interfaces, viscoelastic with fully bonded interfaces, and viscoelastic with viscoelastic interfaces. The results showed that at high temperatures a viscoelastic model that takes into account the viscoelastic behaviour of the interfaces can better predict the pavement response under moving loads. It emerged that the contribution of the interfaces is not negligible. In fact, the elastic and viscoelastic models with fully bonded interfaces led to a wrong estimation of the strain profiles. The obtained results rather show that sliding is occurring at the interfaces and that its mechanical behaviour depends on the temperature and loading frequency.

Overall, the first two parts, dedicated to the study of instrumentation (asphalt strain gauges and temperature probes) deployment for pavement monitoring, led us to conclude that the use of strain sensors can track pavement conditions over its service life and alert for maintenance. However, a large number of sensors is required for the development of data treatment strategies that account for the influence of varying loading conditions (temperature, speed, vehicle trajectory). The deployment of a large sensor network seems to be restricted by the costs of devices available on the market as well as their geometry and

their possible intrusiveness in the road pavement. In this respect, the promising results obtained with the InTRACK motivated the study conducted in the last part of the thesis.

We finally developed an embeddable sensing technology for pavement monitoring that may overcome some of the above mentioned drawbacks. A hysteresis-free, high-stability, embeddable nanocarbon-based strain sensor was fabricated and its implementation for pavement monitoring was validated with accelerated pavement testing. The active nanocarbon material was a carbon-clay nanocomposite: graphene sheets supported on sepiolite are mixed with multi-walled carbon nanotubes, forming a piezoresistive material. It was dispersed in water and drop-casted onto E-glass substrate and polyimide substrate. Electrical, thermal and electromechanical characterizations of both devices are performed in the lab. E-glass and polyimide show a very good linearity with Gauge factor respectively 40 times and 80 times higher than commercial strain gauges. Due to the better compatibility of the substrate with pavement materials and in-situ conditions, six devices on polyimide were further encapsulated between two bitumen-compatible thermoplastic sheets together with commercial strain gauges (for comparison purposes). The sheets were sealed together inside by application of heat on the side of the polymer, which melted together the two sheets. The assembled system was then integrated under a 4 cm-thick bituminous layer using regular pavement construction process. Remote acquisition was carried out via connection to the data acquisition system.

All the sensors (commercial and nano) withstood the installation phase (high temperatures and high compression efforts) without interruption degradation of the signal quality and without discontinuity in resistance values. The sensors remained operational after 80700 dual-wheel loadings. The dynamic sensor responses to different loading configurations was also investigated and the on-site sensitivity to strain was found to be enhanced by a factor of 600 with respect to commercial strain gauges.

We demonstrated how the properties of carbon-based nanotechnologies can be exploited for road pavement application. The proposed technology is thin, bitumen compatible, features high sensitivity as well as reasonable lifetime. In addition, its geometry allows the implementation of a large and relatively compacted sensor network.

Thus, the assembled technology features better design and quality of measurements with respect commercial options. Hence, it is a promising solution for pavement health monitoring and traffic detection.

5.2 Perspectives

This work demonstrates through full-scale applications the relevance of asphalt strain gauges in predicting damage occurrence. It shows how the pavement mechanical conditions of a multi-layered pavement structure can be assessed via asphalt strain gauges and temperature probes as well as the need to develop strategies for sensor data interpretation that take into account the influence of various parameters on pavement behaviour. Finally, it proposed a high sensitive, less intrusive sensing nanotechnology for embedded pavement monitoring.

With respect to the obtained results, further research deserves to be carried out.

In terms of short-term perspectives, we suggest to:

- Develop additional strategies for strain sensor data interpretation. In this thesis we propose a methodology to account temperature influence on strain measured within a road pavement. We suggest to a full-scale validation of the proposed methodology. In addition, it seems interesting to develop similar procedures to account for the influence vehicle speed and vehicle trajectory on strain measurements. Such procedures could be implemented in a monitoring tool and so used to detect the occurrence of damage in a road pavement and evaluate its remaining service life.
- Further investigate the influence of interface contribution on pavement response with temperature and loading frequency, as well as its modes of damage and how they can be effectively detected.
- Further investigate the use of the proposed nanotechnology for traffic detection, notably weigh-in-motion application.
- Optimize the fabrication process of carbon-based strain gauges in order to open the doors to the serial fabrication of the devices with low variability in resistance, gauge factor, and temperature sensitivity.

In terms of long-term perspectives, we suggest to:

- Make the proposed technology wireless. It is known that the presence of cables makes the installation of embedded technologies problematic. A wireless version of the proposed strain sensor should be developed. The device could be powered by using an internal battery. A study should be conducted to evaluate the power consumption of the device, the duration of the battery with respect to the pavement service life, as well as the accessibility for battery charging.

- Investigate the relevance of the system in detecting the occurrence of damage in a road pavement as well as its durability after a larger number of load repetitions by performing full-scale fatigue tests. This will lead to the definition of a reasonable number of devices (and consequent location on a stretch of road) required for an effective evaluation of the pavement mechanical conditions.
- Investigate the compatibility of the proposed technology with road maintenance actions.
- The use of the proposed technology for continuous pavement monitoring could generate a big volume of data. To overcome this issue, the acquisition could be triggered based on pre-defined thresholds (allowing the detection of heavy vehicles only) and over specific time intervals. In addition, from the point of view of data interpretation, coupling a purely mechanical approach (used in this work) with a probabilistic approach could lead to the development of more exploitable techniques for data analyses.

The proposed suggestions could lead to the industrialization of the proposed nanotechnology and the development of more advanced strategies for sensor data interpretation. This could support road owners and road management entities to define cost-effective management plans.

Figure 5.1 reports an example of the implementation and deployment of the proposed technology for health monitoring on a road section according to the proposed suggestions. The sensing layers could be embedded at different depths in the road pavement, at the basis of the structural bituminous layers as well as at the basis of the surface course (thanks to their thin thickness). The number of devices in the traffic direction, as well as the optimal distance between them, should be estimated within a full-scale fatigue test. The devices will provide continuous or punctual strain and temperature measurements. The latter could be used for the calibration of procedures to account for trajectory, speed, and temperature variation, as long as the properties of in-situ materials are known (via FWD measurements or laboratory tests performed on cored samples). Finally, the implementation of the above-mentioned procedures, will lead to the evaluation of road pavement conditions.

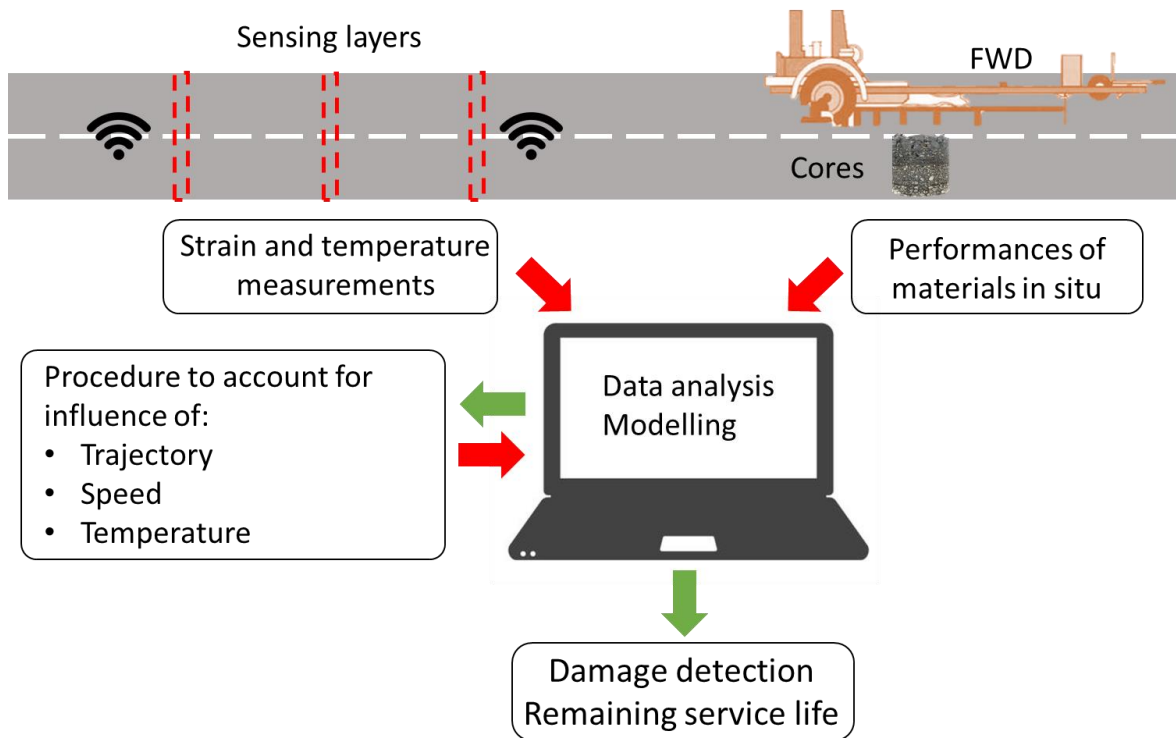


Figure 5.1 Vision of pavement monitoring based on embedded sensors: deployment of the proposed nanotechnology for strain and temperature measurements, assessment of the performances of in-situ materials, calibration of strategies for sensor data analyses, detection of the occurrence of damage and pavement service life.

6 APPENDIXES

6.1 Appendix 1

The following graphs report the evolution of the shape parameters A_1 , A_2 and d_{tot} (see section 2.3.2.2) as a function of the number of loads for sensors Mix1-L1 (Figure 6.1), Mix2-L3 (Figure 6.2), EME2-L1 (Figure 6.3) and EME2-L2 (Figure 6.4).

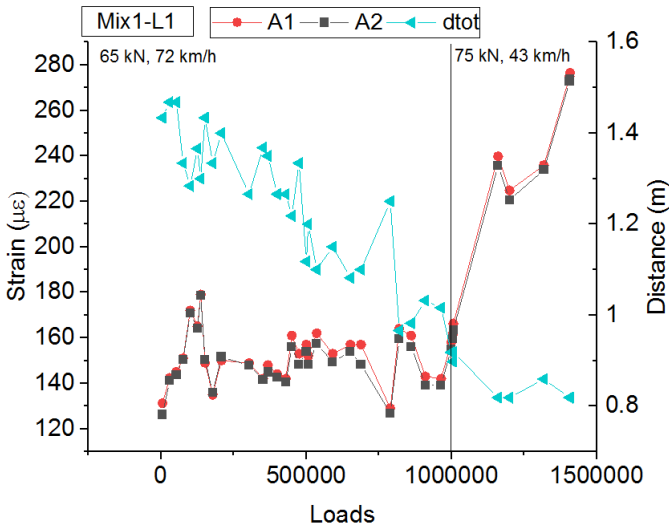


Figure 6.1 Sensor Mix1-L1: evolution of the shape parameters A_1 , A_2 and d_{tot} with the increase of the number of loads.

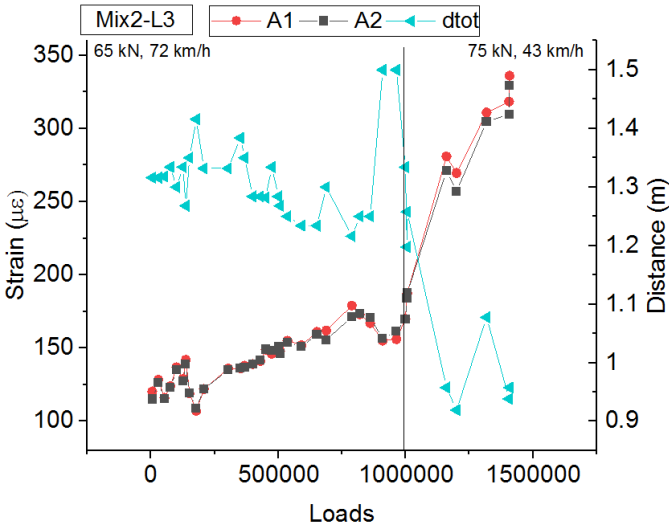


Figure 6.2 Sensor Mix2-L3: evolution of the shape parameters A_1 , A_2 and d_{tot} with the increase of the number of loads.

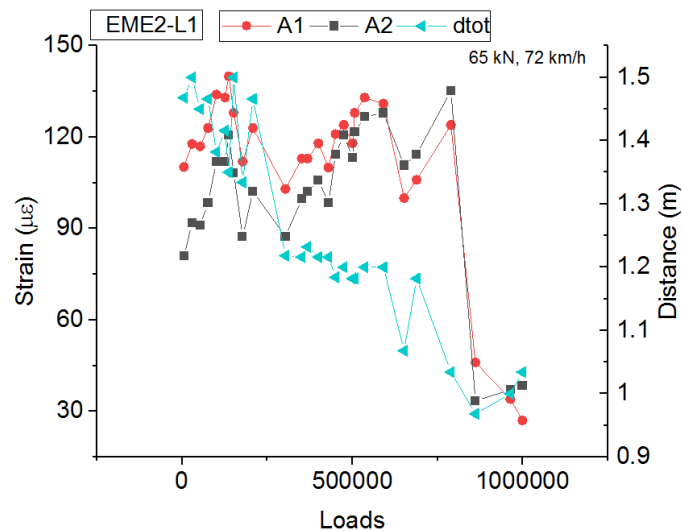


Figure 6.3 Sensor EME2-L1: evolution of the shape parameters A1, A2 and dtot with the increase of the number of loads.

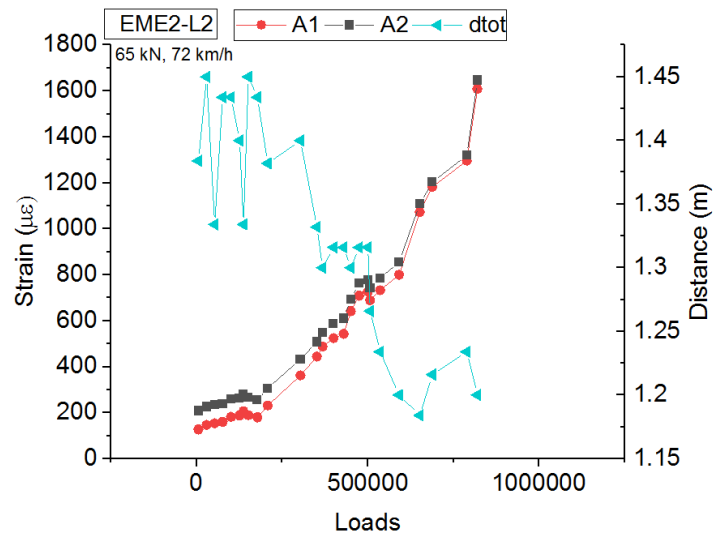


Figure 6.4 Sensor EME2-L2: evolution of the shape parameters A1, A2 and dtot with the increase of the number of loads.

6.2 Appendix 2

The following graphs show the field measured maximum longitudinal strain at the basis of the bituminous the equivalent strain at the reference temperature of 10 °C obtained by applying the methodology fully described in Section 2.5. In particular the results obtained for sensors Mix1-L3 (Figure 6.5), Mix2-L2 (Figure 6.6), EME2-L1 (Figure 6.7) and EME2-L2 (Figure 6.8) are reported below.

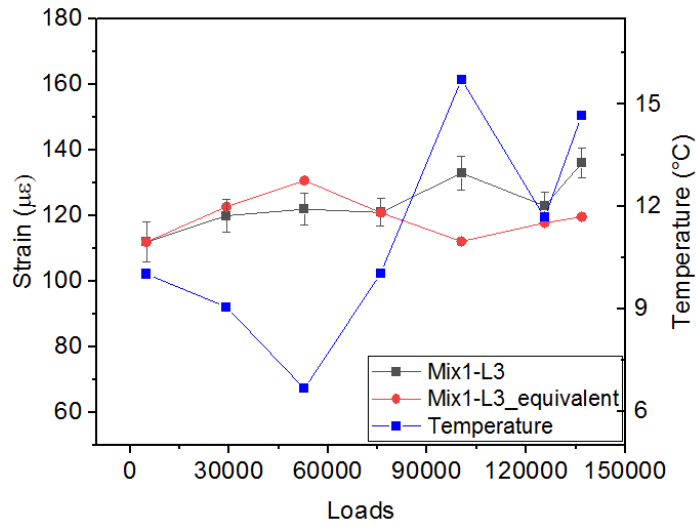


Figure 6.5 Equivalent maximum longitudinal strain at the reference temperature of 10 °C for Mix1-L3. Correction applied in the first 136800 loads.

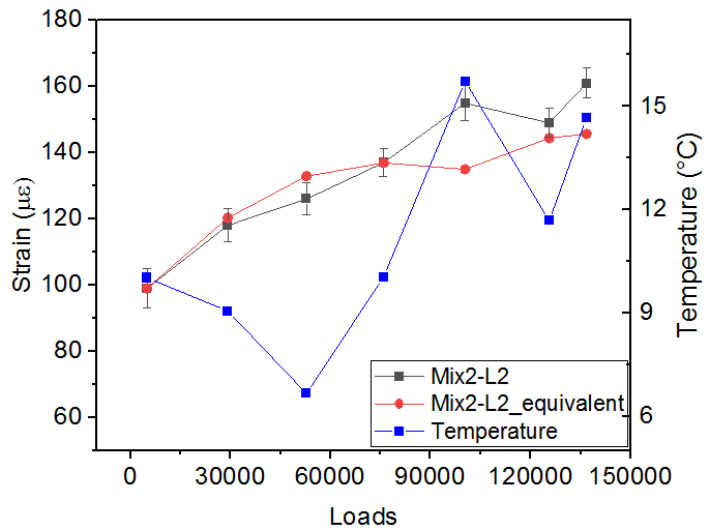


Figure 6.6 Equivalent maximum longitudinal strain at the reference temperature of 10 °C for Mix2-L2. Correction applied in the first 136800 loads.

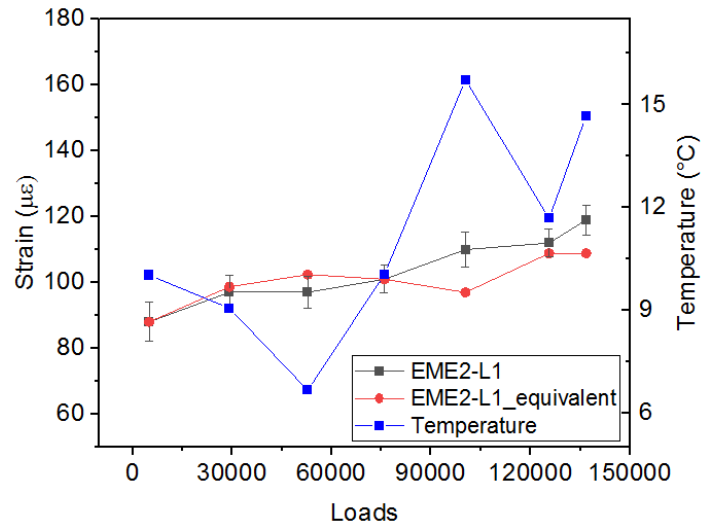


Figure 6.7 Equivalent maximum longitudinal strain at the reference temperature of 10 °C for EME2-L1. Correction applied in the first 136800 loads.

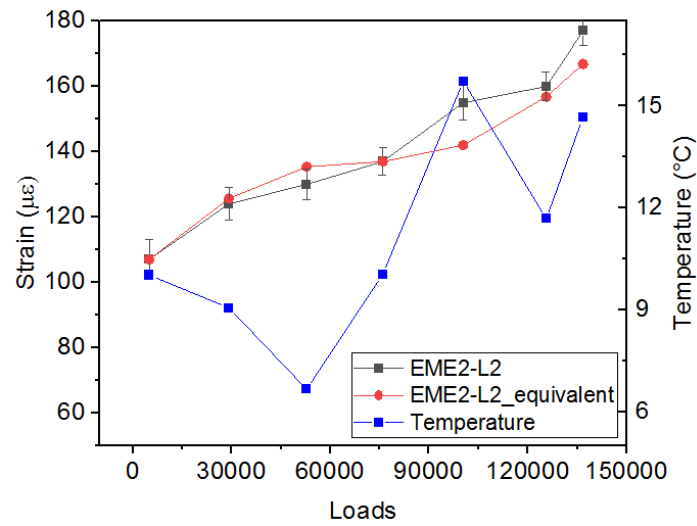


Figure 6.8 Equivalent maximum longitudinal strain at the reference temperature of 10 °C for EME2-L1. Correction applied in the first 136800 loads.

6.3 Appendix 3

Figure 6.9 shows the two truck trajectories defined for the campaign of measurements, T0 (Top) and T1 (Bottom).

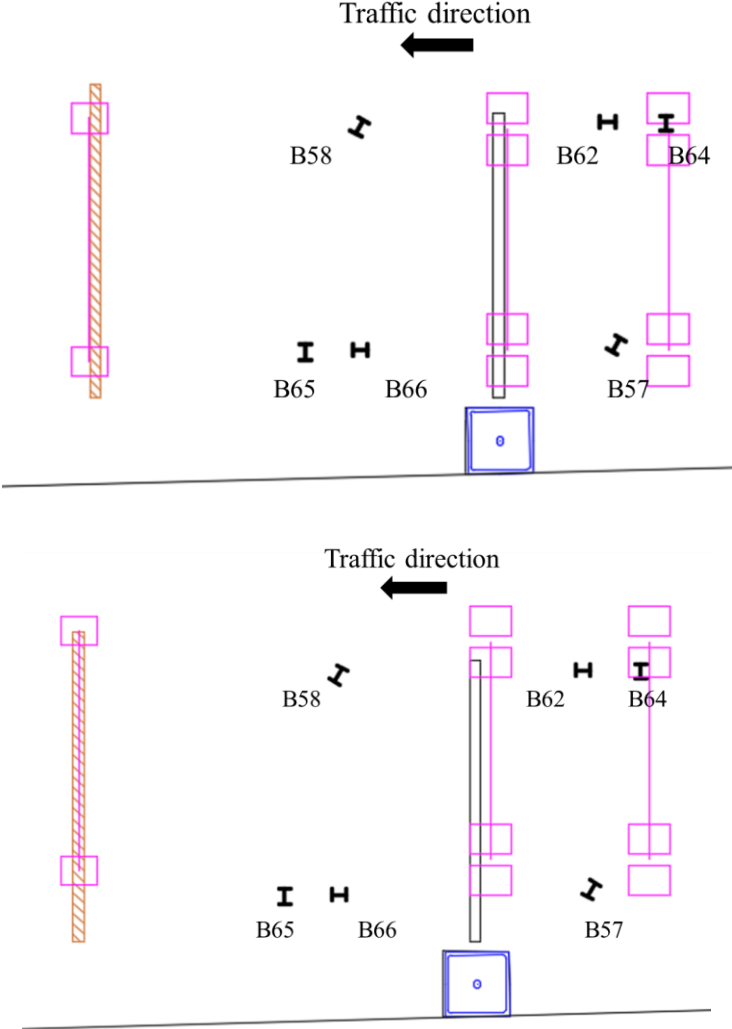


Figure 6.9 (Top) Trajectory T0: $\Delta D_y - \Delta D_{y,ref} = 0$ cm. (Bottom) Trajectory T1: $\Delta D_y - \Delta D_{y,ref} = 30$ cm.

6.4 Appendix 4

Four samples (C7, C8, C9 and C10) were cored in the experimental site following the layout shown in Figure 6.10. The drills were executed around the instrumented area at a distance of about 3.50 m from the sensors in order not to impact the sensors measurements.

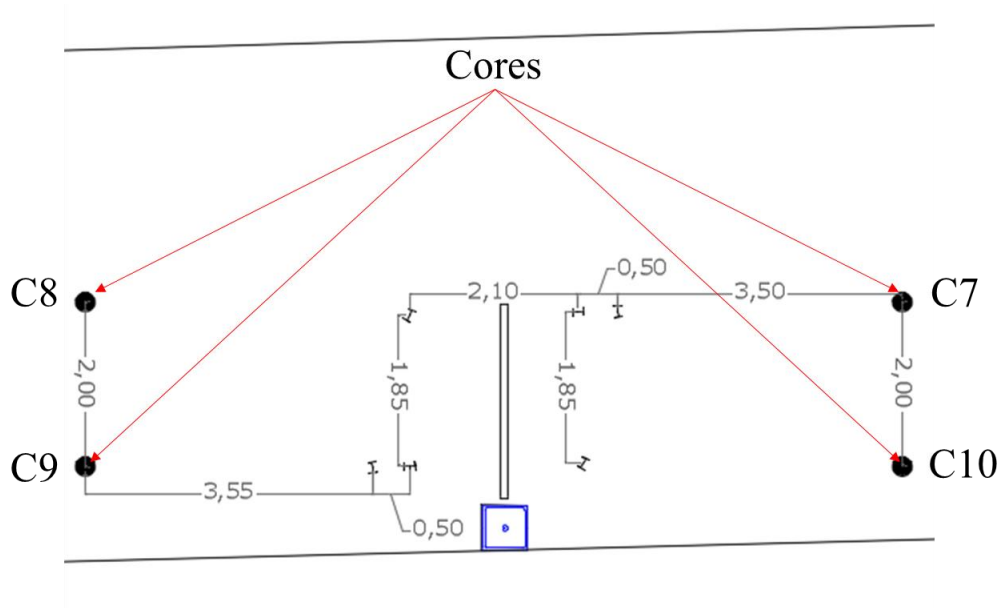


Figure 6.10 Coring plan followed on the experimental site to extract 4 samples: C7, C8, C9 and C10. A coring drill with a diameter of 230 mm was applied down to a depth of about 200 mm.

Table 6.1 Nomenclature, height and picture of the cores extracted in the field.

Details	Picture
Name C7	
Height (mm) 125	
Name C8	
Height (mm) 100	



Name C9
Height (mm) 195



Name C10
Height (mm) 175



6.5 Appendix 5

6.5.1 Bitumen of the tack coat emulsion

The complex modulus test were performed by using the DSR apparatus of the Eiffage Route Research Centre (Figure 6.11) at different temperatures, from $-20\text{ }^{\circ}\text{C}$ to $70\text{ }^{\circ}\text{C}$, and different frequencies, from 0.01 Hz and 10 Hz as shown in Table 6.2. The test results are modelled with the 2S2P1D model, which parameters are listed in Table 6.3.



Figure 6.11 DSR device EC-Twist 502 manufactured by Anton-Paar at the Eiffage Route Research Centre.
Table 6.2 Temperatures and frequencies used for DSR complex modulus test on the bitumen of the tack coat emulsion.

Temperature (°C)	Frequency (Hz)
	0.01
	0.0215
	0.0464
	0.1
-20, -10, 0, 10, 15, 20, 30,	0.215
40, 50, 60, 70	0.464
	1
	2.15
	4.64
	10

Table 6.3 2S2P1D model parameters for the bitumen of the tack coat emulsion.

E_{00} (MPa)	E_0 (MPa)	k	h	δ	τ_E	β
0	2250	0.22	0.5	2.1	0.00011	500

6.5.2 Asphalt mixes

The composition of the BBSG 2 0/10-35/50 used for Layer 1 of the experimental site is reported in Table 6.4.

Table 6.4 Composition of the BBSG 2 0/10-35/50.

Aggregates	Percentage (%)
6/10	33.4
4/6	17.0
0/4	40.0
Filler	4.2
Bitumen	
35/50	5.4

The MTS hydraulic press used for the cyclic indirect test and direct tension-compression test on the asphalt mix is shown in Figure 6.12. The maximum load of the press is 100 kN and

the environmental chamber (MTS 651) allows temperature variations between $-30\text{ }^{\circ}\text{C}$ and $50\text{ }^{\circ}\text{C}$. The press is also equipped with a hydraulic power unit control and a load unit control.

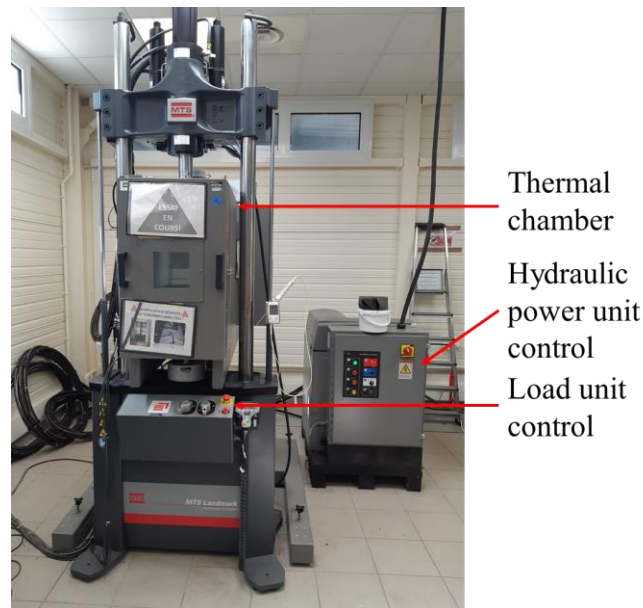


Figure 6.12 Overview of the MTS hydraulic press used for the CIT and DTCT on the asphalt mix. The press is equipped with a hydraulic power control, a load unit control and an environmental chamber (MTS 651).

Table 6.5 reports the air voids content and the 2S2P1D parameters that fit experimental results obtained by performing the cyclic indirect tensile test, the modal test, and the direct tension-compression test on the BBSG 2 0/10-35/50. The tests were carried out on samples from the field and samples manufactured in the lab as shown in Table 3.4.

Table 6.5 2S2P1D model parameters and air void content for the tested specimens (Layer 1).

	Air voids content (%)	E_{00} (MPa)	E_0 (MPa)	k	h	δ	τ_E	β
CITT (Field)	13.1	80	29500	0.24	0.60	2.3	0.015	∞
MT (Field)	13.1	100	28400	0.20	0.56	1.8	0.057	∞
DTCT (lab, vertical)	6.8	50	30500	0.21	0.70	2.2	0.075	∞
DTCT (lab, compacting)	7.5	180	30900	0.21	0.65	2.1	0.075	∞

Some difficulties were found when performing the CITT on disk-shaped samples of Layer 3 extracted from the field. This layer in fact had an air voids content of 24 % and crumbled

very easily. Table 6.6 reports the measurements retained after performing the CITT on Layer 3: temperatures of 15, 25 and 35 °C and frequency of 10 Hz.

Table 6.6 Measurements retained after performing the CITT on a disk-shaped sample of Layer 3: temperatures of 15, 25 and 35 °C and frequency of 10 Hz.

Temperature (°C)	Frequency (Hz)	$ E^* $ (MPa)	Phase angle (°)
15	10	9501	15.2
25	10	5944	18.9
35	10	3624	-

Figure 6.13 reports the results obtained by performing the MT on a beam-shaped samples of Layer 5 extracted from the field. The results are modelled with 2S2P1D model (master curve and Cole-Cole curve). The test was performed at three temperatures (as suggested in (Carret, 2018)): 17 °C, 35 °C and 50 °C. The 2S2P1D parameters are reported in Table 6.7.

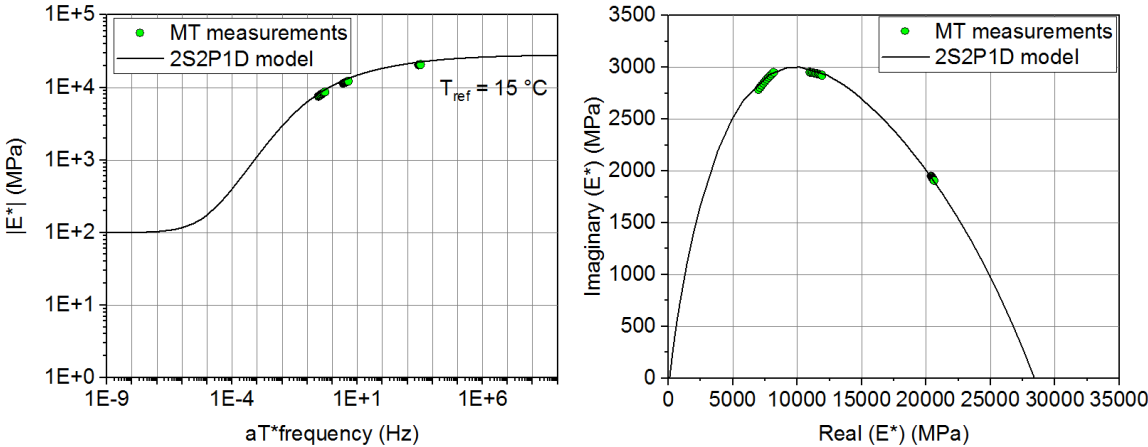


Figure 6.13 2S2P1D model fitting for Layer 5 beam-shaped sample tested under modal test (at 17 °C, 35 °C and 50 °C): (Left) master curve ($T_{ref} = 15 \text{ °C}$), (Right) Cole-Cole diagram.

Table 6.7 2S2P1D model parameters for Layer 5.

E_{00} (MPa)	E_0 (MPa)	k	h	δ	τ_E	β
100	10000	0.28	0.35	1.9	0.04	∞

6.6 Appendix 6

Table 6.8 reports the details concerning all the truck passages, the theoretical loading configuration, as well as the measured surface temperature, the actual truck trajectory, and truck speed.

Table 6.8 Details of all the truck passages: theoretical loading configuration, actual loading configuration and measured surface temperature.

Date: 17/07/2018				
Theoretical loading configuration	Passage n.	Speed (km/h)	$\Delta D_y - \Delta D_{y,ref}$ (cm)	Temperature (°C)
Speed = 10 km/h Trajectory: T0	P1	12	0	50
	P2	12	2	53
	P3	13	-2	53
	P4	13	-10	54
	P5	12	2	54
Speed = 20 km/h Trajectory: T0	P6	22	4	55
	P7	22	-3	55
Speed = 10 km/h Trajectory: T1	P8	12	23	50
	P9	12	30	50
	P10	13	27	50
	P11	17	28	50
Speed = 20 km/h Trajectory: T0	P12	18	-1	36
	P13	21	0	36
	P14	22	-3	36
	P15	21	8	37
	P16	21	-7	37
	P17	21	-6	37

Table 6.9 and Table 6.10 reports some of the measurements recorded respectively the 17th July and the 18th July when the passing truck moves at 20 km/h on the trajectory T0. In the first case the surface temperature is around 55 °C, in the second case around 36 °C. The graphs in the left column group together the signals for each sensor, while in the histograms in the right column data are grouped by axle and by passage.

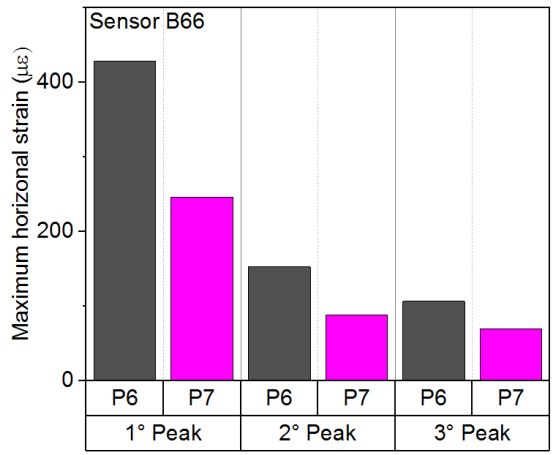
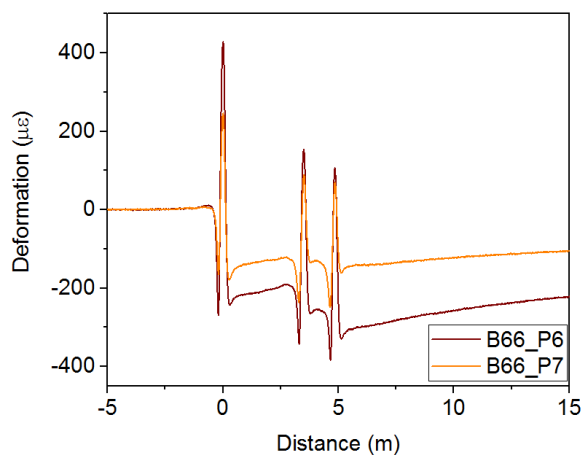
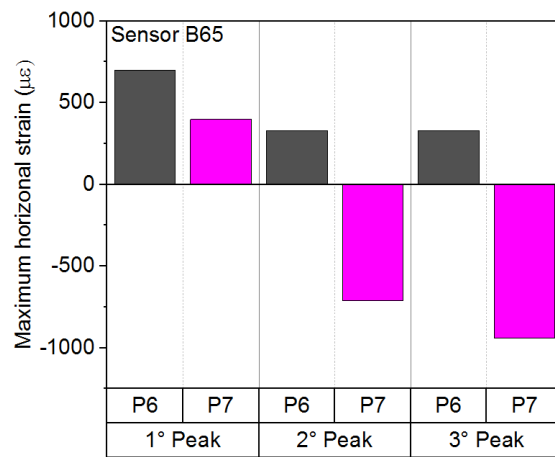
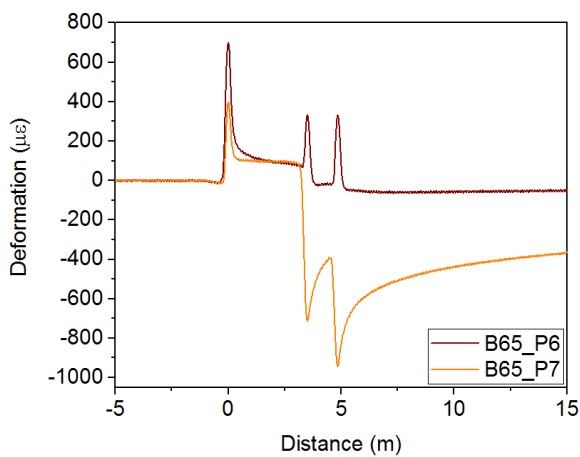
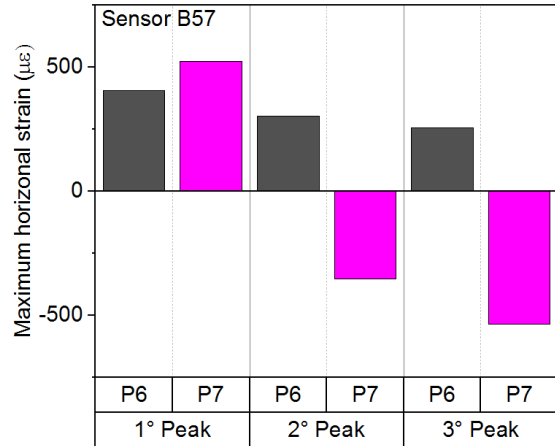
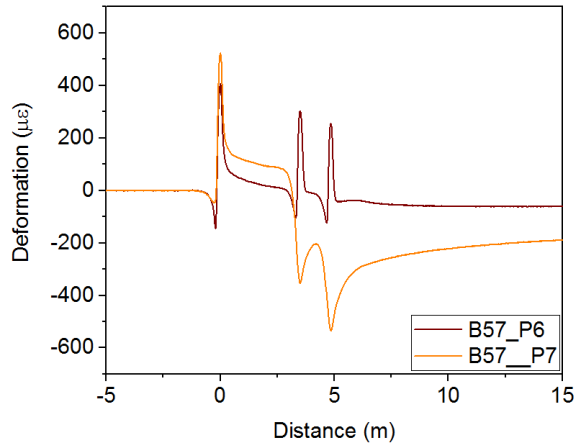
Table 6.9 Deformations measured on the experimental site during the campaign of measurements with a truck: surface temperature = 55 °C, $\Delta D_y - \Delta D_{y,ref} = 0$ cm (trajectory T0), speed = 20 km/h. The signals are grouped per sensors. Positive values correspond to extension.

Theoretical loading configuration:

Date: 17/08/2018

Trajectory = T0

Speed = 20 km/h



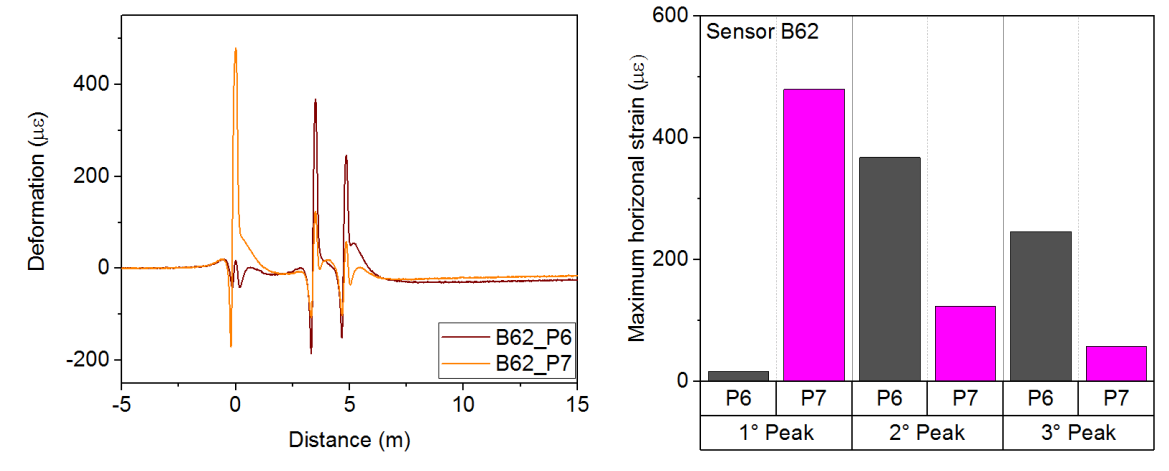
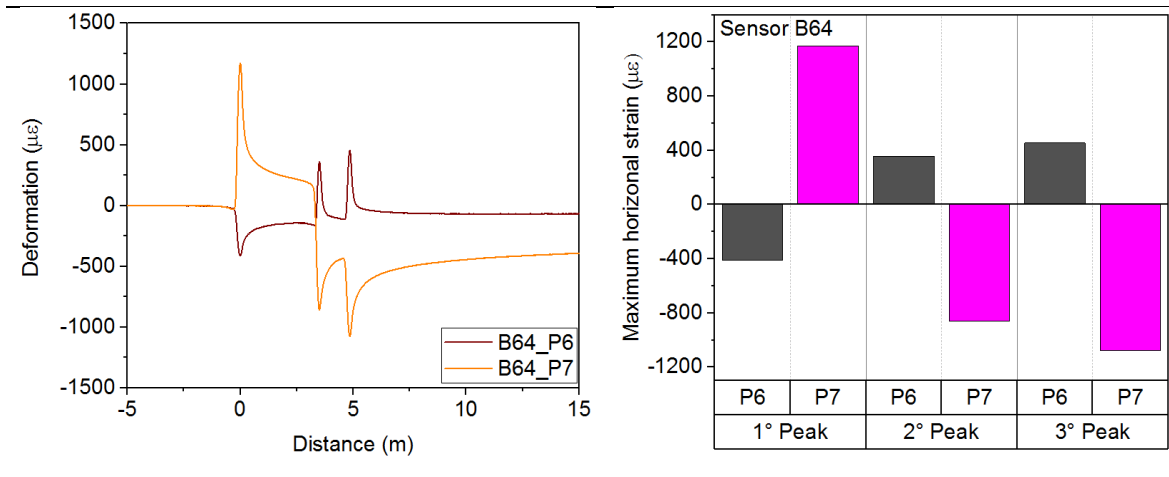


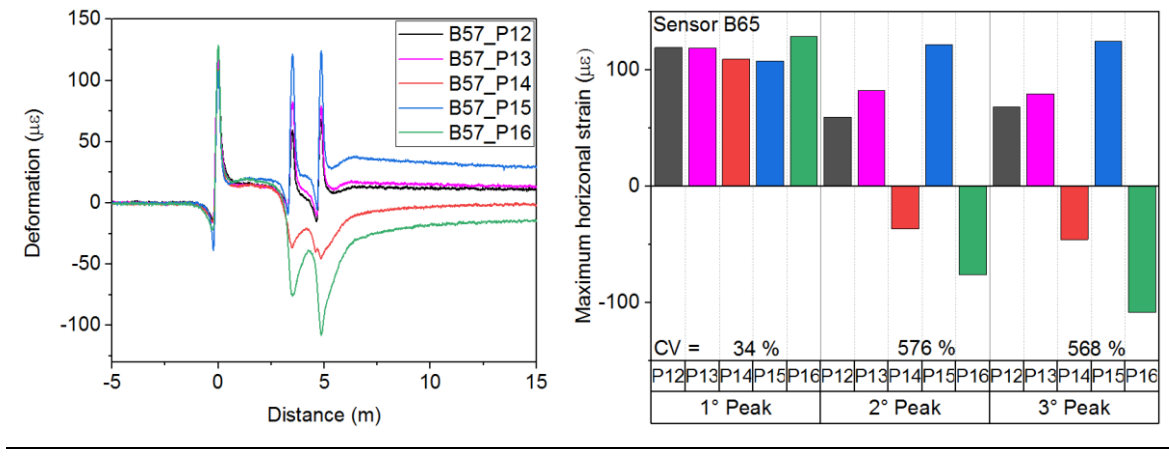
Table 6.10 Deformations measured on the experimental site during the campaign of measurements with a truck: surface temperature from 36 °C to 37 °C, $\Delta D_y - \Delta D_{y,ref} = 0$ cm (trajectory T0), speed = 20 km/h. The signals are grouped per sensors. Positive values correspond to extension.

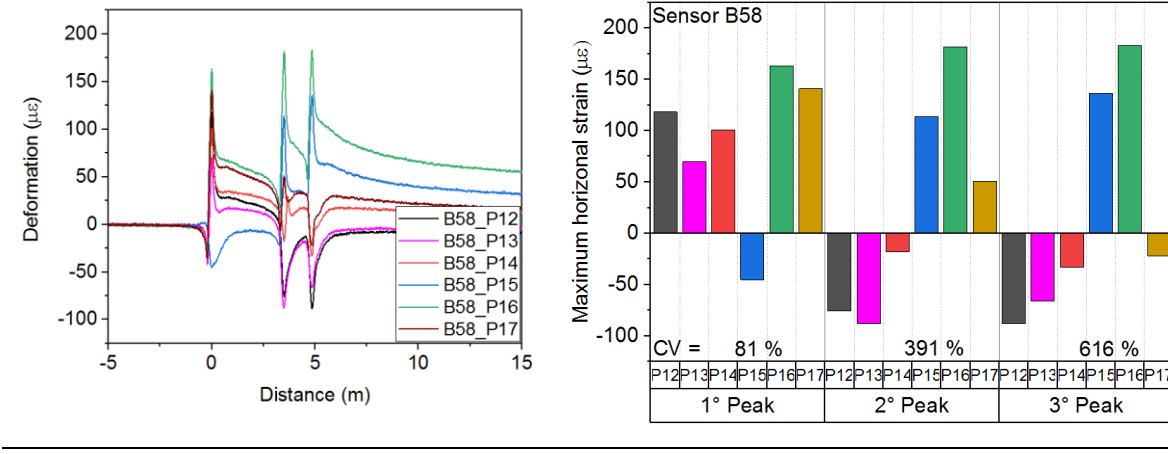
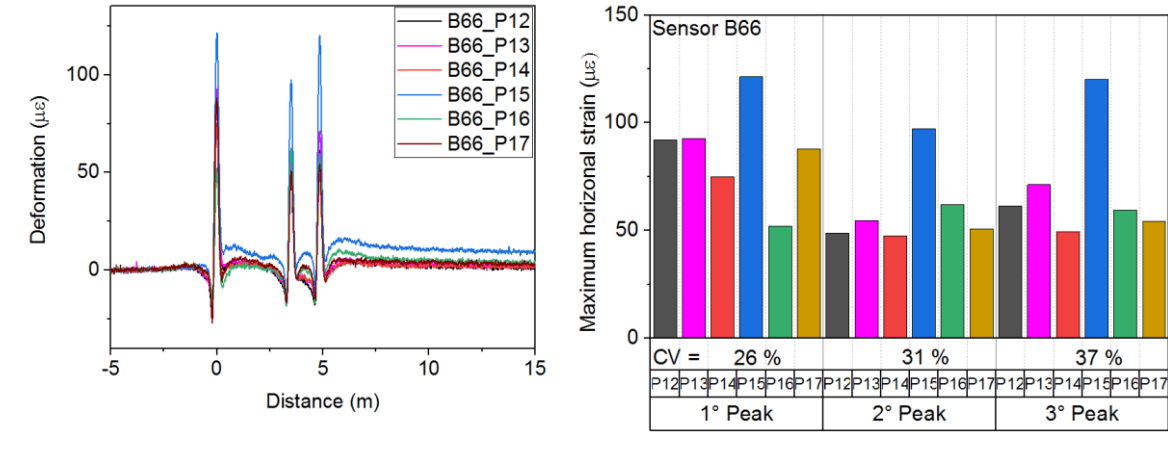
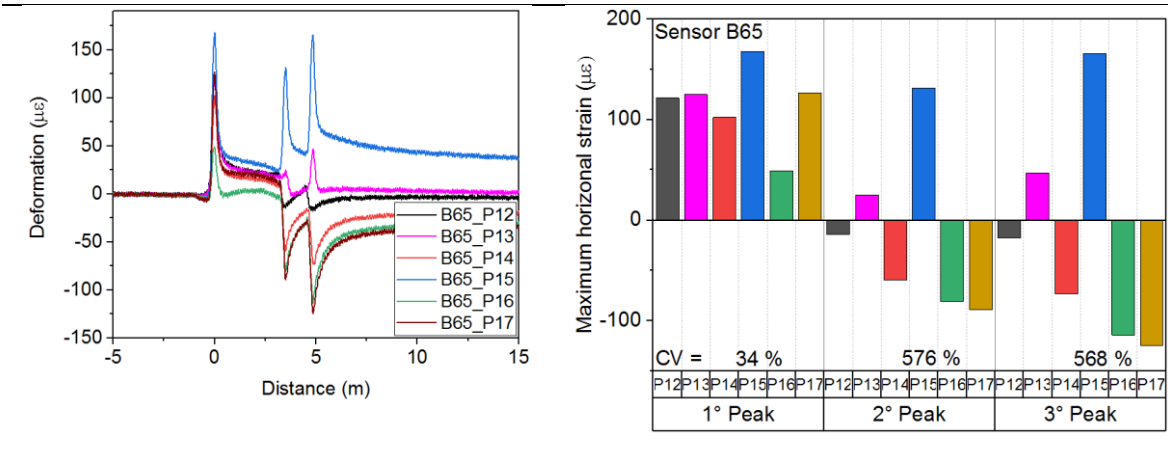
Theoretical loading configuration:

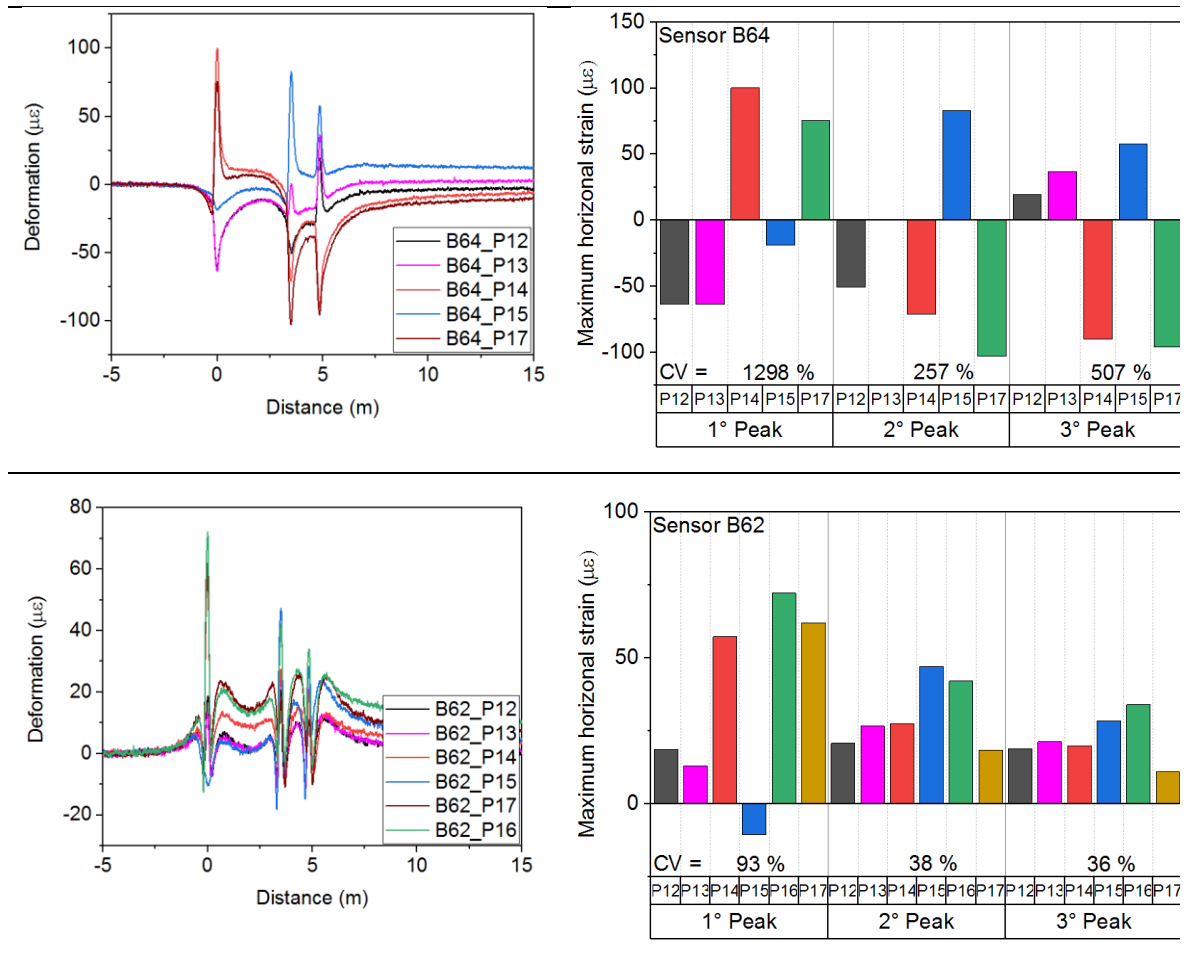
Date: 18/08/2018

Trajectory = T0

Speed = 20 km/h







6.7 Appendix 7

6.7.1 Four-point bending test

The configuration of the four-point bending test is showed in Figure 6.14. Note that $F/2$ is a half of the total applied force (F); L_i is the distance between the loading pins, L_e is the distance between the supporting pins, L , b and d are the dimensions of the substrate (respectively length, width and thickness). In this case, being $L_i = \frac{1}{2} L$ the deformation can be calculated as:

$$\varepsilon = \frac{3FL}{E4bd^2} \quad (6.1)$$

Where E is the Young's modulus of the FR-4 substrate.

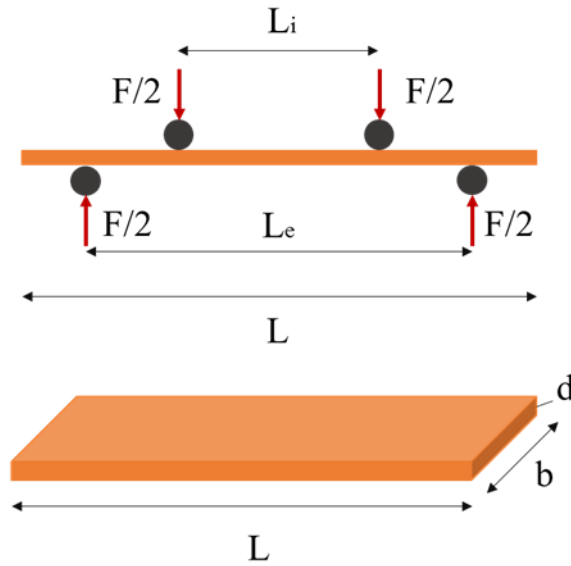


Figure 6.14 Schematics of the four-point bending test.

6.7.2 Gauge factor calculation and regression coefficients

In the linear range it is possible to calculate the gauge factor (defined as $dR/R/\epsilon$) in order to compare the device under study with the commercial and scientific literature. The GF of strain sensors on polyimide is calculated by using the equation for the quarter bridge circuit:

$$GF = 4 \frac{V_0}{V_{ex}} \frac{1}{\epsilon} \quad (6.2)$$

Where:

- V_0 is the output voltage due to the strain ϵ .
- V_{ex} is the excitation voltage.
- ϵ is the applied strain. In this case we refer to the strain measured by the commercial gauges.

6.7.3 Definition of the densification ratio

If d_1 (resp. d_n) is the density of a single drop layer after drying (resp. n -drop layer) ; h_1 (resp. h_n) is the average thickness of a single drop layer after drying (resp. n -drop layer); M_1 (resp. M_n) is the mass of a single drop layer after drying (resp. n -drop layer), then for the same surface of deposition S , the densification ratio d_r of the n -drop layer with respect to the single drop layer density can be approximated as

$$d_r = \frac{d_n}{d_1} \approx \frac{\frac{M_n}{h_n S}}{\frac{M_1}{h_1 S}} \approx \frac{nh_1}{h_n} \quad (6.3)$$

Figure 6.15 shows the densification ratio as a function of the number of drops, which follows a logarithmic law. Note that for $n > 15$ drops, the densification ratio is close to 3, which is consistent with the ratio (3,0) between a single drop thickness (940nm) and the average thickness by drop for a 30-drop layer (310nm).

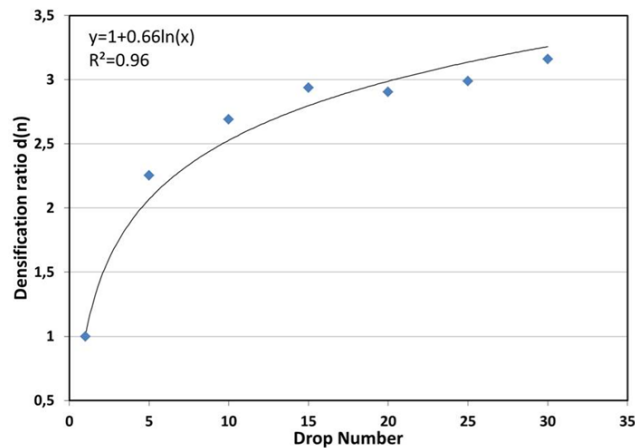


Figure 6.15 Densification ratio as a function of the number of drop.

6.7.4 Resistance of devices on E-glass as a function of the number of drops for batch B34

The following table shows the resistances as a function of the number of drops for different devices in the same batch. Note that 2 additional devices (NA33 and NA34) were fabricated in this batch, but their resistances (respectively 41 k Ω and 22 k Ω) were only measured for 15 drops so is thus not included in the table. Accounting for these two additional devices does not change the average resistance of the 15-drop devices, and increase the standard deviation by less than 80 Ω and 0.3%.

Table 6.11 Values of resistance (k Ω) for different numbers of drops for six devices prepared with the same ink.

Device ID	NA26	NA28	NA29	NA30	NA31	NA32	Average	St dev	Relative st dev
5 drops	300	650	150	53	160	350	280	190	70%
10 drops	71	91	39	26	48	57	55	21	38%

6.7.5 Thermal sensitivity of device NA30 on E-glass

The thermal sensitivity was evaluated for one of the devices of batch B34 (NA30). It was found to be linear with coefficient $-0,066 \text{ k}\Omega/^{\circ}\text{C}$ from 30°C to 55°C ($-0,3\%/^{\circ}\text{C}$ with respect to 30°C resistance), as seen in Figure 6.16.

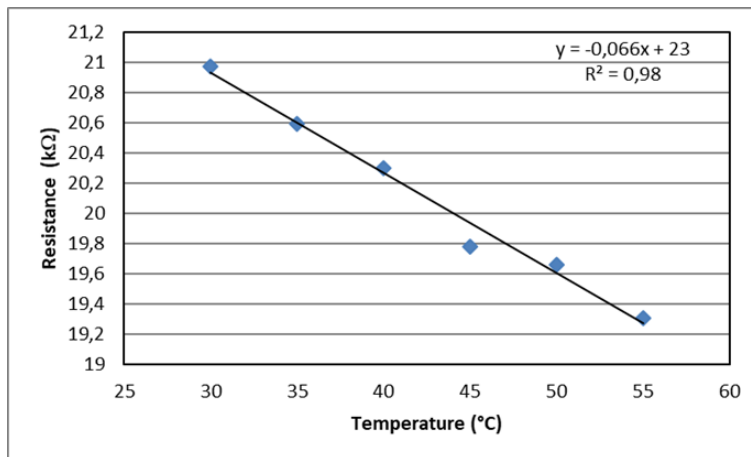


Figure 6.16 Thermal sensitivity of E-glass device NA30.

6.7.6 Loading of the sensors with strain cycles

Figure 6.17-left shows the time response of a typical device (NA30 from batch B34) to 20 strain cycles. Figure 6.17-right shows the corresponding resistance-strain curve. These two figures show the good stability of the device under cyclic loading. The 0.24% strain variability that can be observed on the resistance-strain curve is attributed to small ($<1^{\circ}\text{C}$) ambient temperature variations during trials ($-0.3\%/^{\circ}\text{C}$ for device NA30, see section 6.7.5). One can only observe a slight shift of the baseline resistance during the cycle. Considering the stability of the rest of the cycles, this baseline resistance shift may be due to slight variability in the test setup in the absence of strain rather than to an instability of the device itself.

Note that the hysteresis of the sensor between extension and unloading and the non-linearity (upward of 0.04% strain) are more pronounced here than during ramp tests, probably due to the slightly higher speed of loading.

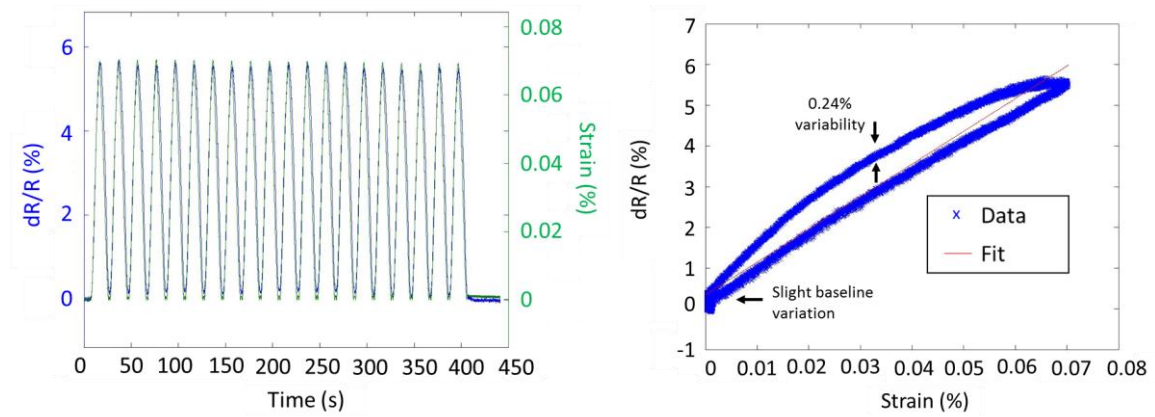


Figure 6.17 NA30 resistance variation under strain cycles at 0.15 mm/s - 0.003%/s - 0.05 Hz. Left – time response. Right – resistance-strain curve.

Figure 6.18 shows the time response of sensor c7 out of P1 batch (average resistance $30\text{k}\Omega \pm 84\%$) to cyclic loading up to 0.06% strain for 13 cycles. The three figures show the good stability of the device under cyclic loading and higher GF than E-glass devices. However the cycles feature a slight downward baseline shift (-0.20% $dR/R/s$) absent in E-glass devices.

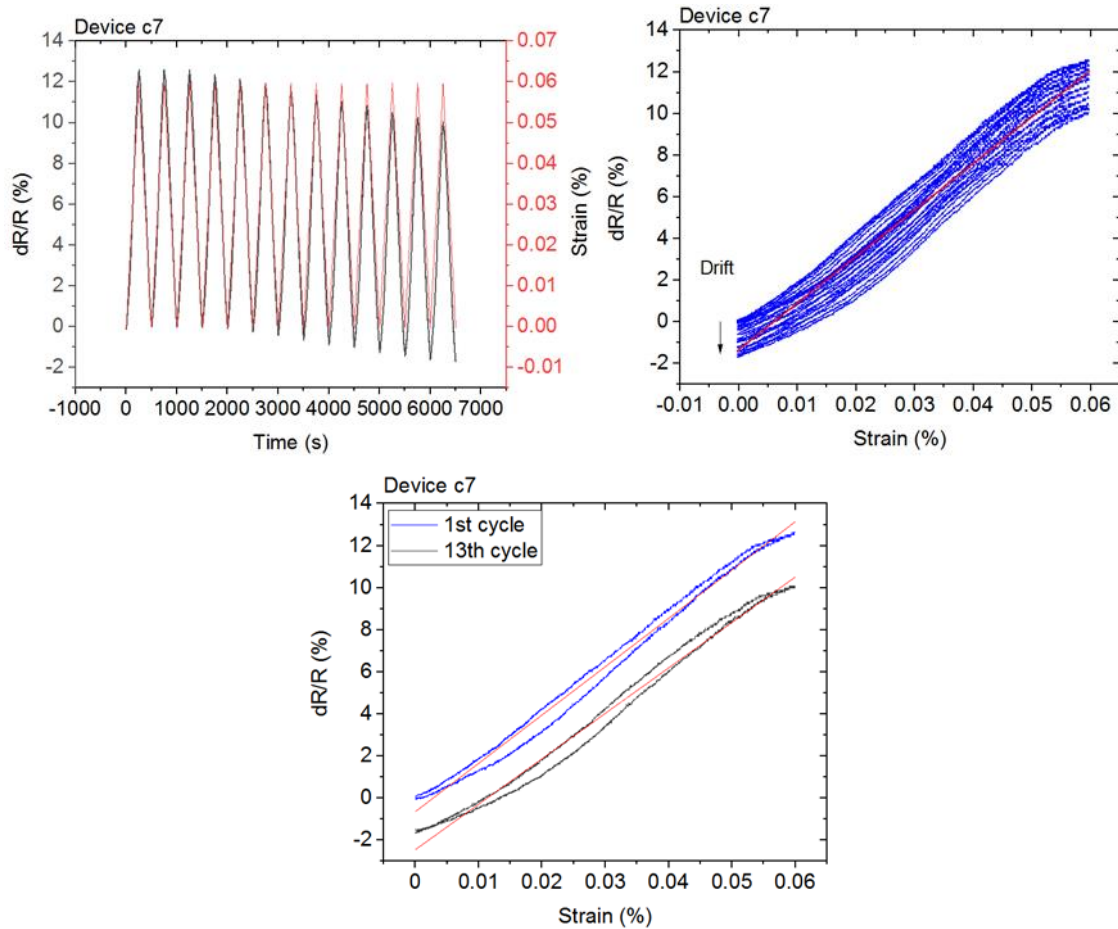


Figure 6.18 Device c7 resistance variation under strain cycles up to 0.06% strain at 2 mHz: (top left) time response, (top right) resistance-strain curve, (bottom) resistance-strain curve, zoom on the 1st and 13th cycle.

6.7.7 Geometry and resistance values for the devices used for pavement embedding

Figure 6.19 shows the coffee ring effect observed on 4 devices on PI PCBs later used for pavement embedding imaged through confocal microscopy. As it can be observed the size of the coffee ring is comparable to the size of the device (unlike for devices in E-glass that are much larger than the coffee ring) which may explain the higher variability of the average resistance for a constant number of drops.

Table 6.12 shows the resistance for the 4 devices. Note that the average resistance is $0.84 \text{ M}\Omega \pm 58\%$.

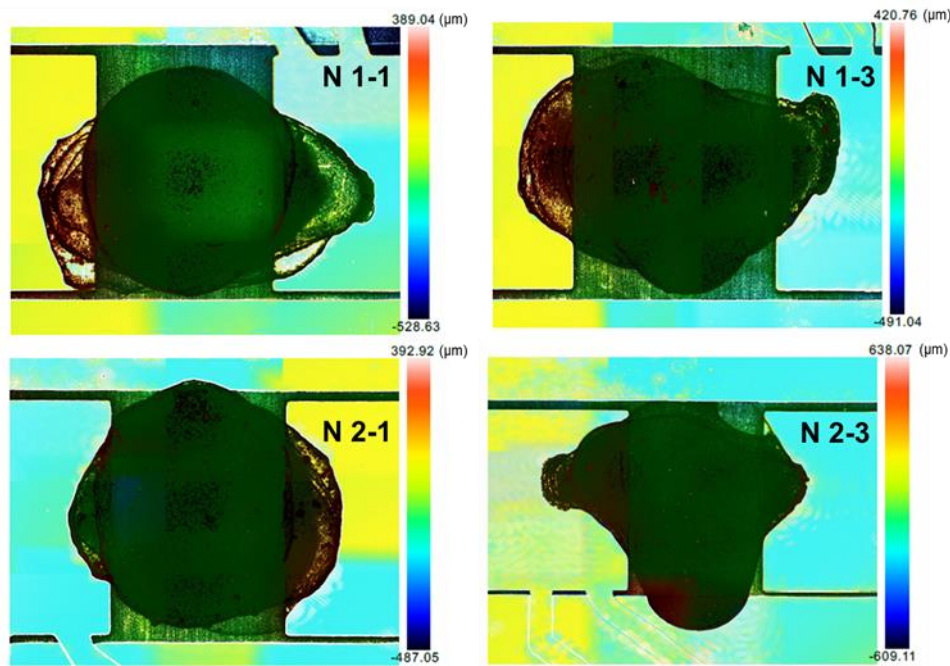


Figure 6.19 4 devices on PI PCBs, later used for embedding in pavement, imaged through confocal microscopy. Note that the colour scale is qualitative only, as confocal microscopy does not provide accurate evaluation of thickness for such type of materials.

Table 6.12 Geometry (mm) and values of resistance (M Ω) for 4 devices batch prepared with the same ink.

Device	Electrodes dimensions (mm ²)	Distance between electrodes (mm)	Initial resistance (M Ω)
N 1-1	49	4	0.47
N 1-3	25	6	0.85
N 2-1	64	4	0.51
N 2-3	64	4	1.51

6.7.8 Sensitivity to wheel passage and on-site GF

Figure 6.20 and Figure 6.21 report two 100 Hz acquisitions of sensors N 2-3 and C 2-3 in loading configuration III (6.5 t – 1.5 km/h – 9.5 °C) and IV (6.5t – 2.5 km/h – 10.1 °C) respectively. The time response is shown in Figure 6.20-left and Figure 6.21-left. The resistance-strain responses in Figure 6.20-right and Figure 6.21-right are used for the calculation of the GF. Please note that for each cycle the GF is calculated on the ascending ramp only where the sensor response is linear. The obtained GFs are respectively $1.2e03 \pm 12\%$ and $1.5e03 \pm 37\%$, which is impressive and show the great potential of the proposed technology for pavement applications.

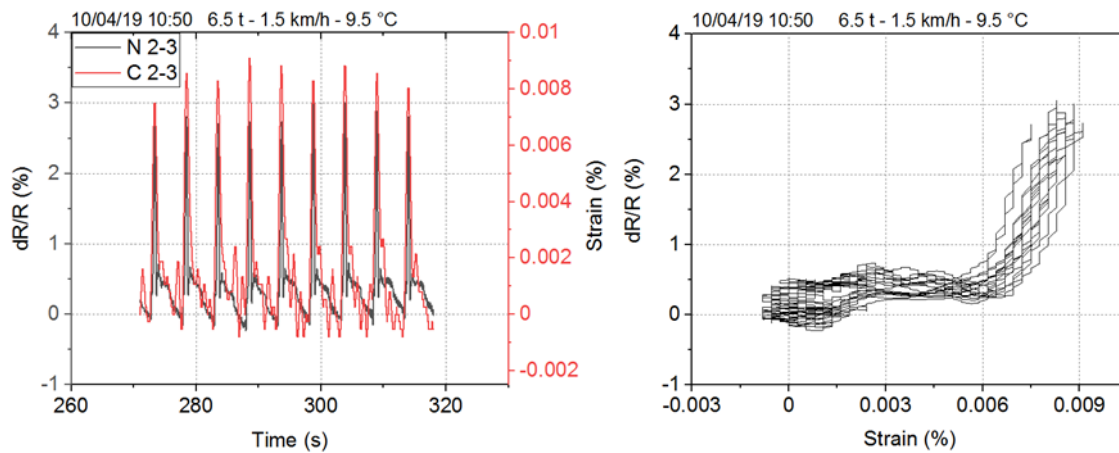


Figure 6.20 Sensors N 2-3 and C 2-3: 100 Hz acquisition on 10/04/2019 at 10:50. Load = 6.5 t, speed = 1.5 km/h, and temperature = 9.5 °C. (Left) time-response. (Right) resistance-strain response.

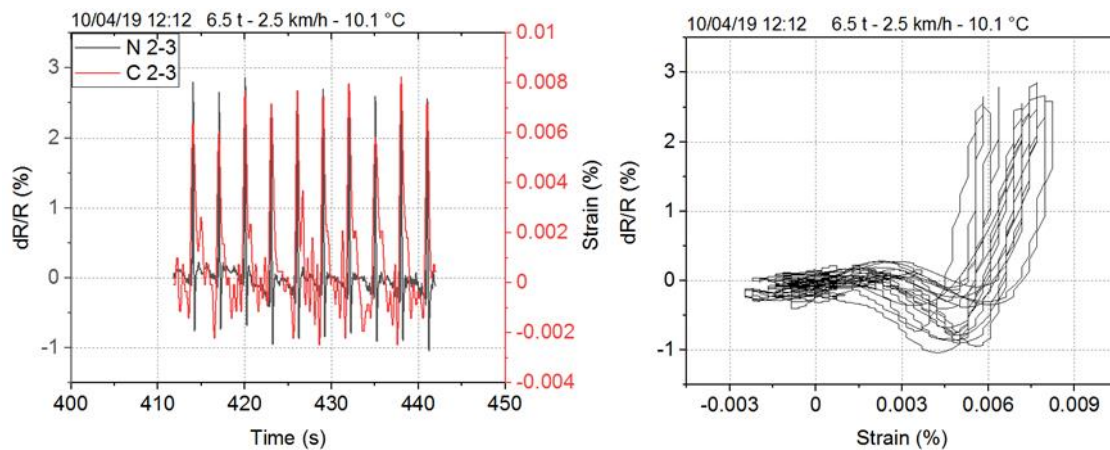


Figure 6.21 Sensors N 2-3 and C 2-3: 100 Hz acquisition on 10/04/2019 at 12:12. Load = 6.5 t, speed = 2.5 km/h, and temperature = 10.1 °C. (Left) time-response. (Right) resistance-strain response.

6.7.9 Regression statistics and coefficients

Table 6.13 Reports the regression statistics and coefficients obtained by carrying out a multiple linear regression for sensors N2-3 and C2-3 in order to evaluate the correlation between the maximum peak values evolution and the different loading configurations.

Table 6.13 Regression statistics and coefficients obtained from the multiple linear regression carried out for sensors N2-3 and C2-3.

Sensor	Regression statistics		Coefficients		
	Multiple R	R square	Intercept	Load	Speed
N 2-3	0.85	0.73	-6.32	2.17	-2.52
C 2-3	0.88	0.78	0.03	-4.54E-03	6.28E-03

7 BIBLIOGRAPHY OF THE AUTHOR

7.1 List of publications

7.1.1 Published papers

M. Barriera, B. Lebental & S. Pouget (2019): Towards road pavement response under moving loads, *Road Materials and Pavement Design*, DOI: 10.1080/14680629.2019.1588780

Barriera, M.; Pouget, S.; Lebental, B.; Van Rompu, J. In Situ Pavement Monitoring: A Review. *Infrastructures* **2020**, 5, 18.

Barriera M., Lebental B., Zakharov D., Villette C., Geisler F., Van Rompu J., Pouget S.. 2020. Monitoring des infrastructures routières: évaluation d'une solution innovante. *Revue Générale des Routes et de l'Aménagement*, Issue 973, pp. 47-51.

Barriera M., Blanc J., Chailleux E., Pouget S., Van Rompu J., Lebental B. (2020) Procedure for Temperature Correction of Strains Measured in a Road Pavement. In: Chabot A., Hornych P., Harvey J., Loria-Salazar L. (eds) *Accelerated Pavement Testing to Transport Infrastructure Innovation. Lecture Notes in Civil Engineering*, vol 96. Springer, Cham. https://doi.org/10.1007/978-3-030-55236-7_50

Manosalvas-Paredes, M.; Roberts, R.; Barriera, M.; Mantalovas, K.. Towards More Sustainable Pavement Management Practices Using Embedded Sensor Technologies. *Infrastructures* **2020**, 5, 4.

7.1.2 Papers under review

Van Rompu J., Barriera M., Lebental B., Blanc J., Chailleux E., Pouget S. Assessing and predicting fatigue damage of road pavement using ASGs and deflection measurements: a full scale test, Road Materials and Pavement Design.

7.1.3 Papers under submission

Barriera M., Bodelot L, Milana E., Daveau N., Pouget, S., Jerbi R., Van Rompu J., Lebental B.. A hysteresis-free, high-stability, embeddable nanocarbon-based strain sensor with 100+ gauge factor validated for pavement monitoring. Carbon

7.2 Presentations in conferences and workshops

- The 7th World Conference on Structural Control and Monitoring (7 WCSCM), Qingdao, China, July 2018.
- Journée des thésards Eiffage, Corbas, France, October 2018 and November 2020.
- Poster at Journée de rentrée de l'EDI 2018, Palaiseau, France, November 2018.
- 2018 STA (Smart Transport Alliance) Annual Conference & Innovation Awards, Brussels, Belgium, November 2018.
- Poster at JTR (Journées Techniques Routes) 2019, Nantes, France, February 2019.
- The 8th EATA (European Asphalt Technology Association) Conference 2019, Granada, Spain, June 2019.
- SMARTI webinar with Highways England, September 2020.

7.3 Awards

1st prize for the poster presented at JTR 2019.

8 BIBLIOGRAPHY

- AASHTO. (1990). *AASHTO Guidelines for Pavement Management Systems* (A. A. of S. H. and T. Officials (ed.)). Washington, D.C, USA: American Association of State Highway and Transportation Officials.
- AASHTO. (1993). Guide for Design of Pavement Structures. In *American Association of State Highway and Transportation Officials*.
- AASHTO. (2008). Mechanistic Empirical Pavement Design Guide: A Manual Practice. In *American Association of State Highway and Transportation Officials* (Issue July).
- AASHTO. (2013). *AASHTO Transportation Asset Management Guide - A Focus on Implementation - Executive Summary*.
- AFNOR. (1992). *NF P98-200-2 - Essais relatifs aux chaussées - Mesure de la déflexion engendrée par une charge roulante* (AFNOR (ed.)). AFNOR.
- AFNOR. (2003). *NF EN 13043-Aggregates for bituminous mixtures and surface treatments for roads, airfields and other trafficked areas*.
- AFNOR. (2007a). *NF EN 13108-1-Bituminous mixtures-Material specifications-Part1: Asphalt concrete*.
- AFNOR. (2007b). *NF EN 1426 - Bitumen and bituminous binders - Determination of needle penetration*.
- AFNOR. (2012a). *NF EN 12697-26 - Bituminous mixtures - Test methods for hot mix asphalt - Part 26: Stiffness*.
- AFNOR. (2012b). *NF EN 14770 - Bitumen and bituminous binders - Determination of complex shear modulus and phase angle - Dynamic Shear Rheometer (DSR)*.
- AFNOR. (2018a). *NF EN 12697-24-Bituminous mixtures - Test methods - Part 24 : resistance to fatigue*.
- AFNOR. (2018b). *NF EN 12697-26 - Bituminous mixtures - Test methods - Part 26: Stiffness* (Vol. 33, Issue June).
- AFNOR. (2019). *NF P98-086 - Dimensionnement structurel des chaussées routières — Application aux chaussées neuves*.
- AFNOR. (2021). *P98-818-7PR, PR NF EN 12697-7 - Bituminous mixtures — Test methods — Part 7: Determination of the bulk density of bituminous specimens by gamma rays*.

- Ai, C., Rahman, A., Xiao, C., Yang, E., & Qiu, Y. (2017). Analysis of measured strain response of asphalt pavements and relevant prediction models. *International Journal of Pavement Engineering*, 18(12), 1089–1097. <https://doi.org/10.1080/10298436.2016.1149836>
- Al-Qadi, I. L., Loulizi, A., Elseifi, M., & Lahouar, S. (2004). The Virginia Smart Road : The Impact of Pavement Instrumentation on Understanding Pavement Performance. *Technical Sessions of the Asphalt Paving Technology: Association of Asphalt Paving Technologists, 2004-3-8 to 2004-3-10, Baton Rouge, LA, USA*, 1–41.
- Alavi, A. H., Hasni, H., Lajnef, N., & Chatti, K. (2016). Continuous health monitoring of pavement systems using smart sensing technology. *Construction and Building Materials*, 114(August), 719–736. <https://doi.org/10.1016/j.conbuildmat.2016.03.128>
- Ameri, M., Nowbakht, S., Molayem, M., & Aliha, M. R. M. (2016). Investigation of fatigue and fracture properties of asphalt mixtures modified with carbon nanotubes. *Fatigue and Fracture of Engineering Materials and Structures*, 39(7), 896–906. <https://doi.org/10.1111/ffe.12408>
- Arnold, G., Fon Sing, P., Saarenketo, T., & Saarenpaa, T. (2017). *Pavement moisture measurement to indicate risk to pavement life* (Issue Research report 611). www.nzta.govt.nz
- Ashish, P. K., & Singh, D. (2019). Use of nanomaterial for asphalt binder and mixtures: a comprehensive review on development, prospect, and challenges. *Road Materials and Pavement Design*, 0(0), 1–47. <https://doi.org/10.1080/14680629.2019.1634634>
- Balageas, D., Fritzen, C.-P., & Güemes, A. (2006). Structural health monitoring. *Structural Health Monitoring*, 493, 13–29. <https://doi.org/10.1098/rsta.2006.1928>
- Banthia, N., Djeridane, S., & Pigeon, M. (1992). Electrical resistivity of carbon and steel micro-fiber reinforced cements. *Cement and Concrete Research*, 22(5), 804–814. [https://doi.org/https://doi.org/10.1016/0008-8846\(92\)90104-4](https://doi.org/https://doi.org/10.1016/0008-8846(92)90104-4)
- Bao, X., & Chen, L. (2012). Recent Progress in Distributed Fiber Optic Sensors. *Sensors (Switzerland)*, 12(7), 8601–8639. <https://doi.org/10.3390/s120708601>
- Barhoum, A., Shalan, A. E., El-Hout, S. I., Ali, G. A. M., Abdelbasir, S. M., Abu Serea, E. S., Ibrahim, A. H., & Pal, K. (2019). A Broad Family of Carbon Nanomaterials: Classification, Properties, Synthesis, and Emerging Applications. In *Barhoum A., Bechelany M., Makhoulf A. (eds) Handbook of Nanofibers* (pp. 1–40). Springer, Cham. https://doi.org/10.1007/978-3-319-42789-8_59-1
- Barksdale, R. D., & National Stone Association, (U.S.). (1996). *The Aggregate handbook*.

- Washington, D.C. (1415 Elliot Pl., N.W., Washington 20007): National Stone Association.
- Benchirouf, A., Sowade, E., Al-Hamry, A., Blaudeck, T., Kanoun, O., & Baumann, R. (2012). Investigation of RFID passive strain sensors based on carbon nanotubes using inkjet printing technology. *International Multi-Conference on Systems, Signals and Devices, SSD 2012 - Summary Proceedings*. <https://doi.org/10.1109/SSD.2012.6198081>
- Blanc, J., Trichet, S., Gouy, T., Coirier, G., Nguyen, M.-L., & Baurdu, Y. (2016). Instrumentation de chaussées - Les jauges de déformations horizontales. *Revue Générale Des Routes et de l'Aménagement*, 940.
- Blanc, J., Chailleux, E., Hornych, P., Williams, R. C., Lo Presti, D., Del Barco Carrion, A. J., Porot, L., Planche, J. P., & Pouget, S. (2019). Bio materials with reclaimed asphalt: from lab mixes properties to non-damaged full scale monitoring and mechanical simulation. *Road Materials and Pavement Design*, 20(sup1), S95–S111. <https://doi.org/10.1080/14680629.2019.1589557>
- Blanc, J., Hornych, P., Sotoodeh-Nia, Z., Williams, C., Porot, L., Pouget, S., Boysen, R., Planche, J. P., Lo Presti, D., Jimenez, A., & Chailleux, E. (2019). Full-scale validation of bio-recycled asphalt mixtures for road pavements. *Journal of Cleaner Production*, 227, 1068–1078. <https://doi.org/10.1016/j.jclepro.2019.04.273>
- Blanc, Juliette, Hornych, P., Duong, N. S., Blanchard, J. Y., & Nicollet, P. (2017). Monitoring of an experimental motorway section. *Road Materials and Pavement Design*, 0(0), 1–16. <https://doi.org/10.1080/14680629.2017.1374997>
- Boussinesq, J. (1885). *Application des potentiels a l'étude de l'équilibre et du mouvement des solides élastiques : principalement au calcul des déformations et des pressions que produisent, dans ces solides, des efforts quelconques exercés sur une petite partie de leur surface*. Paris: Gauthier-Villars.
- Broutin, M., Sadoun, A., Duprey, A., & Voisin, G. (2019). Rétrocalcul HWD du module du sol - Coefficients d'abattement à prendre en compte. *Revue Générale Des Routes et de l'Aménagement*, 965, pp 35-39.
- Burmister, D. M. (1943). THE THEORY OF STRESS AND DISPLACEMENTS IN LAYERED SYSTEMS AND APPLICATIONS TO THE DESIGN OF AIRPORT RUNWAYS. *Proceedings of the Twenty-Third Annual Meeting of the Highway Research Board, Chicago, Illinois November 27-30, 1943*, Vol 23, pp 126–148.
- Burton, A. R., Kurata, M., Nishino, H., & Lynch, J. P. (2016). Fully integrated patterned

- carbon nanotube strain sensors on flexible sensing skin substrates for structural health monitoring. *Sensors and Smart Structures Technologies for Civil, Mechanical, and Aerospace Systems 2016*, 9803, 98030S. <https://doi.org/10.1117/12.2222501>
- Cable, J. K., Klaiber, F. W., & Lee, D. Y. (1988). *Pavement Instrumentation* (Issue March 1988).
- Campanella, C. E., Cuccovillo, A., Campanella, C., Yurt, A., & Passaro, V. M. N. (2018). Fibre Bragg Grating based strain sensors: Review of technology and applications. *Sensors (Switzerland)*, 18(9). <https://doi.org/10.3390/s18093115>
- Carneiro, F. B. L. (1966). Benkelman Beam, Auxiliary Instrument of the Maintenance Engineer. *Transportation Research Record*, 129, 28–59.
- Carret, J.-C. (2018). *Linear viscoelastic characterization of bituminous mixtures from dynamic tests back analysis*. UNIVERSITE DE LYON.
- Cha, C., Shin, S. R., Annabi, N., & Dokmeci, M. R. (2013). Carbon-Based Nanomaterials : Multifunctional Materials for. *ACS Nano*, 7(4), 2891–2897.
- Chabot, A, Chupin, O., Deloffre, L., & Duhamel, D. (2010). ViscoRoute 2.0: A Tool for the Simulation of Moving Load Effects on Asphalt Pavement. *Road Materials and Pavement Design*, 11(2), 227–250. <https://doi.org/10.1080/14680629.2010.9690274>
- Chabot, A, Tamagny, P., Poché, D., & Duhamel, D. (2006). Visco-elastic modelling for asphalt pavements -- software {ViscoRoute}. *International Conference on Asphalt Pavements, \nth{10}, 2006, Québec City, Canada, 1943*, 10.
- Chae, S. H., & Lee, Y. H. (2014). Carbon nanotubes and graphene towards soft electronics. *Nano Convergence*, 1(1), 1–26. <https://doi.org/10.1186/s40580-014-0015-5>
- Chailleux, E., Ramond, G., Such, C., & de La Roche, C. (2006). A mathematical-based master-curve construction method applied to complex modulus of bituminous materials A mathematical-based master-curve construction method applied to complex modulus of bituminous materials. *Road Materials and Pavement Design*, 75–92. <https://doi.org/10.1080/14680629.2006.9690059>
- Chapeleau, X., Blanc, J., Hornych, P., Gautier, J. L., & Carroget, J. (2014). Use of distributed fiber optic sensors to detect damage in a pavement. *7th European Workshop on Structural Health Monitoring, EWSHM 2014 - 2nd European Conference of the Prognostics and Health Management (PHM) Society, June*, 1847–1854. <https://doi.org/10.1201/b17219-59>
- Choquet, P., Juneau, F., & Bessette, J. (2000). New generation of Fabry-Perot fiber optic sensors for monitoring of structures. *Smart Structures and Materials 2000: Sensory*

- Phenomena and Measurement Instrumentation for Smart Structures and Materials*, 3986(June 2000), 418. <https://doi.org/10.1117/12.388132>
- Chun, S., Choi, Y., & Park, W. (2017). All-graphene strain sensor on soft substrate. *Carbon*, 116, 753–759. <https://doi.org/10.1016/j.carbon.2017.02.058>
- Clec'h, P. (2010). *Comportement des enrobés bitumineux sous sollicitation multidirectionnelle*.
- De Boissoudy, A., Gramsammer, J., Keryell, P., & Paillard, M. (n.d.). Appareils d'auscultation. Le deflectographe 04. *Bulletin de Liaison Laboratoires Des Ponts et Chaussées N°129, janvier-février*.
- Deegan, R. D., Bakajin, O., Dupont, T. F., Huber, G., Nagel, S. R., & Witten, T. A. (1997). Capillary flow as the cause of ring stains from dried liquid drops. *Nature*, 389(6653), 827–829. <https://doi.org/10.1038/39827>
- Di Benedetto, Herve, & Corté, J.-F. (2004). Matériaux routiers bitumineux 2: constitution et propriétés thermomécaniques des mélanges. In Lavoisier (Ed.), *Editions Lavoisier: Vol. Vol. 2*.
- Di Benedetto, Hervé, & Corté, J.-F. (2004). Matériaux routiers bitumineux 1: description et propriétés des constituants. In Lavoisier (Ed.), *Editions Lavoisier: Vol. Vol. 1*. <https://doi.org/10.2143/REA.28.1.505102>
- Di Benedetto, Hervé, Olard, F., Sauzéat, C., & Delaporte, B. (2004). Linear viscoelastic behaviour of bituminous materials: From binders to mixes. *Road Materials and Pavement Design*, 5(1), 163–202. <https://doi.org/10.1080/14680629.2003.9689938>
- Di Benedetto, Hervé, Sauzéat, C., Delaporte, B., & Olard, F. (2004). Linear viscoelastic behaviour of bituminous materials: From binders to mixes. *Road Materials and Pavement Design*, 5, 163–202. <https://doi.org/10.1080/14680629.2004.9689992>
- dos Santos, M. C., Maynard, M. C., Aveiro, L. R., da Paz, E. C., & dos Santos Pinheiro, V. (2017). Carbon-Based Materials: Recent Advances, Challenges, and Perspectives. In *Reference Module in Materials Science and Materials Engineering* (pp. 1–12). Elsevier Ltd. <https://doi.org/10.1016/b978-0-12-803581-8.09262-6>
- Du, M., Jing, H., Gao, Y., Su, H., & Fang, H. (2020). Carbon nanomaterials enhanced cement-based composites: Advances and challenges. *Nanotechnology Reviews*, 9(1), 115–135. <https://doi.org/10.1515/ntrev-2020-0011>
- Duhamel, D., Chabot, A., Tamagny, P., & Harfouche, L. (2005). Logiciel de modélisation viscoélastique des chaussées bitumineuses. *Bulletin Des Laboratoires Des Ponts et Chaussées N°258 - 259*, pp 89-103.

- Duong, N. S. (2017). *Instrumentation de chaussées: la route intelligente qui s'auto-détecte?*
- Duong, N. S., Blanc, J., Hornych, P., Bouveret, B., Carroget, J., & Lefeuvre, Y. (2018). Continuous strain monitoring of an instrumented pavement section. *International Journal of Pavement Engineering*, 8436, 1–16. <https://doi.org/10.1080/10298436.2018.1432859>
- Duong, N. S., Blanc, J., Hornych, P., Menant, F., Lefeuvre, Y., & Bouveret, B. (2018). Monitoring of pavement deflections using geophones. *International Journal of Pavement Engineering*, 0(0), 1–11. <https://doi.org/10.1080/10298436.2018.1520994>
- Eswaraiah, V., Balasubramaniam, K., & Ramaprabhu, S. (2011). Functionalized graphene reinforced thermoplastic nanocomposites as strain sensors in structural health monitoring. *Journal of Materials Chemistry*, 21(34), 12626–12628. <https://doi.org/10.1039/c1jm12302e>
- European Commission. (2019). *The European Green Deal*. <https://doi.org/10.2307/j.ctvd1c6zh.7>
- European Union Road Federation. (2014). *Road Asset Management - An ERF position paper for maintaining and improving a sustainable and efficient road network*. Brussels, Belgium: European Union Road Federation.
- European Union Road Federation. (2020). *ERF Road statistics 2020*. <https://erf.be/statistics/>
- Fan, W., Zhang, L., & Liu, T. (2017). Graphene-Carbon Nanotube Hybrids for Energy and Environmental Applications. In *Graphene-Carbon Nanotube Hybrids for Energy and Environmental Applications* (pp. 21–50). SpringerBriefs in Molecular Science. Springer, Singapore. <https://doi.org/10.1007/978-981-10-2803-8>
- Fang, M., Park, D., Singuranayo, J. L., Chen, H., & Li, Y. (2019). Aggregate gradation theory, design and its impact on asphalt pavement performance: a review. *International Journal of Pavement Engineering*, 20(12), 1408–1424. <https://doi.org/10.1080/10298436.2018.1430365>
- Fernandes, F. M., & Pais, J. (2014). Assessment of moisture in road pavements. *15th International Conference on Ground Penetrating Radar, 30 June-4 July, 2014*, 909–912. <https://doi.org/10.1109/ICGPR.2014.6970558>
- Fernandes, Francisco M., & Ruiz-Hitzky, E. (2014). Assembling nanotubes and nanofibres: Cooperativeness in sepiolite-carbon nanotube materials. *Carbon*, 72, 296–303. <https://doi.org/10.1016/j.carbon.2014.02.009>
- Ferry, J. D. (1980). *Viscoelastic properties of polymers*. New York: Wiley.
- Gaborit, P. (2015). *COMPORTEMENT THERMO-MECANIQUE DE STRUCTURES DE*

- CHAUSSEES BITUMINEUSES*. Université de Lyon.
- Gaborit, P., Sauzéat, C., Di Benedetto, H., Pouget, S., Olard, F., Claude, A., Monnet, A. J., Audin, R. M., Sauzéat, C., Di Benedetto, H., Pouget, S., Olard, F., Publics, E. T., Dauphiné, R., & Claude, A. (2014). Investigation of highway pavements using in-situ strain sensors. *3rd International Conference of Transportation Infrastructure, Pisa, Italy, 22-25 April, 2014*.
- Ghaddab, B., Gaudefroy, V., Michelis, F., Aranda, P., & Lebental, B. (2014). An innovative nanosensor for weigh-in-motion applications. *EWSHM - 7th European Workshop on Structural Health Monitoring, October, 1773–1779*.
- Giffney, T., Bejanin, E., Kurian, A. S., Travas-Sejdic, J., & Aw, K. (2017). Highly stretchable printed strain sensors using multi-walled carbon nanotube/silicone rubber composites. *Sensors and Actuators, A: Physical*, 259, 44–49. <https://doi.org/10.1016/j.sna.2017.03.005>
- Glisic, B. (2011). Distributed fiber optic sensing technologies and applications - An overview. *Structural Health Monitoring Technologies 2011 at the ACI Fall 2011 Convention, 16–20 October 2011, 292 SP*, 13–30.
- Goli, A., Ziari, H., & Amini, A. (2017). Influence of carbon nanotubes on performance properties and storage stability of sbs modified asphalt binders. *Journal of Materials in Civil Engineering*, 29(8), 1–9. [https://doi.org/10.1061/\(ASCE\)MT.1943-5533.0001910](https://doi.org/10.1061/(ASCE)MT.1943-5533.0001910)
- Grenier, S. (2007). *ANALYSE DYNAMIQUE DU DEFLECTOMETRE À MASSE TOMBANTE - TOME 1*. FACULTÉ DES SCIENCES ET DE GÉNIE UNIVERSITÉ LAVAL QUÉBEC.
- Gudmarsson, A. (2014). *Resonance Testing of Asphalt Concrete*.
- Gudmarsson, A., Ryden, N., & Birgisson, B. (2012). Characterizing the low strain complex modulus of asphalt concrete specimens through optimization of frequency response functions. *The Journal of the Acoustical Society of America*, 132(4), 2304–2312. <https://doi.org/10.1121/1.4747016>
- Guo, S., Yang, X., Wang, Z., You, L., Dai, Q., & You, Z. (2019). Nanomodified asphalt mixture with enhanced performance. In *Nanotechnology in Eco-efficient Construction* (pp. 187–201). Elsevier Ltd. <https://doi.org/10.1016/b978-0-08-102641-0.00009-8>
- Han, B., Yu, X., & Kwon, E. (2009). A self-sensing carbon nanotube/cement composite for traffic monitoring. *Nanotechnology*, 20(44), 445501. <https://doi.org/10.1088/0957-4484/20/44/445501>
- Henia, M. O., & Braber, R. (2008). *Falling Weight Deflectometer et déflectographe*

- Lacroix : *Comparaison, domaine d'application et perspectives*. 7, 18–23.
<https://doi.org/10.17226/13675>
- Homsi, F. (2011). *ENDOMMAGEMENT DES CHAUSSEES BITUMINEUSES SOUS CHARGEMENTS MULTI-ESSIEUX*. Ecole Centrale de Nantes.
- Horak, E. (2008). Benchmarking the structural condition of flexible pavements with deflection bowl parameters. *Journal of the South African Institution of Civil Engineering*, 50(2), 2–9.
- Horak, E., & Emery, S. (2009). Evaluation of airport pavements with FWD deflection bowl parameter. *2nd European Airport Pavement Workshop, 13-14 May 2009, Amsterdam*.
- Hu, M., Ma, M., Zhao, Z., Yu, D., & He, J. (2016). Superhard sp²-sp³ hybrid carbon allotropes with tunable electronic properties. *AIP Advances*, 6(5).
<https://doi.org/10.1063/1.4952426>
- Huet, C. (1965). *Etude par une méthode d'impédance du comportement viscoélastique des matériaux hydrocarbonés*. PhD Thesis. Impr. Nationale.
- IDRRIM. (2017). *Guide Technique: Manuel de dimensionnement des chaussées neuves à faible trafic*. Paris, France: CEREMA.
- Imai, M., Igarashi, Y., Shibata, M., & Miura, S. (2014). Experimental study on strain and deformation monitoring of asphalt structures using embedded fiber optic sensor. *Journal of Civil Structural Health Monitoring*, 4(3), 209–220.
<https://doi.org/10.1007/s13349-014-0077-4>
- Islam, R., & Tarefder, R. A. (2013). Field Measurement of Vertical Strain in Asphalt Concrete. *International Journal of Scientific & Engineering Research*, 4(2), 1–6.
- JONG, D., & L., D. (1979). *Computer Program BISAR*. Layered Systems under Normal and Tangential Loads; Koninklijke/Shell-Laboratorium.
<http://ci.nii.ac.jp/naid/10015604117/en/>
- Joshi, S. (2017). Linear Variable Differential Transducer (LVDT) & Its Applications in Civil Engineering. *International Journal of Transportation Engineering and Technology*, 3(4), 62. <https://doi.org/10.11648/j.ijtet.20170304.13>
- Kang, I., Schulz, M. J., Kim, J. H., Shanov, V., & Shi, D. (2006). A carbon nanotube strain sensor for structural health monitoring. *Smart Materials and Structures*, 15(3), 737–748. <https://doi.org/10.1088/0964-1726/15/3/009>
- Karimov, K. S., Khalid, F. A., & Chani, M. T. S. (2012). Carbon nanotubes based strain sensors. *Measurement: Journal of the International Measurement Confederation*, 45(5), 918–921. <https://doi.org/10.1016/j.measurement.2012.02.003>

- Kim, J., Yun, J. H., Song, J. W., & Han, C. S. (2009). The spontaneous metal-sitting structure on carbon nanotube arrays positioned by inkjet printing for wafer-scale production of high sensitive gas sensor units. *Sensors and Actuators, B: Chemical*, *135*(2), 587–591. <https://doi.org/10.1016/j.snb.2008.10.023>
- Konsta-Gdoutos, M. S., & Aza, C. A. (2014). Self sensing carbon nanotube (CNT) and nanofiber (CNF) cementitious composites for real time damage assessment in smart structures. *Cement and Concrete Composites*, *53*, 162–169. <https://doi.org/10.1016/j.cemconcomp.2014.07.003>
- Konsta-Gdoutos, M. S., Metaxa, Z. S., & Shah, S. P. (2010). Highly dispersed carbon nanotube reinforced cement based materials. *Cement and Concrete Research*, *40*(7), 1052–1059. <https://doi.org/10.1016/j.cemconres.2010.02.015>
- Laheurte, J.-M., Kabalan, A., Retima, H., Piedallu, E., Michelis, F., & Lebental, B. (2016). Embedded UHF RFID Tag for Durability Monitoring in Concrete. *Wireless Sensor Network*, *08*(07), 137–144. <https://doi.org/10.4236/wsn.2016.87012>
- Lebental, B. (2010). *Instrumentation immergée des matériaux cimentaires par des micro-transducteurs ultrasoniques à nanotubes de carbone : perspectives pour le contrôle non destructif in-situ de durabilité* To cite this version : HAL Id : pastel-00574780 *Instrumentation immerg.* Université Paris-Est, Ecole Doctorale Sciences, Ingénierie et Environnement.
- Lebental, B. (2016). *Nanosensors for sustainable cities*. UNIVERSITE PARIS SUD UFR SCIENCES.
- Lebental, B., Ghaddab, B., Gaudefroy, V., Ruiz-Hitzky, E., Aranda, P., RUIZ-GRACIA, C., & HENNING, B. (2014). *Dispositif d'acquisition, procédé de fabrication de celui-ci, procédé de mesure de force* (Patent No. FR3019291B1).
- Levenberg, E. (2012). Inferring Pavement Properties using an Embedded Accelerometer. *International Journal of Transportation Science and Technology*, *1*(3), 229–246. <https://doi.org/10.1260/2046-0430.1.3.229>
- Li, Xiao, & Goldberg, D. W. (2018). Toward a mobile crowdsensing system for road surface assessment. *Computers, Environment and Urban Systems*, *69*. <https://doi.org/10.1016/j.compenvurbsys.2017.12.005>
- Li, Xueguang, Wei, W., Qin, H., & Hang Hu, Y. (2015). Co-effects of graphene oxide sheets and single wall carbon nanotubes on mechanical properties of cement. *Journal of Physics and Chemistry of Solids*, *85*, 39–43. <https://doi.org/10.1016/j.jpics.2015.04.018>
- Lim, M. J., Lee, H. K., Nam, I. W., & Kim, H. K. (2017). Carbon nanotube/cement

- composites for crack monitoring of concrete structures. *Composite Structures*, 180, 741–750. <https://doi.org/10.1016/j.compstruct.2017.08.042>
- Liu, P., Otto, F., Wang, D., Oeser, M., & Balck, H. (2017). Measurement and evaluation on deterioration of asphalt pavements by geophones. *Measurement: Journal of the International Measurement Confederation*, 109(May), 223–232. <https://doi.org/10.1016/j.measurement.2017.05.066>
- Loamrat, K., Sappakittipakorn, M., Sukontasukkul, P., & Banthia, N. (2014). Effect of Carbon Fiber and Graphite Powder on Resistivity of Cement-based Sensor under Compression. *KMUTNB International Journal of Applied Science and Technology*, 7(1), 29–35. <https://doi.org/10.14416/j.ijast.2014.01.005>
- Loh, K. J., Lynch, J. P., & Kotov, N. A. (2005). Conformable single-walled carbon nanotube thin film strain sensors for structural monitoring. *4th World Conference on Structural Control and Monitoring*, January, 1–8. <http://citeseerx.ist.psu.edu/viewdoc/summary?doi=10.1.1.503.9303>
- Maeijer, P. K. De, Luyckx, G., Vuye, C., Voet, E., Den, W. Van, Vanlanduit, S., Braspeninckx, J., Stevens, N., & Wolf, J. De. (2020). *Fiber Optics Sensors in Asphalt Pavement : State-of-the-Art Review*. 1–16.
- Mangiafico, S. (2014). *Linear viscoelastic properties and fatigue of bituminous mixtures produced with Reclaimed Asphalt Pavement and corresponding binder blends*.
- Manosalvas-Paredes, M., Lajnef, N., Chatti, K., Blanc, J., Thom, N., Airey, G., & Lo Presti, D. (2020). *Monitoring Road Pavement Performance Through a Novel Data Processing Approach, Accelerated Pavement Test Results BT - Accelerated Pavement Testing to Transport Infrastructure Innovation* (Armelle Chabot, P. Hornych, J. Harvey, & L. G. Loria-Salazar (eds.); pp. 545–554). Springer International Publishing.
- Medina, R., Llamas, J., Zalama, E., & Gomez-Garcia-Bermejo, J. (2014). Enhanced automatic detection of road surface cracks by combining 2D/3D image processing techniques. *2014 IEEE International Conference on Image Processing, ICIP 2014*, 778–782. <https://doi.org/10.1109/ICIP.2014.7025156>
- Michelis, F. (2016). *Wireless Nano Sensors for Embedded Durability*.
- Michelis, F., Bodelot, L., Bonnassieux, Y., & Lebental, B. (2015). Highly reproducible, hysteresis-free, flexible strain sensors by inkjet printing of carbon nanotubes. *Carbon*, 95, 1020–1026. <https://doi.org/10.1016/j.carbon.2015.08.103>
- Micro Measurements. (2010). *Selection Criteria - Stress Analysis Gages*. <http://www.vishaypg.com/docs/11504/stress-analysis-selection-criteria.pdf>

- Mobasser, S., & Firoozi, A. A. (2016). Review of Nanotechnology Applications in Science and Engineering. *Journal of Civil Engineering and Urbanism*, 6(4), 84–93.
- Moghaddam, T. B., Karim, M. R., & Abdelaziz, M. (2011). A review on fatigue and rutting performance of asphalt mixes. *Scientific Research and Essays*, 6(4), 670–682. <https://doi.org/10.5897/SRE10.946>
- Nazarian, S., & Bush III, A. J. (1989). Determination of Deflection of Pavement Systems Using Velocity Transducers. *Transportation Research Record*, 12.
- Neves, J., Correia Diogo, A., & de Picado Santos, L. (2015). *Bituminous Binders and Mixtures*. In: Gonçalves M., Margarido F. (eds) *Materials for Construction and Civil Engineering*. Springer, Cham. <https://doi.org/10.1007/978-3-319-08236-3>
- Nie, M., Xia, Y. han, & Yang, H. shan. (2019). A flexible and highly sensitive graphene-based strain sensor for structural health monitoring. *Cluster Computing*, 22, 8217–8224. <https://doi.org/10.1007/s10586-018-1727-9>
- Obitayo, W., & Liu, T. (2012). A review: Carbon nanotube-based piezoresistive strain sensors. *Journal of Sensors*, 2012(April 2012). <https://doi.org/10.1155/2012/652438>
- Olard, F., & Pouget, S. (2015b). A new approach for aggregate grading optimization for mixtures. In *Advances in Asphalt Materials: Road and Pavement Construction*. Elsevier Ltd. <https://doi.org/10.1016/B978-0-08-100269-8.00014-3>
- Olard, F. (2012). GB5 mix design: high-performance and cost-effective asphalt concretes by use of gap-graded curves and SBS modified bitumens. *Road Materials and Pavement Design*, 13(sup1), 234–259. <https://doi.org/10.1080/14680629.2012.657074>
- Olard, F., & Pouget, S. (2015a). 14 - A new approach for aggregate grading optimization for mixtures. In S.-C. Huang & H. B. T.-A. in A. M. Di Benedetto (Eds.), *Woodhead Publishing Series in Civil and Structural Engineering* (pp. 427–457). Woodhead Publishing. <https://doi.org/https://doi.org/10.1016/B978-0-08-100269-8.00014-3>
- Olard, François. (2003). *Enrobés bitumineux a basses températures : Relations entre les propriétés du liant et de l ' enrobé*.
- Olard, François, & Di Benedetto, H. (2003). General “2S2P1D” Model and Relation Between the Linear Viscoelastic Behaviours of Bituminous Binders and Mixes. *Road Materials and Pavement Design*, 4(2), 185–224. <https://doi.org/10.1080/14680629.2003.9689946>
- Olard, François, Di Benedetto, H., Eckmann, B., & Triquigneaux, J. P. (2003). Linear Viscoelastic Properties of Bituminous Binders and Mixtures at Low and Intermediate Temperatures. *Road Materials and Pavement Design*, 4(1), 77–107.

- <https://doi.org/10.1080/14680629.2003.9689941>
- Olard, François, Noël, F., & Loup, F. (2006). Modulus Testing in Indirect Tension Mode. *Road Materials and Pavement Design*, 7, 543–554. <https://doi.org/10.1080/14680629.2006.9690051>
- OMEGA. (n.d.). *Strain Gage Technical Data*. https://www.omega.fr/techref/pdf/STRAIN_GAGE_TECHNICAL_DATA.pdf
- Paquet, J. (1977). Un nouvel appareil d'auscultation des chaussées: Le Curviamètre. *Revue Générale Des Routes et Des Aérodrômes*, Avril, 79–107.
- Parmar, D., Shah, S., Kacha, S., Foundation, M. E., Foundation, M. E., & Foundation, M. E. (2018). Review of Piezo Resistivity effect of Carbon Nano Tube for potential use as sensor. 6(2), 207–210. <https://doi.org/11.25835/IJIK-261>
- Pereira, P., & Pais, J. (2017). Main flexible pavement and mix design methods in Europe and challenges for the development of an European method. *Journal of Traffic and Transportation Engineering (English Edition)*, 4(4), 316–346. <https://doi.org/10.1016/j.jtte.2017.06.001>
- PERRET, J. (2003). *Déformations des couches bitumineuses au passage d'une charge de trafic*. 2786, 263.
- Pokropivny, V. V., & Skorokhod, V. V. (2007). Classification of nanostructures by dimensionality and concept of surface forms engineering in nanomaterial science. *Materials Science and Engineering C*, 27(5-8 SPEC. ISS.), 990–993. <https://doi.org/10.1016/j.msec.2006.09.023>
- Porter, O. J. (1943). FOUNDATIONS FOR FLEXIBLE PAVEMENTS. *Highway Research Board Proceedings*, 22. <https://trid.trb.org/view/104549>
- Pouget, S., & Loup, F. (2013). Thermo-mechanical behaviour of mixtures containing bio-binders. *Road Materials and Pavement Design*, 14(SUPPL.1), 212–226. <https://doi.org/10.1080/14680629.2013.774758>
- Pouget, S., Olard, F., & Hammoum, F. (2016). *GB5® Mix Design: A New Approach for Aggregate Grading Optimization for Heavy Duty Flexible Pavements BT - 8th RILEM International Conference on Mechanisms of Cracking and Debonding in Pavements* (Armelle Chabot, W. G. Buttlar, E. V Dave, C. Petit, & G. Tebaldi (eds.); pp. 17–23). Springer Netherlands.
- Pouget, S., Sauzéat, C., Di Benedetto, H., & Olard, F. (2010). From the Behavior of Constituent Materials to the Calculation and Design of Orthotropic Bridge Structures. *Road Materials and Pavement Design*, 11(sup1), 111–144.

- <https://doi.org/10.1080/14680629.2010.9690329>
- Pouteau, B., Berrada, K., & Drouadaine, I. (2016). Smartvia concept : a 5 years feedback on standalone pavement structure monitoring. *6th Eurasphalt & Eurobitume Congress, 1-3 June, 2016, Prague, Czech Republic*. <https://doi.org/10.14311/ee.2016.202>
- Rajibul Islam, M., Mahmood Ali, M., Lai, M. H., Lim, K. S., & Ahmad, H. (2014). Chronology of fabry-perot interferometer fiber-optic sensors and their applications: A review. *Sensors (Switzerland)*, *14*(4), 7451–7488. <https://doi.org/10.3390/s140407451>
- Ramsden, J. J. (2011). Carbon-Based Nanomaterials and Devices. In *Nanotechnology: An Introduction* (pp. 189–197). Elsevier Inc. <https://doi.org/10.1016/b978-0-08-096447-8.00009-0>
- Rinaldi, A., Proietti, A., Tamburrano, A., De Bellis, G., Mulattieri, M., & Sarto, M. S. (2014). Multilayer graphene-based films for strain sensing. *Proceedings of the IEEE Conference on Nanotechnology*, 585–589. <https://doi.org/10.1109/NANO.2014.6967987>
- Rizvi, H. R., Khattak, M. J., Madani, M., & Khattab, A. (2016). Piezoresistive response of conductive Hot Mix Asphalt mixtures modified with carbon nanofibers. *Construction and Building Materials*, *106*, 618–631. <https://doi.org/10.1016/j.conbuildmat.2015.12.187>
- Roduner, E. (2006). Size matters: Why nanomaterials are different. *Chemical Society Reviews*, *35*(7), 583–592. <https://doi.org/10.1039/b502142c>
- RS PRO. (2018). *Datasheet: RS Pro Wire Lead Strain Gauge 4mm, 120Ω -30°C +180°C RS Stock No: 865-6226*. <https://docs-emea.rs-online.com/webdocs/1588/0900766b815882e1.pdf>
- Ruiz-Hitzky, E., Darder, M., Fernandes, F. M., Zatile, E., Palomares, F. J., & Aranda, P. (2011). Supported graphene from natural resources: Easy preparation and applications. *Advanced Materials*, *23*(44), 5250–5255. <https://doi.org/10.1002/adma.201101988>
- Saevarsdottir, T., Erlingsson, S., & Carlsson, H. (2016). Instrumentation and performance modelling of heavy vehicle simulator tests. *International Journal of Pavement Engineering*, *17*(2), 148–165. <https://doi.org/10.1080/10298436.2014.972957>
- Salençon, J. (2016). *Viscoélasticité pour le Calcul des structures*. Éditions de l'École polytechnique - Mai 2016, 91128 Palaiseau Cedex.
- Salour, F. (2015). *Moisture Influence on Structural Behaviour of Pavements - Field and Laboratory Investigations*. PhD Thesis. KTH, Royal Institute of Technology School of Architecture and the Built Environment, Stockholm, Sweden, April, 2015.

- Sangiorgi, C., Settimi, C., Tataranni, P., Lantieri, C., & Adomako, S. (2018). Thermal Analysis of Asphalt Concrete Pavements Heated with Amorphous Metal Technology. *Advances in Materials Science and Engineering*, 2018. <https://doi.org/10.1155/2018/6382874>
- Santos, A., Amorim, L., Nunes, J. P., Rocha, L. A., Silva, A. F., & Viana, J. C. (2019). Aligned carbon nanotube based sensors for strain sensing applications. *Sensors and Actuators, A: Physical*, 289, 157–164. <https://doi.org/10.1016/j.sna.2019.02.026>
- Sargent, J. F. (2014). *The National Nanotechnology Initiative: Overview, reauthorization, and appropriations issues*. Congressional Research Service Report. <https://fas.org/sgp/crs/misc/RL34401.pdf>
- Sayegh, G. (1966). *Contribution à l'étude des propriétés viscoélastiques des bitumes purs et des bétons bitumineux*. PhD Thesis. Université de Paris.
- Schreuders, H., & Marek, C. (1989). *Implication of Aggregates in the Design, Construction, and Performance of Flexible Pavements* (H. G. Schreuders & C. R. Marek (eds.)). (West Conshohocken, PA: ASTM International, 1989). <https://doi.org/10.1520/STP1016-EB>
- Selvaraj, S. I. (2012). Review on the Use of Instrumented Pavement Test Data in Validating Flexible Pavement Mechanistic Load Response Models. *Procedia - Social and Behavioral Sciences*, 43, 819–831. <https://doi.org/10.1016/j.sbspro.2012.04.157>
- Seppälä, S., Häkkinen, E., Alava, M. J., Ermolov, V., & Seppälä, E. T. (2010). Electrical transport properties of percolating random networks of carbon nanotube bundles. *Epl*, 91(4). <https://doi.org/10.1209/0295-5075/91/47002>
- SETRA; LCPC. (1998). *Catalogue des structures types de chaussées neuves* (SETRA-LCPC (ed.)).
- SETRA, & LCPC. (1994). *Conception et dimensionnement des structures de chaussée — Guide technique*.
- Shintake, J., Piskarev, E., Jeong, S. H., & Floreano, D. (2018). Ultrastretchable Strain Sensors Using Carbon Black-Filled Elastomer Composites and Comparison of Capacitive Versus Resistive Sensors. *Advanced Materials Technologies*, 3(3), 1–8. <https://doi.org/10.1002/admt.201700284>
- Silvestre, J., Silvestre, N., & De Brito, J. (2016). Review on concrete nanotechnology. *European Journal of Environmental and Civil Engineering*, 20(4), 455–485. <https://doi.org/10.1080/19648189.2015.1042070>
- Stankevich, N., Qureshi, N., & Queiroz, C. (2009). Performance-based Contracting for

- Preservation and Improvement of Road Assets. *The World Bank: Transport Notes No.TN-27*, 27, 1–11.
- Sun, L., Zhao, H., Tu, H., & Tian, Y. (2018). The Smart Road: Practice and Concept. *Engineering*, 4(4), 436–437. <https://doi.org/10.1016/j.eng.2018.07.014>
- Swett, L., Mallick, R. B., & Humphrey, D. N. (2008). A study of temperature and traffic load related response in different layers in an instrumented flexible pavement. *International Journal of Pavement Engineering*, 9(5), 303–316. <https://doi.org/10.1080/10298430701576117>
- Tabatabaee, N., & Sebaaly, P. (1990). State-of-the-Art Pavement Instrumentation. *Transportation Research Record*, 246–256. <http://onlinepubs.trb.org/Onlinepubs/trr/1990/1260/1260-022.pdf>
- Tang, W., Yan, T., Wang, F., Yang, J., Wu, J., Wang, J., Yue, T., & Li, Z. (2019). Rapid fabrication of wearable carbon nanotube/graphite strain sensor for real-time monitoring of plant growth. *Carbon*, 147, 295–302. <https://doi.org/10.1016/j.carbon.2019.03.002>
- Timm, D. H., Robbins, M. M., Willis, J. R., Tran, N., & Taylor, A. J. (2013). *NCAT Report 13-03 - FIELD AND LABORATORY STUDY OF HIGH-POLYMER MIXTURES AT THE NCAT TEST TRACK: FINAL REPORT*.
- Transportation Research Board. (2004). *NCHRP SYNTHESIS 325 - Significant Findings from Full-Scale Accelerated Pavement Testing* (T. R. Board (ed.)). Transportation Research Board.
- Transportation Research Board. (2009). *Use of Accelerated Pavement Testing to Evaluate Maintenance and Pavement Preservation Treatments* (Transportation Research Board (ed.); Issue September).
- Tsai, Y. C., & Chatterjee, A. (2018). Pothole Detection and Classification Using 3D Technology and Watershed Method. *Journal of Computing in Civil Engineering*, 32(2), 3–9. [https://doi.org/10.1061/\(ASCE\)CP.1943-5487.0000726](https://doi.org/10.1061/(ASCE)CP.1943-5487.0000726)
- Ullidtz, P. (1987). *Pavement Analysis*. Elsevier. <https://books.google.fr/books?id=bld3QgAACAAJ>
- Ullidtz, Per, Harvey, J., Tsai, B.-W., & Monismith, C. (2006). *Calibration of CalME models using WesTrack Performance Data* (Issue November).
- Vemuru, S. M., Wahi, R., Nagarajaiah, S., & Ajayan, P. M. (2009). Strain sensing using a multiwalled carbon nanotube film. *Journal of Strain Analysis for Engineering Design*, 44(7), 555–562. <https://doi.org/10.1243/03093247JSA535>
- Villette, Lebental, Jerbi, Buisson, Zakharov, Mathew, Tayrac, & Daveau. (2014). *Dispositif*

d'acquisition et un système de mesure comprenant un tel dispositif d'acquisition, servant à déterminer les valeurs de grandeurs susceptibles d'être déterminées à partir de mouvements d'un corps, ou substrat, déformable (Patent No. FR 19 05652).

- Wang, L., Xue, W., Druta, C., & Wang, D. (2012). *Integration of Structural Health Monitoring and Asset Management*.
- Wang, X., Lu, S., Ma, K., Xiong, X., Zhang, H., & Xu, M. (2015). Tensile strain sensing of buckypaper and buckypaper composites. *Materials and Design*, 88, 414–419. <https://doi.org/10.1016/j.matdes.2015.09.035>
- Weinmann, T. L., Lewis, A. E., & Tayabji, S. D. (2004). Pavement sensors used at accelerated pavement test facilities. *Proceedings of the 2nd International Conference on Accelerated Pavement Testing, Sep 26-29, 2004, November*, 1–30. http://scholar.google.com/scholar?hl=en&btnG=Search&q=intitle:No+Title#0%5Cnhttp://www.mrr.dot.state.mn.us/research/MnROAD_Project/index_files/pdfs/Weinmann_T.pdf
- Wen, S., & Chung, D. D. L. (2000). Uniaxial tension in carbon fiber reinforced cement, sensed by electrical resistivity measurement in longitudinal and transverse directions. *Cement and Concrete Research*, 30(8), 1289–1294. [https://doi.org/10.1016/S0008-8846\(00\)00304-5](https://doi.org/10.1016/S0008-8846(00)00304-5)
- Widyatmoko, I. (2016). Sustainability of bituminous materials. In *Sustainability of Construction Materials* (Second Edi). Elsevier Ltd. <https://doi.org/10.1016/b978-0-08-100370-1.00014-7>
- Williams, M. L., Landel, R. F., & Ferry, J. D. (1955). The Temperature Dependence of Relaxation Mechanisms in Amorphous Polymers and Other Glass-forming Liquids. *Journal of the American Chemical Society*, 77(14), 3701–3707. <https://doi.org/10.1021/ja01619a008>
- Wincheski, B., Gardner, J., Sauti, G., Ruth, A., McVay, E., & Siochi, E. (2019). Direct printing of graphene sensors for health monitoring of additively manufactured structures. *AIP Conference Proceedings*, 2102(May). <https://doi.org/10.1063/1.5099711>
- Yamada, T., Hayamizu, Y., Yamamoto, Y., Yomogida, Y., Izadi-Najafabadi, A., Futaba, D. N., & Hata, K. (2011). A stretchable carbon nanotube strain sensor for human-motion detection. *Nature Nanotechnology*, 6(5), 296–301. <https://doi.org/10.1038/nnano.2011.36>
- Yang, Q., Liu, Q., Zhong, J., Hong, B., Wang, D., & Oeser, M. (2019). Rheological and

- micro-structural characterization of bitumen modified with carbon nanomaterials. *Construction and Building Materials*, 201, 580–589. <https://doi.org/10.1016/j.conbuildmat.2018.12.173>
- Yee, M. J., Mubarak, N. M., Abdullah, E. C., Khalid, M., Walvekar, R., Karri, R. R., Nizamuddin, S., & Numan, A. (2019). Carbon nanomaterials based films for strain sensing application—A review. *Nano-Structures and Nano-Objects*, 18, 100312. <https://doi.org/10.1016/j.nanoso.2019.100312>
- Yoo, D. Y., Kim, S., Kim, M. J., Kim, D., & Shin, H. O. (2019). Self-healing capability of asphalt concrete with carbon-based materials. *Journal of Materials Research and Technology*, 8(1), 827–839. <https://doi.org/10.1016/j.jmrt.2018.07.001>
- Yoo, D. Y., You, I., & Lee, S. J. (2017). Electrical properties of cement-based composites with carbon nanotubes, graphene, and graphite nanofibers. *Sensors (Switzerland)*, 17(5). <https://doi.org/10.3390/s17051064>
- Zhang, Dejin, Zou, Q., Lin, H., Xu, X., He, L., Gui, R., & Li, Q. (2018). Automatic pavement defect detection using 3D laser profiling technology. *Automation in Construction*, 96(May), 350–365. <https://doi.org/10.1016/j.autcon.2018.09.019>
- Zhang, Dongzhi, Jiang, C., Tong, J., Zong, X., & Hu, W. (2018). Flexible Strain Sensor Based on Layer-by-Layer Self-Assembled Graphene/Polymer Nanocomposite Membrane and Its Sensing Properties. *Journal of Electronic Materials*, 47(4), 2263–2270. <https://doi.org/10.1007/s11664-017-6052-1>
- Zheng, Y., Li, Y., Dai, K., Wang, Y., Zheng, G., Liu, C., & Shen, C. (2018). A highly stretchable and stable strain sensor based on hybrid carbon nanofillers/polydimethylsiloxane conductive composites for large human motions monitoring. *Composites Science and Technology*, 156, 276–286. <https://doi.org/10.1016/j.compscitech.2018.01.019>
- Zymelka, D., Yamashita, T., Takamatsu, S., Itoh, T., & Kobayashi, T. (2017). Printed strain sensor with temperature compensation and its evaluation with an example of applications in structural health monitoring. *Japanese Journal of Applied Physics*, 56(5). <https://doi.org/10.7567/JJAP.56.05EC02>

Titre : Technologie à base de nano-capteurs pour le monitoring des routes

Mots clés : chaussée, monitoring, instrumentation, modélisation, nanotechnologie

Résumé : Le réseau routier est l'un des atouts majeurs d'un pays. L'évaluation de l'état structurelle des infrastructures de transport routier et de leur évolution dans le temps est essentielle pour l'établissement de plans d'entretien rentables. À cet égard, l'instrumentation des chaussées permet une surveillance continue et à distance sans interruption de la circulation. Cependant, l'instrumentation reste un défi scientifique et technologique majeur en termes de résilience des dispositifs ainsi que de stratégies d'interprétation des données des capteurs. L'objectif global de cette thèse est de prouver la faisabilité du monitoring des routes par technologies de détection embarquées en démontrant l'exploitabilité des données de capteurs pour évaluer le vieillissement de la route et en fournissant une technologie à haute performance et faible intrusion.

Nous proposons, via un essai accéléré à l'échelle 1, une validation des jauges de déformation pour la prédiction de l'endommagement par fatigue d'un revêtement routier. Ainsi, nous avons exploré l'utilisation de capteurs embarqués pour le calcul inverse des conditions mécaniques de la chaussée via l'instrumentation d'une route existante avec un réseau de jauges de déformation. La même section d'essai a servi d'environnement pour une première validation d'une nouvelle technologie de détection basée sur l'utilisation de capteurs de déformation flexibles à base de nanocarbone, testés plus tard dans la chaussée dans le cadre d'un essai accéléré. Nous avons ainsi démontré comment la nanotechnologie proposée pouvait répondre aux enjeux de l'instrumentation des chaussées en termes de géométrie, de compatibilité avec l'environnement routier, et de sensibilité.

Title : Nanosensor technology for road pavement monitoring

Keywords : road pavement, monitoring, instrumentation, modelling, nanotechnology

Abstract : The road network is one of the major assets in our countries. The assessment of pavement conditions and their evolution with time is essential for the establishment of cost-effective maintenance plans. In this respect, pavement instrumentation allows remote and continuous monitoring with no traffic disruption. However it remains a major scientific and technological challenge in terms of devices resilience to the harsh road environment as well as of strategies for sensor data interpretation. The overall goal of this thesis is to prove the feasibility of embedded pavement monitoring by demonstrating the exploitability of embedded sensor data to assess road ageing, and by providing a high performance, low intrusiveness technology.

We propose, via an accelerated pavement test, a validation of asphalt strain gauges as monitoring method for fatigue prediction in a road pavement. Thus, we further explored the use of embedded sensors for inverse calculation of pavement mechanical conditions via the instrumentation of an existing road with a network of asphalt strain gauges. The same trial section was the environment for a first validation of a novel sensing technology based on the use of nanocarbon-based flexible strain sensors, later tested under an accelerated pavement test. Thereby we demonstrated how the proposed nanotechnology can overcome some of the drawbacks of existing sensing devices in terms of geometry, compatibility with the road environment, and sensitivity.